October/octobre
2005

Volume 31, No. 5
E-ISSN 1712-7971
CD-ISSN 1712-798X

CANADIAN JOURNAL OF REMOTE SENSING

JOURNAL CANADIEN DE TÉLÉDÉTECTION

Special issue
Earth observation of Canada's landmass: results and future needs
A workshop in honour of Josef Cihlar
on the occasion of his retirement
Ottawa, 30 September – 1 October 2004

Numéro spécial
L'observation satellitaire de la masse continentale canadienne : résultats et besoins futurs
Un atelier en l'honneur de Josef Cihlar
à l'occasion de son départ à la retraite
Ottawa, 30 septembre – 1 octobre 2004

Published by • Publié par
Canadian Aeronautics and Space Institute
Institut aéronautique et spatial du Canada
105 - 1750, croissant Courtwood Crescent
Ottawa, Ontario, Canada K2C 2B5
Tel./Tél. : 613-234-0191, Fax/Téléc. : 613-234-9039
casi@casi.ca www.casi.ca

Canadian Journal of Remote Sensing / Journal canadien de télédétection

Published six times per year, the *Canadian Journal of Remote Sensing* is the official journal of the Canadian Remote Sensing Society, a constituent society of the Canadian Aeronautics and Space Institute. The Editorial Board invites the submission of new and unpublished papers, research notes, and technical notes for publication in the Journal. Topics — including data acquisition, information processing methods, and applications development — may address technical topics of interest to the Canadian and international remote sensing communities. The Editorial Board examines all submitted papers before acceptance for publication.

Submission of Manuscripts
Submission and review of manuscripts for the *Canadian Journal of Remote Sensing* takes place through the Web site http://mc.manuscriptcentral.com/cjrs-jct. Initial submission should consist of a single file with all figures embedded, in Word, RTF, or PDF format. The submission format should follow the style shown on the inside back cover or on our Web site at http://www.casi.ca/index.php?pg=cjrs. If submission is not possible through the Internet, please contact the Editor to make alternative arrangements.

Page Charges
The author or organization sponsoring the work reported in any paper or article published will be asked to pay publication charges of $125 per page.

The Society is not responsible for statements or opinions expressed in papers or discussions printed in its publication. All communications should be addressed to: Publications Department, Canadian Aeronautics and Space Institute, 105-1750 Courtwood Crescent, Ottawa, ON K2C 2B5, Canada, telephone: 613-234-0191, fax: 613-234-9039, e-mail: casi@casi.ca.

Publishing Services
NRC Research Press
National Research Council Canada
Ottawa, ON K1A 0R6
Canada

Publications Mail Registration No. 40069141

U.S. periodical postage paid at Champlain, N.Y., and at additional mailing offices. Attention U.S. POSTMASTER: Send address changes to the *Canadian Journal of Remote Sensing*, c/o USACAN Media Distribution Center, P.O. Box 2888, Plattsburgh, NY 12901, USA.

Publié six fois par année, le *Journal canadien de télédétection* est la publication officielle de la Société canadienne de télédétection, société constituante de l'Institut aéronautique et spatial du Canada. Le Conseil éditorial sollicite des contributions nouvelles, non-publiées ailleurs, sous forme d'articles de recherche, de notes de recherche, et d'articles de synthèse techniques, pour le Journal. Les sujets doivent intéresser les communautés de télédétection canadienne et internationale, tel que l'acquisition des données, les méthodes de traitement des données, et le développement des applications. Toute soumission doit être acceptée par le Conseil éditorial avant de passer à la publication.

Soumission des manuscrits
La soumission et l'évaluation des manuscrits pour le *Journal canadien de télédétection* se font par le biais du site Web http://mc.manuscriptcentral.com/cjrs-jct. La soumission initiale devrait consister en un fichier unique avec toutes les figures intégrées en format Word, RTF ou PDF. Le format de présentation devrait emprunter le style illustré à l'intérieur du revers ou sur notre site Web http://www.casi.ca/index.php?pg=cjrs. Si vous ne pouvez utiliser Internet, veuillez svp contacter le Rédacteur pour trouver une solution de rechange.

Frais de publication
Des frais de publication de 125 $ par page seront demandés à l'auteur ou à l'organisme parrainant le travail décrit dans toute communication ou article publié.

La Société n'est pas responsable des déclarations ou des opinions exprimées dans les articles ou des discussions publiées dans le Journal. Toutes les communications doivent être adressées au Service des publications, Institut aéronautique et spatial du Canada, 150-1750, croissant Courtwood, Ottawa, ON K2C 2B5, Canada, téléphone : 613-234-0191, télécopieur : 613-234-9039, courrier : casi@casi.ca.

Services d'édition
Presses scientifique du CNRC
Conseil national de recherches Canada
Ottawa, ON K1A 0R6
Canada

N° d'enregistrement postal : 40069141

CJRS is covered by the following ISI® services / Le JCT bénéficie des services suivants de l'ISI® (Institute for Scientific Information) : ISI Web of Science®, Science Citation Index Expanded™, ISI Alerting Services™, Current Contents®/Physical, Chemical and Earth Sciences, and / et Current Contents®/Engineering, Computing, and Technology

October 2005 octobre Volume 31, No. 5

Canadian Journal of Remote Sensing / Journal canadien de télédétection
Contents / Table des matières

Special issue
Earth observation of Canada's landmass: results and future needs
A workshop in honour of Josef Cihlar on the occasion of his retirement
Ottawa, 30 September – 1 October 2004

Numéro spécial
L'observation satellitaire de la masse continentale canadienne : résultats et besoins futurs
Un atelier en l'honneur de Josef Cihlar à l'occasion de son départ à la retraite
Ottawa, 30 septembre – 1 octobre 2004

Cover photo • Page couverture

Participants in "Earth observation of Canada's landmass: results and future needs. A workshop in honour of Josef Cihlar on the occasion of his retirement, Ottawa, 30 September – 1 October 2004".

✦

Les participants de l'atelier « L'observation satellitaire de la masse continentale canadienne : résultats et besoins futurs. Un atelier en l'honneur de Josef Cihlar à l'occasion de son départ à la retraite, Ottawa, 30 septembre – 1 octobre 2004 ».

Publication of the Canadian Journal of Remote Sensing is made possible by a grant from **Geomatics Canada.**

❖

La publication du Journal canadien de télédétection est possible grâce à une subvention de **Géomatique Canada.**

Preface

Special issue
Earth observation of Canada's landmass: results and future needs
A workshop in honour of Josef Cihlar on the occasion of his retirement
Ottawa, 30 September – 1 October 2004

The papers published in this special issue are drawn from the materials presented at the workshop held at the Canada Centre for Remote Sensing (CCRS), Natural Resources Canada, in the fall of 2004, in honor of Josef Cihlar on the occasion of his retirement. Josef received his Ph.D. in physical geography and remote sensing in 1975 from the University of Kansas and started working at CCRS the same year. During these years, he published hundreds of papers, book chapters, and major reports. His outstanding achievements are recognized by a long list of awards, including the following: Autometric Award, the American Society of Photogrammetry, 1984; Certificate of Achievement, Exceptional Collaborative Research and Technology Transfer, Agriculture and Agri-Food Canada, 1994; Head of the Public Service Award for Excellence in Service Delivery, Clerk of the Privy Council, Government of Canada, 1998; Agatha Bystram Award, Leadership in Information Management, 1999; Distinction '99 Award, President of the Treasury Board, Government of Canada; Alouette Award, the Canadian Aeronautics and Space Institute, 2000; Elected Fellow of the Royal Society of Canada, 2000; and Earth Sciences Sector Merit Awards, 2003 and 2004.

For the people who have known Josef for many years, the news of his retirement was difficult to accept. Josef Cihlar was considered as a senior because of his broad knowledge, extensive experience, and brilliant intelligence, not because of his age. He is the type of person who can always offer the best advice for scientific, technical, or life problems. In reaction to the retirement news, there was almost immediate and unanimous agreement that this event should not be reduced simply to a farewell luncheon. Rather, it should be a fitting tribute to a great person and scientist, and in keeping with Josef's spirit of focusing on practical outcomes and outputs, a scientifically useful exercise. The fall 2004 workshop emerged as this tribute and was supported with great enthusiasm. More than 100 attendees (74 of them pictured in the group photo on the front cover of this journal) came from different parts of Canada and the United States for this special occasion.

The relatively short period of time allocated to prepare and complete this special issue (about 1 year) and the fact that many of the presented papers were submitted to other journals meant that not all of the papers presented at the workshop were submitted as manuscripts to this special issue. However, the scope of papers in this issue covers much of the range of presented activities and reflects the major areas of Josef's interests. Dr. Frank Ahern kindly agreed to write a paper giving an overview of Josef Cihlar's career. All papers went through the normal and thorough peer-review process, and we believe they will serve a dual purpose as good science and as a mark of respect to a great person.

We would like to thank the authors, reviewers, and Dr. Joseph R. Buckley, Editor of the *Canadian Journal of Remote Sensing* (CJRS), for providing the opportunity to be guest editors for this special issue of CJRS.

Guest Editors
Alexander Trishchenko and Wenjun Chen
Canada Centre for Remote Sensing
Natural Resources Canada
588 Booth Street, Ottawa, ON K1A 0Y7, Canada
E-mail: trichtch@ccrs.nrcan.gc.ca, wchen@ccrs.nrcan.gc.ca

Préface

Numéro spécial
L'observation satellitaire de la masse continentale canadienne : résultats et besoins futurs
Un atelier en l'honneur de Josef Cihlar à l'occasion de son départ à la retraite
Ottawa, 30 septembre – 1 octobre 2004

Les articles publiés dans ce numéro spécial sont tirés des documents présentés à l'atelier tenu au Centre canadien de télédétection (CCT) de Ressources naturelles Canada, à l'automne 2004, pour souligner la retraite de Josef Cihlar. En 1975, Josef a obtenu son doctorat en géographie physique et en télédétection de l'Université du Kansas et a commencé à travailler au CCT cette même année. Au fil des ans, il a publié des centaines d'articles, de chapitres de livre et de rapports importants. Ses réalisations exceptionnelles lui ont valu de nombreux prix, notamment le prix Autometric de l'American Society of Photogrammetry, en 1984; le certificat de mérite décerné par Agriculture et Agroalimentaire Canada pour la recherche et le transfert de technologie fondés sur la collaboration, en 1994; le Prix du chef de la fonction publique remis par le greffier du Conseil privé du gouvernement du Canada pour l'excellence en prestation de services, en 1998; le prix Agatha-Bystram, pour son leadership en gestion de l'information, en 1999; le prix de distinction présenté par le président du Conseil du Trésor du gouvernement du Canada, en 1999; le prix Alouette de l'Institut aéronautique et spatial du Canada, en 2000, et le prix au mérite du Secteur des sciences de la Terre, en 2003 et en 2004. Il a aussi été élu membre de la Société royale du Canada, en 2000.

Pour ceux qui connaissent Josef depuis de nombreuses années, la nouvelle de sa retraite a été difficile à accepter. Josef Cihlar était considéré comme un vétéran non pas en raison de son âge, mais bien pour ses vastes connaissances, sa très grande expérience et sa brillante intelligence. Il est le genre de personne qui offre toujours les meilleurs conseils que ce soit pour les problèmes scientifiques, techniques ou personnels. Presqu'aussitôt après l'annonce de sa retraite, il a été décidé à l'unanimité qu'un simple dîner d'adieu ne suffirait pas. Cet événement devrait plutôt être souligné par un hommage approprié à une personne extraordinaire et un scientifique exceptionnel et devrait, compte tenu de l'importance que Josef accorde aux résultats pratiques, être un exercice scientifique utile. L'atelier, qui s'est déroulé à l'automne 2004, est devenu cet hommage et a été appuyé avec beaucoup d'enthousiasme. Plus de 100 participants (74 d'entre eux se trouvent sur la photo de groupe publiée sur la page couverture de la revue) sont venus de différentes régions du Canada et des États-Unis pour cette occasion spéciale.

En raison du peu de temps dont nous disposions pour la préparation et l'élaboration de ce numéro spécial (environ 1 an) et du fait qu'un grand nombre des articles présentés ont été soumis à d'autres revues, ce ne sont pas tous les articles présentés à l'atelier qui ont été soumis comme manuscrits pour ce numéro spécial de la revue. Cependant, les articles publiés dans ce numéro couvrent une bonne partie des différentes activités présentées et reflètent les principaux domaines d'intérêt de Josef. Dr. Frank Ahern a généreusement accepté de rédiger un article dans lequel il donne un aperçu de la carrière de Josef Cihlar. Tous les articles ont fait l'objet de l'évaluation habituelle et exhaustive par des pairs, et nous croyons qu'ils présentent un contenu scientifique solide et constituent une marque de respect envers cet homme extraordinaire.

Nous souhaitons remercier les auteurs, les réviseurs et le rédacteur du *Journal canadien de télédétection* (JCT), Dr. Joseph R. Buckley, pour nous avoir donné la possibilité de contribuer à titre de rédacteurs invités à ce numéro spécial du JCT.

Rédacteurs invités
Alexander Trishchenko et Wenjun Chen
Centre canadien de télédétection
Ressources naturelles Canada
588, rue Booth, Ottawa, ON K1A 0Y7, Canada
Courriel : trichtch@CCT.rncan.gc.ca, wchen@CCT.rncan.gc.ca

Can. J. Remote Sensing, Vol. 31, No. 5, pp. 315–323, 2005

Review / Synthèse

Josef Cihlar: a career of science and service to Canada and the world

Frank Ahern

Abstract. The academic world has a long-standing tradition to honour outstanding researchers and academics with a symposium. Josef Cihlar is certainly well deserving of this honour, and this special issue of the *Canadian Journal of Remote Sensing* serves to document the proceedings of the symposium held for Josef in October 2004. In this paper I review his career to highlight the contributions he has made to his department, Canada, and the world. These contributions include a very substantial addition to the scientific literature, including many papers published in the leading remote sensing journals. They also include critical contributions to the remote sensing programs of the Canada Centre for Remote Sensing and Canada. He has provided a fertile environment for research that has stimulated productive careers of numerous colleagues and younger scientists. Even more significantly, Josef Cihlar has provided influential leadership for the Canadian Global Change Program and the international effort to determine Earth's terrestrial carbon budget. The totality of these accomplishments amounts to a most remarkable career.

Résumé. Le milieu académique a une longue tradition d'honorer les chercheurs et les professeurs émérites par le biais d'un symposium. Josef Cihlar est certainement tout désigné pour cet honneur et ce numéro spécial du *Journal canadien de télédétection* se veut un témoignage en présentant les comptes rendus du symposium tenu pour Josef en octobre 2004. Dans cet article, nous passons en revue sa carrière afin de souligner les contributions qu'il a apportées à son ministère, au Canada et au monde. Ses réalisations incluent un apport très substantiel à la littérature scientifique, dont plusieurs articles publiés dans les revues de télédétection les plus prestigieuses. Elles incluent également des contributions critiques visant les programmes de télédétection du Centre canadien de télédétection et du Canada. Il a créé un environnement fertile pour la recherche qui a permis de stimuler la carrière productive de plusieurs collègues et jeunes chercheurs. Plus significativement, Josef Cihlar a fait preuve d'un leadership qui a su influencer le Programme canadien des changements à l'échelle du globe et l'effort international en vue de déterminer le bilan du carbone planétaire. L'ensemble de ces réalisations constitue l'assise d'une carrière remarquable.
[Traduit par la Rédaction]

Introduction

"Canada is a country made for remote sensing." So spoke Dr. Larry Morely, the driving force that brought the Canada Centre for Remote Sensing (CCRS) into being and led it as Director General during the initial years. The challenge of making remote sensing a reality for Canada brought out the best in a team of scientists, engineers, technicians, directors, and administrators. Over the next 25 years CCRS scientists and engineers were recognized around the world for their knowledge and innovation in data acquisition, data storage and processing, and the development and dissemination of practical applications of the emerging technology. Among many shining stars, the Sirius was Josef Cihlar (**Figure 1**).

A refugee to Canada after the 1968 Soviet invasion of Czechoslovakia, Josef completed a career of remarkable achievement and service in 2004. At the time of his retirement, he was so loved and respected by the scientists, technicians, and administrators who worked for him that they organized a workshop to honour him. This paper is the outgrowth of an invited oral presentation at that workshop. The intent is to provide a permanent written record of his exemplary career. Those who knew him and worked with him should enjoy having this memento. Those who come later can see what "aiming high" is all about.

Curriculum vitae

To provide a framework, I review Josef's life journey here in text and with the aid of a whimsical graphic (**Figure 2**).

Josef Cihlar was born in Kozmice, Czechoslovakia, on the 6th of October 1944 in a family that farmed for a living. Except for shortages, the war did not cause direct hardship to his family. After the war, the Communist Party took power in a bloodless coup in 1948, but again this did not affect the Cihlar family for several years. Josef enjoyed working on the farm and found a love for horses that has become an important part of his post-retirement activities.

Josef's village became a farming collective in 1956. Josef's horizons began to expand as he grew older. He studied at the University of Agriculture in Prague from 1962 to 1967,

Received 14 February 2005. Accepted 9 August 2005.

F. Ahern. TerreVista Earth Imaging, 441 Cormac Road, Cormac, ON K0J 1M0, Canada (e-mail: f-ahern@nrtco.net).

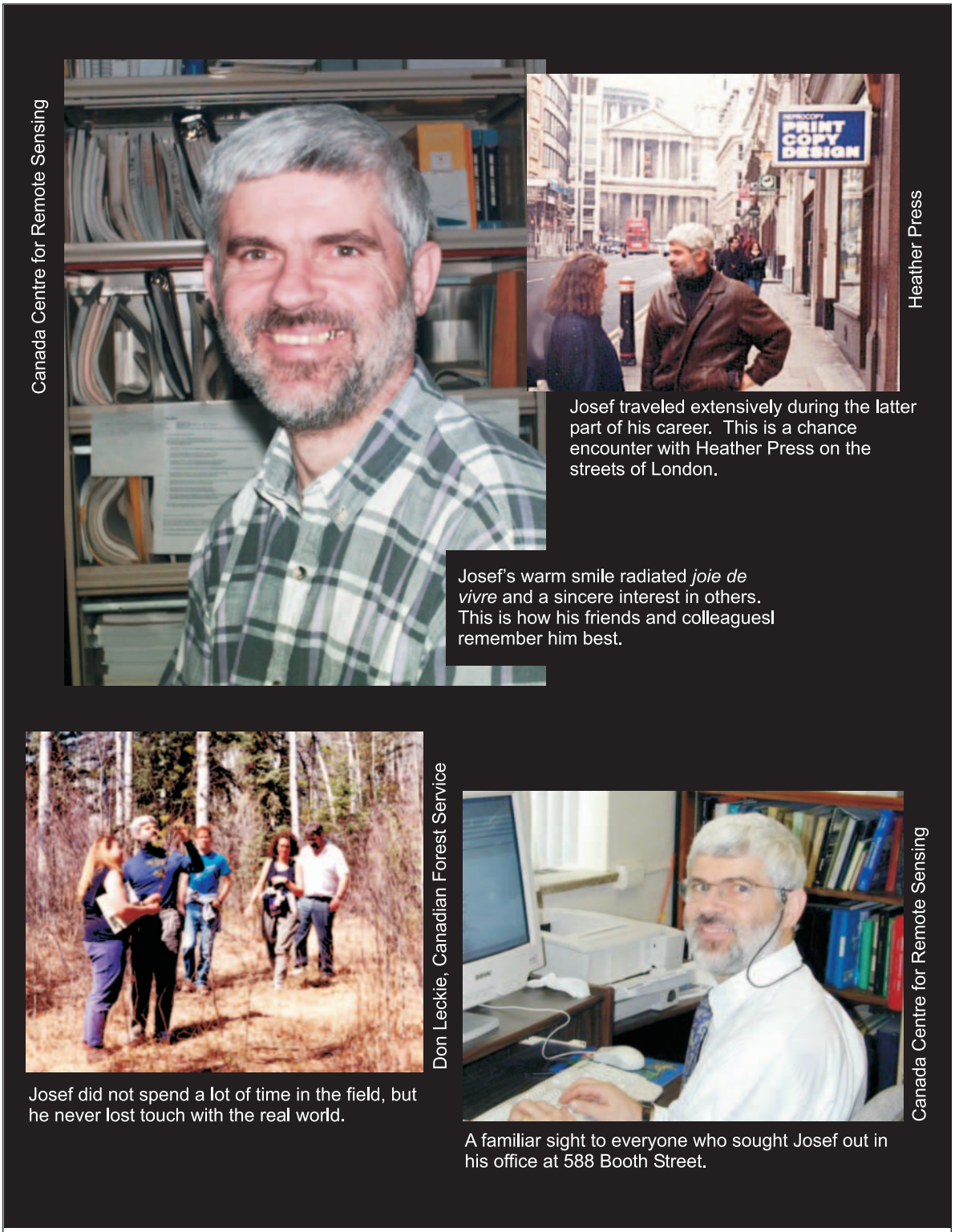

Figure 1. Josef Cihlar.

receiving a B.Sc. in agricultural engineering, including a bachelor's thesis in soil water management and drainage. He completed 1 year of compulsory military service in August 1968, 2 weeks before the Soviet invasion. Before that cataclysmic event, he had been making plans to study overseas in an English-speaking country. His first choice was the University of Guelph. Josef obtained a student visa and moved to Canada just before studies in the West were forbidden by the increasingly pro-Soviet regime. He earned an M.Sc. degree in soil science under Richard Protz in 1971, exploring the use of

colour aerial photography for soil mapping. Just before his graduation in 1971, he married Rosemary McCaw of Milford, Ontario.

The appeal of remote sensing became irresistible, and soil science remained the application that drove his interest. He chose the University of Kansas for doctoral studies because of its excellent program in radar, one of only two or three in the world at that time. He wanted to find out if radar could provide information on subsoil conditions, particularly soil moisture. Fawwaz Ulaby, an immigrant from Syria, had recently arrived at Kansas, beginning his ascent toward becoming a most prolific and respected academic in the field of microwave remote sensing. Josef gravitated to Ulaby as both a mentor and role model. He could not have picked a better person to emulate than this renowned leader and researcher. In 1975 Josef presented and defended his dissertation, "Soil moisture and temperature regimes and their importance to microwave remote sensing of soil water," and was awarded a Ph.D. in geography and remote sensing.

By the time he defended his dissertation, Josef had already accepted a job offer from the Applications Division of CCRS. Both he and Rosemary wanted to return to Canada.

It is worth noting that the CCRS of 1975 differed from many federal agencies that had research scientists on staff. While research scientists in many departments seemed to think that they were entitled to pursue pure research of their own choosing, that attitude was not highly regarded at CCRS. Research direction was strongly guided by senior management. Practical, operational use of the new technology was the priority, together with infrastructure that would support those applications, such as innovative sensors, efficient means for data processing, data storage, and data dissemination. Josef flourished in this climate.

Josef quickly began pursuing and publishing innovative research and working with users to get the results adopted operationally. He rapidly demonstrated interest and ability in leadership as well. He won a competition for head of the Applications Development Section in 1979, a position he held until 1991. Soon after taking on this new challenge, he assembled six teams to develop and implement remote sensing for agriculture, forestry, geology, hydrology, ice, and oceans. Each team was headed by a scientist who either was already producing world-class results or would soon begin to do so in the effective environment Josef and CCRS management provided. This was a "golden age" for the development of remote sensing technology in Canada. Many of the approaches developed at CCRS were world firsts. Many were adopted internationally, and CCRS earned a reputation abroad of providing excellent results on a modest budget.

During this time, Josef's management approach was to ensure that each of the six discipline leaders had adequate resources and was pursuing sensible goals on an ambitious timetable. This left him time to become involved in planning the RADARSAT mission, one of Canada's biggest space triumphs of the 20th century. From 1983 to 1985 Josef put a tremendous amount of time and energy toward defining the user requirements for RADARSAT data. He was instrumental in mobilizing the user community, many of whom initially viewed RADARSAT as a technology toy rather than a serious tool.

RADARSAT had been planned and justified almost entirely as a means to deliver ice imagery to support oil exploration and sovereignty in the Arctic. Under Josef's leadership many new applications were examined. Those that looked practical were pursued; those that did not were discarded. As oil prices declined during the early 1980s, RADARSAT required broader justification and support. Josef's applications group proposed numerous additional applications for RADARSAT (Cihlar et al., 1982).

As the 1980s drew to a close, Josef recognized the importance of climate change. The reception at CCRS of Josef's new obsession ranged from lukewarm acceptance to

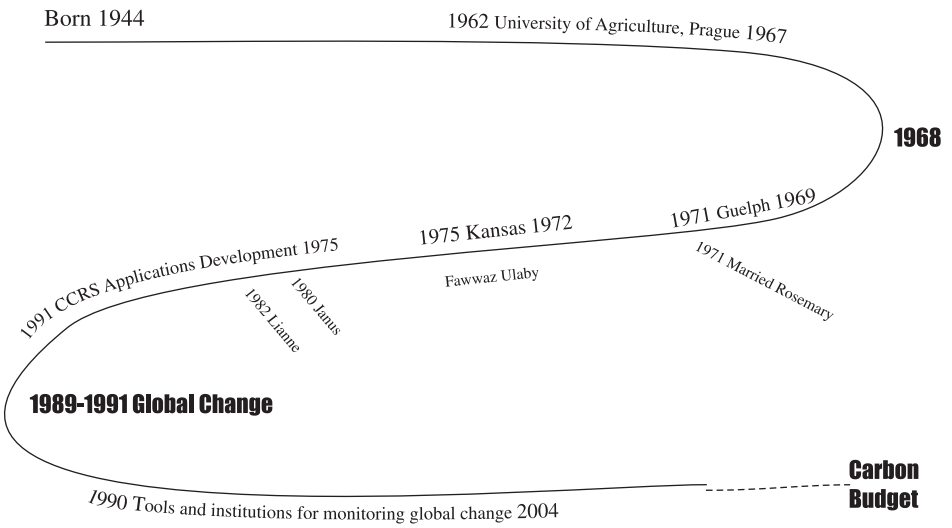

Figure 2. The life journey of Josef Cihlar. This figure summarizes the major events of Josef's life.

outright hostility. He turned to the Royal Society of Canada, found some support, and got a modest program underway (Cihlar et al., 1989). From that base he led or contributed substantially to several initiatives that linked remote sensing to climate change. His energy level was incredible, he began to make converts, and more substantial funding began to flow from several sources including CCRS, the Canadian Space Agency (CSA), and the National Aeronautics and Space Administration (NASA). By 1991 CCRS had a Global Monitoring Section with Josef as its head.

The new section needed new scientists. Josef became his own talent scout and soon landed bright, energetic, and devoted scientists from around the world, particularly China and Eastern Europe.

By the mid-1990s Josef was becoming a major international presence. I review that aspect of his career later in the paper. Suffice it to say that he made a major mark on a number of international endeavours that were aimed at monitoring global change.

At the time he announced his intention to retire in 2004, Josef was leading efforts that were making major advances on two fronts: to monitor the processes that determine Canada's carbon budget domestically, and to establish the institutions and methods to do the same on a global basis. This is why "carbon budget" is shown as the long-term objective in **Figure 2**. Many have wondered why Josef chose to retire when he was still going strong and the carbon budget objective was still not close at hand. For Josef, the joy of work came in pursuing the objective more than achieving it. He realized that he had reached a time for another turning point in his life, to find new objectives and pursue them with the same energy and determination.

Achievement and service

Scientific productivity

One simple measure of a scientist's research output is to count papers. By the end of 2004 Josef had published over 260 research papers, technical reports, or articles, including over 130 in refereed journals. It is even more instructive to read the titles, authors, and journals of his list of publications. The majority of his refereed publications appear in major national and international journals. Josef's coauthors include many well-known and respected Canadian and international scientists. The titles show perseverance toward clearly defined goals in a number of areas: heat loss from buildings, applications of microwave remote sensing, particularly of soil, and of course the terrestrial component of Earth's carbon budget. In the latter, Josef and his group had to develop a large amount of new methodology to use, calibrate, and correct continental datasets, particularly with the advanced very high resolution radiometer (AVHRR)[1] sensor. This work was just not getting done satisfactorily elsewhere, and Josef made sure it got done at CCRS. In so doing, his group developed a very solid scientific and technical foundation for subsequent global monitoring efforts.

What comes across in reading his list of publications is Josef's ability to assemble large, highly talented teams, keep them focused on a long-term goal, and keep them working harmoniously to achieve his vision. This is a common pattern of career progression for an outstanding scientist. It can produce an exponential growth, a chain reaction effect, which can be called the science cascade (see **Figure 3**). Josef produced two science cascades during his career, first through the applications development program of the 1980s, and subsequently through a larger cascade in the global change program of the 1990s. He was also very effective at partnering with other organizations.

Perhaps his most notable achievement was pioneering global change research in Canada. Josef realized that global climate change was going to be very important for the 21st century, before most others in Canada. He got a Canadian global change program up and running at CCRS despite a reception from most CCRS managers that was skeptical at best. His approach was one of persistent persuasion. According to one senior CCRS manager, he employed logic that could not be denied and was continually questing for more resources, but in a way that was patient rather than unpleasant. Compared to other seekers of support, he was more patient, more willing to listen and explain, and did not appear to be overstating his case.

Service to CCRS, Canada, and the world

The productivity discussed in the previous section, and the international leadership that went with it, alone would have been enough to propel Josef to the top of the research scientist category within the Government of Canada, but his career was distinguished even more by service to CCRS, Canada, and the world.

This characteristic first emerged in a 1979 review of the status of the usage of remote sensing for forestry, wildlife, wildlands, and biophysical inventory (Cihlar and Rubec, 1979). This led to a wider study of the status of remote sensing at the provincial level throughout Canada, recommendations to increase the transfer of remote sensing technology to the provinces (Cihlar, 1980), and ultimately the establishment of a

[1] This was the primary optical sensor on the National Oceanic and Atmospheric Administration (NOAA) polar-orbiting weather satellite series. Although the resolution might have been "very high" for a weather satellite, the 1.1 km resolution (at nadir) was very low compared with that of the optical sensors in general use by CCRS. AVHRR had the advantage of providing total coverage of all of Canada every day. Of course, much of Canada is covered with clouds every day. A technique developed and refined at CCRS, called compositing, picks the clearest pixels from images acquired over time periods of 7–10 days, producing a reasonably cloud free image of the country for that time interval. Although AVHRR data lack the spatial resolution of data from satellites like Landsat, they provide superior temporal resolution and spatial extent, and thus are very complementary to the higher resolution data. AVHRR data have now been superceded by data from more recent sensors, but the methods developed for AVHRR data can now be applied to the improved data from these newer sensors.

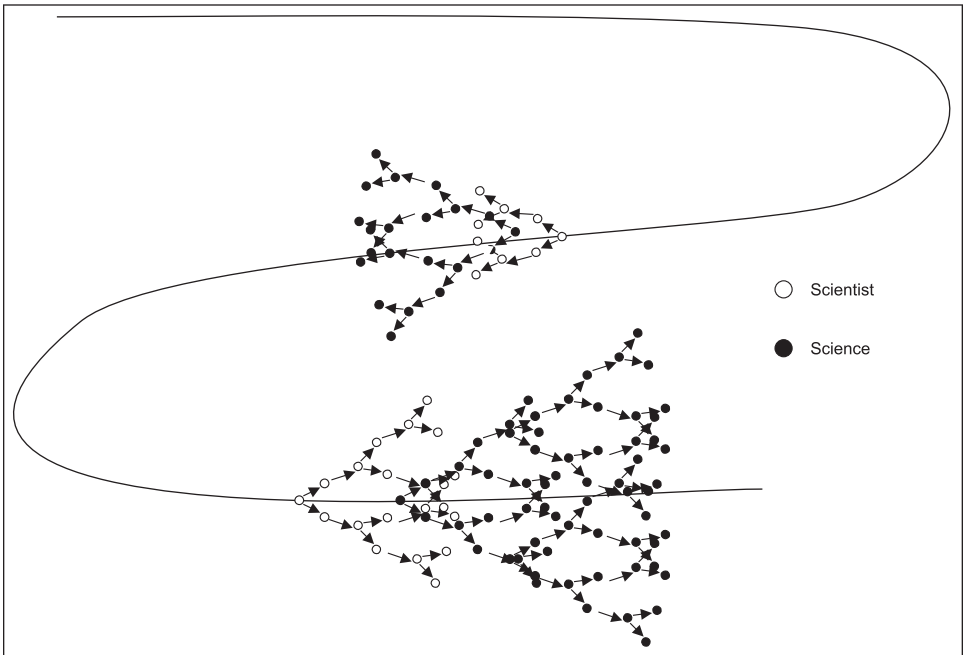

Figure 3. Two science cascades initiated by Josef Cihlar.

technology transfer section at CCRS. Josef was the originator of the concept that led to the technology transfer program at CCRS and provided management and leadership during its establishment phase.

Once the applications development effort was in the capable hands of the various discipline coordinators, Josef turned his attention to his first love: the application of synthetic aperture radar (SAR) data. The development of RADARSAT was making the transition to phase B, where credible practical applications for the data needed to be made. At the same time, the original justification for RADARSAT was becoming quite shaky.[2] Josef led a group that developed the user requirements for renewable land resources in Canada (i.e., agriculture, forestry, wetlands, rangeland). The report produced a very convincing case for the practical value of the C-HH SAR data proposed for RADARSAT for these applications. Josef then went on to lead the group that defined all of the applications of RADARSAT. The final RADARSAT phase B user requirements document produced under Josef's leadership appeared in 1985 (Cihlar et al., 1985).

Canadian Global Change Program

Josef's association with the Canadian Global Change Program began in 1988. Several visionary senior Canadian earth scientists had initiated the program under the auspices of the Royal Society of Canada. Josef's initial contribution was to ensure that the essential role of data from earth observation satellites was recognized (Cihlar et al., 1989). He also provided foresight into the types of data that would be required and the kinds of information to be derived from the data. One interesting project he initiated was the Canadian Global Change Encyclopedia (Cihlar et al., 1990). This was funded as part of Canada's activities under the International Space Year (1992) and attempted to demonstrate the value of multilayer continental and global datasets through a user-friendly data exploration software package.

His studies for the Canadian Global Change Program showed the magnitude of the task at hand. Although it was expected that much of the information could be derived from relatively coarse data, with 1 km resolution, the data volumes and data handling and processing requirements were immense, even with the technology on the horizon at that time. Undaunted, Josef set out to make it happen. The early 1990s showed a dramatic increase in the size and scope of Josef's research ambitions and the underpinning funding and infrastructure. He truly became a scientific entrepreneur during this time. When it became apparent that funding and other resources within CCRS could not expand enough to achieve his goals, Josef learned to tap numerous external sources, including Canada's Green Plan, CSA, the Royal Society of Canada, and NASA.

This quest for resources could have become all-consuming, but during this time Josef also proposed and executed the Northern Biosphere Observation and Modelling Experiment (NBIOME) (Cihlar et al., 1989; 1995; Cihlar, 1991).

NBIOME was an ambitious, but all-Canadian enterprise. Its objectives were as follows: (*i*) to investigate the effect of climate change on Canada's ecosystems, (*ii*) to map the land

[2] The original justification for RADARSAT was for ice mapping to support exploration and extraction of oil from Canada's High Arctic. In the early 1980s the price of oil began to stabilize and then fell, making this justification much less tenable.

cover of Canada, (*iii*) to look for evidence of land cover change, (*iv*) to model the carbon budget of Canada, and (*v*) to model ecosystem change.

It was apparent that a program of national scope and ambitious objectives would best be carried out by engaging scientists from other departments and from Canadian universities. Josef convened several workshops, and a science plan was developed. The actual execution took several years and involved scientists from CCRS, the Canadian Forest Service, and other organizations.

Shortly after NBIOME got underway, Josef was instrumental in helping to formulate and initiate a NASA-sponsored project called BOREAS, after the god of the north wind. BOREAS was a new undertaking for CCRS and Canada. It was a Canadian response to a new way of doing science at NASA. NASA was developing an Earth Observation System (EOS) to provide essential data for climate change studies. EOS became a billion-dollar program. Millions of dollars were available for one component, called Earth Systems Science. In essence, NASA intended to understand how the major earth systems function using an engineering approach. The complex systems were broken into simpler components that were given names, together with lists of input and output variables. They were interconnected with appropriate lines, creating massive, complicated "wiring diagrams". The role of terrestrial ecosystems in the global climate system became a priority at NASA and in the international scientific community, the latter initially clustered around the International Satellite Land Surface Climatology Project.

Among of the first systems to come under NASA's scrutiny were the carbon and water cycles because of their importance in the exchange of energy and in determining the concentration of CO_2, CH_4, and other greenhouse gasses in Earth's atmosphere. NASA's approach was to invite teams of forefront scientists to long, intense, 3- to 5-day workshops to hammer out a program plan. The program would draw the wiring diagrams, determine which boxes were well understood and which needed more study, determine how to create computer models of the entire system, and determine how to use space technology (and other technologies if necessary) to obtain the data to make the model work. NASA quickly learned that major aspects of how Earth functions were not really well known. Being NASA, they did not let that stop them. They chose major areas of uncertainty and invited more forefront scientists to more gruelling workshops to make plans for massive studies to determine how Earth works. One of the first of these massive studies was the Boreal Ecosystem–Atmosphere Study (BOREAS) (Sellers et al., 1995). BOREAS was an effort to determine how the boreal forest functions within the global climate system, and Canada was chosen as the study site. Numerous Canadian scientists were invited to the initial workshops, but NASA was prepared to do BOREAS in Canada with minimal Canadian participation if necessary.

Fortunately for Canada, and for NASA, several senior Canadian scientists, including Josef, recommended that Canada should participate in BOREAS in a major way. They realized that BOREAS represented a unique opportunity for Canada and Canadian scientists to increase scientific understanding of a major Canadian biome that is important both ecologically and economically. At Josef's suggestion, CCRS agreed to support establishment of a BOREAS Secretariat in his section. In Canada, as in NASA, BOREAS consisted of substantial forefront research together with a large amount of backbreaking work. The BOREAS Secretariat helped ensure that Canadian scientists would have an opportunity to participate significantly in the forefront research. The BOREAS Secretariat also facilitated fieldwork in Canada by scientific teams from outside the country. Josef served as the Canadian coordinator for BOREAS from 1992 to 1996.

During the early stages of NBIOME and BOREAS, Josef needed to populate his new section with research scientists eager and able to take on these new challenges. Josef attracted some remarkable young talent from China and Eastern Europe in these years just following the Tiananmen Square massacre and the breakup of the Soviet Union. Both NBIOME and BOREAS moved forward. NBIOME began to lay the groundwork for processing AVHRR data at a nationwide scale. BOREAS validated NASA's engineering systems approach to modelling Earth, leading to an even larger project with Brazil in the Amazon. It was a training ground for many young scientists and developed scientific methodology that continues to produce the knowledge necessary to model Earth's complex systems.

At the same time a lot of the basic infrastructure to acquire and handle the needed datasets had to be developed, essentially from scratch. At the time Josef began to discern the need for national, continental, and global datasets, CCRS had very little capability of using 1 km resolution data; except for the Crop Information System,[3] all of the data acquired, processed, and archived by CCRS ranged in resolution from 30 m (Landsat) to 1 m (Multidetector Electro-optical Imaging Sensor, MEIS). These high-resolution images were processed as individual multispectral images. Very little capability existed to handle multi-image datasets. Therefore, in addition to leading efforts to understand the functioning of the boreal forest and other Canadian ecosystems, Josef's section led the development of the basic infrastructure needed to observe Canada as a biophysical entity. These developments included the following: (*i*) the capability to acquire and archive 1.1 km AVHRR data for all of Canada on a daily basis; (*ii*) a facility to produce composite images by extracting the clearest (most cloud free) pixels, based on an earlier system developed for the Crop Information System (Adair et al., 2002; Cihlar et al., 2002); (*iii*) a number of techniques to reduce the effects of residual cloud and haze contamination (Cihlar and Howarth, 1994);

[3] The Crop Information System, developed for the Canadian Wheat Board, used daily imagery from the AVHRR sensor on the NOAA weather satellites to provide information on the growing conditions in the Canadian Prairies.

(*iv*) methods to correct for variations in illumination and viewing geometry inherent in the data (Cihlar and Huang, 1994; Cihlar et al., 1994; Wu et al., 1995; Li et al., 1996); (*v*) significant developments in automated land cover classification for both coarse-resolution (~1 km) and fine-resolution (~25 m) data (Cihlar et al., 1996; 1997; 1998; Beaubien et al., 1999), innovations that decreased the amount of intervention required by expert interpreters, a prerequisite for classification of large areas in a consistent way; and (*v*) methods for combining coarse- and fine-resolution data.

By 1995 Josef had assembled a large and productive research group. It was exceptional in its enthusiasm for hard work and single-minded pursuit of the goals that Josef had established years earlier. Once the basic infrastructure began to be available, the research team began to turn its efforts toward demonstrating the kinds of data products that were necessary for climate change research. In most cases these were produced for all of Canada at 1 km resolution and were done in a way that could be turned into routine production with little modification. The highlights include the following: (*i*) annual maps of the area burned by large forest fires using AVHRR data (Li et al., 2000); (*ii*) the leaf area index for Canada's vegetation at 10-day intervals throughout the growing season (Chen and Cihlar, 1998); (*iii*) the amount of photosynthetically active radiation falling on Canada's vegetation, and the fraction of that radiation that was absorbed, at 10-day intervals throughout the growing season (Li et al., 1997); (*iv*) the land surface temperature; (*v*) measures of vegetation productivity (Liu et al., 2000); and (*vi*) maps of net primary productivity and net ecosystem productivity (Liu et al., 2002).

The final two products are essential inputs into calculations of Canada's carbon budget that use biophysical process modelling. They require most of the earlier products in the list, which in turn require the basic infrastructure described earlier.

In addition to producing these products, Josef's group devoted considerable effort to validating the outputs of each step along the way, so credible error estimates were available. These showed that some of the errors were larger than desired, and the products have been criticized for this shortcoming. This is the way science progresses, however: to reach far, go as far as possible, and then make refinements to improve the weak links.

In short, Josef led a prolonged, well-focused effort that produced and validated an entire system for deriving critical carbon-budget variables from daily coarse-resolution data, starting nearly from scratch.

The international arena

In 1988 Josef jumped into the international arena by becoming active in the International Geosphere–Biosphere Programme (IGBP), a massive international program designed to deliver a rapid expansion in knowledge of the interactions between the biosphere and the geosphere (all nonliving parts of Earth). His influence quickly expanded. Not only was he a knowledgeable and convincing proponent for his ideas concerning effective use of space observations in IGBP, but he was also willing to take on a large amount of the hard, unglamorous work. He helped organize and lead workshops of experts, chaired plenary and breakout sessions, helped achieve consensus, and typically contributed much more than his share of writing up reports after the meetings.

The international arena is a complex playing field with real and imaginary components, where only the insightful can distinguish the real from the imaginary. It is populated with large numbers of organizations and initiatives, always named with acronyms, and even larger numbers of participating individuals. There are many big egos and rigid institutions. To make a meaningful contribution requires intelligence, a great memory, diplomacy, determination, and lots of hard work.

Figure 4 is a roadmap to help follow and appreciate Josef's international contributions. These began in 1988 when he initially co-proposed a global land cover mapping initiative based on 1 km resolution satellite data from the AVHRR sensor. In 1990 he joined the IGBP Land Cover Change working group and helped define the data processing methodology and the validation strategy. This initiative finally reached fruition in 1999 when the first land cover map of the entire Earth was released, at 1 km resolution.

While IGBP emphasized actual science, Josef realized that a lasting contribution required efforts to develop international institutions and policies to ensure that effective observations would be made and the appropriate information products would be derived from these observations. One of the outgrowths of the 1992 Earth Summit in Rio de Janeiro was an initiative designed to lead toward coordinated global observations of the environment. Three observing systems were proposed, called the Global Terrestrial Observing System (GTOS), the Global

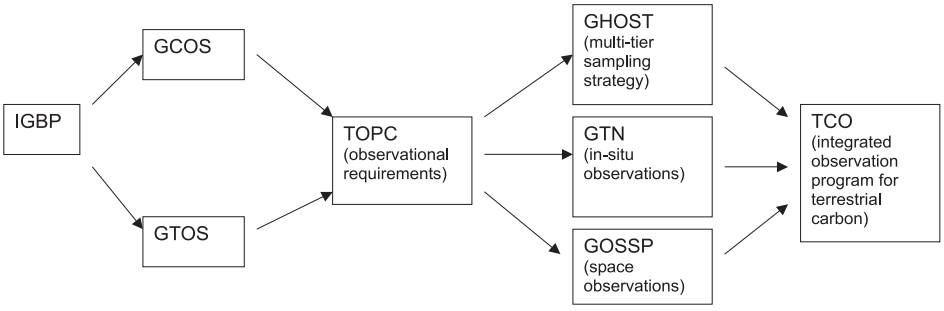

Figure 4. Flow chart of Josef Cihlar's international activities.

Climate Observing System (GCOS), and the Global Ocean Observing System (GOOS). Josef became a member of the Canadian GCOS task force in 1994 and played a leading role in defining observational requirements. There was a lot of commonality between the observational requirements for GCOS and those of GTOS, so a joint panel called the Terrestrial Observation Panel for Climate (TOPC) was formed to determine the observational requirements and propose means to achieve them. Josef became its chairman from 1995 to 2001. During this time, multiple meetings in far-flung places resulted in (*i*) an innovative multi-tier sampling strategy to collect the required observations from ground to space, called GHOST; (*ii*) much more detailed definitions of the observations needed from space through a panel called the Global Observing Systems Space Panel (GOSSP); and (*iii*) a similar definition of in situ observations through development of the Global Terrestrial Network (GTN) concept.[4]

The primary aim of these efforts was to provide the information needed to determine the natural and anthropogenic effects on terrestrial ecosystems, including the impact of climate change. When GCOS and GTOS became members of the International Global Observing Strategy Partnership (IGOS-P), TOPC proposed to develop a terrestrial carbon "theme" in 1999. Following IGOS-P approval, Josef played a major role in an international effort to plan and implement the Terrestrial Carbon Observation (TCO) initiative. This work carried on through 2002 and resulted in two benchmark reports that illuminated the path forward to achieve the observations and modelling needed for a reliable terrestrial carbon budget. As a result of this work, the Conference of the Parties of the Climate Change Convention is actually addressing issues related to climate observation, capacity, and requirements, and the international community has made a commitment to a sustained international program of Earth observation and data through the international Group on Earth Observation.

Thus Josef made multiple, major contributions to the international effort to understand the terrestrial carbon cycle. Under its EOS program, NASA is beginning to produce products to support carbon budget studies that are reminiscent of the products produced for Canada by Josef's group in the 1990s. An international consortium has produced a global land cover map that improves significantly upon the initial land cover map produced by the IGBP. International institutions endorse these efforts and embrace their findings. Gradually, a well-supported international capability to monitor Earth's most important processes is being built. These institutions and the infrastructure will help ensure that political decisions that influence the future health of our planet are made with open information that is based on the best possible science. Josef Cihlar can be proud of his contribution to this effort.

Personal characteristics

In reviewing Josef's career, one cannot help but ponder the personal characteristics that underpinned his remarkable career. To approach this subject, the author interviewed many of Josef's coworkers, fellow scientists and engineers within CCRS and beyond, and some of his managers. The following personal characteristics were mentioned time and again: (*i*) vision; (*ii*) hard work (Josef is legendary for his ability to work hard and seems to enjoy it immensely); (*iii*) people management (the teams he has assembled work very well together; he encourages diverse points of view but makes sure there are no interpersonal conflicts); (*iv*) focus (he is able to keep the big picture and all the details clearly in focus at all times; one scientist who worked with him early in his career said "He drew a lot of charts and crazy network diagrams"); (*v*) a charismatic leader who was able to draw out the best from everyone; and (*vi*) a very honest person.

It is also illuminating to provide some insightful quotations from these interviews: "He is very determined, sometimes to a fault. He is always convinced that his way is best. His team was also convinced, which sometimes made it hard for outsiders to work with his team." "He is able to achieve his objectives despite others with their own agendas." "He is able to put science into a practical policy context." "He has a challenging mind." "He pushes the envelope of technical capabilities; the results are not always correct, but they are always thought-provoking." "He has little time for small talk." "He is a good diplomat." "He is a good scientific entrepreneur without being unpleasant. He was able to assemble resources by producing compelling arguments and chipping away at management bit by bit." "His memory is rather scary at times. He can suggest something to one of his scientists and then inquire 6 months later how it worked out, often to the person's embarrassment." "He is tough, yet fair." "He leads people to work to their full potential."

Conclusion

The period between 1972 and 2000 will be remembered as the time when remote sensing took off. The discipline progressed from promise to practicality. The Canada Centre for Remote Sensing (CCRS) played a major role in that progression, primarily because of the corporate culture, which encouraged ambitious undertakings by both scientists and engineers, constrained only by clearly articulated goals, modest but not parsimonious budgets, and a sense of accountability to the Canadian taxpayer. In this fertile environment, numerous scientists and engineers were able to produce remarkable achievements through their dedicated, consistently superior work. Among this creative lot, Josef Cihlar stands out for his scientific achievements, his truly significant institution-building contributions for Canada and the international

[4] It is useful to note that this planning led to concrete action. For example, two GTN networks were established during Josef's tenure, one for glaciers and one for permafrost.

community, and his personal characteristics of foresight, leadership, hard work, and persuasiveness. It is a fitting tribute that his research group volunteered to honour him with a workshop in his name, and the *Canadian Journal of Remote Sensing* produced this special issue as a lasting, written record of his career and accomplishments.

References

Adair, M., Cihlar, J., Park, B., Fedosejevs, G., Erickson, A., Keeping, R., Stanley, D., and Hurlburt, P. 2002. GeoComp-n, an advanced system for generating products from coarse and medium resolution optical satellite data. Part 1: System characterization. *Canadian Journal of Remote Sensing*, Vol. 28, No. 1, pp. 1–20.

Beaubien, J., Cihlar, J., Simard, G., and Latifovic, R. 1999. Land cover from multiple Thematic Mapper scenes using a new enhancement — classification methodology. *Journal of Geophysical Research*, Vol. 104, No. D22, pp. 27 909 – 27 920.

Chen, J.M., and Cihlar, J. 1998. *BOREAS RSS-07: regional LAI and FPAR images from 10-day AVHRR-LAC composites*. CD-ROM. BOREAS Information System, Distributed Active Archive Center, NASA Goddard Space Flight Center, Greenbelt, Md. 16 pp.

Cihlar, J. (Editor). 1980. *Transfer of federal technology to the provinces: Proceedings of the Workshop on the Transfer of Federal Technology to the Provinces*, 20–21 November 1980, Ottawa, Ont. 162 pp.

Cihlar, J. 1991. Northern Biosphere Observation and Modelling Experiment. In *Proceedings of the 14th Canadian Symposium on Remote Sensing*, 6–10 May 1991, Calgary, Alta. Canadian Aeronautics and Space Institute, Ottawa, Ont. pp. 158–163.

Cihlar, J., and Howarth, J. 1994. Detection and removal of cloud contamination from AVHRR composite images. *IEEE Transactions on Geoscience and Remote Sensing*, Vol. 32, pp. 427–437.

Cihlar, J., and Huang, F. 1994. Effect of atmospheric correction and viewing angle restriction on AVHRR data composites. *Canadian Journal of Remote Sensing*, Vol. 20, No. 2, pp. 132–137.

Cihlar, J., and Rubec, C. 1979. *The 1978 status of applications of remote sensing data in forestry, wildlife, and wildlands projects in Canada*. Energy, Mines and Resources Canada, ISSN Report 0705-5749. 95 pp.

Cihlar, J., Audet, M.H., Goodison, B.E., Hardy, N.E., Kourtz, P., Mack, A.R., McQuillan, A.K., Prout, N., Jano, A., Parry, J., Parashar, S., Teillet, P.M., Thomson, K.P.B., and Whiting, J. 1982. Renewable land resources study team report. In *RADARSAT Mission Requirements Document*. Canada Centre for Remote Sensing, Ottawa, Ont. RADARSAT Report 82-7, Appendix A. 55 pp.

Cihlar, J., Brown, R., Falkingham, J., Freeman, N., Henein, J.-C., McNutt, L., and Slaney, V.R. 1985. *RADARSAT phase B mission requirements document*. Canada Centre for Remote Sensing, Ottawa, Ont. RADARSAT Report 85-01. 54 pp. and Appendix.

Cihlar, J., LeDrew, E., Edel, H., Evans, W., McKay, D., McNutt, L., and Royer, A. 1989. *Contribution of satellite observations to the Canadian Global Change Program*. Canada Centre for Remote Sensing and the Royal Society of Canada, Ottawa, Ont., Canadian Global Change Program Report No. 3. 43 pp.

Cihlar, J., Simard, R., Manore, M., Baker, R., Clark, D., Kineman, J., Allen, J., and Ruzek, M. 1990. Global Change Encyclopedia: a project for the International Space Year. *Advances in Space Research*, Vol. 11, No. 3, pp. 249–253.

Cihlar, J., Apps, M., Baskerville, G., Desjardins, R., Holling, C.S., Parkinson, D., and Stewart, J.W. 1993. *Northern Biosphere Observation and Modelling Experiment: Science Plan*. Royal Society of Canada, Ottawa, Ont., Canadian Global Change Program Report IR93-1. 61 pp.

Cihlar, J., Manak, D., and Voisin, N. 1994. AVHRR bidirectional reflectance effects and compositing. *Remote Sensing of Environment*, Vol. 48, pp. 77–88.

Cihlar, J., Band, L., Beaubien, J., Chen, J., Desjardins, R., Fisher, T., Holling, C., Li, Z., Royer, A., Stocks, B., and Teillet, P. 1995. *Northern Biosphere Observation and Modelling Experiment (NBIOME)*. Progress Report. 34 pp.

Cihlar, J., Ly, H., and Xiao, Q. 1996. Land cover classification with AVHRR multichannel composites in northern environments. *Remote Sensing of Environment*, Vol. 58, pp. 36–51.

Cihlar, J., Beaubien, J., Xiao, Q., Chen, J., and Li, Z. 1997. Land cover of the BOREAS Region from AVHRR and Landsat data. *Canadian Journal of Remote Sensing*, Vol. 23, pp. 163–175.

Cihlar, J., Xiao, Q., Beaubien, J., Fung, K., and Latifovic, R. 1998. Classification by Progressive Generalization: a new automated methodology for remote sensing multichannel data. *International Journal of Remote Sensing*, Vol. 19, pp. 2685–2704.

Cihlar, J., Chen, J., Li, Z., Latifovic, R., Fedosejevs, G., Adair, M., Park, W., Fraser, R., Trishchenko, A., Guindon, B., Stanley, D., and Morse, D. 2002. GeoComp-n, an advanced system for the processing of coarse and medium resolution satellite data. Part 2: Biophysical products for Northern ecosystems. *Canadian Journal of Remote Sensing*, Vol. 28, No. 1, pp. 21–44.

Li, Z., Cihlar, J., Zhang, X., Moreau, L., and Ly, H. 1996. The bidirectional effects of AVHRR measurements over boreal regions. *IEEE Transactions on Geoscience and Remote Sensing*, Vol. 34, No. 6, pp. 1308–1322.

Li, Z., Moreau, L., and Cihlar, J. 1997. Estimation of photosynthetically active radiation absorbed at the surface. *Journal of Geophysical Research*, Vol. 102, No. D24, pp. 29 717 – 29 727.

Li, Z., Nadon, S., Cihlar, J., and Stocks, B.J. 2000. Satellite mapping of Canadian boreal forest fires: validation and comparison of algorithms. *International Journal of Remote Sensing*, Vol. 21, pp. 3071–3082.

Liu, J., Chen, J.M., and Cihlar, J. 2000. *BOREAS TE-16: net primary productivity distribution over the BOREAS region*. CD-ROM. BOREAS Information System, Distributed Active Archive Center, NASA Goddard Space Flight Center, Greenbelt, Md. 19 pp.

Liu, J., Chen, J.M., Cihlar, J., and Chen, W. 2002. Net primary productivity mapped for Canada at 1 km resolution. *Global Ecology and Biogeography*, Vol. 11, pp. 115–129.

Sellers, P., Hall, F., Margolis, H., Kelly, R., Baldocchi, D., den Hartog, J., Cihlar, J., Ryan, M., Goodison, B., Crill, P., Ranson, J., Lettenmeier, D., and Wickland, D. 1995. The Boreal Ecosystem–Atmosphere Study (BOREAS): an overview and early results from the 1994 field year. *Bulletin of the American Meteorological Society*, Vol. 76, pp. 1549–1577.

Wu, A., Li, Z., and Cihlar, J. 1995. Effects of land cover type and greenness on AVHRR bidirectional reflectances: analysis and removal. *Journal of Geophysical Research*, Vol. 100, pp. 9179–9192.

Can. J. Remote Sensing, Vol. 31, No. 5, pp. 324–346, 2005

Generating historical AVHRR 1 km baseline satellite data records over Canada suitable for climate change studies

Rasim Latifovic, Alexander P. Trishchenko, Ji Chen, William B. Park, Konstantin V. Khlopenkov, Richard Fernandes, Darren Pouliot, Calin Ungureanu, Yi Luo, Shusen Wang, Andrew Davidson, and Josef Cihlar

Abstract. Satellite data are an important component of the global climate observing system (GCOS). To serve the purpose of climate change monitoring, these data should satisfy certain criteria in terms of the length of observations and the continuity and consistency between different missions and instruments. Despite the great potential and obvious advantages of satellite observations, such as frequent repeat cycles and global coverage, their use in climate studies is hindered by substantial difficulties arising from large data volumes, complicated processing, and significant computer resources required for archiving and analysis. Successful examples of satellite earth observation (EO) data in climate studies include, among others, analyses of the earth's radiation budget (Earth Radiation Budget Experiment (ERBE), Scanner for Radiation Budget (ScaRaB), and Cloud and the Earth's Radiant Energy System (CERES)), cloudiness (International Satellite Cloud Climatology Project (ISCCP)), vegetation research (Global Inventory Modeling and Mapping Studies (GIMMS)), and the National Oceanic and Atmospheric Administration – National Aeronautics and Space Administration (NOAA–NASA) Pathfinder Program. Despite several attempts, the great potential of the advanced very high resolution radiometer (AVHRR) 1 km satellite data for climate research remains substantially underutilized. To address this issue, the generation of a comprehensive satellite data archive of AVHRR data and products at 1 km spatial resolution over Canada for 1981–2004 (24 years) has been initiated, and a new system for processing at level 1B has been developed. This processing system was employed to generate baseline 1 day and 10 day year-round clear-sky composites for a 5700 km × 4800 km area of North America. This region is centred over Canada but also includes the northern United States, Alaska, Greenland, and surrounding ocean regions. The baseline products include top-of-atmosphere (TOA) visible and near-infrared reflectance, TOA band 4 and band 5 brightness temperature, a cloud – clear – shadow – snow and ice mask, and viewing geometry. Details of the data processing system are presented in the paper. An evaluation of the system characteristics and comparison with previous results demonstrate important improvements in the quality and efficiency of the data processing. The system can process data in a highly automated manner, both for snow-covered and snow-free scenes, and for daytime and nighttime orbits, with high georeferencing accuracy and good radiometric consistency for all sensors from AVHRR NOAA-6 to AVHRR NOAA-17. Other processing improvements include the implementation of advanced algorithms for clear sky – cloud – shadow – snow and ice scene identification, as well as atmospheric correction and compositing. At the time of writing, the assembled dataset is the most comprehensive AVHRR archive at 1 km spatial resolution over Canada that includes all available observations from AVHRR between 1981 and 2004. The archive and the processing system are valuable assets for studying different aspects of land, oceans, and atmosphere related to climate variability and climate change.

Résumé. Les données satellitaires sont une composante importante du système d'observation du climat à l'échelle du globe (GCOS). Pour les besoins du suivi du changement climatique, ces données devraient satisfaire certains critères en termes de durée des observations et de continuité et de cohérence entre les différentes missions et instruments. En dépit du potentiel énorme et des avantages évidents des observations satellitaires, comme la répétitivité fréquente de passage et une couverture globale, leur utilisation dans les études climatiques est limitée par des difficultés substantielles résultant des volumes importants de données, de la complexité des traitements et de la nécessité de disposer de ressources informatiques importantes pour l'archivage et l'analyse des données. Des exemples de réussite dans l'utilisation des données satellitaires d'observation de la Terre (OT) dans le contexte des études climatiques incluent notamment des analyses du bilan radiatif de la Terre (ERBE, SCaRaB, CERES), de la nébulosité (ISCCP), des études sur la végétation (GIMMS) et le programme Pathfinder NOAA–NASA. Malgré plusieurs tentatives, le grand potentiel des données AVHRR à 1 km de résolution pour la

Received 8 August 2005. Accepted 2 September 2005.

R. Latifovic,[1] A.P. Trishchenko, J. Chen,[2] W.B. Park, K.V. Khlopenkov, R. Fernandes, D. Pouliot,[2] C. Ungureanu,[2] Yi Luo,[2] S. Wang, A. Davidson, and J. Cihlar. Canada Centre for Remote Sensing (CCRS), Natural Resources Canada, 588 Booth Street, Ottawa, ON K1A 0Y7, Canada.

[1]Corresponding author (e-mail: Rasim.Latifovic@CCRS.NRCan.gc.ca).
[2]Under contract to CCRS from Noetix Research Inc.

recherche sur le climat demeure substantiellement sous utilisé. Dans cette optique, la génération d'une archive complète de données satellitaires composée de données et produits AVHRR à la résolution spatiale de 1 km au-dessus du Canada pour la période 1981–2004 (24 ans) a été initiée et un nouveau système de traitement au niveau 1B a été développé. Ce système de traitement a été utilisé pour générer des images synthèse temporelles de ciel clair de référence de 1 jour et 10 jours à longueur d'année pour une surface de 5700 × 4800 km2 en Amérique du nord. Cette région est centrée au-dessus du Canada, mais elle couvre également le nord des États-Unis, l'Alaska, le Groenland et les régions océaniques limitrophes. Les produits de référence comprennent la réflectance au sommet de l'atmosphère (TOA) dans le visible et l'infrarouge, la température de brillance TOA de la bande 4 et 5, un masque de classification nuage – ciel clair – ombre – neige-glace et la géométrie de visée. On présente dans cet article des détails sur le système de traitement des données. Une évaluation des caractéristiques du système et une comparaison avec les résultats antérieurs témoignent d'améliorations importantes dans la qualité et l'efficacité du traitement des données. Le système peut traiter des données d'une façon hautement automatisée, à la fois pour les images avec de la neige et les images sans neige et pour les orbites de jour et de nuit, avec une précision élevée au plan de la géo-référenciation ainsi qu'une bonne cohérence radiométrique pour tous les capteurs AVHRR, de NOAA-6 à NOAA-17. Parmi les améliorations apportées au plan du traitement, notons la mise en place d'algorithmes avancés pour l'identification des images de ciel clair – nuages – ombre – neige et de la glace, de même que pour la correction atmosphérique et la réalisation d'images synthèse. Au moment de rédiger cet article, l'ensemble de données ainsi assemblé constitue l'archive la plus complète de données AVHRR à 1 km de résolution au-dessus du Canada comprenant toutes les observations AVHRR disponibles entre 1981–2004. L'archive et le système de traitement constituent des outils précieux pour l'étude des différents aspects terrestres, océaniques et atmosphériques reliés à la variabilité climatique et au changement du climat.
[Traduit par la Rédaction]

Introduction

Satellite data are a key component of the Global Climate Observing System (GCOS). The GCOS implementation plan, released by the World Meteorological Organization (WMO) in October 2004 in support of the United Nations Framework Convention on Climate Change (UNFCCC), identifies satellite data as an important "means of obtaining observations globally for comparing climate variability and change over different parts of the Earth" (World Meteorological Organization, 2004). Satellite earth observation (EO) data contribute to all three major components of GCOS: atmospheric, oceanic, and terrestrial. Satellite observations have essential advantages over other sources of information, such as global coverage and high frequency of observations. They deliver a large number of geophysical products that relate to various components of the earth climate system.

To date, the use of EO data in climate research has mostly been limited to coarse spatial resolution imagery. Several successful examples of this kind include the National Aeronautics and Space Administration (NASA) Earth Radiation Budget Experiment (ERBE) (Barkstrom and Smith, 1986), the Scanner for Radiation Budget (ScaRaB) (Kandel et al., 1998), the Cloud and the Earth's Radiant Energy System (CERES) (Wielicki et al., 1996), the International Cloud Climatology Project (ISCCP) (Rossow and Schiffer, 1999; Zhang et al., 2004), and the Equal Area Scalable Earth-Grid (EASE-Grid) microwave brightness temperature dataset generated by the US National Snow and Ice Data Center (NSIDC) (Armstrong et al., 1994). The radiation budget datasets were obtained from broadband sensors with coarse spatial resolution (i.e., pixel sizes ranging from 15 to 60 km). The ISCCP cloud dataset combined data from the advanced very high resolution radiometer (AVHRR) onboard National Oceanic and Atmospheric Administration (NOAA) spacecraft, data acquired with the US geostationary operational environmental satellites (GOES), the European geostationary meteorological satellite (METEOSAT), and the Japanese geostationary meteorological satellite (GMS). The original spatial resolution of the ISCCP data is about 30 km, and pixels with an approximate size of 4 km × 4 km or larger are selected to represent the 30 km × 30 km area. Other examples of climate data records derived from environmental satellites are described by the US National Research Council (NRC, 2004). A key to the successful application of the aforementioned datasets was the implementation of thorough processing algorithms and the generation of a regular archive of various geophysical products for the entire period of observation.

The AVHRR radiometer is one of the most widely used satellite sensors. There are three types of AVHRR radiometer: (*i*) AVHRR-1 flown onboard TIROS-N, NOAA-6, NOAA-8, and NOAA-10; (*ii*) AVHRR-2 flown onboard NOAA-7, NOAA-9, NOAA-11, NOAA-12, and NOAA-14; and (*iii*) AVHRR-3 currently operational onboard NOAA-15, NOAA-16, NOAA-17, and NOAA-18 (Goodrum et al., 2000; Kidwell, 1998). The AVHRR-1 has four channels (red, near infrared (NIR), 3.7 μm, and 11 μm), the AVHRR-2 has five channels (red, NIR, 3.7 μm, 11 μm, and 12 μm), and the AVHRR-3 has six channels (red, NIR, 1.6 μm, 3.7 μm, 11 μm, and 12 μm), although only five channels of AVHRR-3 can be operational at any one time. As such, channels 3A (1.6 μm) and 3B (3.7 μm) work interchangeably. The spectral bands and instantaneous field of view (IFOV) of the AVHRR channels are given in **Table 1**. The dual-gain concept was implemented in AVHRR-3 to enhance the radiometric resolution for dark scenes (Goodrum et al., 2000). Three types of imagery are produced by the AVHRR radiometers: global area coverage (GAC), local area coverage (LAC), and direct-readout high-resolution picture transmission (HRPT) data (Kidwell, 1998; Cracknell, 1997). The LAC and GAC data are recorded

Table 1. The range of spectral bands (in μm) for different AVHRR series.

Channel	AVHRR-1: NOAA-6, NOAA-8, NOAA-10	AVHRR-2: NOAA-7, NOAA-9, NOAA-11, NOAA-12, NOAA-14	AVHRR-3: NOAA-15, NOAA-16, NOAA-17, NOAA-18	IFOV (mrad)
1	0.58–0.68	0.58–0.68	0.58–0.68	1.39
2	0.725–1.100	0.725–1.100	0.725–1.100	1.41
3A	—	—	1.59–1.63	1.51
3B	3.55–3.93	3.55–3.93	3.55–3.93	1.51
4	10.50–11.50	10.30–11.30	10.30–11.30	1.41
5	Band 4 repeated	11.50–12.50	11.50–12.50	1.30

onboard and transmitted to the ground when the satellite passes over designated receiving stations. Both HRPT and LAC data provide imagery at ~1.1 km spatial resolution at nadir. The GAC data are produced by averaging four pixels along a scan line and skipping every fifth pixel. Every third line of the original HRPT image is processed and included in the GAC output record. As a result, GAC pixels actually represent an area of 1.1 km by 4 km, with a distance of 3.3 km between centres of scan lines. The pixel size at the edges of the swath increases by ~3–4 times.

A number of global satellite data products are available from AVHRR. In most cases, available datasets are geophysical parameters derived from the NOAA AVHRR GAC level 1B products with 8 km × 8 km spatial resolution and a temporal resolution ranging from 7 days to 1 month. The AVHRR Pathfinder Program administered jointly by NOAA and NASA generated a variety of data products for atmospheric, land, and ocean applications (University Corporation for Atmospheric Research, 1994). The Pathfinder Atmosphere (PATMOS) climate dataset provides global gridded parameters related to clouds and radiation budget components (Stowe et al., 2002). The aerosol (Ignatov and Nalli, 2002; Ignatov et al., 2004) and sea surface temperature (SST) (Reynolds et al., 2002) products are key datasets employed in weather and climate research and are produced on a regular basis. The AVHRR data are also used over North America for the automated monitoring of snow cover (Romanov et al., 2000). The NOAA National Climatic Data Center (NCDC) Satellite Services Branch (SSB) routinely generates weekly and monthly global vegetation index and climatological products (Gutman et al., 1995; Gutman and Ignatov, 2002; Kidwell, 1997). The NOAA third-generation vegetation product provides global coverage with 0.15° resolution. The NOAA–NASA Pathfinder normalized difference vegetation index (NDVI) dataset is a widely used global dataset at an 8 km × 8 km spatial resolution and a 10 day temporal resolution. It was produced using a maximum value composites (MVC) algorithm (James and Kalluri, 1994). Several issues with the Pathfinder product complicate the derivation of consistent spatial and temporal land surface parameters and trends, however (Stockli and Vidale, 2004). A number of alternative vegetation products were produced from AVHRR GAC data within the framework of the International Satellite Land-Surface Climatology Project (ISLSCP), including the Global Inventory Modeling and Mapping Studies (GIMMS) dataset (Tucker et al., 2004; 2005) and the Fourier-adjusted, sensor and solar zenith angle corrected, interpolated, reconstructed adjusted (FASIR) NDVI datasets (Los et al., 2000). An interesting dataset has been produced in the framework of the Polar Pathfinder Project (Fowler et al., 2002). This dataset includes two daily composites produced from AVHRR GAC observations (daytime and nighttime scenes) over northern and southern polar regions. The AVHRR Polar Pathfinder data cover areas from 48.4°N and 53.2°S poleward and are available from 1981 through 2000. These global and polar region datasets are valuable sources of information for certain applications. They are of limited use, however, for studies that require finer spatial and temporal resolution. Also, as emphasized by data providers, all of the aforementioned datasets may contain certain biases and artificial trends due to various deficiencies in the data processing technology and must be used with caution in climate studies (Lanfredi et al., 2002; Simoniello et al., 2004).

To take advantage of full-resolution AVHRR imagery, the development of the global 1 km AVHRR dataset was initiated within the framework of the International Geosphere Biosphere Programme (IGBP) (Townshend et al., 1994). The Global Land 1-KM AVHRR Project, with the US Geological Survey (USGS) EROS Data Center (EDC) as a lead agency, was established to coordinate this large international activity. As a result of these efforts, a global AVHRR dataset at 1 km spatial resolution and 10 day intervals (G1KA) was produced for the period of April 1992 to May 1996. An evaluation of this dataset concluded that, although the project achieved a significant success, the reprocessing of data is still required to improve the overall quality of the data product. Issues with image registration accuracy and the relatively low success rate of processed scenes (40%) were just two of several problems that need to be resolved (Teillet et al., 2000).

There is a strong need for information on terrestrial vegetation dynamics, ocean and land water properties, and snow and ice conditions at 1 km spatial resolution for climate research and other applications (Townshend et al., 1994; Adair et al., 2002; Cihlar et al., 2002). The AVHRR can provide this capability for more than the past 20 years. Since the 1980s, the Canada Centre for Remote Sensing (CCRS) has received AVHRR data and carried out a significant applications development that addressed various needs of AVHRR data users in Canada. These products have been used by many other Canadian government departments, including Environment Canada (EC), Statistics Canada, Parks Canada Agency (PCA),

Agriculture and Agri-Food Canada (AAFC), the Department of Fisheries and Oceans Canada (DFO), and the Canadian Forestry Service (CFS). These departments use the AVHRR products for a variety of applications. For example, the Canadian Ice Service (CIS) of EC integrates the AVHRR data into the ice information products. The DFO acquires and processes the 1 km AVHRR imagery to obtain information about sea surface properties. The Canadian Wheat Board and Agriculture Financial Services Corporation use the AVHRR data for crop prediction and insurance purposes. The Canadian Wildland Fire Information System (CWFIS) established by the CFS uses the Fire Monitoring, Mapping and Modeling (Fire M3) system to detect forest fires using 1 km AVHRR data (available from http://fire.cfs.nrcan.gc.ca).

The AVHRR data also significantly complement new satellite EO systems, such as the moderate-resolution imaging spectroradiometer (MODIS) (Salomonson et al., 1989), medium-resolution imaging spectrometer (MERIS) (Rast and Bezy, 1999), and VEGETATION (VGT) sensors (Saint, 1992), which provide data at similar or finer (250–500 m) spatial resolutions. It is expected that AVHRR will also overlap with the future US National Polar-orbiting Operational Environmental Satellite System (NPOESS) and the NPOESS Preparatory Project (NPP) system. The overlap between the AVHRR and other sensors can be used to ensure consistency of satellite climate data records (CDR) and bridge the gap between historical AVHRR observations and data from future systems. To meet the CDR requirements, however, historical AVHRR data must be processed with technologies that are comparable in accuracy to that of currently implemented technology (e.g., those used for generating MODIS and MERIS data products), as well as the expected accuracies of future sensor systems (e.g., visible infrared imager – radiometer suite VIIRS–NPP). This requirement is difficult to achieve on a global scale. Reprocessing the G1KA dataset and expanding it back and forward to cover the entire period of AVHRR data availability is clearly a major and challenging undertaking.

To address the need for 1 km AVHRR imagery over the Canadian landmass for climate change and other applications, the work on reprocessing all historical AVHRR data at the original 1 km spatial resolution has been initiated at CCRS with support from the Canadian Space Agency (CSA). This work is carried out within the framework of a new scientific program Reducing Canada's Vulnerability to Climate Change (RCVCC), established by the Earth Sciences Sector (ESS) of Natural Resources Canada (NRCan). Among many others, the RCVCC program includes a research activity focused on generating national-scale medium-resolution EO data products for environmental and climate applications. This research activity is aimed at improving the processing technology and generation of consistent and comprehensive satellite records with the most accurate image georeferencing, sensor calibration, correction for viewing and illumination conditions, and advanced atmospheric correction. This work is built upon many years of research with AVHRR data at CCRS (Cihlar et al., 1998; Latifovic et al., 2003; Teillet et al., 2000; Trishchenko, 2002; 2005; Trishchenko et al., 2002a; 2002b). This study is a continuation of work on the generation of Canada-wide AVHRR 1 km imagery and the geophysical product initiated earlier using the geocoding and compositing (GeoComp) and GeoComp-n (new) systems as described by Adair et al. (2002) and Cihlar et al. (2002). Although the GeoComp-n system was viewed as a significant technological development at the end of the 1990s, it is limited by its ability to achieve the performance required for climate change applications. These limitations include the relatively low success rate of fully processed scenes (on average about 40%), the inability to handle data format for several historical AVHRR sensors, and frequent georeferencing errors. In addition, the GeoComp and GeoComp-n systems were not designed for the automated processing of nighttime and winter scenes with snow–ice coverage, and their compositing and cloud–clear-sky detection algorithms needed improvement. More details regarding the use of GeoComp-n for generating national AVHRR archives are provided in the next section.

The primary goal of this new effort is to produce the first complete record of AVHRR NOAA observations ever collected over Canada at a spatial resolution of 1 km and suitable for climate change applications. The longer term goal is to maintain the established satellite archive and expand it with data from present-day AVHRRs and other sensors such as MODIS Terra&Aqua, Systeme pour l'Observation de la Terre (SPOT-4 and SPOT-5) VGT, MERIS ENVISAT, and the future VIIRS to be launched on NPOESS and NPP platforms. The primary focus of this paper is to provide details on the implementation of data processing that generates the baseline output product, which is a close equivalent to level 1B NOAA data. These data constitute the fundamental basis of all subsequent steps in generating higher level products. Any inconsistencies, inaccuracies, and possible biases will immediately degrade the quality of further products and can possibly lead to erroneous conclusions regarding climate trends and climate change impacts. As such, at this stage we have taken the most care to ensure high data quality in terms of geolocation, radiometric calibration, and pixel clear-sky identification.

This paper is organized as follows. The next section describes the previously developed capacity in terms of data collection and processing technology at CCRS. The following section provides details about the development of the AVHRR raw data archive. The three following sections give details of the new system design, discuss its implementation issues, provide an example of the long-term dataset derived using newly developed technology, and present an analysis of ice conditions over Hudson Bay over the past 20 years. The final section concludes the paper with a summary and recommendations.

Previous capacity

Availability of AVHRR data at 1 km over Canada

The major source of the raw AVHRR HRPT imagery at 1 km spatial resolution at CCRS is the Prince Albert Satellite Station (PASS). Although at the present time the AVHRR data reception at this station is almost complete and includes several daytime and nighttime scenes each day, it was much more fragmentary in the past.

All the data acquired by PASS are archived. Information pertaining to acquired scenes, such as date, time, scene location, crude estimation of cloudiness, and browse images, is stored in the CCRS Earth Observation Catalogue (CEOCat) (available from http://ceocat.ccrs.nrcan.gc.ca). In the 1990s, the AVHRR data stream into the CCRS archive from PASS was complemented by AVHRR data collected by the DFO receiving station in Mont-Jolie, Quebec, and some limited data from the EC AVHRR reception in Downsview, Ontario. The AVHRR imagery available from the CCRS archive has been processed for the period 1990–2004 from April to October to generate 1 km Canada-wide clear-sky composites and various geophysical products. This national coverage was produced through a partnership between the Manitoba Remote Sensing Centre and CCRS using the GeoComp and GeoComp-n systems. Prior to initiation of the work described in this paper, this data archive was the most comprehensive AVHRR 1 km archive in Canada.

An analysis of the contents of the CEOCat archive at CCRS showed that (*i*) no processed data exist for the cold season period spanning October–April; and (*ii*) the temporal coverage of raw data in the 1980s, and during cold seasons for most years, was sparse and insufficient for producing good quality time series. It was thus concluded that the existing national temporal and spatial AVHRR data coverage was insufficient for generating the satellite-based CDR (NRC, 2004) and that obtaining and processing additional data from other sources was required.

GeoComp-n AVHRR data processing systems

During the mid-1970s, CCRS proposed and developed the digital image correction system (DICS) (Guindon et al., 1992). The success of this system initiated the development of the more advanced GeoComp system for processing AVHRR data (Robertson et al., 1992). For the period 1993–1999, almost all AVHRR data collected at CCRS have been processed using the GeoComp system. Since 2000, this system has been replaced by the GeoComp-n system (Adair et al., 2002; Cihlar et al., 2002). The GeoComp-n system was reasonably adequate for resource management applications such as fire detection and crop monitoring and other operational activities that require short-term satellite products during the summer season; however, it was not designed for generating consistent high-quality satellite-derived thematic climate data records (TCDR) (NRC, 2004) such as the diurnal cycle of surface temperature, radiation and cloudiness, snow cover, ice freeze-up and breakup dates, and others that require the processing of observations acquired during winter and summer seasons over land and water. Studying long-term trends also requires highly accurate geolocation and instrument calibration that is consistent among all sensors over all periods of observation. These features also need improvement in GeoComp-n. Furthermore, the GeoComp-n system required frequent software maintenance and updates to implement new algorithms, incorporate new sensor parameters and data products, and fix various problems with data processing. It was also concluded that the GeoComp-n system was not flexible enough or efficient enough to be used in generating all possible output data products suitable for climate change applications. The system was also difficult to use for multiple reprocessing attempts due to its high demand for computer resources. Thus, it was decided to develop a completely new system capable of generating high-quality satellite-based climate data records.

New 1 km AVHRR archive over Canada at CCRS

To fill the gaps existing in the CCRS archive, and to achieve the complete spatial and temporal coverage by the AVHRR imagery over Canada, additional data have been obtained from NOAA. We acquired all 1 km AVHRR imagery (HRPT and LAC) ever collected over Canada that were stored in the NOAA Comprehensive Large Array-data Stewardship System (CLASS) (formerly the Satellite Active Archive (SAA); available from http://www.class.noaa.gov/nsaa/products/welcome). The newly assembled satellite data archive contains observations collected by the AVHRR instrument onboard the series of polar-orbiting satellites spanning NOAA-6 through NOAA-17. Therefore, the new archive now includes the AVHRR 1 km observations acquired by CCRS, DFO, and EC satellite stations and data from the NOAA CLASS archive. By volume, approximately one third of all orbit segments in the new archive were obtained from PASS. PASS preprocesses the AVHRR data using the NOAA AVHRR Transcription and Archive System (NATAS). The same system was also used to preprocess AVHRR data acquired by DFO and EC receiving stations. The data over Canada obtained from CLASS were acquired at the Wallops Island (WI) and Fairbanks, Alaska (formerly Gilmore Creek (GC)), satellite stations. The data in the NOAA CLASS archive are stored as a level 1B (L1B) data type (description is available at http://www2.ncdc.noaa.gov/docs/ intro.htm). Several changes in L1B format have been made over the years. All modifications for historical and current sensors are supported by our new system. A certain redundancy exists in the data collected due to an overlap between Canadian and US receiving stations and adjacent orbit segments. Nonetheless, all initial records are archived in their original form, and the redundancy issue is addressed later during processing.

The newly assembled archive contains approximately 10 terabytes (TB) of raw data and is estimated to increase annually by 0.6 TB. The total number of files reaches nearly 200 000.

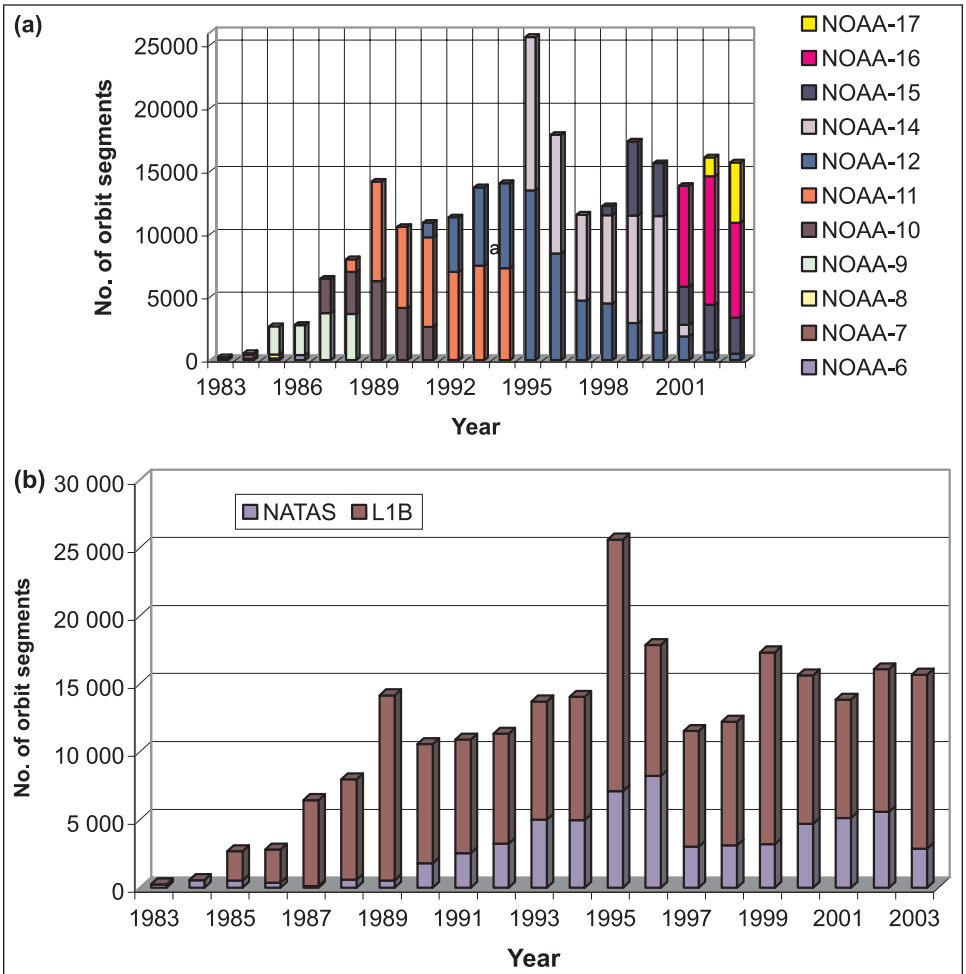

Figure 1. The structure of the 1 km AVHRR archive over Canada collected at CCRS from national and US sources. Content by (a) sensor and (b) data source. NATAS is the CCRS-supported format, and L1B is the NOAA-supported format.

Figure 1a illustrates the archive contents by acquisition year and satellite mission. The graph reveals an irregular distribution of the data acquired over the entire time frame. Earlier in this period (1981–1983) only a few thousand orbit segments acquired from NOAA-6, NOAA-7, and NOAA-8 are available (**Figure 1b**). We concluded that the generation of regular spatially and temporally complete national coverages of Canada at 1 km resolution is not possible for this period. After 1983, the record is much more comprehensive and provides a sufficient number of image segments for generating regular spatially and temporally complete national coverages, especially after 1985. In recent years, the average number of files per year is close to 15 000. The peak number of data files per year is observed for 1995, when it totalled approximately 25 000. Such a large number is also explained by the overlap between files and scene segmentation into smaller pieces in the original archive systems.

Despite some gaps at the beginning of the record, this collection is presently the most comprehensive historical AVHRR 1 km archive assembled for Canada. The new archive provides repeated daily measurements from multiple sensors and may be used for generating products needed for studying changes in the diurnal cycles of land surface properties, fractional cloud coverage, and radiation budgets. The overlap between consecutive AVHRR sensors permits sensor intercalibration and improved sampling for retrievals of the bidirectional reflectance distribution function (BRDF). The BRDF is important for normalizing measurements to a common viewing geometry, albedo retrievals, and accounting for satellite orbital drift in long-term trend analysis.

EODM: the new AVHRR data processing system

System overview

The new earth observation data manager (EODM) system has been developed to facilitate the generation of AVHRR 1 km data records useful in a wide range of environmental and climate applications. The component of the EODM that generates baseline products at the level equivalent to L1B has been completed, tested, and employed in processing AVHRR

1 day, 10 day, and monthly clear-sky composite products. The second stage, which generates various output geophysical quantities, is under development. Presently, the EODM also provides the postseasonal correction of (*i*) AVHRR clear-sky composite products, (*ii*) SPOT VGT S10 data, and (*iii*) MODIS 16 day BRDF–albedo products (MOD43B1).

AVHRR data processing is supported by the following five primary functions: (1) data import, quality control, and calibration; (2) geocoding and refinement using the ground-control points (GCPs); (3) image resampling; (4) scene identification; and (5) clear-sky composite product generation. These five components are used to generate the baseline product (i.e., georeferenced orbit segment). Since the calibration and georeferencing information have been *applied* to the data, this data type cannot strictly speaking be defined as level 1B, although in terms of the value-added information it can be considered as L1B equivalent. The output includes the following data layers: (*i*) AVHRR TOA reflectance for bands 1 and 2; (*ii*) TOA radiance (W/(m^2·cm^{-1}·sr)) for band 3; (*iii*) TOA brightness temperature for bands 4 and 5; (*iv*) pixel cloud – clear – shadow – snow and ice mask; and (*v*) viewing geometry (solar zenith, viewing zenith, and corresponding azimuths angles). The implementation of functions 1–5 is described in the following subsections. All data are reprojected into Lambert conic conformal (LCC) geographic projection with the parameters listed in **Table 2**.

Systematic postseasonal correction is developed to be applied to the basic AVHRR, SPOT VGT S10, and MODIS MOD43B1 products to fill the gaps, produce spatially and temporally complete series, and remove false outliers in the data records. Because the major objective of the current paper is concerned with the baseline processing of historical AVHRR data, the postseasonal correction and processing steps related to higher level products are described only briefly later.

Table 2. Parameters of the Lambert conic conformal (LCC) projection and earth ellipsoid used in the earth observation data manager (EODM) system.

Earth ellipsoid	
Major semiaxis, *a* (m)	6 378 137
First eccentricity	0.00669438002290
Ellipsoid flattening, *f*	0.00335281068118
Projection	
First parallel (°)	49.00
Second parallel (°)	77.00
Central meridian (°)	–95.00
Upper left corner (m)	–2600000.0 E, 10500000.0 N
Lower right corner (m)	3100000.0 E, 5700000.0 N
Easting	0
Northing	0
Gridbox size, *x* (m)	1000
Gridbox size, *y* (m)	1000

Data import, quality control, and calibration

The EODM AVHRR processing package supports the processing of AVHRR 1 km imagery in the NOAA L1B and NATAS formats. All modifications of the NOAA L1B formats from NOAA-6 to NOAA-7 are maintained as described in the *NOAA polar orbiter data user's guide* (Kidwell, 1998; Goodrum et al., 2000).

Based on the data header record, the EODM initializes the appropriate module that performs data conversion into internal format, adjusts for missing lines, and performs the analysis and refinement of internal calibration data to calculate scan line specific calibration gain and offset. A set of quality tests is built into EODM to prevent errors in estimating the intercept and gain. The refinement in the calibration of thermal channels because of noise, solar blackbody contamination, and nonlinear corrections is conducted following the methodology presented in Trishchenko et al. (2002a; 2002b) and Trishchenko (2005). Computed values are compared with the average values derived from a large number of orbits before being used in the calibration routine.

The calibration of the visible (VIS), near-infrared (NIR), and shortwave infrared (SWIR) bands (SWIR exists only for the AVHRR-3 type radiometer) is based on the time-dependent piecewise linear calibration method developed at CCRS (Cihlar and Teillet, 1995).

The general formula for calibration of AVHRR optical channels is as follows:

$$L_{Ei} = \frac{C_{Ei} - C_{0i}}{G_i} \tag{1}$$

where i denotes AVHRR channel (1, 2, or 3A); L_{Ei} is earth radiance (W/(m^2·cm^{-1}·sr)); and C_{0i} and G_i are the offset and gain, respectively, and are calculated according to

$$C_{0i} = A \times (\text{no. of days since launch}) + B$$

$$G_i = C \times (\text{no. of days since launch}) + D \tag{2}$$

where the coefficients A, B, C, and D are specified for each channel i and updated for various time intervals (i.e., Equation (2) describes the piecewise linear approximation). The values of C_{0i} and G_i currently implemented in the EODM system are provided in **Table 3**. There are two sets (two lines) for each optical channel of AVHRR-3 onboard NOAA-15, NOAA-16, and NOAA-17. They correspond to low (1st line) and high (2nd line) gain modes. The prelaunch values or coefficients provided by NOAA in the operational mode are still used in EODM for some sensors (marked by an asterisk in **Table 3**). Work is being performed to conduct the sensor cross-calibration for all sensors included in **Table 3** to ensure the radiometric consistency of time series over the entire period. It has also been recently discovered that the calibration of AVHRR NOAA-12, NOAA-14, and NOAA-15 in **Table 3** needs to be

updated according to recommendations by Tahnk and Coakley (2001; 2002).

Image georeferencing

Image georeferencing is the critically important step that ensures suitability of long-term AVHRR data series for climate change studies. Noise in the data at the local scale caused by erroneous pixel locations may destroy any real climate signal or produce artificial trends. The errors in pixel location, for example, can be the probable source of large systematic negative NDVI trends in the GIMMS dataset in the vicinity of the land–water interface as noticed by Lanfredi et al. (2002) and are considered as artefacts.

There are several potential sources of errors in determining pixel location. The most important of these are (*i*) errors in the prediction of the spacecraft centre of mass position, (*ii*) errors in determining the time of observations that occur due to spacecraft clock drift, (*iii*) uncertainties in the knowledge of spacecraft attitude angles, (*iv*) misalignment in the instrument position on the platform, and (*v*) simplifications in the computational algorithms used. A good discussion of these factors for AVHRR NOAA is given by Brunel and Marsouin (2000).

The basic algorithms for AVHRR geometric correction are described in the *NOAA polar orbiter data user's guide* (Kidwell, 1997; Goodrum et al., 2000). More detailed theory is given by D'Souza and Sandford (1996). Currently, the image georeferencing information embedded in the NOAA L1B data is produced by the Advanced Earth Location Data System (AELDS) (http://www.osdpd.noaa.gov/PSB/PPP/NAVIGATION/overview.html). This system replaced an older version and improved the average accuracy of pixel location in L1B data by about 50%. The earth location error at the satellite subpoint region still remains within 2–4 km, however, whereas errors near the limb often are as large as 10 km (http://www.osdpd.noaa.gov/PSB/PPP/NAVIGATION/overview.html). An example of recent L1B data for AVHRR NOAA-17 is shown in **Figure 2a**. The coastline contours are also plotted in the AVHRR image. The systematic shift of more than two lines is observed relative to the expected position of coastlines. Based on the aforementioned information, it was concluded that L1B georeferencing cannot be used in generating AVHRR-based climate data records over Canada, and that these data must be recomputed with better accuracy. Since earth location segments in the CCRS NATAS data are not provided, the pixel location must be derived using the satellite orbital model.

Due to the extremely large data volume, image georeferencing (i.e., the computation of accurate positions for each pixel in the selected geographic projection) must be automated. Due to potential earth location errors in the L1B data files and the absence of geolocation information in the NATAS data, the EODM system needs a special module that can function in automated mode and should provide quality assurance (QA) for image spatial location accuracy. Accuracy at the level of 1 pixel cannot be achieved by employing the nominal orbital and AVHRR scanning models, and thus special refinement and QA procedures must be designed.

The basic geometric correction in EODM employs the orbit model that computes the satellite position and the geometry model that accounts for AVHRR scanning and the relative orientation of the Sun and Earth. Orbit navigation in the EODM system is designed as a two-step process. The first step consists of initializing either the Brouwer–Lyddane orbit model (Brouwer, 1959; Lyddane, 1963) as described by the *NOAA polar orbiter data user's guide* (Kidwell, 1998; Goodrum et al., 2000) using ephemeris data provided in the TIROS Bulletin United States (TBUS) or initializing the SGP4 orbit model (Lane and Hoots, 1979) using the North American Aerospace Defence (NORAD) command two-line elements (TLE) ephemeris data. The choice of model depends on the epoch of ephemeris data in TBUS or TLE. The one closest to the time of AVHRR scene acquisition is selected.

The location and viewing geometry for each pixel are computed using the selected orbital model initialized by the most appropriate ephemeris data. This information is then used to resample raw imagery into a geographic reference projection (in our case, the LCC projection (**Table 2**)). The error in predicting the satellite centre of mass position leads to a systematic image shift along the satellite track, leading to error in the line number (Brunel and Marsouin, 2000; Trishchenko, 1994). When the epoch time of ephemeris data is close to the time of data acquisition, the satellite orbit prediction error is usually small (less than 2–3 km). This error increases as the time difference between the epoch of ephemeris data and time of scene acquisition increases (**Figure 3a**). Computations shown in **Figure 3a** were conducted for NOAA-9 in 1985, NOAA-14 in 1995, and NOAA-17 in 2003. On average, the error increases as a quadratic function of time. The error is approximately 1–3 km when epoch time is less than 24 h old but can grow to 10–30 km after 1 week. This issue is especially serious for historical data in the 1980s when TBUS data are less accurate and not always available on a regular basis. Normally, TBUS data are updated every day. For various reasons, some data are missing for early satellites. The distribution of average time intervals in days between TBUS data is presented in **Figure 3b**. One can see that for NOAA-6, NOAA-7, and NOAA-8 the average interval is close to 2 days and frequently is longer than 3 or more days. To minimize error, the SGP4 model with TLE ephemeris data is used concurrently with the Brouwer–Lyddane model as previously described.

Due to the relatively slow growth of satellite orbit prediction with time, this error can be viewed as a constant systematic shift along the satellite track for each particular scene. This error can be easily corrected using the GCPs method and applying a linear shift to the entire image. The satellite clock drift causes a similar effect (shift along the orbital track) and can be corrected in the same way. These errors are a spatial translation type of error. Other types of errors are those related to uncertainties in satellite attitude angles or instrument misalignment (Brunel and Marsouin, 2000; Trishchenko and Andrievsky, 1994). An example of variations of roll, yaw, and

Table 3. Piecewise linear model (PWL) calibration coefficients A–*D* for AVHRR optical channels.

			VIS				NIR				SWIR			
Sensor	Year	Launch date	*A*	*B*	*C*	*D*	*A*	*B*	*C*	*D*	*A*	*B*	*C*	*D*
NOAA-6*	1979	27–06–1979	0.000	1.790	0.0000	38.410	0.0000	2.830	0.000	32.650				
NOAA-7	1981	23–06–1981	-1.7390×10^{-4}	1.738	0.0000	36.000	-3.0310×10^{-4}	2.555	0.000	37.000				
NOAA-7	1982		-1.6910×10^{-4}	1.737	0.0000	36.000	-2.9320×10^{-4}	2.533	0.000	37.000				
NOAA-7	1983		-1.6300×10^{-4}	1.734	0.0000	36.000	-2.8060×10^{-4}	2.546	0.000	37.000				
NOAA-7	1984		1.5700×10^{-4}	1.728	0.0000	36.000	-2.6860×10^{-4}	2.535	0.000	37.000				
NOAA-8	1983	12–12–1983	0.0000	1.830	0.0000	39.260	0.0000	2.810	0.000	39.410				
NOAA-9	1985	12–12–1984	-2.2380×10^{-4}	1.731	-3.8560×10^{-4}	38.040	-4.2000×10^{-4}	2.501	–1.818	40.070				
NOAA-9	1986		-2.7590×10^{-4}	1.751	-1.7730×10^{-4}	37.960	-2.2730×10^{-4}	2.427	-8.022×10^{-4}	39.680				
NOAA-9	1987		-2.4570×10^{-4}	1.728	-1.3010×10^{-4}	37.930	-1.4310×10^{-4}	2.364	-2.036×10^{-4}	39.240				
NOAA-9	1988		-1.3650×10^{-4}	1.607	-2.3810×10^{-4}	38.050	-1.6110×10^{-4}	2.384	1.099×10^{-5}	39.000				
NOAA-9	1989		-2.3300×10^{-4}	1.792	0.0000	37.000	-2.1870×10^{-4}	2.595	0.000	39.600				
NOAA-9	1990		-2.1930×10^{-4}	1.766	0.0000	37.000	-2.1100×10^{-4}	2.581	0.000	39.600				
NOAA-9	1991		-2.0650×10^{-4}	1.738	0.0000	37.000	-2.0360×10^{-4}	2.565	0.000	39.600				
NOAA-9	1992		-1.9430×10^{-4}	1.707	0.0000	37.000	-1.9640×10^{-4}	2.546	0.000	39.600				
NOAA-9	1993		-1.8290×10^{-4}	1.673	0.0000	37.000	-1.8950×10^{-4}	2.526	0.000	39.600				
NOAA-9	1994		-1.7210×10^{-4}	1.638	0.0000	37.000	-1.8280×10^{-4}	2.504	0.000	39.600				
NOAA-9	1995		-1.6200×10^{-4}	1.600	0.0000	37.000	-1.7640×10^{-4}	2.480	0.000	39.600				
NOAA-10*	1986	17–09–1986	0.0000	1.791	0.0000	33.300	0.0000	2.839	0.000	32.800				
NOAA-11	1988	24–09–1988	-2.3330×10^{-4}	1.704	1.2200×10^{-4}	39.980	–9.5780	2.606	1.632×10^{-4}	39.970				
NOAA-11	1989		-3.0790×10^{-5}	1.684	5.8150×10^{-5}	39.990	-3.0490×10^{-4}	2.542	4.929×10^{-5}	39.990				
NOAA-11	1990		5.4120×10^{-5}	1.646	-4.2360×10^{-5}	40.040	9.1080×10^{-5}	2.358	-1.284×10^{-4}	40.070				
NOAA-11	1991		1.3000×10^{-6}	1.689	-1.4290×10^{-4}	40.120	4.4190×10^{-5}	2.397	-3.062×10^{-4}	40.220				
NOAA-11	1992		2.0100×10^{-5}	1.666	-2.4350×10^{-4}	40.240	3.2880×10^{-5}	2.410	-4.842×10^{-4}	40.430				
NOAA-11	1993		2.8040×10^{-5}	1.654	3.8320×10^{-4}	39.260	-4.5840×10^{-5}	2.533	8.901×10^{-4}	38.290				
NOAA-11	1994		-5.6010×10^{-5}	1.815	0.0000	40.000	-1.3000×10^{-4}	2.701	0.000	40.000				
NOAA-12	1991	14–05–1991	-4.9630×10^{-5}	1.615	0.0000	40.300	-4.5813×10^{-5}	2.087	0.000	40.000				
NOAA-12	1992		-4.8730×10^{-5}	1.615	0.0000	40.300	-4.5218×10^{-5}	2.087	0.000	40.000				
NOAA-12	1993		-4.7659×10^{-5}	1.614	0.0000	40.300	-4.4504×10^{-5}	2.087	0.000	40.000				
NOAA-12	1994		-4.6625×10^{-5}	1.613	0.0000	40.300	-4.3807×10^{-5}	2.086	0.000	40.000				
NOAA-12	1995		-4.5624×10^{-5}	1.612	0.0000	40.300	-4.3127×10^{-5}	2.085	0.000	40.000				
NOAA-12	1996		-4.4654×10^{-5}	1.610	0.0000	40.300	-4.2462×10^{-5}	2.084	0.000	40.000				
NOAA-12	1997		-4.3714×10^{-5}	1.608	0.0000	40.300	-4.1812×10^{-5}	2.083	0.000	40.000				
NOAA-12	1998		-4.2805×10^{-5}	1.606	0.0000	40.300	-4.1177×10^{-5}	2.081	0.000	40.000				
NOAA-12	1999		-4.1924×10^{-5}	1.604	0.0000	40.300	-4.0557×10^{-5}	2.079	0.000	40.000				
NOAA-12	2000		-4.1068×10^{-5}	1.601	0.0000	40.300	-3.9950×10^{-5}	2.077	0.000	40.000				
NOAA-12	2001		-4.0239×10^{-5}	1.598	0.0000	40.300	-3.9357×10^{-5}	2.075	0.000	40.000				
NOAA-12	2002		-3.9436×10^{-5}	1.595	0.0000	40.300	-3.8777×10^{-5}	2.073	0.000	40.000				
NOAA-12	2003		-3.8656×10^{-5}	1.592	0.0000	40.300	-3.8210×10^{-5}	2.071	0.000	40.000				
NOAA-12	2004		-3.7898×10^{-5}	1.588	0.0000	40.300	-3.7655×10^{-5}	2.068	0.000	40.000				
NOAA-12	2005		-3.7898×10^{-5}	1.588	0.0000	40.300	-3.7655×10^{-5}	2.068	0.000	40.000				
NOAA-14	1995	30–12–1994	-2.5200×10^{-4}	1.686	0.0000	41.000	-4.2550×10^{-4}	2.087	0.000	41.000				
NOAA-14	1996		-1.2490×10^{-4}	1.639	0.0000	41.000	-3.8370×10^{-5}	1.946	0.000	41.000				
NOAA-14	1997		-1.2490×10^{-4}	1.639	0.0000	41.000	-3.8370×10^{-5}	1.946	0.000	41.000				
NOAA-14	1998		-1.2490×10^{-4}	1.639	0.0000	41.000	-3.8370×10^{-5}	1.946	0.000	41.000				
NOAA-14	1999		-1.2490×10^{-4}	1.639	0.0000	41.000	-3.8370×10^{-5}	1.946	0.000	41.000				
NOAA-14	2000		-1.2490×10^{-4}	1.639	0.0000	41.000	-3.8370×10^{-5}	1.946	0.000	41.000				

Table 3 (*concluded*).

Sensor	Year	Launch date	VIS				NIR				SWIR			
			A	*B*	*C*	*D*	*A*	*B*	*C*	*D*	*A*	*B*	*C*	*D*
NOAA-15*	1998	13–05–1998	1.3900×10^{-6}	3.269	0.0000	38.500	3.5640×10^{-5}	4.636	0.000	40.400	0.0000	47.420	0.0000	3.8900×10^{1}
			4.8340×10^{-6}	1.137	0.0000	336.900	1.3040×10^{-5}	1.696	0.000	338.800	0.0000	7.064	0.0000	4.2370×10^{2}
NOAA-16*	2000	21–09–2000	0.0000	3.653	0.0000	38.500	0.0000	5.920	0.000	39.300	0.0000	44.944	0.0000	38.2000
			0.0000	1.250	0.0000	339.700	0.0000	2.011	0.000	432.100	0.0000	7.142	0.0000	432.1000
NOAA-17*	2002	24–06–2002	0.0000	3.449	0.0000	40.900	0.0000	5.609	0.000	40.000	0.0000	48.948	0.0000	3.9000×10^{1}
			0.0000	1.177	0.0000	341.000	0.0000	1.879	0.000	345.400	0.0000	6.974	0.0000	4.3320×10^{2}

*Values based on prelaunch coefficients provided by NOAA.

Figure 2. Georeferencing accuracy of the AVHRR NOAA-17 image from 14 August 2003 (1923 UTC) of the northern part of Vancouver Island, B.C. (a) Level L1B original image. Average shift along the orbital track of about two lines is observed. (b) Correction developed in the paper is applied that removes L1B bias.

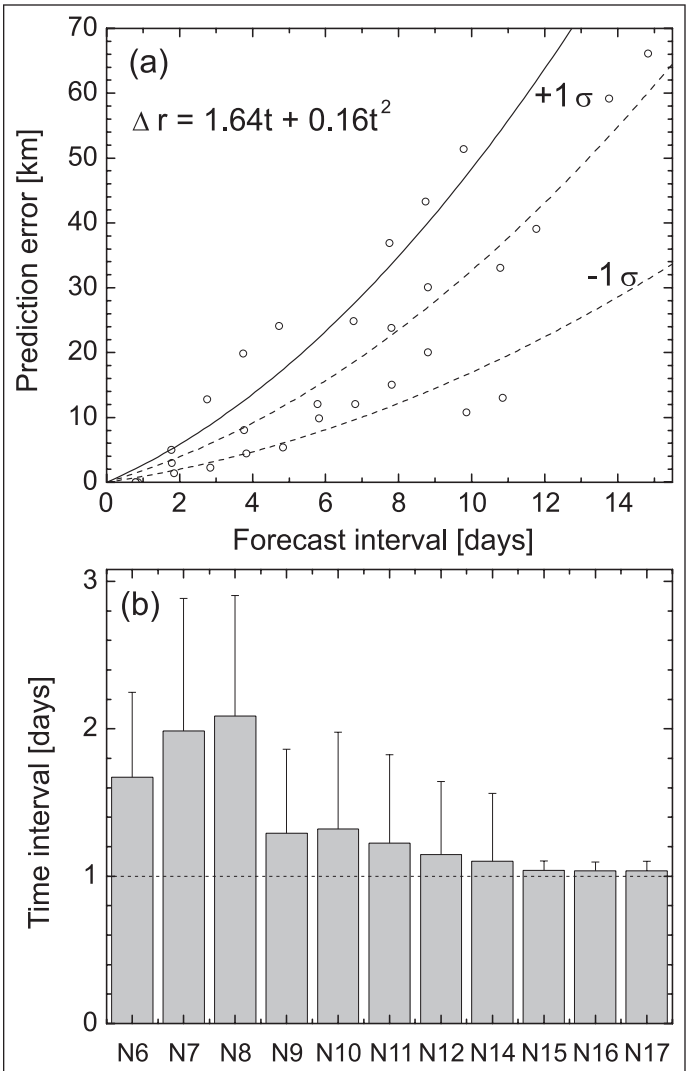

Figure 3. (a) Growth of the orbit prediction error (Δr) with time (t). (b) Average time interval between acquisition time and the TBUS epoch time. Normally, TBUS data are updated every day. For various reasons, some data are missing for early satellites. Vertical bars denote standard deviation, and N6–N17 denotes NOAA-6 to NOAA-17.

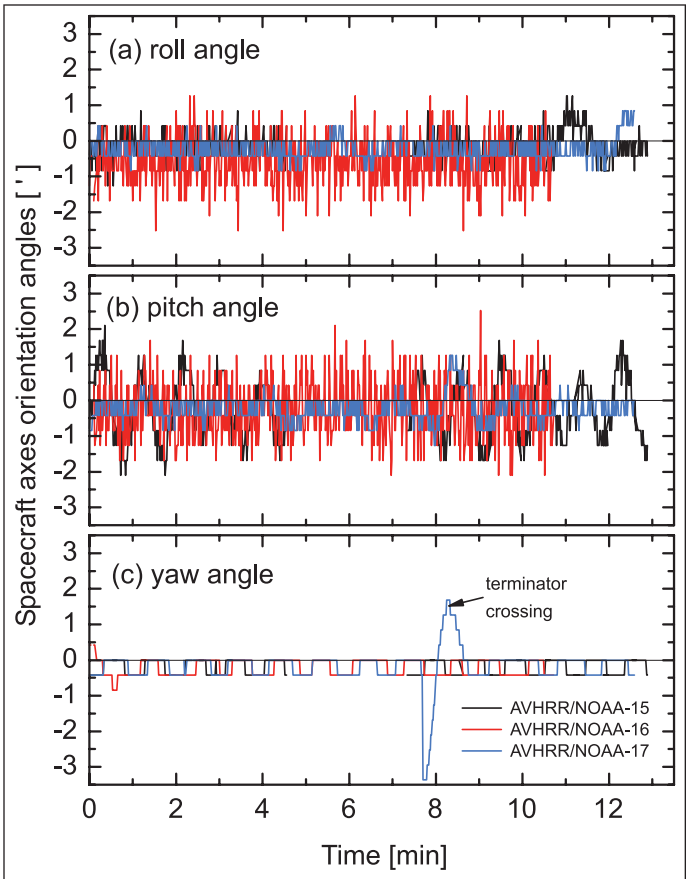

Figure 4. An example of spacecraft orientation angles for AVHRR NOAA-15, NOAA-16, and NOAA-17: (a) roll angle, (b) pitch angle, and (c) yaw angle. Typical amplitudes are below 2′.

pitch angles for AVHRR-3 type radiometers within a single scene is presented in **Figure 4**. One can see that amplitudes are typically less than 2′ and often less than 1′. Larger amplitudes may occur occasionally, as is the case for NOAA-17 yaw angles shown in **Figure 4c** during the crossing of the terminator plane. The data shown in **Figure 4** were extracted directly from HRPT data formatted for AVHRR-3. For earlier radiometers (AVHRR-1 and AVHRR-2) this information was not included in HRPT telemetry. According to the estimates presented in Brunel and Marsouin (2000), neglecting such variations in the AVHRR processing will generally lead to errors that are less than 1 km. It is still possible that some systematic misalignment may exist that will require the introduction of constant biases to the attitude angles, similar to the one described by Trishchenko (1994) and Brunel and Marsouin. If known, such an error can be explicitly corrected by introducing systematic offsets in the orientation of the instrument axes. If unknown in advance, this error can be combined with the random errors related to attitude angles. It is important to note that this error cannot be neglected when it is large.

The subpixel georeferencing refinement to account for systematic shifts and errors related to uncertainties in the attitude angles is performed using GCPs automatically collected by a chip-matching procedure. The chip-matching procedure is conducted for the AVHRR scene transformed into LCC projection using nominal orbital model georeferencing. When the chip-matching procedure is completed, the parameters of the second-order polynomial that minimizes errors in the location of chips are determined. This second-order polynomial transformation is applied to the coordinates of the entire image.

Two chip databases, one for the summertime and one for the wintertime, are employed in the chip-matching procedure. These databases were extracted from a number of precisely georeferenced clear-sky AVHRR orbits. The distribution of chips is shown in **Figure 5**. Each database contains several thousand chips capturing linear or boundary terrain features (e.g., coastlines, lakeshores, or river branches). Chips are evenly distributed over Canada, Greenland, Alaska, and the northern US. Every chip is a subset of 64 pixels × 64 pixels

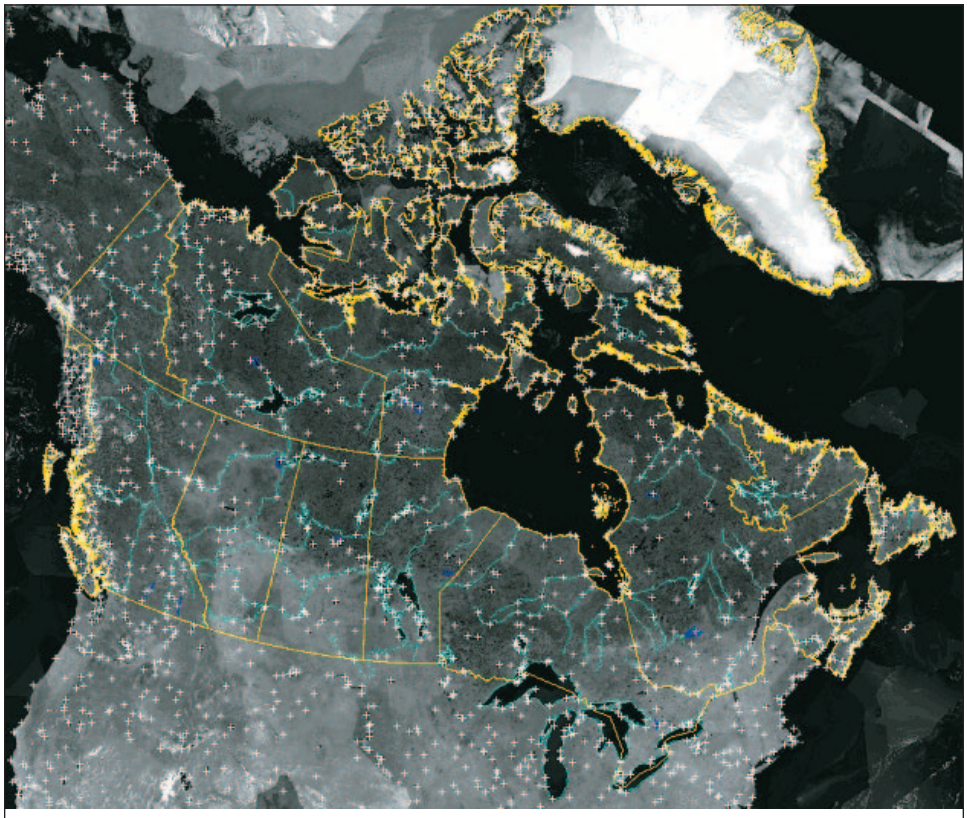

Figure 5. Location of image chips with GCPs used for improving the image registration.

extracted from AVHRR NIR and IR bands. The NIR band is used because it provides better land–water contrast (Cracknell, 1997). The IR band is used for nighttime and winter orbit segments.

To accurately position a chip image within the AVHRR swath, a digital image matching procedure based on a correlation surface is implemented (see Guindon (1985), and Cracknell and Paithoonwattanakij (1989)). An AVHRR image and a chip image with common coordinate grids are systematically displaced over an XY search window. A match surface is generated and matching is quantified using Pearson's correlation coefficient. The exact location of the "best match position" is subsequently computed as the maximum peak value of the correlation surface.

Frequently, the correlation coefficient alone cannot guarantee an accurate chip location. A false correlation peak in the matching surface can result because of the presence of shadows, clouds, or noise in the data. For this reason, only the chips with the higher correlation coefficients ($R^2 > 0.70$) are considered. The final GCP set is selected using the following additional rules:

(1) The dominant error is the along-track location error, which can be positive or negative. Suggested displacements by GCPs along the orbit track should point to the same direction along the subsatellite track.

(2) If clouds cover the search window, the chip matching will not be performed. A conservative threshold in the VIS band is used as a cloud indicator.

(3) If the suggested displacement exceeds the half size of the search window, the chip is rejected because the best location is outside of this window.

(4) The remaining chips that passed rules 1, 2, and 3 are used to compute the average displacements along x and y axes (AD_x, AD_y) and their standard deviations (S_x, S_y). Displacement thresholds T_x and T_y used to determine the final GCP list are computed using the equation $T_{x,\,y} = 2.045 S_{x,y}^{0.5791}$. The rationale for this criterion is that more consistent displacements suggested by GCPs will have a lower standard deviation, and thus thresholding needs to be more rigorous.

A large number of GCPs in the chip database ensures the high success rate of geometrically well corrected scenes. The final image rectification is implemented using a quadratic polynomial fitted to the refined GCPs based on a least-squares estimation procedure. The georeferencing accuracy is assessed by computing the root mean square error (RMS) for each GCP. This method ensures the accuracy of pixel locations only in the vicinity of the GCP, however. Frequently, the GCPs are not distributed uniformly across the scene. In such a case, the correction based on a quadratic polynomial model can cause significant distortions in the part of an image where no GCPs

were located. Two additional steps are implemented to control the accuracy:

(1) The magnitude of distortion is calculated as the difference in pixel locations determined by the orbit model and the polynomial fit. If this difference exceeds the thresholds $AD_x \pm 3S_x$ or $AD_y \pm 3S_y$ estimated from GCPs, the pixel is flagged as distorted.

(2) The convex hull buffer (Chen, 2003) is used to delineate the part of the image without distortion where high georeferencing accuracy is achieved.

Figure 6 shows an example of the convex hull buffer generated using selected GCPs and marks the area where the pixel location accuracy is estimated to be better than 1 km. Applying the convex hull mask reduces the volume of useful data. For many applications, however, this is not a significant drawback because the parts of an image outside the convex hull buffer are in most cases covered with clouds and therefore cannot be used. For other applications, such as cloud and radiation research, where georeferencing accuracy requirements are not so stringent, the convex hull buffer can be increased. Presently, a special flag is introduced that marks pixels inside and outside the convex hull. This flag is used later in the analysis and during the clear-sky compositing procedure to ensure that only pixels with the highest earth location accuracy are used. An example of the corrected image as previously described is shown in **Figure 2b**. One can see that the biases observed in L1B data were corrected with a very good accuracy.

The implementation of the georeferencing scheme described here leads to substantial increases in the rate of successfully processed scenes relative to GeoComp-n results (from ~40% to nearly 80%). Because the convex hull method was not implemented in GeoComp-n, the large georeferencing errors produced by GeoComp-n frequently remained undetected. This is demonstrated in **Figure 7**, which shows an example of a clear-sky composite image produced for AVHRR NOAA-16 for 21–31 August 2002. **Figure 7a** shows the image produced by GeoComp-n using the maximum NDVI method, and **Figure 7b** shows the image obtained using the EODM processing approach described in this paper. The striking feature is the substantial reduction in the size of Dubawnt Lake relative to its original boundaries. This occurred because land pixels were erroneously placed over water, and during the compositing step the GeoComp-n picked up land pixels instead of clear-sky water pixels because of their higher NDVI. One can also see that maximum NDVI compositing always leads to the selection of cloudy pixels over water because NDVI values for cloud scenes are slightly larger that those for water (although both are near zero). Numerous small lakes visible in **Figure 7b** are also missing in **Figure 7a**. Similar types of errors caused by inaccurate pixel positions also occur for land pixels.

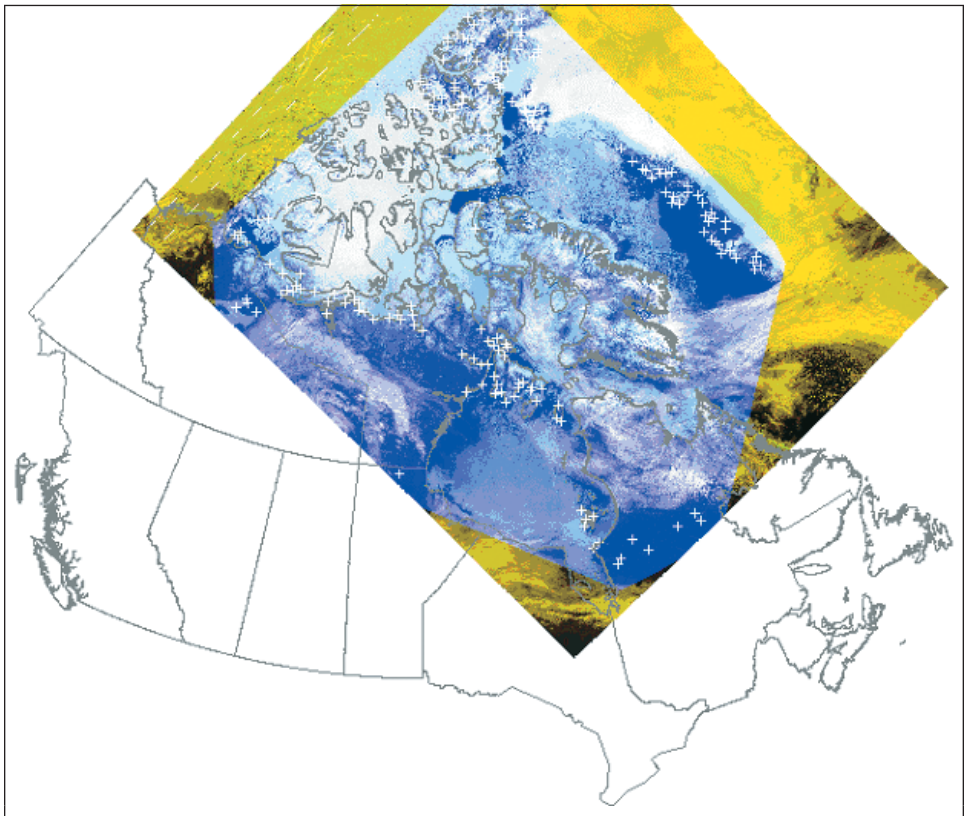

Figure 6. Convex hull mask (shown in blue) that encircles the area where pixel geolocation accuracy is estimated better than prescribed threshold (1.0 km). Mask is then used in the compositing procedure to ensure high georeferencing accuracy for every pixel included in the output composite image.

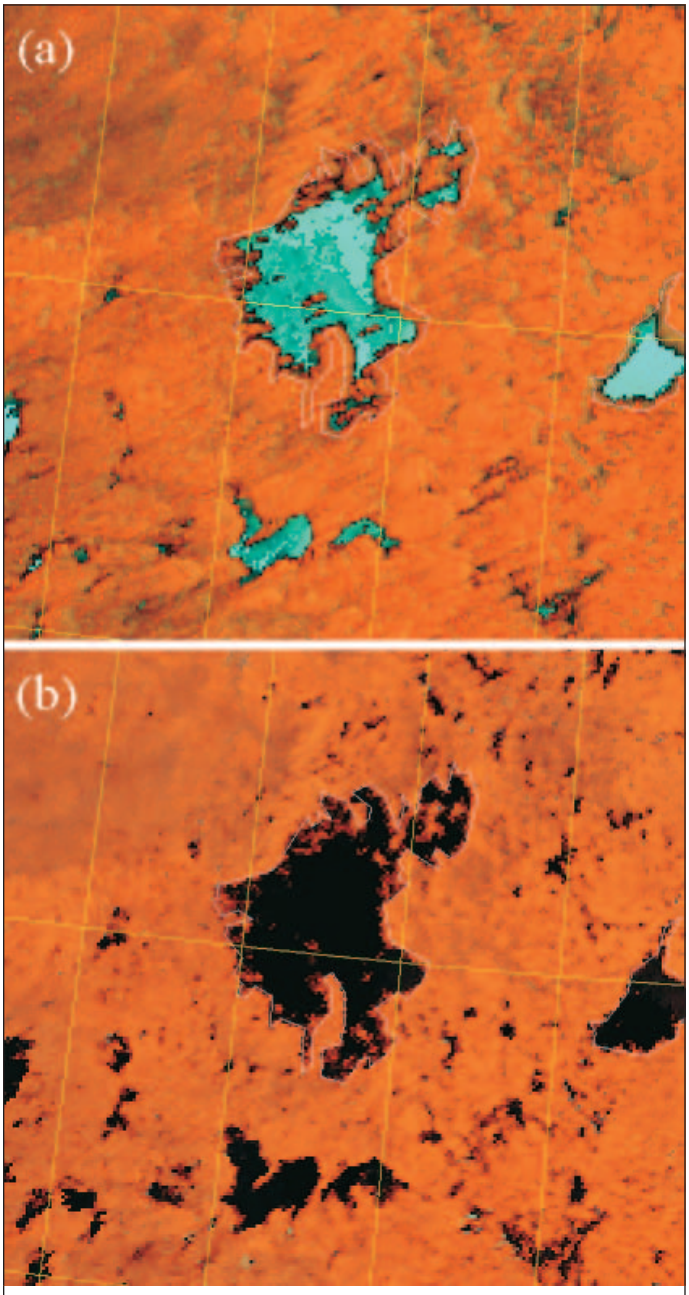

Figure 7. Comparison between two clear-sky composite images produced by (a) GeoComp-n and (b) EODM systems using AVHRR NOAA-16 for 21–31 August 2003. The area around Dubawnt Lake, Nunavut Territory, is shown.

These errors must be corrected if the data are to be used in climate studies. It is likely that these types of problems can substantially reduce the quality of many global datasets derived from GAC data because georeferencing errors and cloud-shadow contamination were not always controlled properly, especially in the early years.

Pixel scene identification

The pixel scene identification procedure implemented in EODM is described in detail by Khlopenkov and Trishchenko.[3] The algorithm is implemented to operate for daytime and nighttime scenes during snow-free and snow seasons over water and land areas. It substantially improved the cloud detection scheme used earlier (Cihlar et al., 2004).

The procedure is applied to full-resolution AVHRR data calibrated and georeferenced during previous steps. The method incorporates several tests: (*i*) the comparison of channel 4 (11 μm) brightness temperature with the temperature map generated from the North American regional reanalysis data (available from http://dss.ucar.edu/pub/narr/), (*ii*) a reflectance threshold test based on VIS–NIR reflectance, (*iii*) a snow versus cloud test based on the reflectance in channel 3 (1.6 or 3.7 μm), (*iv*) an NDVI test, (*v*) texture uniformity and thermal uniformity tests, and (*vi*) the use of differences between thermal channels 4 and 5 to detect thin ice clouds.

The unique characteristic of the scene identification algorithm is its incorporation of all tests to produce an aggregated effective cloudiness index. This aggregated index has better reliability than a simple sequence of separate tests and allows for a distinction between the different levels of cloudiness. Other features of the algorithm are a dynamic correction for the sun glint from water pixels, the generation of snow–ice maps for cloud-free and thin-cloud pixels, and the calculation of a cloud-shadow mask. An example of a cloud mask is given in **Figure 8**. **Figure 8a** shows the AVHRR VIS channel, and **Figure 8b** shows the generated cloud mask and clear-sky land and water, snow and ice, and cloud shadows.

The scene identification mask is used as an input layer in generating clear-sky composites. It is also used for cloud property retrievals, water temperature retrievals, and land surface applications such as the retrieval of surface albedo, land cover, NDVI, leaf area index, and snow and ice mapping.

Clear-sky compositing

Compositing the single scenes over certain time intervals (1 day, 10 days, 1 month) to produce a single image with the best selection of clear-sky pixels is a standard procedure. It allows for the production of datasets with reduced contamination due to clouds and haze. Several compositing methods have been proposed in the past. They are usually variants of so-called "maximum (or minimum) value compositing (MVC)" techniques.

The maximum NDVI method is often used to generate composite data for studying terrestrial vegetation. It is frequently implemented with a threshold that limits the satellite view zenith angle (VZA). The minimum VIS band value compositing method is used as a preferable tool for producing composite data for mapping forest fires (Fraser and Li., 2002), snow and ice, and water bodies. Although very good for

[3] K.V. Khlopenkov and A.P. Trishchenko. CLEAR: the new cloud, clear-sky, snow/ice and snow detection algorithm for historical AVHRR 1-km observations. *Journal of Atmospheric and Oceanic Technology*. In preparation.

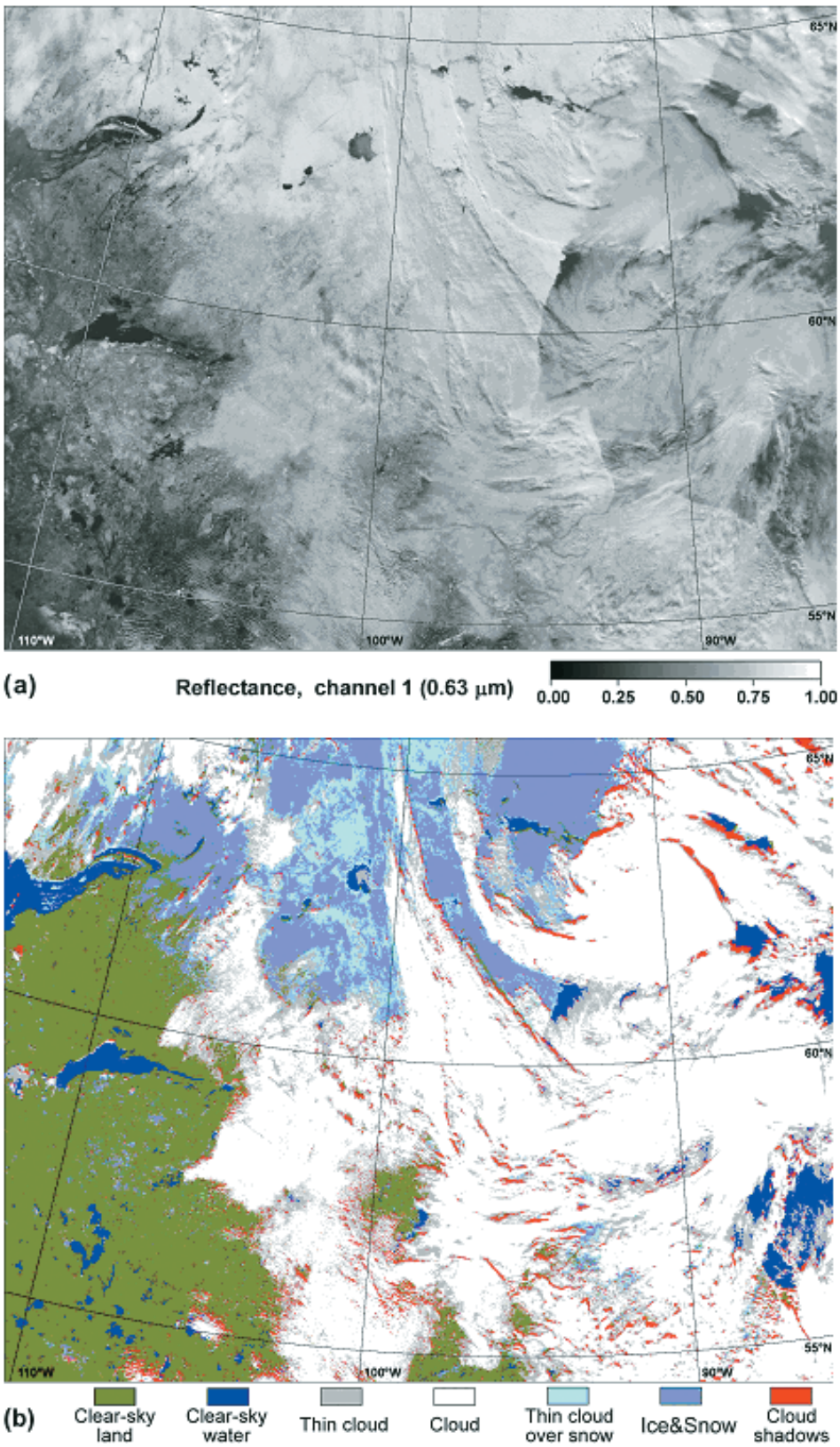

Figure 8. An example of the cloud mask produced using the automated cloud – clear-sky detection algorithm developed for historical AVHRR data processing (Khlopenkov and Trishchenko, in preparation[3]) using AVHRR NOAA-16 on 22 October 2002 (1946 UTC): (a) AVHRR channel 1; (b) generated cloud mask and clear-sky land and water, cloud shadows, and snow and ice.

removing clouds and haze, this approach has a problem because of the preferable selection of cloud shadows over truly clear-sky pixels and discriminating snow from clouds. By switching maximum NDVI and minimum VIS over land and water, and introducing some weighting coefficients, one can design a more complex combined method "maximum NDVI – minimum VIS". This method works efficiently over both water and land surfaces but is still vulnerable to cloud shadows and is not effective for discriminating between snow and clouds. Optical bands can be used only during daytime scenes. For nighttime and winter composites, a maximum surface temperature method can be implemented. The rationale behind this approach is that in most cases clouds are colder then the earth's surface. The weakness is that, under some conditions such as in high-mountain regions and low-cloud conditions, this assumption is not correct.

The compositing technique developed and implemented in EODM relies on the scene identification mask and cloudiness index derived for each pixel as described in the previous section. Pixels identified as shadow-free are rated based on the magnitude of the cloudiness index (a certain equivalent of cloud–haze optical depth). The pixel that has the smallest index for the compositing interval is then selected. When index values are similar, the pixel that has smaller values of VZA and the solar zenith angle (SZA) is selected.

Examples of composite images derived by the four methods described previously are shown in **Figure 9**. These images were derived using (*i*) the minimum VIS and VZA < 55° method (**Figure 9a**); (*ii*) the maximum NDVI and VZA < 55° method (**Figure 9b**); (*iii*) the maximum NDVI and minimum VIS and VZA < 55° method (**Figure 9c**); and (*iv*) the EODM compositing method, which takes into account the cloud-shadow mask and cloudiness index (**Figure 9d**). From these

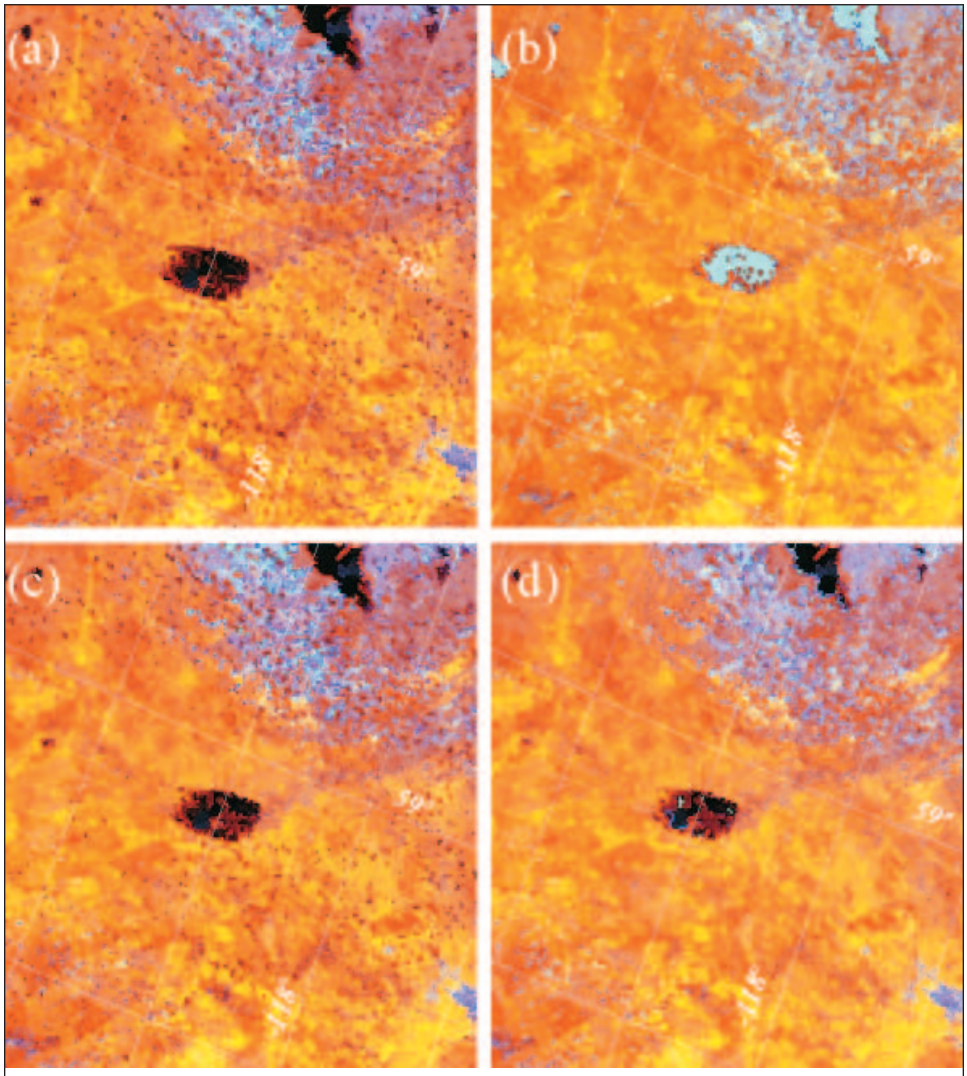

Figure 9. Examples of VIS channel clear-sky composite images generated using different compositing criteria. (AVHRR NOAA-14 for 1–10 June 1997): (a) minimum VIS and VZA < 55°; (b) maximum NDVI and VZA < 55°; (c) maximum NDVI and minimum VIS and VZA < 55°; (d) EODM compositing that takes into account cloud-shadow mask and cloudiness index.

images, it appears that the best results are achieved for the EODM compositing procedure (method *iv*). The other methods are vulnerable to cloud-shadow contamination (methods *i* and *iii*) or bad performance over water (method *ii*).

For quantitative estimates, the composite images shown in **Figure 9** were analyzed for variability of spectral reflectance within the spectrally stable land cover type representing coniferous high-density forest. We expect that the best method provides the smallest range of variation in spectral reflectance for this land cover type. The average coefficients of variation (CV) in the VIS and NIR bands were lowest for the composites generated using the cloudiness index (CV = 48%). The "maximum NDVI and minimum VIS" method yields CV = 53%. The composite generated using the "Min RED" method gives CV = 55%, and the "Max NDVI" method had the highest variability, with CV = 73%. Therefore, conclusions derived from visual analysis of **Figure 9** are consistent with quantitative statistical results.

Overall EODM system performance

The initial system performance was conducted using the rate of successfully processed orbits, georeferencing accuracy, and the radiometric consistency of generated products.

The georeferencing performance was evaluated for the period July–August and for the winter period (October–April) from 1985 to 2004. A total of 80 956 orbit segments in NATAS and HRPT-L1B format were processed using 60 CPU units. Overall, 10% of all orbits were rejected by the quality-control routine because of corrupted data, large numbers of missing lines, or other problems in the telemetry or header records. Most of the rejected orbit segments were acquired in the early 1980s, indicating lower data quality for this period. Nearly 75% of processed orbits were precisely georeferenced using a sufficient number of GCPs. The remaining 25% of processed orbit segments were georeferenced using only the orbit model with variable pixel location accuracy depending on the quality of ephemeris data. The success rate was similar for all years and depended mainly on the scene size, the availability of ephemeris data, and raw data quality.

A substantially higher success rate in georeferencing was achieved when processing NATAS data for winter and summer (82%) compared with the L1B data (67.5%). The most important reason for this difference was the difference in the average scene size (5400 lines for NATAS data versus 2700 lines for L1B data). The size of the scene influences the success rate because a longer orbit increases the probability of finding more GCPs, and thus achieving better georeferencing accuracy. Processing was somewhat more successful for recent years mainly due to better data reception and a higher quality of orbital information.

Table 4 shows a comparison between GeoComp-n and EODM for the summer of 2002. The same NATAS orbit segments were used with both systems to generate six 10 day composites for July and August 2002. The peak of the growing season was selected for the comparison period because atmospheric conditions were most favourable during this time for processing systems to achieve the greatest number of successfully processed orbits. **Table 4** also shows that additional L1B orbit segments were used for generating composites with the EODM but not with the GeoComp-n system. The reason for this is that the NOAA L1B format for data acquired in the summer of 2002 from AVHRR NOAA-16 is not supported in GeoComp-n. The EODM successfully processed 36% more AVHRR orbits than the GeoComp-n system. This is a significant improvement because a larger number of initial orbits for generating composites provides more options in selecting clear-sky observations with the highest georeferencing accuracy and with more favourable viewing geometry.

An attempt to analyze the radiometric consistency of the generated time series was conducted using the Lake Athabasca sand dunes (**Figure 10**). Despite its small size, variable relief, and proximity to a large lake, the sand dunes appears to be the most radiometrically stable bright reference target in Canada and was identified for initial data consistency assessment. Top-of-atmosphere VIS and NIR reflectance time series extracted from 10 day composites for the period July–August 1985–2004 of the 16 pixels covering the sand dunes are shown in **Figure 10a**. The time series do not reveal any systematic trend in the TOA reflectances for the period analyzed. Furthermore, a *Z* test (at $\alpha = 0.05$) does not show any statistically significant difference among measurements acquired with various

Table 4. Comparison between GeoComp-n and EODM rate of successful processing.

	No. of orbit segments in NATAS (CCRS) format			No. of orbit segments in L1B (NOAA) format	
Time interval (2002)	All input	EODM processed	GeoComp-n processed	All input	EODM processed
1–10 July	80	73	37	129	78
11–20 July	60	55	34	128	84
21–31 July	85	73	41	141	76
1–10 Aug.	76	61	40	128	63
11–20 Aug.	78	56	40	114	56
21–31 Aug.	81	54	45	140	68
Overall	460	372	237	780	425
Success rate (%)		80.8	51.5		54.5

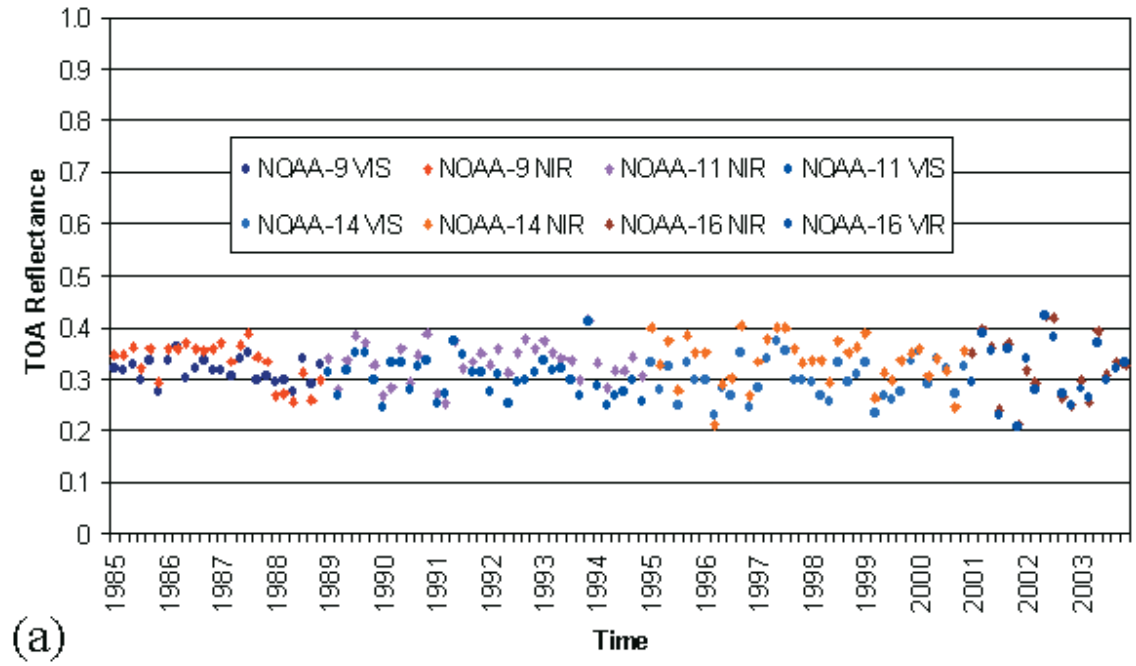

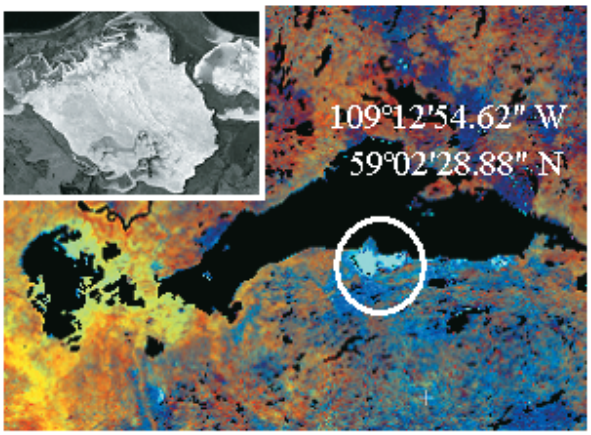

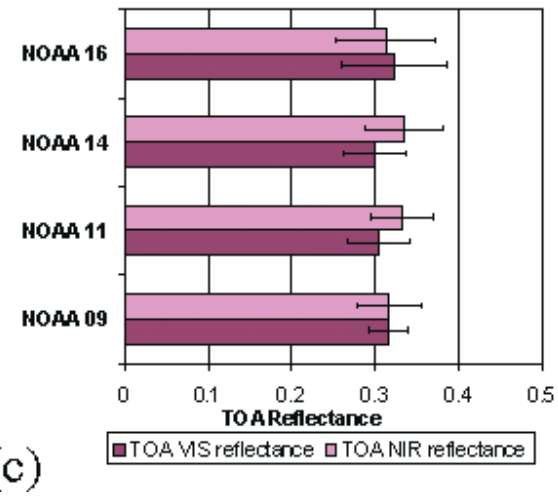

Figure 10. The visible and NIR TOA reflectance time series of the Lake Athabasca sand dunes (circled in b) extracted from 10 day composites for the period July–August 1985–2004. The horizontal bars in (c) represent standard deviation.

AVHRR sensors (**Table 5**). The variability within the time series (expressed as the CV) is quite high (12.7% for VIS channels and 13.9% for NIR channels) (**Figure 10c**), however. The source of these uncertainties can be partially explained by variable acquisition conditions (i.e., viewing geometry, atmospheric state, variability in soil moisture, and remaining cloud and haze contamination). Nevertheless, these results demonstrate the reasonable radiometric consistency derived with calibration coefficients currently implemented in EODM processing, although work is ongoing to refine the calibration.

Table 5. Mean and standard deviation (SD) values of visible (VIS) and near-infrared (NIR) TOA reflectance for several AVHRR sensors over the Athabasca sand dunes region shown in **Figure 10**.

	VIS		NIR	
	Mean	SD	Mean	SD
NOAA-9	0.3158	0.0230	0.3158	0.0386
NOAA-11	0.3033	0.0376	0.3325	0.0376
NOAA-14	0.2994	0.0374	0.3350	0.0461
NOAA-16	0.3225	0.0630	0.3128	0.0594

Note: *Z*-test values for the samples are between 0.74 and 0.96, which means a very high probability of agreement (no significant difference) between mean values. $Z_{crit} = 1.96$ at 95% confidence level $P(Z \leq z)$.

Further processing

The baseline products generated with EODM provide TOA reflectance and brightness temperature with variable geometry. Some limited analyses can be conducted employing the relative variations in the baseline datasets to study the dynamics of some geophysical parameters such as growing season length (Fillol and Royer, 2001; Duchemin et al., 1999) and vegetation, snow, and ice cover. Additional processing of these data is required to derive surface properties and various geophysical products, however. In the EODM, the postseasonal correction procedure (ABC3: atmospheric, bidirectional, and contamination correction of the CCRS; Cihlar et al., 2004) is implemented. The ABC3 performs atmospheric corrections of TOA reflectance employing the advanced version of the algorithm initially proposed by Rahman and Dedieu (1994). This method has been augmented to incorporate local topographic effects (Trishchenko et al., 2000). The parameterization of atmospheric attenuation and aerosol correction has also been improved and tuned to MODTRAN-4 computations (Trishchenko et al., 2002c). Surface reflectances are then normalized to a common viewing geometry using a nonlinear temporal angular BRDF model (NTAM) (Latifovic et al., 2003). This normalization removes, to a large degree, the surface anisotropic effects present in the composite data. Detecting and replacing contaminated observations in composite data are performed using the CECANT algorithm (Cihlar et al., 1999). The 10 day corrected composites, together with other relevant environmental data, are further employed to generate geophysical data records. The postseasonal correction for the SPOT VGT data is similar to the AVHRR procedure, with specific parameters tuned to VGT channels. The postseasonal corrections of MODIS MOD43B1 data are described by Trishchenko et al. (2005) and Luo et al. (2005).

Application example

As an example of derived multiyear AVHRR 1 km satellite baseline product and EODM system performance, we present a brief analysis of the trend and variability of sea ice cover over Hudson Bay. Several recent studies have shown that the extent and duration of arctic sea ice have been decreasing over the past few decades (Smith, 1998; Parkinson et al., 1999; Parkinson and Cavalieri, 2002; Belchansky et al., 2005). It is likely that this decrease has occurred due to changing climate. Sea ice and snow cover are important components of the earth climate system. They affect the radiation budget, heat transfer, ocean thermohaline circulation, and water budgets. Historical data collected with AVHRR NOAA can provide the longest available record of large-scale melt and freeze-up of sea ice at a very detailed spatial resolution. In the following example, we present some results relevant for studying the length of the ice melt season over Hudson Bay.

The reflectance time series of TOA VIS reflectance was generated for July–August for the period 1985–2004. The time series was derived using the EODM processing approach and clear-sky compositing described earlier in the paper. **Figure 11a** shows the sequence of 10 day composite images generated. The time series of sea ice extent was estimated based on the proportion between ice and water reflectance. Assuming a linear spectral mixing of ice and water in the AVHRR VIS channel,

$$\rho = \rho_w f_w + \rho_i f_i; \quad 1 = f_w + f_i, \tag{3}$$

ice fraction is simply computed by inverting Equation (3), where f_i is the ice fraction, f_w is the water fraction, ρ is the reflectance measured, ρ_i is the ice reflectance, and ρ_w is the water reflectance. The average VIS reflectance in the study area was 0.38 ± 0.048 for ice (ρ_i) and 0.04 ± 0.0078 for water (ρ_w). These reflectances were estimated by the visual inspection and identification of continuous open water and ice fields.

Figure 11a shows the sequence of 20 false colour images as RGB (red, NDVI; green, NIR; blue, VIS) produced for the period 1–10 July. The sea ice extent time series over Hudson Bay and James Bay are presented in **Figure 11b**. The upper line represents estimated fractions of ice cover for the period 1–10 July for every year since 1985. The peak in the graph, corresponding to the late breakup of ice in 1992, coincides with strong El Niño – Southern Oscillation (ENSO) and North Atlantic Oscillation (NAO) events as discussed by Mysak et al. (1996) and Gough et al. (2004). Low air temperatures in 1992 may also be related to the Pinatubo eruption in 1991, when a large volume of volcanic ash particles was injected into the atmosphere and reduced surface solar radiation (Lucht et al., 2002). The early breakup in 1998 and 1999, when Hudson Bay and James Bay were free of ice (see **Figure 11a**), is in agreement with observations that 1998 was the warmest year of the last century in Canada (Atkinson et al., 2005; CCAF Summer 1998 Project Team, 2001).

Based on these time series, a decreasing trend in the extent of sea ice is statistically evident for the period 1–10 July between 1985 and 2004. The average decrease in surface area is estimated to be approximately 1.5% per year. When the outlier in 1992 is removed from the time series, the average decrease in Hudson Bay and James Bay sea ice extent for the period 1–10 July is ~1.3% per year. The results obtained in this case study are generally in good agreement with the reported increases in the length of the melt season (Smith, 1998; Parkinson et al., 1999). These studies have used passive microwave data to show that the length of the melt season in Hudson Bay increased at a rate of 0.45 days per year between 1979 and 1996.

Summary and conclusion

The new system earth observation data manager (EODM) developed for generating AVHRR 1 km and other medium-resolution satellite-based climate data records is described. The results and the contents of the newly assembled AVHRR 1 km data archive are presented. At this time, the archive represents the most complete collection of AVHRR 1 km imagery ever acquired over Canada. The existing national coverage collected

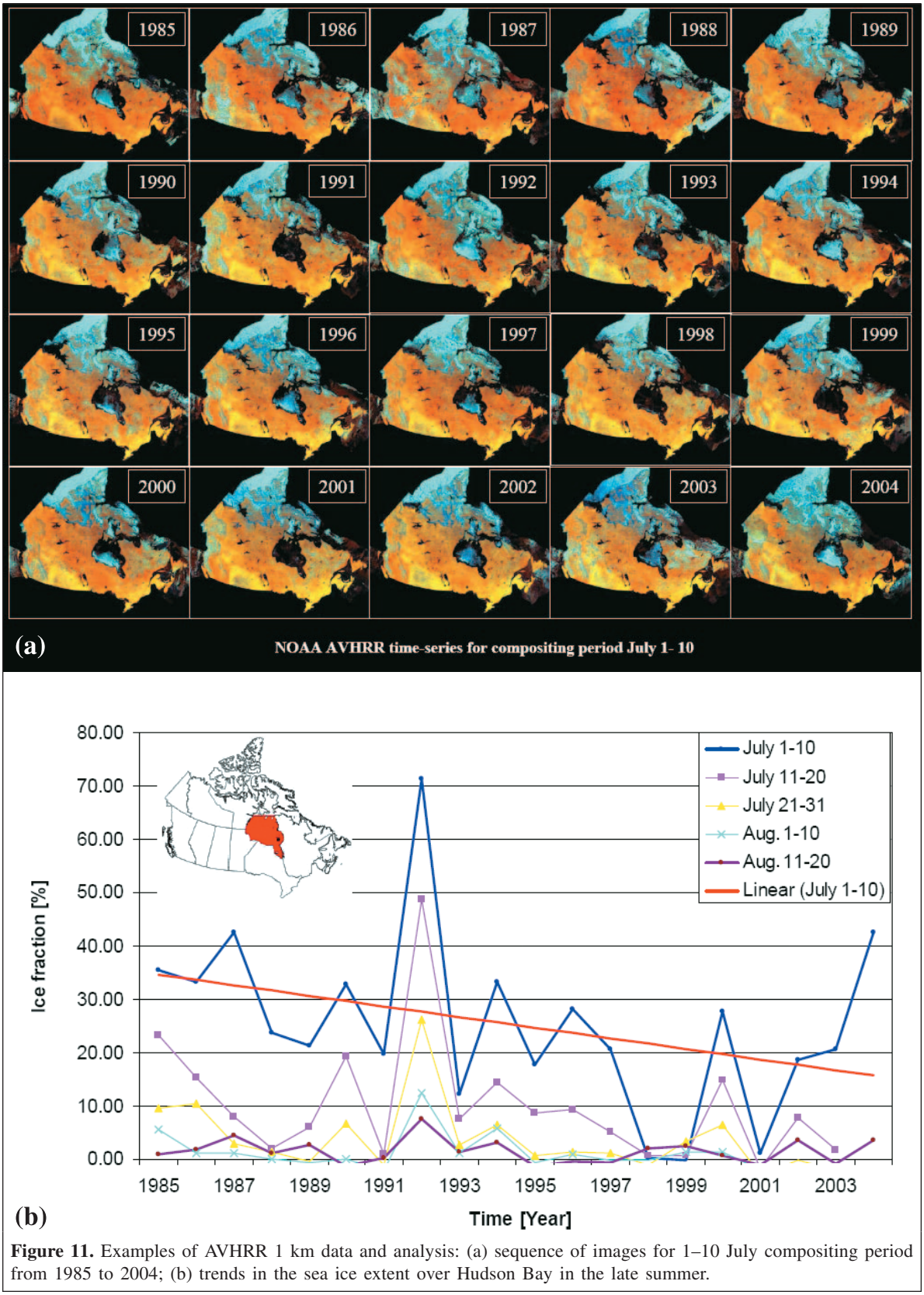

Figure 11. Examples of AVHRR 1 km data and analysis: (a) sequence of images for 1–10 July compositing period from 1985 to 2004; (b) trends in the sea ice extent over Hudson Bay in the late summer.

by Canadian ground-receiving stations is significantly extended with NOAA L1B CLASS data collected by two additional US ground-receiving stations. Currently, this archive consists of HRPT and LAC measurements from all NOAA satellites that have been acquired since 1981 throughout the entire year, both day and night. The data volume

is still not adequate to produce a complete data series for the period 1981–1984, but the 1985–2004 data coverage is quite satisfactory.

The new EODM system demonstrated substantial improvements in the quality of data processing. It has a 36% higher success rate for processing NATAS data files than the previous system. The overall success rate (the ratio of successfully processed orbits to the number of input orbits) is now close to 75%. Georeferencing accuracy is much improved (~1 pixel) and carefully controlled using chip matching and convex hull approaches. This quality-control procedure ensures that only the pixels processed with acceptable geolocation accuracy are used in further analysis. The EODM system supports the processing of all historical AVHRR data formats from NOAA-6 to NOAA-17. A new pixel scene identification scheme was developed that produces detailed clear sky – cloud – shadow – ice and cloud snow masks. The compositing procedure implemented in EODM employs an effective cloudiness index. This provides much improved cloud screening and a better quality of clear-sky composite data products.

The application example showing an analysis of sea ice extent over Hudson Bay illustrates the capabilities of the newly developed EODM system and the unique value of medium-resolution 1 km AVHRR satellite information for climate change research.

The MODIS and VGT data described in the paper are available through the NRCan public archive GEOGRATIS (http://geogratis.cgdi.gc.ca/; http://geogratis.cgdi.gc.ca/download/EO_Data/MODIS/; http://geogratis.cgdi.gc.ca/download/EO_Data/Spot_Veget/). The AVHRR baseline product produced by the EODM system will be made publicly available in early 2006. Users can obtain available data by contacting the authors at CCRS.

Acknowledgements

This work was conducted at the Canada Centre for Remote Sensing (CCRS), Earth Sciences Sector, Natural Resources Canada, as part of the project J28 of the program "Reducing Canada's Vulnerability to Climate Change". This work was partially supported by the Canadian Space Agency under the Government Related Initiative Program (GRIP) grant to CCRS. The help of the NOAA staff and use of data from the NOAA Comprehensive Large Array-data Stewardship System are gratefully acknowledged. The authors are very grateful to Gunar Fedosejevs (CCRS) for careful reading of the manuscript and useful suggestions.

References

Adair, M., Cihlar, J., Park, B., Fedosejevs, G., Erickson, A., Keeping, R., Stanley, D., and Hurlburt, P. 2002. GeoComp-n, an advanced system for generating products from coarse and medium resolution optical satellite data. Part 1: System characterization. *Canadian Journal of Remote Sensing*, Vol. 28, No. 1, pp. 1–20.

Armstrong, R., Knowles, K., Brodzik, M., and Hardman, M. 1994. *DMSP SSM/I pathfinder daily EASE-Grid brightness temperatures, August 1987 to December 2003*. CD-ROM. National Snow and Ice Data Center, Boulder, Colo. [Updated 2005.]

Atkinson, D.E., Brown, R., Alt, B., Agnew, T., Burgess, M., Duguay, C., Henry, G., Jeffers, S., Koerner, R., Lewkowicz, A.G., McCourt, S., Melling, H., Sharp, M., Smith, S., Woo, M-k., and Young, K. 2005. Canadian cryospheric response to an anomalous warm summer. *Atmosphere–Ocean*. 70 pp. In press.

Barkstrom, B.R., and Smith, G.L. 1986. The earth radiation budget experiment: science and implementation. *Reviews of Geophysics*, Vol. 24, pp. 379–390.

Belchansky, G.I., Douglas, D.C., Eremeev, V.A., and Platonov, N.G. 2005. Variations in the Arctic's multiyear sea ice cover: a neural network analysis of SMMR-SSM/I data, 1979–2004. *Geophysical Research Letters*, Vol. 32, L09605, doi:10.1029/2005GL022395.

Brouwer, D. 1959. Solution of the problem of artificial satellite theory without drag. *Astronomical Journal*, Vol. 64, pp. 378–396.

Brunel, P., and Marsouin, A. 2000. Operational AVHRR navigation results. *International Journal of Remote Sensing*, Vol. 21, pp. 951–972.

CCAF Summer 1998 Project Team. 2001. *The state of the Arctic cryosphere during the extreme warm summer of 1998: documenting cryospheric variability in the Canadian Arctic*. CCAF Final Report. Available from http://www.socc.ca/summer/ftp/ftp.html.

Chen, J. 2003. *A linear constraint optimization for the displacement operator in map generalization*. M.Sc. thesis, Carleton University, Ottawa, Ont. pp. 23–25.

Cihlar, J., and Teillet, P.M. 1995. Forward piecewise linear calibration model for quasi-real time processing of AVHRR data. *Canadian Journal of Remote Sensing*, Vol. 21, No. 1, pp. 20–27.

Cihlar, J., Chen, J.M., Li, Z., Huang, F., Latifovic, R., and Dixon, R. 1998. Can interannual land surface signal be discerned in composite AVHRR data? *Journal of Geophysical Research, Atmospheres*, Vol. 103, No. D18, pp. 23 163 – 23 172.

Cihlar, J., Latifovic, R., Chen, J., and Li, Z. 1999. Testing near-real time detection of contaminated pixels in AVHRR composites. *Canadian Journal of Remote Sensing*, Vol. 25, pp. 160–170.

Cihlar, J., Chen, J., Li, Z., Latifovic, R., Fedosejevs, G., Adair, M., Park, W., Fraser, R., Trishchenko, A., Guindon, B., Stanley, D., and Morse, D. 2002. GeoComp-n, an advanced system for the processing of coarse and medium resolution satellite data. Part 2: Biophysical products for Northern ecosystems. *Canadian Journal of Remote Sensing*, Vol. 28, No. 1, pp. 21–44.

Cihlar, J., Latifovic, R., Chen, J.M., Trishchenko, A.P., Du, Y., Fedosejevs, G., and Guindon, B. 2004. Systematic corrections of AVHRR image composites for temporal studies. *Remote Sensing of Environment*, Vol. 89, pp. 217–233.

Cracknell, A.P. 1997. *The advanced very high-resolution radiometer (AVHRR)*. Taylor and Francis, London, UK. 534 pp.

Cracknell, A.P., and Paithoonwattanakij, K. 1989. Pixel and sub-pixel accuracy in geometrical correction of AVHRR imagery. *International Journal of Remote Sensing*, Vol. 10, pp. 661–667.

D'Souza, G., and Sandford, T.D.G. 1996. Techniques for geometric correction of NOAA AVHRR imagery. In *Advances in the use of NOAA AVHRR data for land applications*. Edited by G. D'Souza, A.S. Belward, and J.P.

Malingreau. Kluwer Academic Publishers, Dordrecht, The Netherlands. Chapt. 7, pp. 153–194.

Duchemin, B., Guyon, D., and Lagouarde, J.P. 1999. Potential and limits NOAA-AVHRR temporal composite data for phenology and water stress monitoring of temperate forest ecosystem. *International Journal of Remote Sensing*, Vol. 20, No. 5, pp. 895–917.

Fillol, E., and Royer, A. 2001. Analyse de la variabilité phénologique des regions boréales et subartiques du Canada par télédétection. In *Proceedings of the 23rd Canadian Symposium on Remote Sensing*, 23–26 August 2001, Québec City, Que. Canadian Aeronautics and Space Administration (CASI), Ottawa, Ont.

Fowler, C., Maslanik, J., Haran, T., Scambos, T., Key, J., and Emery, W. 2002. *AVHRR Polar Pathfinder twice-daily 5 km EASE-Grid composites*. Digital media. National Snow and Ice Data Center, Boulder, Colo. Available from http://nsidc.org/data/nsidc-0066.html [accessed 15 June 2005].

Fraser, H.R., and Li, Z. 2002. Estimating fire-related parameters in boreal forest using SPOT VEGETATION. *Remote Sensing of Environment*, Vol. 82, pp. 95–110.

Global Climate Observing System. 2003. *The second report on the adequacy of the global observing system for climate in support of the UNFCCC*. Available from htpp://www.wmo.ch/web/gcos/Second_Adequacy_Report.pdf [accessed 15 June 2005].

Goodrum, G., Kidwell, K.B., and Winston, W. (Editors). 2000. *NOAA KLM user's guide*. Revised ed. US Department of Commerce, NESDIS, NOAA, National Climatic Data Center, Satellite Data Services Division, Washington, D.C. Available from http://www2.ncdc.noaa.gov/docs/klm/index.htm.

Gough, W.A., Cornwell, A.R., and Tsuji, L.J.S. 2004. Trends in seasonal sea ice duration in southwestern Hudson Bay. *Arctic*, Vol. 57, pp. 299–305.

Guindon, B. 1985. Automated control point acquisition in radar-optical image registration. *Canadian Journal of Remote Sensing*, Vol. 11, No. 1, pp. 103–112.

Guindon, B., Fisher, T.A., and Guertin, F.E. 1992. The evolution of operational satellite image geocoding in Canada. *International Archives of Photogrammetry and Remote Sensing*, *Washington, D.C.*, Vol. 29, pp. 286–288.

Gutman, G.G., and Ignatov, A. 1995. Global land monitoring from AVHRR: potentials and limitations. *International Journal of Remote Sensing*, Vol. 16, pp. 2301–2309.

Gutman, G.G., Tarpley, D., Ignatov, A., and Olson, S. 1995. The enhanced NOAA global land datasets from the advanced very high resolution radiometer. *Bulletin of the American Meteorology Society*, Vol. 76, pp. 1141–1156.

Ignatov, A., and Nalli, N.R. 2002. Aerosol retrievals from the multiyear multisatellite AVHRR Pathfinder Atmosphere (PATMOS) dataset for correcting remotely sensed sea surface temperature. *Journal of Atmospheric and Oceanic Technology*, Vol. 19, pp. 1986–2008.

Ignatov, A., Cos, S., Laszlo, I., Nalli, N., and Kidwell, K. 2004. Operational aerosol observations (AEROBS) from AVHRR/3 on board NOAA-KLM satellites. *Journal of Atmospheric and Oceanic Technology*, Vol. 21, pp. 3–26.

James, M.E., and Kalluri, S.N.V. 1994. The Pathfinder AVHRR land dataset: an improved coarse resolution dataset for terrestrial monitoring. *International Journal of Remote Sensing*, Vol. 15, pp. 3347–3363.

Kandel, R., Viollier, M., Raberanto, P., Duvel, J.P., Pakhomov, L.A., Golovko, V.A., Trishchenko, A.P., Mueller, J., Raschke, E., and Stuhlmann, R. 1998. The ScaRaB earth radiation budget dataset. *Bulletin of the American Meteorology Society*, Vol. 79, pp. 765–783.

Kidwell, K.B. 1997. *NOAA global vegetation index. User's guide. Revision*. Available from http://www2.ncdc.noaa.gov/docs/gviug/cover.htm [accessed 15 June 2005].

Kidwell, K.B. (Editor). 1998. *NOAA Polar Orbiter data user's guide*. US Department of Commerce, NESDIS, NOAA, National Climatic Data Center, Satellite Data Services Division, Washington, D.C.

Lane, M.H., and Hoots, F.R. 1979. *General perturbation theories derived from 1965 Lane drag theory*. Project Space Track Report No. 2, Aerospace Defence Command, Peterson AFB, Colo.

Lanfredi, M., Simoniello, T., and Macchiato, M. 2002. Comment on "Variations in northern vegetation activity inferred from satellite data of vegetation index during 1981 to 1999" by L. Zhou et al. *Journal of Geophysical Research*, Vol. 108, No. D12, 4346, doi:10.1029/2002JD003046, 2003.

Latifovic, R., Cihlar, J., and Chen, J.M. 2003. A comparison of BRDF models for the normalisation of satellite optical data to a standard sun–target–sensor geometry. *IEEE Transactions on Geoscience and Remote Sensing*, Vol. 41, pp. 1889–1898.

Los, S.O., Collatz, G.J., Sellers, P.J., Malmström, C.M., Pollack, N.H., DeFries, R.S., Bounoua, L., Parris, M.T., Tucker, C.J., and Dazlich, D.A. 2000. A global 9-year biophysical land-surface data set from NOAA AVHRR data. *Journal of Hydrometeorology*, Vol. 1, pp. 183–199.

Lucht, W., Colin, I.C., Myneni, R.B., Sitch, S., Friedlingstein, P., Cramer, W., Bousquet, P., Buermann, W., and Smith, B. 2002. Climatic control of the high-latitude vegetation greening trend and Pinatubo effect. *Science (Washington, D.C)*, Vol. 296, No. 5573, pp. 1687–1689.

Luo, Y., Trishchenko, A.P., Latifovic, R., and Li, Z. 2005. Surface bidirectional reflectance and albedo properties derived using a land cover-based approach with Moderate Resolution Imaging Spectroradiometer observations. *Journal of Geophysical Research*, Vol. 110, No. D1, D01106, 10.1029/2004JD004741.

Lyddane, R.H. 1963. Small eccentricities or inclinations in the Brouwer theory of the artificial satellite. *Astronomical Journal*, Vol. 68, pp. 555–558.

Mysak, L.A., Ingram, R.G., Wang, J., and Van der Baaren, A. 1996. The anomalous sea-ice extent in Hudson Bay, Baffin Bay and Labrador Sea during three simultaneous NOA and ENSO episodes. *Atmosphere–Ocean*, Vol. 34, pp. 313–343.

NRC. 2004. *Climate data record from environmental satellites*. National Research Council (NRC) of the National Academies, The National Academies Press, Washington, D.C.

Parkinson, C.L., and Cavalieri, D.J. 2002. A 21 year record of Arctic sea ice extents and their regional, seasonal and monthly variability and trends. *Annals of Glaciology*, Vol. 34, pp. 441–446.

Parkinson, C.I., Cavalieri, D.J., Gloersen, P., Zwally, H.J., and Comiso, J.C. 1999. Arctic sea ice extents, areas and trends, 1978–1996. *Journal of Geophysical Research*, Vol. 104, pp. 20 837 – 20 856.

Rahman, H., and Dedieu, G. 1994. SMAC: a simplified method for the atmospheric correction of satellite measurements in the solar spectrum. *International Journal of Remote Sensing*, Vol. 15, pp. 123–143.

Rast, M., and Bezy, J.L. 1999. The ESA medium resolution imaging spectrometer MERIS: a review of the instrument and its mission. *International Journal of Remote Sensing*, Vol. 20, No. 9, pp. 1681–1702.

Reynolds, R.W., Rayner, N.A., Smith, T.M., Stokes, D.C., and Wang, W. 2002. An improved in situ and satellite SST analysis for climate. *Journal of Climate*, Vol. 15, pp. 1609–1625.

Robertson, B., Erickson, A., Friedel, J., Guindon, B., Fisher, T., Brown, R., Teillet, P., D'Iorio, M., Cihlar, J., and Sancz, A. 1992. GeoComp, a NOAA AVHRR geocoding and compositing system. In *Proceedings of the ISPRS Conference, Commission 2*, August 1992, Washington, D.C. pp. 223–228.

Romanov, P., Gutman, G., and Csiszar, I. 2000. Automated monitoring of snow cover over North America with multispectral satellite data. *Journal of Applied Meteorology*, Vol. 39, pp. 1866–1880.

Rossow, W., and Schiffer, R. 1999. Advances in understanding clouds from ISCCP. *Bulletin of the American Meteorological Society*, Vol. 80, pp. 2261–2284.

Saint, G. 1992. *VEGETATION onboard SPOT 4, mission specifications*. Laboratoire d'études et de recherches en télédétection spatiale, Toulouse, France. Report LERTS No. 92102. 40 pp.

Salomonson, V.V., Barnes, W.L., Maymon, P.W., Montgomery, H.E., and Ostrow, H. 1989. MODIS Advanced facility instrument for studies of the earth as a system. *IEEE Transactions on Geoscience and Remote Sensing*, Vol. 27, No. 2, pp. 145–153.

Simoniello, T., Cuomo, V., Lanfredi, M., Lasaponara, R., and Macchiato, M. 2004. On the relevance of accurate correction and validation procedures in the analysis of AVHRR-NDVI time series for long-term monitoring. *Journal of Geophysical Research*, Vol. 109, D20107, doi:10.1029/2004JD004819.

Smith, M.D. 1998. Recent increase in the length of the melt season of perennial Arctic sea ice. *Geophysical Research Letters*, Vol. 25, No. 5, pp. 655–658.

Stockli, R., and Vidale, P.L. 2004. European plant phenology and climate as seen in a 20-year AVHRR land-surface parameter dataset. *International Journal of Remote Sensing*, Vol. 25, No. 17, pp. 3303–3330.

Stowe, A., Jacobowitz, H., Ohring, G., Knapp, K., and Nalli, N. 2002. The advanced very high resolution radiometer Pathfinder Atmosphere (PATMOS) climate dataset: initial analyses and evaluations. *Journal of Climate*, Vol. 15, pp. 1243–1260.

Tahnk, W.R., and Coakley, J.A., Jr. 2001. Updated calibration coefficients for NOAA-14 AVHRR channels 1 and 2. *International Journal of Remote Sensing*, Vol. 22, pp. 3053–3057.

Tahnk, W.R., and Coakley, J.A., Jr. 2002. Improved calibration coefficients for NOAA-12 and NOAA-15 AVHRR visible and near-IR channels. *Journal of Atmospheric and Oceanic Technology*, Vol. 19, pp. 1826–1833.

Teillet, P.M., El Saleous, N., Hansen, M.C., Eidenshink, J.C., Justice, C.O., and Townshend, J.R.G. 2000. An evaluation of the global 1-km AVHRR land dataset. *International Journal of Remote Sensing*, Vol. 21, pp. 1987–2021.

Townshend, J.R.G., Justice, C.O., Skole, D., Malingreau, J.-P., Cihlar, J., Teillet, P.M., Sadowski, F., and Ruttenberg, S. 1994. The 1-km AVHRR global data set: needs of the International Geosphere Biosphere Program. *International Journal of Remote Sensing*, Vol. 15, pp. 3319–3332.

Trishchenko, A.P. 1994. On accuracy of automated image georeferencing of the data from the METEOR-3 satellites. *Issledovanie Zemli iz Kosmosa (Earth Research from Space)*, Vol. 3, pp. 62–68.

Trishchenko, A.P. 2002. Removing unwanted fluctuations in the AVHRR thermal calibration data using robust techniques. *Journal of Atmospheric and Oceanic Technology*, Vol. 19, No. 12, pp. 1939–1954

Trishchenko, A.P. 2005. Solar irradiance and brightness temperature for SWIR channels of AVHRR and GOES imagers. *Journal of Atmospheric and Oceanic Technology*. In press.

Trishchenko, A.P., and Andrievsky, A.N. 1994. Analysis of spacecraft and digital data pixel location accuracy for satellites METEOR. In *Microwave instrumentation and satellite photogrammetry for remote sensing of the Earth*. Edited by J.B. Lurie, P. Pampaloni, and J.C. Shiue. Proceedings of SPIE, Vol. 2313, pp. 15–25.

Trishchenko, A.P., Li, Z., Park, W., and Cihlar, J. 2000. Correction for the BRDF and topography effects in satellite retrieval of surface spectral reflectance in solar spectral region. In *Current problems in atmospheric radiation*. Edited by S.W. Smith and Yu.M. Timifeev. Deepak Publishing, Hampton, Va. pp. 44–47.

Trishchenko, A.P., Cihlar, J., and Li, Z. 2002a. Effects of spectral response function on the surface reflectance and NDVI measured with moderate resolution sensors. *Remote Sensing of Environment*, Vol. 81, pp. 1–18.

Trishchenko, A.P., Fedosejevs, G., Li, Z., and Cihlar, J. 2002b. Trends and uncertainties in thermal calibration of the AVHRR radiometers onboard NOAA-9 to -16. *Journal of Geophysical Research*, Vol. 107, No. D24, ACL 17-1 to ACL 17-13, doi:10.1029/2002JD002353.

Trishchenko, A.P., Hwang, B., and Li, Z. 2002c. Atmospheric correction of satellite signal in solar domain: impact of improved molecular spectroscopy. In *Proceedings of the 12th ARM Science Team Meeting*, 8–12 April 2002, St. Petersburg, Fla. 7 pp. Available from http://www.arm.gov/publications/proceedings/conf12/extended_abs/trishchenko-ap.pdf.

Trishchenko, A.P., Ungureanu, C., Khlopenkov, K.V., Park, W., Latifovic, R., and Fernandes, R. 2005. *Bi-directional reflectance properties of the land surface over Canada derived from MODIS multispectral observations at 1-km spatial resolution*. Available from http://geogratis.cgdi.gc.ca/download/EO_Data/MODIS/.

Tucker, C.J., Pinzon, J.E., and Brown, M.E. 2004. *Global inventory modeling and mapping studies (GIMMS) satellite drift corrected and NOAA-16 incorporated normalized difference vegetation index (NDVI), monthly 1981–2002*. Dataset documentation. 23 pp. Available from http://islscp2.sesda.com/ISLSCP2_1/.

Tucker, C.J., Pinzon, J.E., Brown, M.E., Slayback, D., Pak, E.W., Mahoney, R., Vermote, E., and El Saleous, N. 2005. An extended AVHRR 8-km NDVI data set compatible with MODIS and SPOT Vegetation NDVI data. *International Journal of Remote Sensing*. In press.

University Corporation for Atmospheric Research. 1994. *The NOAA–NASA Pathfinder Program*. University Corporation for Atmospheric Research (UCAR), Boulder, Colo. 23 pp.

Wielicki, B.A., Barkstrom, B.R., Harrison, E.F., Lee, R.B., III, Smith, G.L., and Cooper, J.E. 1996. Clouds and the Earth's radiant energy system (CERES): an Earth observing system experiment. *Bulletin of the American Meteorological Society*, Vol. 77, pp. 853–868.

World Meteorological Organization. 2004. *Implementation plan for the global observing system for climate in support of the UNFCCC*. GCOS-92. World Meteorological Organization (WMO), Geneva, Switzerland. WMO/TD-No.1219. 153 pp.

Zhang, Y., Rossow, W.B., Lacis, A.A., Oinas, V., and Mishchenko, M.I. 2004. Calculation of radiative fluxes from the surface to top of atmosphere based on ISCCP and other global data sets: refinements of the radiative transfer model and the input data. *Journal of Geophysical Research*, Vol. 109, No. D27, D19105, doi:10.1029/2003JD004457.

Can. J. Remote Sensing, Vol. 31, No. 5, pp. 347–363, 2005

Multitemporal land cover mapping for Canada: methodology and products

Rasim Latifovic and Darren Pouliot

Abstract. A mapping methodology is presented for generating a land cover time series from coarse spatial resolution earth observation data. Historically, this has been a difficult task because of inconsistencies that can arise between maps due to inherent noise present in satellite observations. The new methodology reduces the inconsistency by incorporating several information sources unique to the presented approach of updating an existing land cover map backward and forward in time. It consists of change detection and a local evidence classification decision rule that incorporates the local spectral similarity for each class, local land cover proportions, and expected class changes based on the previous class and change direction. The methodology has been implemented to produce land cover maps of Canada for 1985, 1990, 1995, and 2000 from data acquired by the series of National Oceanic and Atmospheric Administration (NOAA) – advanced high-resolution radiometer (AVHRR) sensors. Accuracy assessment based on medium-resolution (30 m) reference data shows that land cover data produced with this new approach have an overall accuracy similar to that of other 1 km resolution land cover maps of Canada, but this product maintains high consistency between years, with a thematic resolution of 12 classes. An analysis of spatial and temporal patterns of land cover disturbances demonstrates the potential application of the multitemporal land cover time series.

Résumé. On présente une méthodologie de cartographie pour la génération d'une série chronologique du couvert à partir de données d'observation de la Terre à résolution spatiale grossière. Traditionnellement, ceci a toujours constitué une tâche difficile à cause des incohérences qui peuvent se manifester entre les cartes dues au bruit inhérent présent dans les observations satellitaires. La nouvelle méthodologie réduit cette incohérence en incorporant plusieurs sources d'information uniques à l'approche présentée de mise à jour d'une carte existante du couvert antérieurement et postérieurement dans le temps. Celle-ci repose sur la détection du changement et une classification basée sur l'évidence locale utilisant une règle de décision qui incorpore la similarité spectrale locale pour chaque classe, les proportions locales du couvert et les changements de classe anticipés basés sur la classe précédente et la direction du changement. La méthodologie a été implantée pour produire des cartes du couvert du Canada pour 1985, 1990, 1995 et 2000, à partir des données acquises par la série de capteurs AVHRR de NOAA. L'évaluation de la précision basée sur des données de référence à résolution moyenne (30 m) montre que les données du couvert produites à l'aide de cette nouvelle approche ont une précision globale similaire à celle des autres cartes du couvert du Canada à une résolution de 1 km, mais ce produit conserve une cohérence élevée au cours des années avec une résolution thématique de 12 classes. Une analyse des patrons spatiaux et temporels des perturbations du couvert démontre le potentiel d'application des séries chronologiques multi-temporelles du couvert.
[Traduit par la Rédaction]

Introduction

Long-term observations of the earth system sustained over decades are a critical first step for providing the information necessary for scientists, decision makers, and stakeholders to assess human impacts and vulnerability associated with environmental change. Among the most important environmental parameters that summarize the physical, biotic, and climatic components of terrestrial ecosystems are distributions of vegetation, water, snow and ice, and other land cover types. These land surface characteristics are needed for parameterization of climatic, ecological, and natural resources applications at global and regional scales.

The current approach to defining surface parameters at the regional scale in the absence of field-derived parameters is to use coarse-resolution satellite data as a primary source of information. Mapping vegetation and land cover on a yearly basis at regional and global scales using remotely sensed data has a rich history of application. The first regional product, a land cover map of Africa, based on National Oceanic and Atmospheric Administration (NOAA) – advanced high-resolution radiometer (AVHRR) data was produced by Tucker et al. (1984). Subsequently, Townshend et al. (1987) created a map of South America, Cihlar et al. (1999) created a map for Canada, and global land cover maps were produced by Loveland and Belward (1997; for the International Geosphere–Biosphere Programme (IGBP)), DeFries and Townshend (1994), and Hansen et al. (2003). More recent global maps have been produced from SPOT VEGETATION data (Latifovic et al., 2004) and moderate resolution image spectroradiometer

Received 15 December 2004. Accepted 20 May 2005.

R. Latifovic.[1] Canada Centre for Remote Sensing, Natural Resources Canada, 588 Booth Street, Ottawa, ON K1A 0Y7, Canada.

D. Pouliot. Noetix Research Inc., 588 Booth Street, Ottawa, ON K1A 0Y7, Canada.

[1]Corresponding author (e-mail: Rasim.Latifovic@CCRS.NRCan.gc.ca).

(MODIS) data (Strahler et al., 1999). Nonetheless, there have been few attempts at producing a long-term land cover time series of sufficient length, consistency, and continuity for studying patterns of environmental variability and change. This is a difficult task due to noise present in long-term satellite data acquired over large areas with 1 km spatial resolution. There are many reasons for inconsistency in long-term satellite data; some of them are because of differences in atmospheric conditions (aerosol, haze, and water vapor content) and acquisition geometry (bidirectional effects, geometric misregistration, and variable ground pixel size) (Cihlar et al., 2004), and others are in relation to vegetation phenology (Stöckli and Vidale, 2004), sensor-related noise, cross-sensors calibration (Trishchenko et al., 2001), and drift in equatorial crossing time.

Standard procedures for temporal land cover evaluation have employed change detection analysis based on different techniques including image differencing, principal component analysis, and postclassification comparison. Recent developments in this area have utilized spectral mixture analysis, artificial neural networks, and integration of geographic information systems (GIS) and remote sensing data. Comprehensive overviews of change detection techniques are presented in Coppin et al. (2004) and Lu et al. (2004). To be successful, a change detection analysis requires, as a prerequisite, multitemporal image registration, radiometric and atmospheric correction, or normalization between images at the same spatial and spectral resolution (Coppin and Bauer, 1996; Jensen, 1996). Data preprocessing is a crucial part of change detection analysis because the level of achievable change detection accuracy will depend, to a large extent, on the degree to which these prerequisites are met.

Multitemporal comparison between classified maps requires high accuracy that is difficult to achieve with coarse-resolution data. Maxwell et al. (2002a; 2002b) produced a land cover time series (1990–1995) for the state of Colorado from AVHRR data following a supervised classification approach. The average overall accuracy of these maps was good (~82%), but the error for postclassification change detection could range from 0% to 38% depending on the nature of the errors in the individual maps. It is difficult to determine the exact magnitude, but it is widely recognized that the accuracy of postclassification change detection is approximately the product of the two input classification accuracies (Coppin et al., 2004). For the aforementioned case, change detection accuracy would be ~67%. In addition to the potential for very large error, this approach is also very labor intensive, requiring a substantial amount of time and expertise to create the classified products.

The MODIS global land cover product is another example of a land cover time series. It employs the latest technology in sensor development, calibration, and processing techniques. However, it does not extend sufficiently far back in time for meaningful temporal analysis, and rigorous validation of products is still pending. In moderate-resolution data (e.g., Landsat), there are numerous examples of the post-detection classification approach (Hall et al., 1991; Miller et al., 1998; Mas, 1999; Foody, 2001; Latifovic et al., 2005).

Although typically performed separately, land cover mapping and change detection are techniques that are highly complementary for the objective of multitemporal land cover mapping. The method we present in this paper consists of two main steps: (*i*) change detection with an existing land cover map, and (*ii*) classification of these changes to create an updated land cover product. The updates can be applied periodically to the baseline land cover product to extend the temporal dimension of the land cover time series.

The objective of this study was to develop a methodology to produce a consistent land cover time series at a regional scale that can be used for tracking environmental changes resulting from human and natural disturbances. Here, consistency refers to the overall agreement between two land cover maps and should not be lower than the expected amount of change that an area would expect to experience over a selected time interval. The specific objectives were as follows: (*i*) develop a multitemporal land cover mapping methodology, (*ii*) apply the methodology to create a time series of Canada from 1985 to 2000, and (*iii*) analyze the time series for general temporal and spatial trends.

The "Method" section of this paper gives an overview of the proposed multitemporal mapping approach. The section titled "Method implementation and product generation" provides particulars on the methodology, parameters used, data processing, and product generation for Canada, describes qualitative and quantitative evaluation procedures, and discusses limitations and possible improvements. In the "Time series analysis" section, an analysis of spatial and temporal patterns of disturbances demonstrates the use of the generated multiyear land cover database.

Method

Method overview

The multiyear land cover mapping procedure was designed specifically to maintain high consistency between land cover maps created on separate dates. For this, an existing map is updated to another year rather than creating completely new classifications for each year. The approach uses (*i*) change detection to identify areas that require updating and (*ii*) a local classification decision rule to determine the class for a pixel to be updated. **Figure 1** provides an overview of the processing steps involved in the updating procedure. A more detailed description of each step is provided in the following sections.

Change detection

The change detection technique uses a change vector approach to combine complementary information sources into a single indicator of change (IC). This indicator is based on the Euclidean distance between spectral bands and their texture

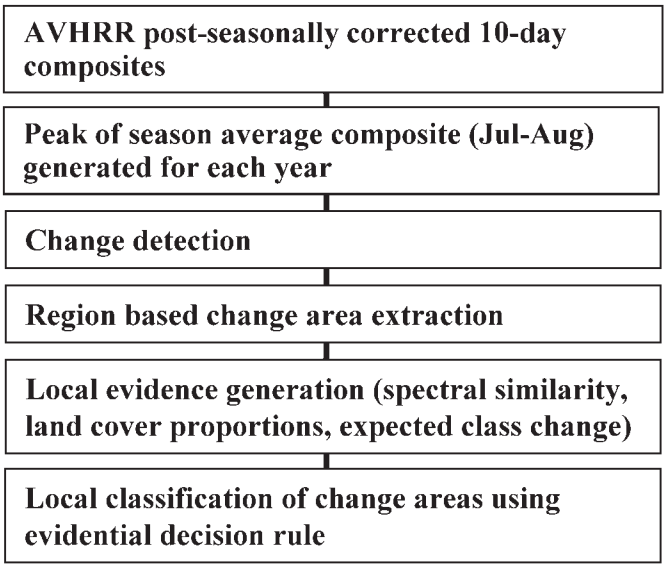

Figure 1. Overview of processing steps used for map updating.

transforms scaled to a common range. IC is calculated to represent the change magnitude as follows:

$$\mathrm{IC} = \sqrt{\sum_{i=1}^{n} (x_{it} - x_{it+\Delta t})^2} \tag{1}$$

where x_{it} is the pixel value for band i at time t, and $x_{it+\Delta t}$ is the value for the same band at time $t + \Delta t$.

Thresholds used for extracting change should be locally specified such that local influences (e.g., land cover type) on the change magnitude do not cause substantial error in change extraction. Ideally, training samples from an independent data source are needed to determine thresholds. In the absence of such data, visual comparison can be used, but with an associated increase in the subjectivity of the map production.

Local classification

The decision rule applied in the local classification uses information around a change object extracted as measures of evidence. For this application, these evidential measures include (*i*) local spectral signature evidence (LSSE), (*ii*) local class proportion evidence (LCPE), and (*iii*) expected class change evidence (ECCE) based on the previous pixel class and change direction.

Local spectral signature evidence

Local spectral signature evidence is a measure of the local spectral similarity between a pixel and each class within a specified sampling window. Spectral similarity is defined as the Euclidean distance between a change pixel to be classified and classes present in the sampling window using Equation (2). The Euclidean distance values are inverted so that larger values represent distances closer to a given class vector and normalized to sum to one:

$$\mathrm{LSSE}_j = \frac{1}{\sqrt{\sum_{i=1}^{n} (x_i - m_{ij})^2}} \tag{2}$$

where x_i is the pixel value for band i, and m_{ij} is the mean value for band i and class j.

Two competing objectives are considered for defining the parameters used to control the size of the sample window: (*i*) generating signatures that effectively capture local spectral properties, and (*ii*) ensuring that all plausible signatures are included in the signature set for the local classification. The size of the window controls how well these criteria are met. Creating larger windows reduces the advantage gained by local processing (i.e., class signatures that are highly representative of the image area being classified), whereas small windows are sensitive to high-frequency noise and are more likely to exclude important land cover types from the classification decision. Generally, it is considered better to specify larger windows, as they are less susceptible to noise and are more likely to have all land cover types well represented.

Within the local window, signatures are generated using land cover data from the base land cover map with change areas removed. In generating LSSE of a class considered highly transient over the time period of interest, an option is provided to use a set of global signatures that can be inserted into the local signature set as a possible class for every change object. For example, classes representing disturbance should use globally defined signatures because the base map used for signature training will bias the signatures due to increased levels of vegetation found in these areas farther back or ahead in time.

Local class proportion evidence

Local class proportions are used to aid the classification decision when the surrounding landscape is considered to have some influence on the pixel being classified. For example, in backward updating an area to $t - \Delta t$, there is a greater likelihood that the land cover class of the area is that which surrounds it because of similar environmental factors (temperature, precipitation, soil, and topographic position) that are known to influence land cover distribution. This is also the case for forward updating $t + \Delta t$, as a given class is more likely to be developing towards the most frequently occurring land cover class around the change area for the same environmental factors and because the surrounding vegetation in this case is a potential seed source for recruitment post-disturbance. To include a measure of the local land cover proportion in the classification decision, the land cover proportions within a given distance of the change boundary are extracted and divided by the total area in this buffer.

Expected class change evidence

Two useful sources of information unique to this map-updating methodology include the change direction and the reference class value. With this information, constraints can be

developed to limit the classification decision to the most likely class value and remove or reduce the potential for highly unlikely classes to be considered. For example, a pixel classified as a recent burn at time t should not be classified as high-density conifer forest at time $t + \Delta t$ ($\Delta t = 5$). The time span of 5 years is not sufficient to allow for mature conifer redevelopment. This type of knowledge can be extremely useful in constraining the classification process. To utilize this information in the classification decision, expected change weight matrices were created for the time periods $t - \Delta t$ and $t + \Delta t$ and separately for positive and negative changes. Weights were assigned to reflect the expected changes that would most likely occur depending on the change direction and reference class value. The values in the weight matrices were normalized by dividing each individual weight by the sum of the weights for a given class value.

Evidence-based classification decision rule

To classify a pixel, three different rules were considered. **Figure 2** shows a flow diagram that summarizes the criteria used to determine which rule to apply.

The first rule was designed to ensure that a pixel was correctly identified as change and that it should be updated. For this, the maximum LSSE value is compared with the LSSE value associated with the reference classification label (i.e., class value for the map to be updated). If the difference between the maximum and the reference class LSSE value is less than a defined threshold, the pixel is not changed from its reference class.

The second rule is used to assign a pixel to a class in which the LSSE measure provides strong support. It recognizes that LSSE in this case can be used as the single information source in the classification decision.

If neither of the conditions for the first two rules are met, then the LSSE, LCPE, and ECCE are used to calculate a final evidence measure. It is implemented using Dempster's rule of combination to combine the three evidence sources into a single value representing the support for each land cover class. The updated pixel label is defined as the class with the maximum support. Descriptions of Dempster's rule of combination applied to spatial data are given in Moon (1990), Srinivasan and Richards (1990), Peddle (1995a; 1995b), and Comber et al. (2004). A unique advantage of this approach is that it explicitly accounts for uncertainty associated with the evidential measures.

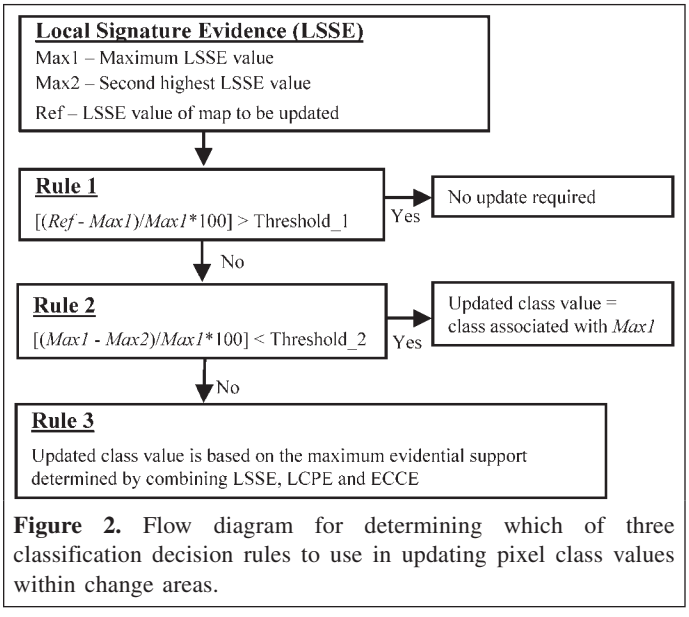

Figure 2. Flow diagram for determining which of three classification decision rules to use in updating pixel class values within change areas.

The three evidential measures are combined (E_c) using orthogonal summation denoted as follows:

$$E_c = \text{LSSE} \oplus \text{LCPE} \oplus \text{ECCE} \quad (3)$$

where $\oplus$ represents the combination calculated for two sources i and j and set of labels A as

$$m_c = K^{-1} \sum_{Ai \cap Aj = An} m_1(Ai) m_2(Aj) \quad (4)$$

$$K = 1 - \sum_{Ai \cap Aj = \phi} m_1(Ai) m_2(Aj) \quad (5)$$

In the implementation, m is the mass or evidence value assigned to a class for a given source. The set of evidence values is referred to as an evidential vector, which is multiplied by a user-defined uncertainty factor to reflect the confidence with which a given evidence source has on the final decision. In Equation (4), K can be considered a measure of the extent of conflict between the two sources, and ϕ is the mass assigned to the null set, i.e., sum of mass contributed to conflicting labels.

Method implementation and product generation

The methodology described in the previous section was used to prepare consistent coarse-resolution land cover time series for 1985–2000 over Canada at 5-year time increments. Further description of procedure implementation, data preprocessing, and product evaluation is provided in the following sections.

Expected annual land cover change in Canada

Sources of change in Canada include forest harvesting, urban development, transportation corridors, mining, agriculture expansion–contraction, storms, fire, flooding, and insect and disease damage. To develop some insight into the expected annual change, a simple estimate was derived based on reported change sources for forested areas and assumed levels of change for others. Based on the annual average area of fire (2 million ha/year) and harvesting (1 million ha/year) from the National Forestry Database Program (Canadian Council of Forest Ministers, 2004) and an assumed annual average for other change sources of 2 million ha/year, the total percent change in respect to Canada's landmass (~100 million ha) is ~0.5%/year. The area affected by defoliation was not included in this estimate because moderate defoliation is difficult to detect in

coarse-resolution imagery. Further, the reported area is inflated because the same area can be counted several times for each insect found to be impacting the area. It is important to note that the exact value was not required, just a reasonable estimate that could be used to guide selection of the updating interval and evaluate map consistency. Based on the annual change estimate over a 5-year period, cumulative change can be assumed to be approximately 3%. At this time interval, overall consistency of multitemporal land cover maps between time steps is expected to be greater than 90%, considering an assumed standard error of the 5-year change estimate of ±5%.

Data and preprocessing

Satellite data

Satellite data acquired by AVHRR sensors NOAA 11 and 14 were used in this study because they were the only available data at the spatial and temporal resolution suitable for regional land cover mapping for the period of interest. Average images of red, near-infrared (Nir), and normalized difference vegetative index (NDVI) for the peak of the season (July 15 – August 15) and for each year (1985–2000) were created from 10-day post-seasonally corrected composites. The preprocessing prior to averaging included atmospheric correction, bidirectional reflectance normalization to a common viewing geometry, cloud screening, and seasonal profile interpolation following the methodology described in Cihlar et al. (2004). To improve multiyear data consistency, several normalization approaches based on robust regression were explored (Fernandes and Leblanc, 2005; Olthof et al., 2005). The normalization was applied to subsequent 10-day composites and average peak-of-season images. Normalization coefficients were derived following two sampling approaches: (*i*) sampling the whole image and (*ii*) ecozone-based stratified sampling. **Table 1** shows difference statistics for these modifications to the normalization procedure. Normalizing the 10-day composites improved results slightly over normalizing the peak-of-season average images. The ecozone-stratified normalization produced the best results and thus was used as the normalization approach in this work.

Base map used for updating

The base map used for the updating procedure was the land cover map of Canada 1995 produced by Cihlar et al. (1999). This reference map was selected because it was produced using similarly processed AVHRR data available for this work and it is a widely accepted map product used by other Canadian government organizations. The map consists of the 31 classes summarized in **Table 2**.

Parameterization of change detection procedure

The coefficient of variation in a 5 × 5 pixel window was used as the texture transformation in the change detection procedure. This was considered a useful first-order texture measure that combines local variance and brightness into a single spatial discriminator. In calculating the change indicator (Equation (1)), the differences between bands were scaled to the range 0–1 for the spectral data and 0–0.5 for the texture data. This was done to normalize the weight of each input band. The reduced range for texture data was applied to moderate the influence of these bands in the change magnitude calculation.

To determine change thresholds, fire databases (Zhang et al., 2004a; 2004b; Fraser et al., 2004) and selected Landsat scenes were used. The fire databases covered the complete time period and were the main source of training data. Sources of Landsat data included a change database for the period 1998–2000 (Fraser et al., 2005), Landsat mosaic for 1990 available from the National Aeronautics and Space Administration (NASA; http://www.esad.ssc.nasa.gov/), and Landsat scenes for 2000 from the Center for Topographic Information (available from http://geogratis.cgdi.gc.ca/).

Almost all areas in the fire databases were identified by the change detection technique, but their areal extents were different. Thus, because the fire databases were constructed using more sophisticated procedures or coarse-resolution data

Table 1. Comparison of normalization methods based on robust regression using the 1995 composite as reference and 2000 as the composite to be corrected.

Method	Mean difference	Standard deviation difference	Mean absolute difference	Standard deviation absolute difference
Red band				
Peak-of-season composite (not normalized)	–4.47	33.52	15.30	30.15
Normalized peak-of-season composite	–1.15	30.82	14.63	27.14
Peak-of-season composite created from normalized 10-day composites	1.04	29.06	14.36	25.30
Ecozone-normalized peak-of-season composite	–0.01	25.26	14.03	21.00
Nir band				
Peak-of-season composite (not normalized)	17.92	30.21	24.89	24.78
Normalized peak-of-season composite	–0.24	30.80	17.12	25.60
Peak-of-season composite created from normalized 10-day composites	0.58	29.89	17.02	24.58
Ecozone-normalized peak-of-season composite	0.85	26.50	12.44	23.00

Note: All values are in digital numbers (DN).

Table 2. Summary of the 1995 31-class land cover legend, aggregate 12-class legend, and IGBP 16-class legend.

(A) 1995 31-class legend.

Class	Label
1	High density needleleaf forest
2	Med density needleleaf forest
3	Med density northern forest
4	Low density southern forest
5	Low density northern forest
6	Deciduous forest
7	Mixed needleleaf forest
8	Mixed uniform forest
9	Mixed heterogenous forest
10	Mixed broadleaf forest
11	New disturbance
12	Old disturbance
13	Transition tree shrubland
14	Wetland tree shrubland
15	Wetland medium density shrubs
16	Grassland
17	Lichen and other
18	Shrub and lichen
19	Heather and herbs
20	Low vegetation cover nonforest
21	Very low vegetation cover nonforest
22	Barren
23	Cropland high biomass
24	Cropland med biomass
25	Cropland low biomass
26	Cropland–woodland
27	Woodland–cropland
28	Cropland–other
29	Urban and built-up
30	Water
31	Snow/ice

(B) 1995 12-class legend.

Class	1995 31-class label	Label
1	1, 2, 3, 4	Conifer forest
2	6	Deciduous forest
3	7, 8, 9, 10	Mixed forest
4	11, 12	Disturbance
5	5, 13, 14, 15	Shrubland
6	16	Grassland
7	17, 18, 19, 20, 21, 22	Low vegetation and barren
8	23, 24, 25	Cropland
9	26, 27, 28	Cropland/woodland
10	29	Urban and built-up
11	30	Water
12	31	Snow/ice

(C) IGBP 16-class legend.

1	1, 2, 3, 4	Evergreen needleleaf forest
2		Evergreen broadleaf forest
3		Deciduous needleleaf forest
4	6, 10	Deciduous broadleaf forest
5	7, 8, 9	Mixed forest
6	15	Closed shrublands
7	11, 12	Open shrublands

Table 2 (*concluded*).

(C) IGBP 16-class legend.

Class	1995 31-class label	Label
8	5, 13	Woody savannas
9		Savannas
10	16	Grasslands
11	14	Permanent wetlands
12	23, 24, 25, 26, 27, 28	Croplands
13	29	Urban and built-up
14		Cropland/natural vegetation mosaic
15	31	Snow and ice
16	17, 18, 19, 20, 21, 22	Barren or sparsely vegetated

with higher spectral dimensions, burned areas from these databases for the change period were added to the change maps. A sieve filter was also applied to remove identified change areas less than 6 pixels in size considered to be mostly the result of noise. The direction of change required for the updating procedure was assigned to the change areas based on the difference in NDVI between the two dates. For forward updating, if NDVI was greater for the earlier date, then the pixel was assigned as negative change. If it was smaller for the earlier date, then it was assigned as positive change. This was reversed for backward updating.

Feature selection for classification procedure

To determine the best combination of data to be used for updating, a separability analysis (Bhattacharya; Richards, 1986) of the original 31 classes in the 1995 land cover map was conducted. Additional information and data transformations evaluated included surface temperature, texture, smoothing, and compositing period. Surface temperature was derived from AVHRR data and processed using the methods outlined in Cihlar et al. (2004). Texture data were derived using the coefficient of variation in the same manner as that used for change detection. Smoothing was applied using a 3 × 3 filter that did not include zero values in the average. Extreme values were also removed if they were two times larger than their surrounding nonzero neighbours. Three composites representing early season (11 and 21 April), mid-season (1, 11, and 21 July, 1 and 11 August), and late season (11 and 21 October) were generated for the red, Nir, and NDVI data from the 10-day AVHRR composite data. **Table 3** gives the average and minimum separability for the different data combinations examined. Overall, the separabilities were low, suggesting a reduced classification capability at the 31-class thematic level. The highest separability was obtained with the three composites periods for the red, Nir, and NDVI data. However, this data combination was not used for several reasons. First, data from the beginning and end of the growing season may be of reduced quality because measurements are strongly affected by clouds, haze, snow, and ice during these times. Second, several studies have shown that higher dimensionality may improve separability of training data, but often leads to overfitting and poor classification results (Jain et al., 2000). Third, the improved separability was not considered to be of sufficient magnitude to warrant tripling the data input and processing load. For these reasons, the smoothed peak-of-season composite of red, Nir, and NDVI that produced the next highest separability was used for map updating.

Table 3. Bhattacharya separability measures for the different data combinations tested.

	Separability	
Data combination	Avg.	Min.
Red, Nir, NDVI	1.64	0.24
3 × 3 average filtered red, Nir, NDVI	1.70	0.30
Red, Nir, NDVI, RedTex	1.67	0.29
Red, Nir, NDVI, NirTex	1.66	0.25
Red, Nir, NDVI, NDVITex	1.67	0.28
Red, Nir, NDVI, SurfTemp	1.70	0.26
Early, mid, late season red composites	1.03	0.01
Early, mid, late season Nir composites	1.24	0.11
Early, mid, late season NDVI composites	1.21	0.03
Early, mid, late season red, Nir composites	1.65	0.32
Early, mid, late season red, Nir, NDVI composites	1.78	0.38

Note: Spectral composites are peak-of-season composites unless specified otherwise in the table.

Parameterization for local classification

The window size used for local classification was based on a visual assessment of the 1995 land cover distribution in Canada. It showed that window sizes of 400 km in the north–south direction and 800 km in the east–west direction should contain all locally suitable land cover classes while still being small enough to capture local spectral signature characteristics. The smaller value for the north–south direction was used to minimize the effects of more rapidly changing land cover in this direction.

Weight matrices were developed considering geographic and temporal development constraints. The weight matrices used in this implementation are shown in **Figure 3**. Each row of the matrices represents the evidence assigned to reflect the likelihood of the base map becoming one of the other map classes. The following were the most significant rules used in defining weights:

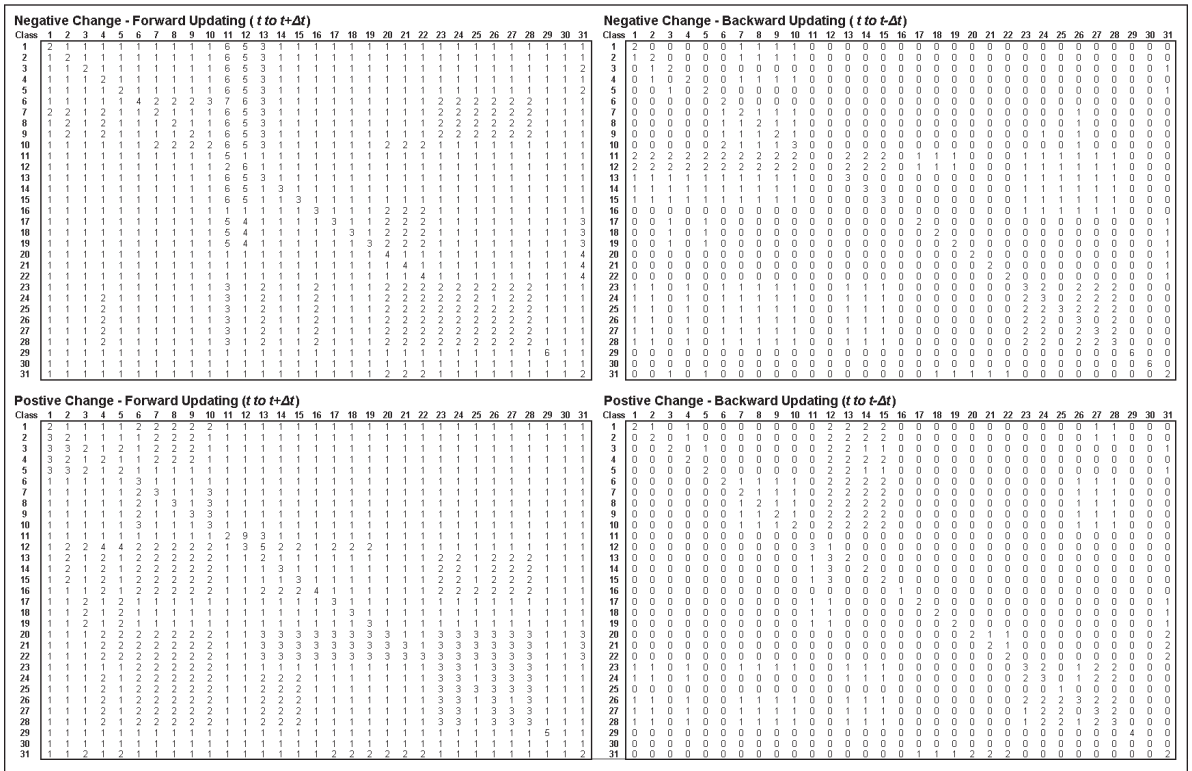

Figure 3. Weight matrices used for local classification.

(1) Classes with a northern distribution (3, 5, 17–22, and 31) were likely to remain as one of these northern classes.

(2) Classes with a southern distribution (1–2, 6–10, and 23–28) were likely to remain as one of these southern classes.

(3) A high weight was assigned for a class in t to be the same class in $t + \Delta t$ or $t - \Delta t$.

(4) For positive change, the following temporal trend was considered most likely for t to $t + \Delta t$ in forested areas: recent disturbance (class 11) → old disturbance (class 12) → shrub (classes 13–15) → forest (classes 1–10). For $t - \Delta t$, disturbance classes had a generally higher likelihood for conversion to forest and shrub classes.

(5) For negative change, a class in t was assigned a high weight for conversion to recent and old disturbance at $t + \Delta t$ in forested areas. For $t - \Delta t$, forest and shrub classes had a higher weight for conversion to disturbance classes.

Thresholds used for determining which of the three classification rules (**Figure 2**) to apply were 5% for rule 1 and 25% for rule 2. The buffer around change areas used in extracting LCPE was set at 8 pixels. For evidential combination, the weights were set at 0.7 for LSSE, 0.4 for LCPE, and 0.8 for ECCE if the change direction was positive. If negative, the weight for LCPE was changed to 0.1, as the surrounding land cover was considered to have little influence on the classification decision in this situation. The high weight given to ECCE was used because LSSE provides little discrimination between classes in this case and therefore it is of reduced reliability. These parameters were empirically determined by processing sample areas taken from eastern, central, and northwestern Canada and comparing the results with the available reference data.

Product evaluation

The derived 1985–2000 land cover time series contains four maps of Canada at several levels of thematic detail based on three land cover legends: (*i*) 31-class land cover legend; (*ii*) aggregated versions to 12 classes, representing the collapsed hierarchy of the 31-class legend; and (*iii*) 16 classes based on the IGBP scheme (**Table 2**).

Qualitative evaluation

The generated land cover time series was visually assessed following a comparison with available fine-resolution reference data based on the procedure suggested by Mayaux (2002). **Figure 4** shows two example areas from this assessment. Larger disturbances in both examples are detected, but their spatial shape and extent differ considerably from those of the Landsat imagery. Comparison of the lakes in the AVHRR and Landsat data shows that much of this difference is due to the spatial resolution capabilities of AVHRR. Small disturbances tend to be more frequently missed, such as the harvested areas in the lower section of **Figure 4b**. In this case, the change detection procedure often detected these disturbances, but only

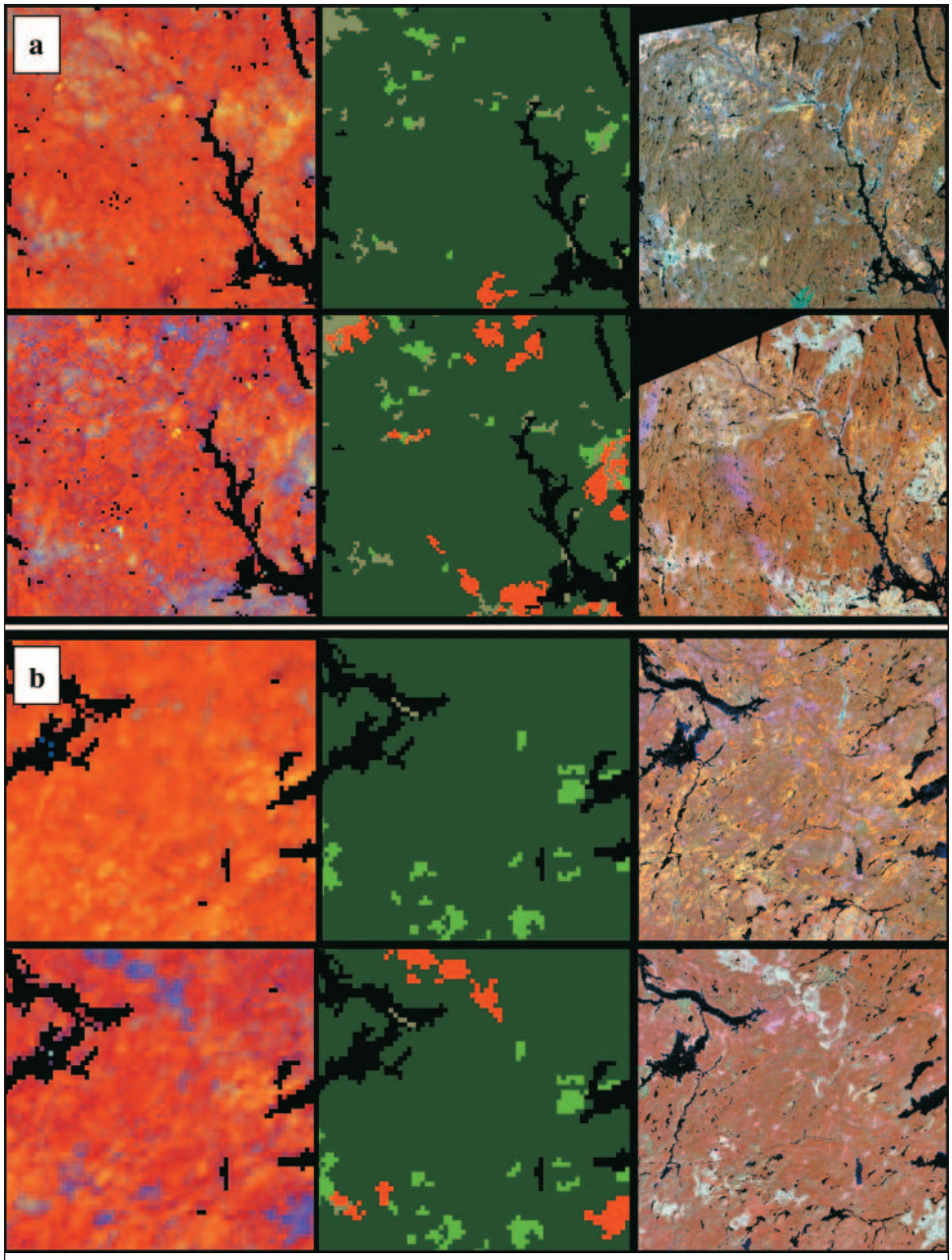

Figure 4. Example comparisons with Landsat imagery: (a) an area just below the Manicouagan reservoir in Quebec; (b) an area just above Lake Nipigon in north-central Ontario. In each example, the first column shows the AVHRR data, the second column the land cover map, the third column the TM–ETM+ Landsat imagery, the first row 1990 data, and the second row 2000 data. AVHRR data are displayed as follows: red, NDVI; green, Nir; blue, red. For the land cover, red shows disturbances, dark green shows conifer forest, light green shows mixed forest, and brown shows shrub. Landsat imagery is displayed as follows: red, Nir; green, shortwave infrared; blue, red.

a few pixels were identified and were later removed by the sieve filter.

The map products were also examined for the generally expected trend of forest disturbance and reestablishment. If the updating was correct, then the land cover changes should follow a logical temporal trajectory. Such an examination is demonstrated in **Figure 5**, which shows two sample areas of the classified images from 1985–2000. The examples support the expected trend of forest disturbance and regrowth. The results are also spatially convincing, having relatively homogenous clusters created in change areas that blend well into their surroundings. The first example (**Figure 5a**) shows areas that were disturbed and are, or have, redeveloped to their predisturbance state. The second example (**Figure 5b**) depicts

an area of overall reduction of coniferous and mixed forest from 1985 to 2000.

Quantitative evaluation

Consistency assessment

Consistency among the four maps is above the 90% expected for change areas in Canada over a 5-year period. Overall agreement for the 31-class legend was 96.1% for 1985–1990, 93.5% for 1985–1995, and 92.3% for 1985–2000. For the 12-class legend this same trend is seen with higher consistency, as agreements become more likely with fewer classes. Overall agreement for the 12-class legend was 97.3% for 1985–1990, 95.3% for 1985–1995, and 94.2% for 1985–2000. The lower rate of change in consistency with the longer time intervals is due to classes redeveloping towards their original predisturbance state over time.

Medium-resolution accuracy assessment

Quantitative accuracy assessment of multitemporal land cover products is difficult because of the lack of available reference data and the cost of developing a suitable database that could be used for validation of each time step. Fortunately, a medium-resolution database for 2000 was developed previously that could be used to assess and validate various aspects of the presented methodology. The Satellite Database for the Land Cover of Canada (SILC) is a 30 m resolution land cover database consisting of 33 classified Landsat thematic mapper (TM) – enhanced thematic mapper plus (ETM+) scenes (Latifovic et al., 2002). Total sample size is 9% of the Canadian landmass. Scenes were selected using the purposive selection algorithm (Cihlar et al., 2000) to obtain a subset of scenes that represent the distribution of land cover across Canada. Classification was carried out following the enhancement classification method (Beaubien et al., 1999), with 46 land cover classes based on a modified National Vegetation Classification System (NVSC) Federal Geographic Data Committee (FGDC) classification system. Accuracy evaluation at a thematic resolution of 28 classes for 10 of the 33 scenes showed the overall accuracy to be 90.3% (Beaubien et al., 2001). For comparison with the land cover products in this study, the SILC data were resampled to 1 km pixel resolution, and the dominant land cover type within the 1 km pixel footprint was taken as the pixel label. The relative proportion of the dominant land cover type was also determined and used to create a second reference image representing the dominant fraction percent. To facilitate the direct comparison of the multitemporal land cover maps with SILC, the SILC legend was converted to the 31-class legend of the 1995 land cover map and the 16-class legend of the IGBP (**Table 4**).

The four maps were compared with the SILC database using three different legends (**Table 2**) and different ways of representing the SILC data. Comparisons included the dominant pixel fraction and dominant pixel fraction above 60%

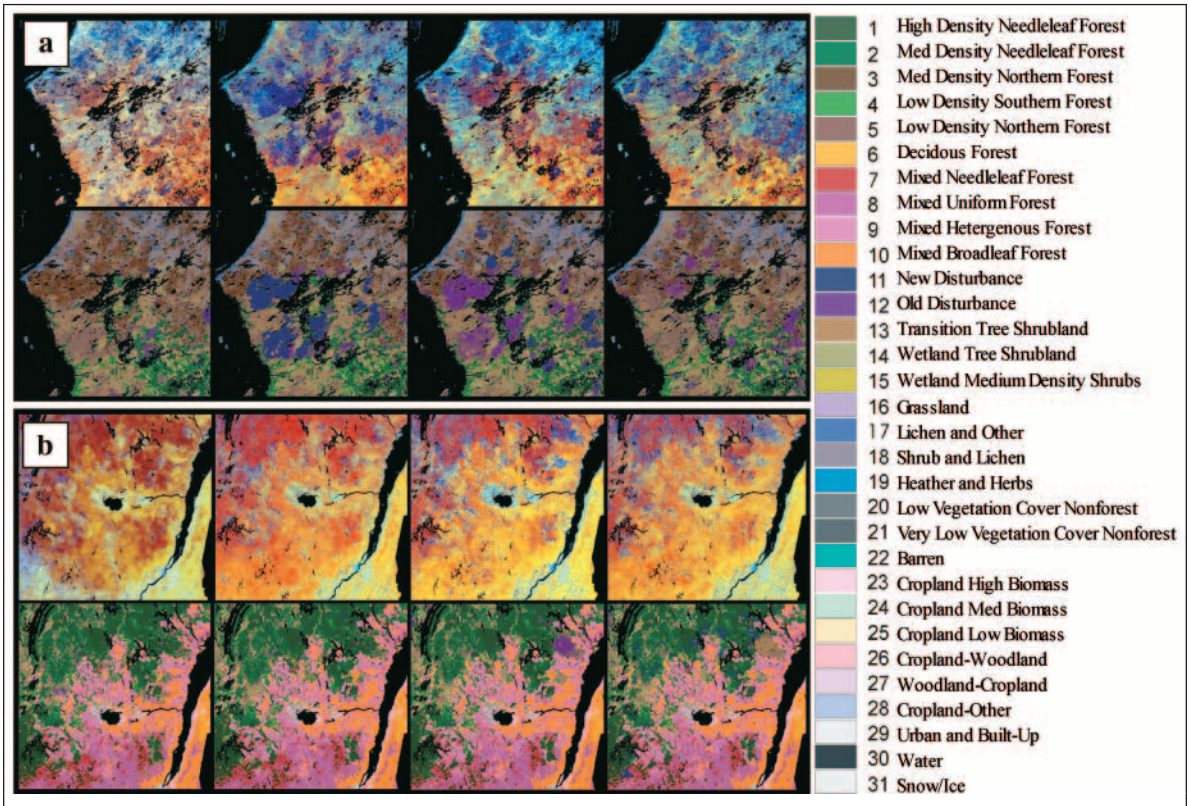

Figure 5. Example areas of classified maps: (a) east of James Bay in northern Quebec; (b) southern Quebec along the St. Lawrence River. For each example area, the top row is the AVHRR data displayed as follows: red, NDVI; green, Nir; blue, red. The second row is the classification result.

for the entire SILC database and the areas identified as change. The different fraction thresholds were used for evaluating the method-labeling accuracy of homogenous pixels. Comparison for just change areas was also included so that the accuracy of the updating methodology could be more effectively evaluated.

Comparison using the entire SILC database showed that the best overall accuracy of 61.5% was achieved with the 12-class legend (**Table 5**). This was considerably higher than the accuracies obtained with the other legends and reveals the important dependence of accuracy on thematic resolution. The low accuracy found with the 31-class legend was expected because of a large number of mixed pixels with low homogeneity and considerable overlap of class spectral properties. For pixels with a dominant fraction greater than 60%, accuracies were much higher (47.3%–74.5%) depending on the legend used. Only slight differences were found between accuracies produced for the different years. In this case, using the entire SILC database tended to mask the effects of the improvement made by the updating procedure because the change areas only represent a small proportion of the SILC database. This combined with look-up table error for converting the FGDC legend to the 1995 legend were the main factors for the slight differences seen between the comparisons for the different years.

The results considering only the change areas showed that the 2000 map was in greater agreement than other land cover maps with the SILC database. This was expected because the SILC data were collected between 1998 and 2000. Overall accuracies in 2000 compared with 1995 increased by 6.8% for the 31-class legend and 7.8% for the 12-class legend. This increase was even more pronounced (ranging from 12.6% to 14.4%) when only pixels with a dominant fraction above 60% were included.

To identify the improvement gained by using local instead of global signatures, a simple Euclidean distance classification was performed using both methods of signature generation and compared with the SILC database. For the 31-class legend, overall accuracies in the change areas were 19.3% using local signatures and 18.0% using global signatures. For the 12-class legend, overall accuracies were 47.1% and 44.7% for local and global signatures, respectively, showing that local signatures increased the accuracy by 2.5%. The results here also provide insight into the improvement gained by the evidence-based classification, which was an increase of 16.8% over the simple Euclidean distance classification using global signatures.

It was also of interest to determine how well commission errors from the change detection procedure were corrected by the local classification methodology. For this assessment, 500 randomly located change objects of random size (5–200 pixels) were selected in areas identified as no-change in the 1995–2000 change map. These "false" changes were then classified using the local classification methodology with the 2000 AVHRR data and the overall accuracy calculated using the original 1995 land cover map for these false change areas. Results showed that reclassification accuracy was 41% for the 31-class legend and 72% for the 12-class legend.

Comparison using the IGBP legend is of interest because it allows for evaluation of the map accuracy relative to other maps of the region produced through global mapping initiatives. In Latifovic and Olthof (2004), the same SILC database and dominant fraction assessment procedure as that used here showed that the range of accuracies observed for four different global land cover products within Canada was 29%–49%. In this study, the 2000 land cover product achieved a higher accuracy estimate (52%), suggesting that it is possibly a better representation of Canada than the global products. In this case, the global mapping objective reduces the flexibility with which the map can be created to capture local variability, which can be more easily accounted for in regional-level mapping applications. Likely the most important factor is that a direct one-to-one merge of the different map legends was not possible due to overlap in class definitions leading to some degree of inherent error.

Limitations of medium-resolution accuracy assessment

The sampling objective used in the construction of the SILC database was to capture the land cover variability within Canada with the fewest possible scenes to minimize costs. Thus, the Landsat scenes in the database were distributed most frequently in areas of high land cover variability such as mountainous areas of British Columbia and transition zones between broad biomes. These areas are typically the most difficult to classify because of a greater occurrence of mixed pixels or topographic effects, and they only represent a small portion of the Canadian landmass. Complete random sampling would be more desirable so that sampling reflects the area distribution of land cover. The analysis within the change areas was the most influenced by the SILC sampling objective. For the analysis considering only change areas, the sample size was drastically reduced (only 6.8% of the SILC area), making the results more sensitive to errors in either the SILC database, 2000 land cover, or change detection inputs. The SILC sample scenes also miss the majority of the high temporal and spatial change areas and are most prevalent in areas where change accuracy is expected to be the lowest, such as areas with strong topography leading to high proportions of false change detection.

Another limitation of this validation is the effect of the conversion table used to merge the 46-class FGDC legend used in SILC with the 31-class legend. Some of the SILC database classes do not clearly associate with a single class in the 31-class legend. Thus, changes in how classes are merged can have a substantial impact on accuracy assessment. In the SILC database, for example, numerous old burns are labeled as low vegetation cover, whereas in the land cover time series these areas are labeled as old disturbance, resulting in error. Unfortunately, changing either class in an attempt to improve agreement results in similar or greater error.

Table 4. Look-up table for converting the SILC legend to the 16-class IGBP legend and 1995 31-class legend.

Federal Geographic Data Committee (FGDC) classification		16-class IGBP	1995 31-class
Tree dominated (tree crown density > 25%)			
1	Evergreen forest (>75% cover) — old	1	1
2	Evergreen forest (>75% cover) — young	1	4
3	Deciduous forest (>75% cover)	4	10
4	Mixed coniferous (50%–75% coniferous) — old	5	9
5	Mixed coniferous (50%–75% coniferous) — young	5	9
6	Mixed deciduous (25%–50% coniferous)	5	9
7	Evergreen open canopy (40%–60% cover) — moss–shrub understory	1	1
8	Evergreen open canopy (40%–60% cover) — lichen–shrub understory	1	2
9	Evergreen open canopy (25%–40% cover) — shrub–moss understory	1	4
10	Evergreen open canopy (25%–40% cover) — lichen (rock) understory	1	5
11	Deciduous open canopy (25%–60% cover)	4	10
12	Deciduous open canopy — low regenerating to young broadleaf cover	4	10
13	Mixed evergreen–deciduous open canopy (25%–60% cover)	5	9
14	Mixed deciduous (25%–50% coniferous trees; 25%–60% cover)	5	9
15	Low regenerating to young mixed cover	5	9
Shrub dominated			
16	Deciduous shrubland (>75% cover)	6	14
Herb dominated			
17	Grassland, prairie region	10	16
18	Herb – shrub – bare cover, mostly after perturbations	7	5
19	Shrubs–herb–lichen–bare	7	19
20	Wetlands	11	14
21	Sparse coniferous (density 10%–25%), shrub–herb–lichen cover	8	5
22	Sparse coniferous (density 10%–25%), herb–shrub cover	8	13
23	Herb–shrub	16	18
24	Shrub–herb–lichen–bare	16	18
25	Shrub – herb – lichen – water bodies	16	18
26	Lichen–shrub–herb, bare soil or rock outcrop	16	17
27	Lichen–shrub–herb, bare soil – rock outcrop, water bodies	16	17
28	Low vegetation cover (bare soil, rock outcrop)	16	21
29	Low vegetation cover, with snow	16	20
30	Woodland–cropland	0	27
31	Cropland–woodland	0	26
32	Annual row-crop forbs and grasses — high biomass	12	23
33	Annual row-crop forbs and grasses — medium biomass	12	24
34	Annual row-crop forbs and grasses — low biomass	12	25
Nonvascular dominated			
35	Lichen barren	16	18
36	Lichen–shrub–herb–bare	16	19
37	Sparse coniferous (density 10%–25%), lichen–shrub–herb cover	16	13
Vegetation not dominant			
38	Rock outcrop, low vegetation cover	16	21
39	Recent burns	7	11
40	Mostly bare disturbed areas (e.g., cutovers)	7	11
41	Low vegetation cover	16	12
42	Urban and built-up	13	29
43	Water bodies	0	0
44	Mixes of water and land	0	0
45	Snow/ice	15	31
46	Clouds	0	0

Table 5. Overall and kappa accuracy measures for various comparisons with the SILC database.

	1985		1990		1995		2000	
	Overall	Kappa	Overall	Kappa	Overall	Kappa	Overall	Kappa
31-class land cover comparison with SILC database								
SILC	27.10	0.255	27.18	0.256	27.12	0.253	27.73	0.260
SILC dominant fraction > 60%	46.10	0.431	46.09	0.431	45.95	0.427	47.30	0.440
SILC change areas only	18.82	0.170	18.40	0.152	17.16	0.138	23.94	0.216
SILC change areas only dominant fraction > 60%	27.79	0.266	26.03	0.237	23.23	0.208	35.85	0.350
16-class IGBP land cover comparison with SILC database								
SILC	51.69	0.466	51.63	0.477	51.80	0.476	52.06	0.470
SILC dominant fraction > 60%	66.15	0.609	66.80	0.617	66.23	0.610	66.88	0.618
SILC change areas only	34.73	0.290	36.08	0.310	34.37	0.281	37.33	0.321
SILC change areas only dominant fraction > 60%	30.42	0.227	31.85	0.245	31.15	0.241	41.05	0.354
12-class land cover comparison with SILC database								
SILC	60.46	0.552	60.73	0.555	60.72	0.555	61.50	0.564
SILC dominant fraction > 60%	72.69	0.667	72.60	0.666	72.60	0.666	74.05	0.684
SILC change areas only	36.46	0.247	36.25	0.205	36.31	0.235	43.97	0.301
SILC change areas only dominant fraction > 60%	42.45	0.298	39.35	0.242	42.02	0.343	56.35	0.439

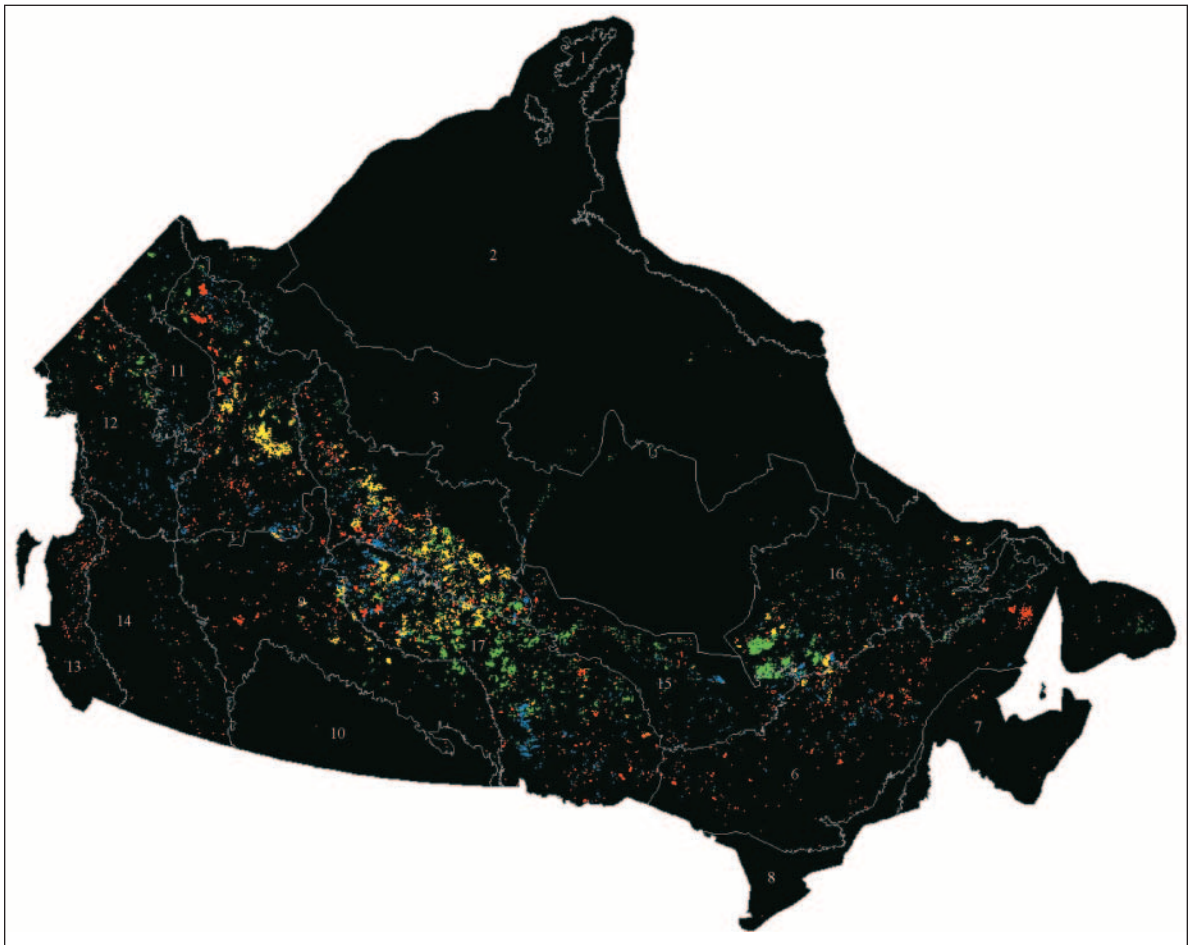

Figure 6. Temporal pattern of disturbance: blue, 1985; green, 1990; yellow, 1995; red, 2000. Numbers indicate ecozone polygon referred to in the text and **Table 6**.

Table 6. Percent land cover area to the total ecozone area for selected ecozones.

		Land cover class					
Ecozone	Year	Conifer forest (1)	Deciduous forest (2)	Mixed forest (3)	Disturbance (4)	Shrubland (5)	Grassland (6)
Taiga Shield West (5)	1985	57.15	0.00	0.06	4.16	9.92	0.00
	1990	54.08	0.00	0.07	6.21	10.16	0.00
	1995	46.76	0.00	0.07	13.65	10.22	0.00
	2000	46.39	0.00	0.07	14.26	10.17	0.00
Boreal Shield East (6)	1985	39.21	1.25	41.18	0.41	14.05	0.00
	1990	39.29	1.15	42.08	0.33	13.17	0.00
	1995	38.79	1.35	41.80	0.69	13.32	0.00
	2000	37.35	1.35	41.80	2.05	13.44	0.00
Prairies (10)	1985	0.02	0.00	0.85	0.00	0.91	10.35
	1990	0.02	0.00	0.85	0.00	0.91	10.39
	1995	0.02	0.00	0.85	0.00	0.91	10.39
	2000	0.02	0.00	0.85	0.00	0.91	10.38
Boreal Cordillera (12)	1985	41.81	0.04	4.51	0.81	30.15	0.00
	1990	40.89	0.04	4.26	1.26	30.48	0.00
	1995	40.19	0.04	4.31	1.67	30.49	0.00
	2000	40.37	0.04	4.26	1.65	30.45	0.00
Taiga Shield East (16)	1985	43.50	0.00	0.02	1.33	8.09	0.00
	1990	40.55	0.00	0.03	3.97	8.25	0.00
	1995	39.19	0.00	0.03	5.14	8.31	0.00
	2000	41.43	0.00	0.03	3.26	8.23	0.00
Boreal Shield West (17)	1985	80.95	0.00	9.50	2.87	5.77	0.00
	1990	76.63	0.00	9.55	6.68	6.05	0.00
	1995	74.27	0.00	9.95	9.13	5.58	0.00
	2000	75.80	0.00	9.79	6.47	6.91	0.00
Canada	1985	30.91	0.40	12.88	0.88	10.99	0.55
	1990	30.06	0.38	12.99	1.60	10.89	0.56
	1995	28.99	0.40	12.89	2.68	10.92	0.56
	2000	29.12	0.40	12.87	2.55	10.99	0.56

Note: Class and ecozone numbers are given in parentheses.

Factors affecting land cover database consistency and potential improvements

An account of the potential error sources in the methodology is useful to identify areas of improvement and to better educate users on the potential limitations that may translate to map uncertainty. The error sources include AVHRR data, change detection, the base map used for updating, and local classification. The methods used for preprocessing the AVHRR data have been well established and validated. However, there is potential for improvements and advancements in data processing, which are continually being explored.

Change detection offers some potential for improvement, as reclassification of false change areas was 76% for the 12-class legend. However, considering that false change is only a small portion of the total change area and that the majority of this error will be correctly reclassified reduces the sensitivity of the method to commission error. Regardless, improvements made will benefit the final product accuracy. More advanced change detection techniques or fusion of change methods could lead to improved results. The main difficultly with change detection is the selection of appropriate change indicators and thresholds. The simplest way to achieve this is with improved training data.

The accuracy of the base map is important because it is used for signature generation and to constrain the classification using the expected class change weight matrix. Thus, an accurate base map is an important factor. Unfortunately, there is little that can be done to improve the map once it is selected or produced without recreating the classification using an improved methodology or data.

More rigorous development of the weight matrices used to represent expected class changes could be developed. The weight matrix significantly constrains the classification, and the more effectively this matrix is specified, the more accurate the time series developed will be. Ideally, a group of experts should be assembled to give input for the development of the weight matrix. However, this will depend on the availability of such expertise.

Time series analysis

The multiyear land cover database supports a generally accepted conclusion that a land cover product should be based on earth observation rather then survey map compilation, and that a database spatial resolution of 1 km is currently appropriate for meeting the wide range of emerging global and

Low vegetation (7)	Cropland (8)	Cropland–woodland (9)	Urban (10)	Snow–ice (12)
28.69	0.00	0.02	0.00	0.00
29.46	0.00	0.02	0.00	0.00
29.27	0.00	0.02	0.00	0.00
29.09	0.00	0.01	0.00	0.00
2.98	0.10	0.70	0.11	0.00
3.02	0.11	0.73	0.11	0.00
3.08	0.12	0.73	0.11	0.00
3.04	0.13	0.73	0.11	0.00
0.02	66.94	20.51	0.40	0.00
0.02	66.97	20.44	0.40	0.00
0.02	66.97	20.44	0.40	0.00
0.02	66.98	20.44	0.40	0.00
20.82	0.00	0.00	0.00	1.85
20.93	0.00	0.00	0.00	2.14
21.63	0.00	0.00	0.00	1.66
20.94	0.00	0.00	0.00	2.29
47.06	0.00	0.00	0.00	0.01
47.19	0.00	0.00	0.00	0.01
47.32	0.00	0.00	0.00	0.00
47.05	0.00	0.00	0.00	0.00
0.64	0.03	0.19	0.02	0.03
0.78	0.07	0.19	0.02	0.03
0.75	0.07	0.18	0.02	0.04
0.72	0.08	0.17	0.02	0.03
27.97	4.74	2.79	0.11	7.77
28.15	4.80	2.73	0.11	7.73
28.28	4.82	2.72	0.11	7.63
28.11	4.81	2.72	0.11	7.75

regional modeling applications (Loveland et al., 2000). The methodology for generating the land cover time series was employed at the 31-class level because it is the highest thematic level available for the 1995 land cover base map. This allows for numerous aggregate legends to be devised for various analysis tasks of interest. It also allows for tracking a single well-defined class through time with an associated level of uncertainty. The exact thematic resolution and legend used will depend on the objectives of the analyst balancing the objective with the allowable uncertainty. To recognize the range of applications in which the multiyear land cover database can provide information, an example is presented of analyzing spatial and temporal patterns and their variations for the period 1985–2000 over the Canadian landmass.

An analysis of class area can be performed using different thematic resolutions and stratification schemes. The land cover composition for 17 Canadian ecozones as defined by the Ecological Stratification Working Group (Marshall and Schut, 1999) was used in this study. The analysis was performed using the legend with 12 major land cover types. **Figure 6** shows the spatial distribution of disturbance through time and readily depicts areas with extensive spatial and high temporal disturbance. The size distribution of disturbance is also evident, with the majority of large disturbances occurring in ecozones 4 and 5 and the northern portion of ecozone 17. These disturbances are predominately the result of fire, but other causes include harvesting, mining, and severe insect defoliation. In the southern portion of ecozone 17 the smaller sized disturbances are mostly due to forest harvesting. In the far north (ecozones 1–3), little land cover disturbance has been identified, as the annual spatial dynamics and surface variability of snow and ice make it difficult to determine significant land cover change in these areas. The combined effects of annual snow and ice and topography also reduce detection capabilities in western British Columbia. In the prairie ecozone (ecozone 10), annual fluctuations in moisture can lead to dramatically different appearance of surface types, making disturbance more difficult to detect. Davidson and Wang (2004) found that the shortwave surface albedo of grasslands was almost two times more variable than that of forest cover types.

Table 6 presents results of the percent class area to total ecozone area for selected ecozones from 1985 to 2000. As with **Figure 6**, this table highlights ecozones with highly variable and stable land cover distribution through time. Ecozones 5, 16, and 17 have the most significant forest cover change for the 20-year period analyzed. The changes in ecozones 5, 16, and 17 contribute to a reduction in the total forest area of 2.1%, 1.4%, and 4.4% respectively. Following the forest area through time shows the majority of the disturbance for ecozones 16 and 17 occurred in the period 1985–1990, but the majority of disturbance for ecozone 5 occurred in the period 1990–1995. Examination of change for all of Canada shows an overall reduction of coniferous forest area from 1985 to 2000. This is in part due to high fire incidence years occurring in 1989 and 1995 and due to a limited ability to backward update disturbed areas. The difficultly is that the unique spectral response of disturbance changes quickly to appear similar to that of other land cover classes within a few years depending on location. In the north, vegetation redevelopment is slower and thus the disturbance signal is maintained for a longer time, whereas in the south the disturbance signal can dissipate much more rapidly (Zhang et al., 2004b). In forward updating, knowledge of post-disturbance succession captured in the ECCE reduces this problem. In backward updating, however, this knowledge cannot be applied in the same manner, resulting in underestimation of disturbance. In 2000, the loss of forest is beginning to be offset by regeneration of 1985–1990 disturbed areas. No significant change in the cropland class with regards to an increase or decrease in area is seen, which is consistent with census data (Statistics Canada, 2001). However, the land cover products underestimate the total area by 2% for the combined cropland and cropland–woodland classes. The difference is mostly due to the inability of detecting cropland areas less than 1 km^2 with coarse-resolution satellite imagery. All other land covers appear to be relativity stable over the time period examined.

Conclusion

In this research, a new map-updating methodology was developed and used to create a land cover time series over Canada for the period 1985–2000. The multiyear data follow logical temporal and spatial trends in land cover and were highly consistent between years, with overall agreement greater than 92%. Comparison with a medium-resolution reference database showed the map accuracy to be 61% at a thematic resolution of 12 classes, and it had a accuracy similar to that of other global land cover products. It also showed that the methodology considerably improved the accuracy of areas identified as change as the date of the land cover map came closer to the date of the validation database (SILC, increase of 8%). These maps could be used in a variety of ways to assess land cover changes through time and as inputs to regional-level ecosystem process models. Further development of the methodology and modifications of products will be considered as errors are identified through more detailed accuracy evaluations.

Acknowledgements

This research has been completed as a part of the Natural Resources Canada Earth Sciences Sector program Reducing Canada's Vulnerability to Climate Change, partially supported by the Canadian Space Agency founded project Climate Change and Ecosystem Impact. We would like to thank Goran Pavlic and Robert Fraser for providing the fire and Landsat change databases used in the study. We would also like to thank Gunar Fedosejevs and Bert Guindon for their valuable reviews of this manuscript and two anonymous reviewers.

References

Beaubien, J., Cihlar, J., Simard, G., and Latifovic, R. 1999. Land cover from multiple thematic mapper scenes using a new enhancement-classification methodology. *Journal of Geophysical Research*, Vol. 104, pp. 27 909 – 27 920.

Beaubien, J., Latifovic, R., Cihlar, J., and Simard, G. 2001. *BOREAS follow-on DSP-01 Landsat TM land cover mosaic of the BOREAS transect*. Oak Ridge National Laboratory Distributed Active Archive Center, Oak Ridge, Tenn. Available from http://www.daac.ornl.gov [accessed 11 December 2004].

Canadian Council of Forest Ministers. 2004. *National Forestry Database Program.* Available from http://nfdp.ccfm.org [accessed 10 September 2004].

Cihlar, J., Beaubien, J., Latifovic, R., and Simard, G. 1999. *Land cover of Canada version 1.1*. CD-ROM. Natural Resources Canada, Ottawa, Ont.

Cihlar, J., Latifovic, R., Chen, J., Beaubien, J., and Li, Z. 2000. Selecting representative high-resolution sample images for land cover studies: part 1 methodology. *Remote Sensing of Environment*, Vol. 71, pp. 26–42.

Cihlar, J., Latifovic, R., Chen, J., Trishchenko, A., Du, Y., Fedosejevs, G., and Guindon, B. 2004. Systematic corrections of AVHRR image composites for temporal studies. *Remote Sensing of Environment*, Vol. 89, pp. 217–233.

Comber, A.J., Law, A.N.R., and Lishman, J.R. 2004. A comparison of Bayes', Dempster-Shafer and Endorsement theories for managing knowledge uncertainty in the context of land cover monitoring. *Computers, Environment and Urban Systems*, Vol. 28, pp. 311–327.

Coppin, P., and Bauer, M. 1996. Digital change detection in forest ecosystems with remote sensing imagery. *Remote Sensing Reviews*, Vol. 13, pp. 207–234.

Coppin, P., Jonckheere, I., Nackaerts, K., Muys, B., and Lambin, E. 2004. Digital change detection methods in ecosystem monitoring: a review. *International Journal of Remote Sensing*, Vol. 25, No. 9, pp. 1565–1596.

Davidson, A., and Wang, S. 2004. The effects of sampling resolution on the surface albedos of dominant land cover types in the North American boreal region. *Remote Sensing of Environment*, Vol. 93, pp. 211–224.

DeFries, R., and Townshend, J. 1994. NDVI-derived land cover classification at global scales. *International Journal of Remote Sensing*, Vol. 15, pp. 3567–3586.

Fernandes, R., and Leblanc, S. 2005. Appropriate linear regression techniques for the calibration of remote sensing models: when classical linear regression should not be used. *Remote Sensing of Environment*, Vol. 95, pp. 303–316.

Foody, G. 2001. Monitoring the magnitude of land-cover change around the southern limits of the Sahara. *Photogrammetric Engineering and Remote Sensing*, Vol. 67, pp. 841–847.

Fraser, R., Hall, R., Landry, R., Lynham, T., Raymond, D., Lee, B., and Li, Z. 2004. Validation and calibration of Canada-wide-resolution satellite burned area maps. *Photogrammetric Engineering and Remote Sensing*, Vol. 70, pp. 451–460.

Fraser, R., Abuelgasim, A., and Latifovic, R. 2005. A method for detecting large-scale forest cover change using course spatial resolution imagery. *Remote Sensing of Environment*, Vol. 30, pp. 414–427.

Hall, F., Botkin, D., Strebel, D., Woods, K., and Goetz, S. 1991. Large-scale patterns of forest succession as determined by remote sensing. *Ecology*, Vol. 72, pp. 628–640.

Hansen, M., DeFries, R., Townshend, J., and Sohlberg, R. 2003. Global land cover classification at 1 km spatial resolution using a classification tree approach. *International Journal of Remote Sensing*, Vol. 21, pp. 1331–1364.

Jain, A., Duin, R., and Mao, J. 2000. Statistical pattern recognition: a review. *IEEE Transactions on Pattern Analysis and Machine Intelligenc*e, Vol. 22, pp. 4–37.

Jensen, J. 1996. *Introductory digital image processing: a remote sensing perspective*. Prentice-Hall Inc., Englewood Cliffs, N.J.

Latifovic, R., and Olthof, I. 2004. Accuracy assessment using sub-pixel fractional error matrices of global land cover products derived from satellite data. *Remote Sensing of Environment*, Vol. 90, pp. 153–165.

Latifovic, R., Beaubien, J., and Cihlar, J. 2002. *Land cover classification of Landsat ETM+ scene 26 July 1999 Path 09/Row 23. Satellite information for land cover of Canada (SILC) project*. Canada Centre for Remote Sensing, Natural Resources Canada, Ottawa, Ont.

Latifovic, R., Zhu, Z., Cihlar, J., Giri, C., and Oltholf, I. 2004. Land cover mapping of North and Central America — Global Land Cover 2000. *Remote Sensing of Environment*, Vol. 89, pp. 116–127.

Latifovic, R., Fytas, K., Chen, J., and Paraszczak, J. 2005. Assessing land cover change resulting from large surface mining development.

International Journal of Applied Earth Observation and Geoinformation, Vol. 7, pp. 29–48.

Loveland, T., and Belward, A. 1997. The IGBP-DIS global 1 km land cover data set, DISCover: first result. *International Journal of Remote Sensing*, Vol. 18, pp. 1389–3296.

Loveland, T., Reed, B., Brown, J., Ohlen, D., Zhu, Z., Yang, L., and Merchant, J. 2000. Development of a global land cover characteristics database and IGBP DISCover from 1 km AVHRR data. *International Journal of Remote Sensing*, Vol. 21, pp. 1303–1330.

Lu, D., Mausel, P., Brondizio, E., and Moran, E. 2004. Change detection techniques. *International Journal of Remote Sensing*, Vol. 25, pp. 2365–2407.

Marshall, I., and Schut, P. 1999. *A national ecological framework for Canada*. A cooperative product by Ecosystems Science Directorate, Environment Canada, and Research Branch, Agriculture and Agri-Food Canada, Ottawa, Ont. Available from http://sis.agr.gc.ca/cansis/nsdb/ecostrat/intro.html [accessed 9 August 2004].

Mas, J. 1999. Monitoring land-cover changes: a comparison of change detection techniques. *International Journal of Remote Sensing*, Vol. 20, pp. 139–152.

Maxwell, S., Hoffer, R., and Chapman, P. 2002a. AVHRR composite period selection for land cover classification. *International Journal of Remote Sensing*, Vol. 23, pp. 5043–5059.

Maxwell, S., Hoffer, R., and Chapman, P. 2002b. AVHRR channel selection for land cover classification. *International Journal of Remote Sensing*, Vol. 23, pp. 5061–5073.

Mayaux, P. 2002. GLC 2000 project — guidelines for quality control. In *Proceedings of the GLC 2000 Meeting, Ispra, Italy, March 2002*. Available from http://www-gvm.jrc.it/glc2000/publications.htm [accessed 2 August 2004].

Miller, A., Bryant, E., and Birnie, R. 1998. An analysis of land cover changes in the northern forest of New England using multitemporal Landsat MSS data. *International Journal of Remote Sensing*, Vol. 19, pp. 245–265.

Moon, W. 1990. Integration of geophysical and geological data using evidential belief function. *IEEE Transactions on Geoscience and Remote Sensing*, Vol. 28, pp. 711–720.

Olthof, I., Pouliot, D., Fernandes, R., and Latifovic, R. 2005. Landsat ETM+ radiometric normalization comparison for northern mapping applications. *Remote Sensing of Environment*, Vol. 95, pp. 388–398.

Peddle, D. 1995a. Knowledge formulation for supervised evidential classification. *Photogrammetric Engineering and Remote Sensing*, Vol. 61, pp. 409–417.

Peddle, D. 1995b. MERCURY⊕: an evidential reasoning image classifier. *Computers and Geosciences*, Vol. 21, pp. 1163–1176.

Richards, J.A. 1986. *Remote sensing digital image analysis*. Springer-Verlag, New York.

Srinivasan, A., and Richards, J. 1990. Knowledge-based techniques for multi-source classification. *International Journal of Remote Sensing*, Vol. 11, pp. 505–525.

Statistics Canada. 2001. *2001 census of agriculture*. Available from http://www.statcan.ca/english/agcensus2001/index.htm [accessed 11 October 2004].

Stöckli, R., and Vidale, P.L. 2004. European plant phenology and climate as seen in a 20-year AVHRR land-surface parameter dataset. *International Journal of Remote Sensing*, Vol. 25, pp. 3303–3330.

Strahler, A., Muchoney, D., Borak, J., Friedl, M., Gopal, S., Lambin, E., and Moody, A. 1999. *MODIS land cover product algorithm theoretical basis document (ATBD), version 5.0*. NASA EOS_MTPE Documentation, NASA, Washington, D.C.

Townshend, J., Justice, C., and Kalb, V. 1987. Characterization and classification of South American land cover types using satellite data. *International Journal of Remote Sensing*, Vol. 8, pp. 1189–1207.

Trishchenko, A.P., Cihlar, J., and Li, Z. 2001. Effects of spectral response functions on surface reflectance and NDVI measured with moderate resolution satellite sensors. *Remote Sensing of Environment*, Vol. 81, pp. 1–18.

Tucker, C., Townshend, J., and Goff, T. 1984. Continental land cover classification using meteorological satellite data. *Science (Washington, D.C.)*, Vol. 227, pp. 369–375.

Zhang, Q., Pavlic, G., Chen, W., Fraser, R., Leblanc, S., and Cihlar, J. 2004a. A semi-automatic segmentation procedure for feature extraction in remotely sensed imagery. *Computers and Geosciences*, Vol. 31, pp. 289–296.

Zhang, Q., Pavlic, G., Chen, W., Latifovic, R., Fraser, R., and Cihlar, J. 2004b. Deriving stand age distribution in boreal forests using SPOT/VEGETATION and NOAA AVHRR imagery. *Remote Sensing of Environment*, Vol. 91, pp. 405–418.

Can. J. Remote Sensing, Vol. 31, No. 5, pp. 364–376, 2005

Canada-wide foliage clumping index mapping from multiangular POLDER measurements

Sylvain G. Leblanc, Jing M. Chen, H. Peter White, Rasim Latifovic, Roselyne Lacaze, and Jean-Louis Roujean

Abstract. In this paper, vegetation canopy structural information is retrieved over Canada from multiangular Advanced Earth Observing Satellite (ADEOS-1) polarization and directionality of the earth's reflectance (POLDER) data based on canopy radiative transfer simulations using the Five-Scale model. The retrieval methodology makes use of the angular signature of the reflectance at the hot spot, where the sun and view angles coincide, and at the dark spot, where the reflectance is at its minimum. The POLDER data show that the normalized difference hot spot dark spot (NDHD) constructed from the hot spot and dark spot reflectances has no correlation with the nadir-normalized normalized difference vegetation index (NDVI), from which vegetation properties are often inferred, indicating that this angular index has additional information. Five-Scale simulations are used to assess the effects of foliage distribution on this angular index for different crown sizes, spatial distribution of crowns and foliage inside crowns, and foliage density variations. The simulations show that the NDHD is related to canopy structure quantified using a clumping index. This latter relationship is further exploited to derive a Canada-wide clumping index map at 7 km by 7 km resolution using spaceborne POLDER data. This map provides a critical new source of information for advanced modelling of radiation interaction with vegetation and energy and mass (water and carbon) exchanges between the surface and the atmosphere.

Résumé. Dans cet article, on extrait l'information structurale du couvert de végétation au-dessus du Canada à partir de données multi-angulaires POLDER de ADEOS-1 basé sur des simulations du modèle de transfert radiatif Five-Scale. La méthodologie d'extraction utilise la signature angulaire de la réflectance au point anti-spéculaire (hot spot), où les angles solaire et de visée se rencontrent, et au point sombre (dark spot), où la réflectance est à son minimum. Les données POLDER montrent que le NDHD (« normalized difference hot spot dark spot ») construit à partir des réflectances au point anti-spéculaire et au point sombre n'est pas corrélé au NDVI normalisé au nadir, à partir duquel les propriétés de la végétation sont souvent déduites, indiquant que cet indice angulaire contient plus d'information. Les simulations de Five-Scale sont utilisées pour évaluer les effets de la répartition du feuillage sur cet indice angulaire pour différentes dimensions de couronne, la répartition spatiale des couronnes et du feuillage à l'intérieur des couronnes et les variations de densité du feuillage. Les simulations montrent que le NDHD est relié à la structure du couvert quantifiée par le biais d'un indice d'agrégation. Cette relation est exploitée davantage pour dériver une carte d'indice d'agrégation à l'échelle du Canada à une résolution de 7 km × 7 km utilisant des données satellitaires POLDER. Cette carte fournit une nouvelle source critique d'information pour la modélisation avancée des interactions du rayonnement avec la végétation et des échanges d'énergie et de masse (eau et carbone) entre la surface et l'atmosphère.
[Traduit par la Rédaction]

Introduction

Quantitative assessment of vegetation properties from satellite imagery has matured greatly in recent years. Many retrieval techniques now exist to quantify vegetation density and vigour. However, the remote sensing information used in these techniques is usually based on single-view reflectance, particularly in considering vegetation indices such as the normalized difference vegetation index (NDVI). The vegetation amount is well characterized by the leaf area index (LAI), which gives an estimate of the foliage surface per unit of ground surface. The LAI retrieval is achieved from different remote sensing sensors and different methods (Myneni et al., 1997; Chen et al., 2002; Privette et al., 2002; Roujean and

Received 4 February 2005. Accepted 14 June 2005.

S.G. Leblanc.[1] Canada Centre for Remote Sensing (CCRS), Natural Resources Canada, Centre spatial John H. Chapman, 6767 Route de l'aéroport, St. Hubert, QC J3Y 8Y9, Canada.

J.M. Chen. Department of Geography and Program in Planning, University of Toronto, 100 St. George Street, Room 5047, Sidney Smith Hall, Toronto, ON M5S 3G3, Canada.

H.P. White and R. Latifovic. Canada Centre for Remote Sensing (CCRS), Natural Resources Canada, 588 Booth Street, Ottawa, ON K1A 0Y7, Canada.

R. Lacaze. Medias-France, CNES-BPI 2102, 18, av. Edouard Belin, 31401 Toulouse Cedex 04, France.

J.-L. Roujean. Météo-France, CNRM, 42, avenue G. Coriolis, 31057 Toulouse Cedex, France.

[1]Corresponding author (e-mail: Sylvain.Leblanc@CCRS.NRCan.gc.ca).

Lacaze, 2002; Fernandes et al., 2003). In most situations, a random distribution of the LAI is assumed within the pixel area. Occasionally, land cover segmentation is used with different relationships to compensate for the structural and spatial patterns of different vegetation types. As canopy structure varies even within a given vegetation type, however, land cover segmentation is not always sufficient for LAI retrieval. Therefore, it seems necessary to use additional information. A complement to single-look and nadir optical data is to consider multiangular sensor systems such as the multiangular imaging spectroradiometer (MISR) onboard the TERRA satellite and Advanced Earth Observing Satellite (ADEOS-1) polarization and directionality of the earth's reflectance (POLDER) that acquire multiple view angle reflectance on a single orbit. Asner (2000) showed early results of the advantage of using angular measurements for land applications. Some studies have incorporated the angular signature or non-nadir data into LAI retrieval (Bicheron and Leroy, 1999; Knyazikhin et al., 1998), and other studies have shown the potential of angular measurements in retrieving information about foliage organization (Lacaze et al., 2002; Leblanc et al., 2002; Pinty et al., 2001, Widlowski et al., 2001). The heterogeneity of the foliage distribution can be quantified by a clumping index based on Beer–Lambert's law (Nilson, 1971):

$$P(\theta) = \exp\left[\frac{-G(\theta)\Omega(\theta)L}{\cos\theta}\right], \tag{1}$$

where $(P\theta)$ is the gap fraction at view zenith angle θ, L is the leaf area index, $(G\theta)$ is the projection of unit leaf area in the θ direction, and $\Omega(\theta)$ is the clumping index. $\Omega(\theta)$ greater than unity implies that the foliage is regularly distributed, $\Omega(\theta) = 1$ represents a random distribution, and $\Omega(\theta)$ less than unity implies that the foliage is clumped. The clumping index is generally found as follows:

$$\Omega(\theta) = \frac{\ln[P_c(\theta)]}{\ln[P_r(\theta)]} = \frac{L_e(\theta)}{L} \tag{2}$$

where $P_c(\theta)$ is the gap fraction measured in the clumped canopy; $P_r(\theta)$ is the theoretical gap fraction from Equation (1), with $\Omega(\theta) = 1$; and $L_e(\theta)$ is the so-called effective LAI (Chen and Cihlar, 1995) that represents the LAI obtained from inversion of Equation (1) without clumping considerations such as $L_e(\theta) = \Omega(\theta)L$. Although LAI mapping is often performed from remote sensing data, some empirical data and model simulations have shown that the nadir remote sensing signal may be more related to the effective LAI, or the gap fraction, than to the LAI (Chen and Cihlar, 1996; Leblanc et al., 2002). To retrieve a more precise LAI from remote sensing data, the clumping index may be needed.

The gap fraction can easily be estimated from optical instrument data such as hemispherical photographs (e.g., Leblanc et al., 2005), whereas the LAI is a more difficult parameter to measure. Although Equation (1) is a simplified expression of the complexity of light transmittance through a canopy, it is usually adequate for direct light transmittance and is the basis of field optical LAI retrieval (e.g., Lang and Xiang, 1986; Chen and Cihlar, 1995; Leblanc et al., 2005). For needleleaf species, the clumping index is usually separated into two components, namely clumping at a scale larger and smaller than the shoot:

$$\Omega(\theta) = \frac{\Omega_E(\theta)}{\gamma_E} \tag{3}$$

where $\Omega_E(\theta)$ is the clumping of foliage elements, leaves for broadleaf species and shoots for needleleaf species; and γ_E is the ratio of needles to shoots, which accounts for clumping of needles into shoots (Chen et al., 1997). The following different methods have been used for in situ estimation of the clumping index $\Omega_E(\theta)$ in vegetated canopies: (*i*) measurement of the LAI with allometric relationships compared with the effective LAI obtained with optical instruments (Kucharik et al., 1997) using Equation (2), which allows $\Omega(\theta)$ to be estimated directly but generally with the assumption that the foliage elements are randomly oriented, i.e., $G(\theta) = 0.5$; (*ii*) the finite-length averaging method applied to optical instruments (Lang and Xiang, 1986; Leblanc et al., 2005) in which a logarithmic averaging of the gap fraction scheme is used over finite lengths in the inversion of Equation (1), compared with the logarithm of the mean gap fraction (effective LAI); (*iii*) the gap size accumulation distribution method applied to optical instruments (Chen and Cihlar, 1995; Leblanc, 2002) in which large gaps that contribute to the gap fraction but are not possible in a random foliage distribution are removed from the gap fraction based on a theoretical random gap size distribution; and (*iv*) the Piélou aggregation index applied to optical instruments (Walter et al., 2003) in which sequences of gaps and nongaps are used to infer the clumping index.

The clumping index can be used to improve the modelling of the carbon cycle, as it allows a better segmentation of the solar radiation distribution in sunlit and shaded leaves as compared to models that relate carbon absorption to the intercepted solar radiation only (Chen et al., 2003). Several studies (Du Pury and Farquhar, 1997; Wang and Leuning, 1998; Chen et al., 1999b; Liu et al., 2002) favour using a sunlit – shaded leaf separation based on Norman (1993) for canopy-level photosynthesis simulations and thus require the clumping index. Previous studies have used a constant clumping index for a given land cover type, associated with LAI based on remote sensing (e.g., Liu et al., 1997). It has been shown that clumping index variation for a given effective LAI can have important effects on the gross and net primary productivity of a forest stand (Chen et al., 2003). Previous studies have shown that the multiangular measurement is related to the clumping index (Lacaze et al., 2002; Chen et al., 2003). Based on these studies, the goal of this paper is to develop an algorithm for mapping the clumping index for Canada from POLDER multiangular reflectance. The hot spot, where sun and view geometry

coincide, and the dark spot, where the reflectance is at its minimum (see **Figure 1**), form the basis of retrieving the clumping index from the angular signature.

Material and method

Data

Data from the POLDER sensor onboard the ADEOS-1 Japanese platform are used in this study by virtue of the ability of the sensor to measure the same ground surface (pixel) at up to 14 viewing angles during a single overpass under clear sky conditions (Deschamps et al., 1994). The POLDER sensor is a push-broom charge-coupled device (CCD) matrix with a wide field of view lens (114°) that gives a swath of about 2400 km, which allows the same ground area to be viewed during successive orbital passes. Because of this high frequency of revisiting sequence, the directional space is well covered after a few days, thereby increasing the chances of sampling the hot spot phenomenon. POLDER nadir pixel size is 6 km by 7 km, but we use a grid of 7 km by 7 km in this study to account for footprint consideration, since the multitemporal registration is estimated at 0.3 pixels (Leroy et al., 1997).

Reprocessed POLDER data using the sea-viewing wide field-of-view sensor (SeaWiFS) OC2-v4 algorithm (Fougnie et al., 2001) are used in this study. ADEOS-1 failed at the end of June 1997, and therefore only the data from 15 to 30 June are used to get as closed as possible to the peak growing season conditions within Canada. Although POLDER data are available in several bands, the present study employs directional data from the near-infrared (NIR) band (centred at 865 nm) for the following reasons: (*i*) more consistent reflectance values are obtained at NIR than at visible wavelengths due to reduced atmosphere absorption and scattering (e.g., Fernandes et al., 2003), (*ii*) better fit of bidirectional distribution function (BRDF) kernel models to NIR directional data with a high coefficient of determination (R^2) and low root mean square error (RMSE) (Leblanc et al., 2002), and (*iii*) reduced specular effect on NIR reflectance of water bodies that are very common within the Canadian landmass at 7 km by 7 km resolution (Lacaze, 1999; Pavlic et al., 2002).

Data processing

Within POLDER, pixel cover type composition was determined using a 1998 land cover map of Canada derived from Système Pour l'Observation de la Terre (SPOT-4) VEGETATION 1 km spatial resolution data (Cihlar et al., 2002.). The land cover map was resampled into spatial resolution equivalent to POLDER data using a non-overlapped 7 by 7 running window. Each 7 km by 7 km pixel was characterized with the dominant cover type. The running window was also used to estimate the percent cover of needleleaf species in the POLDER pixel. The needleleaf percentage was calculated based on all pixel types in the 7 by 7 windows, not just the dominant type. Pixels with cover type described as high conifer content were assumed to be 100% conifer, and mixed pixels were given the value of 50%. Even with these assumptions, less than 3% of the land pixels are pure conifers at 7 km resolution. For each of the 7 km by 7 km pixels, the centre coordinate is transformed into the nearest POLDER grid position and an automated routine searches for all POLDER measurements available for the given period (15–30 June 1997). Up to 200 reflectance values from different view and solar geometries are extracted for a single pixel coordinate.

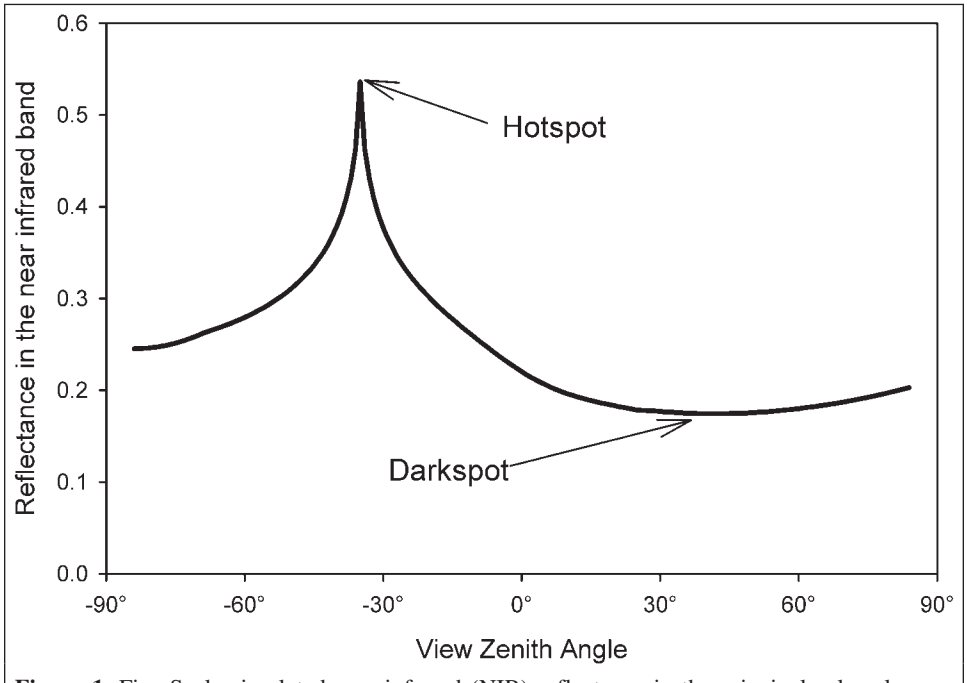

Figure 1. Five-Scale simulated near-infrared (NIR) reflectance in the principal solar plane.

Five-Scale model

Foliage density and distribution can significantly alter the remote sensing signal. Moreover, foliage clumping is a characteristic that can occur at different scales. The present study encompasses clumping at the shoot, branch, crown, and distribution of crown scales levels, corresponding to the four scales of the Four-Scale canopy radiative transfer model (Chen and Leblanc, 1997). The latest version of the model is used and is now called Five-Scale (Leblanc and Chen, 2000). Five-Scale is a combination of the Four-Scale and LIBERTY (Dawson et al., 1998) models. The ability of Five-Scale to reproduce directional reflectance has been validated with PARABOLA (Chen and Leblanc, 1997) and airborne POLDER data (Leblanc et al., 1999). Five-Scale is a geometric–optical canopy radiative transfer model. It simulates the directional reflectance of forest canopies using crowns as geometric objects such as cylinder and cone for conifers and spheroid for deciduous. These geometric objects are composed of foliage elements that can be grouped to form branches. The complex solar radiation multiple scattering of plant canopies is simulated with view factors that allow calculation of the amount of radiation reaching shaded portions and the enhancement of sunlit portions of the canopy and background (Chen and Leblanc, 2001). Five-Scale is used here to relate the LAI, clumping index, and other canopy architectural parameters to the canopy directional reflectance. The foliage clumping index is not a Five-Scale input parameter. The index $\Omega(\theta)$ is calculated based on Equation (2), where $P_c(\theta)$ is the clumped canopy gap fraction as calculated by Five-Scale, and $P_r(\theta)$ is the random canopy gap fraction computed with Beer-Lambert's law (Equation (1), with $\Omega(\theta) = 1$). Five-Scale completely separates orientation effects of clumping and foliage elements, i.e., $G(\theta)$ is completely independent of $\Omega(\theta)$. Angularly independent foliage clumping at the branch level can be entered as an input parameter (Ω_B), or a branch architecture can be used to simulate the clumping of foliage in branches. The clumping of needles into shoots is assumed to be angularly independent and is quantified by the ratio of needles to shoots γ_E (Chen et al., 1997). To remove species bias that may be found by using specific optical and canopy structures variables, the simulations were performed with different optical factors for background and foliage and canopy structures, which encompass more than the naturally occurring conditions in Canada. Twenty-two sets of optical properties are used, corresponding to different cases of red and NIR bands (see **Table 1**). However, the focus in this study is on the NIR band simulations.

FLAIR model

Although Five-Scale is computationally efficient, it is still too slow for inversion or to fit large angular datasets. Look-up-table or neural network methods could be used but are not necessary for the purpose of this study. Instead, the Four-Scale linear model for anisotropic reflectance (FLAIR) (White et al., 2001b; 2002) is used to parameterize the BRDF of all POLDER pixels. FLAIR is a linear kernel-like model developed from the Four-Scale model (Chen and Leblanc, 1997). Although simplifications were performed in developing FLAIR, efforts were also made not to limit the model to specific canopy characteristics while maintaining direct relationships between canopy architecture and model coefficients. This has resulted in a model with five descriptors of the canopy: multiple scattering factors at foliage and background level, reflectivity of foliage and background, and the canopy gap fraction relative to the effective LAI. FLAIR applications were demonstrated in White

Table 1. Five-Scale model input parameters for forest simulations.

Parameter	Value used in simulations
Density (no. of stems/ha)	500, 750, 1000, 2000, 3000, 4000, 6000
Leaf area index, LAI	0.5, 1.0, 2.0, 3,0, 4.0, 5.0, 6.0, 7.0, 8.0, 10.0, 12.0
Needle to shoot ratio (shoot clumping), $\gamma_{\backslash 45}$	1.0 (deciduous), 1.4 (coniferous)
Crown shape	Spheroid, cone + cylinder
Foliage clumping in branches, Ω_B	0.8, 1.0 (no clumping)
Tree clumping, m_2	No clumping, 10
Crown height, H_b (m)	5, 10, 20, 40
Crown base height, H_a (m)	0.0, 10.0
Crown radius, R (m)	0.5, 0.7, 1.0, 2.0, 3.0, 5.0
Foliage orientation, α_L (°)	Random, 75, 25
Branch orientation, α_B (°)	Random, 75, 25
Background reflectivity	
NIR	0.15, 0.35
Red	0.05, 0.10
Foliage reflectivity	
NIR	0.35, 0.50, 0.60
Red	0.05, 0.10, 0.15
Foliage transmittance	
NIR	0.35, 0.45
Red	0.05, 0.15

Note: Symbols refer to those used in Chen and Leblanc (1997) and Leblanc et al. (1999).

Table 2. Angular indices from the literature.

Index	Formula	Reference
Anisotropy index, ANIX	$ANIX = \rho_{Max}/\rho_{Min} = \rho_H/\rho_D$	Sandmeier et al., 1998
Hot spot dark spot index, HDS	$HDS = (\rho_H - \rho_D)/\rho_D = ANIX - 1$	Chen et al., 1999a; 2003; Lacaze et al., 2002
Normalized difference hot spot dark spot, NDHD	$NDHD = (\rho_H - \rho_D)/(\rho_H + \rho_D) = (ANIX - 1)/(ANIX + 1)$	Leblanc et al., 2001; 2002; Nolin et al., 2002

Note: ρ_{Max} and ρ_{Min} are the maximum and minimum measured reflectances, respectively. ρ_H and ρ_D are the hot spot and dark spot reflectances, respectively.

et al. (2001a; 2002). A FLAIR version with six free parameters is used here, where the effective LAI is replaced by the true LAI and the clumping index.

FLAIR was originally developed to be inverted using the simplex method (White et al., 2001b). The Powell method (Press et al., 1994) is used to retrieve the six FLAIR parameters. A negative merit function was used when reflectivity and proportion parameters were outside the 0–1 range and when the shaded foliage and background excitance were larger than half that of their sunlit counterparts. By using the FLAIR-retrieved parameters and resimulating the full BRDF at a common solar zenith angle, the hot spot and dark spot reflectances can be obtained to calculate any of the anisotropic indices listed in **Table 2**. Based on previous simulated tests (Leblanc et al., 2002), only the normalized difference hot spot dark spot (NDHD) is used because it showed a more linear relationship with the clumping index when fixed optical properties are used.

Results and discussion

Normalization and extrapolation

As previously stated, the POLDER acquisition design gives a wide range of view angles for a given ground area, up to more than 200 for the data used here. Nevertheless, it does not allow the hot spot to be found for all pixels, especially within a short time span. FLAIR is used here as a normalization and extrapolation tool to obtain the reflectance at any sun and view geometries from the available POLDER data. For this study, the angles of interest correspond to the reflectance at the hot spot, the dark spot, and the nadir geometries, all normalized at a common solar zenith angle (SZA) of 35°, which is representative of the mean SZA for Canada during the month of June. The hot spot and nadir reflectance values are found by simulating the reflectance at the exact angular geometry. The theoretical dark spot is found as the lowest simulated reflectance on the forward-scattering part of the principal solar plane for a view zenith angle of less than 65°, but for our purposes using a fixed geometry dark spot at 60° or letting the dark spot angle varies makes negligible differences.

Figure 2a shows how the largest reflectance values, which are usually found near the hot spot, are transformed by FLAIR into the hot spot reflectance at SZA of 35°. FLAIR-normalized reflectance values are more often larger than the highest measured reflectance values. The values most affected by the FLAIR normalization are from pixels where none of the view

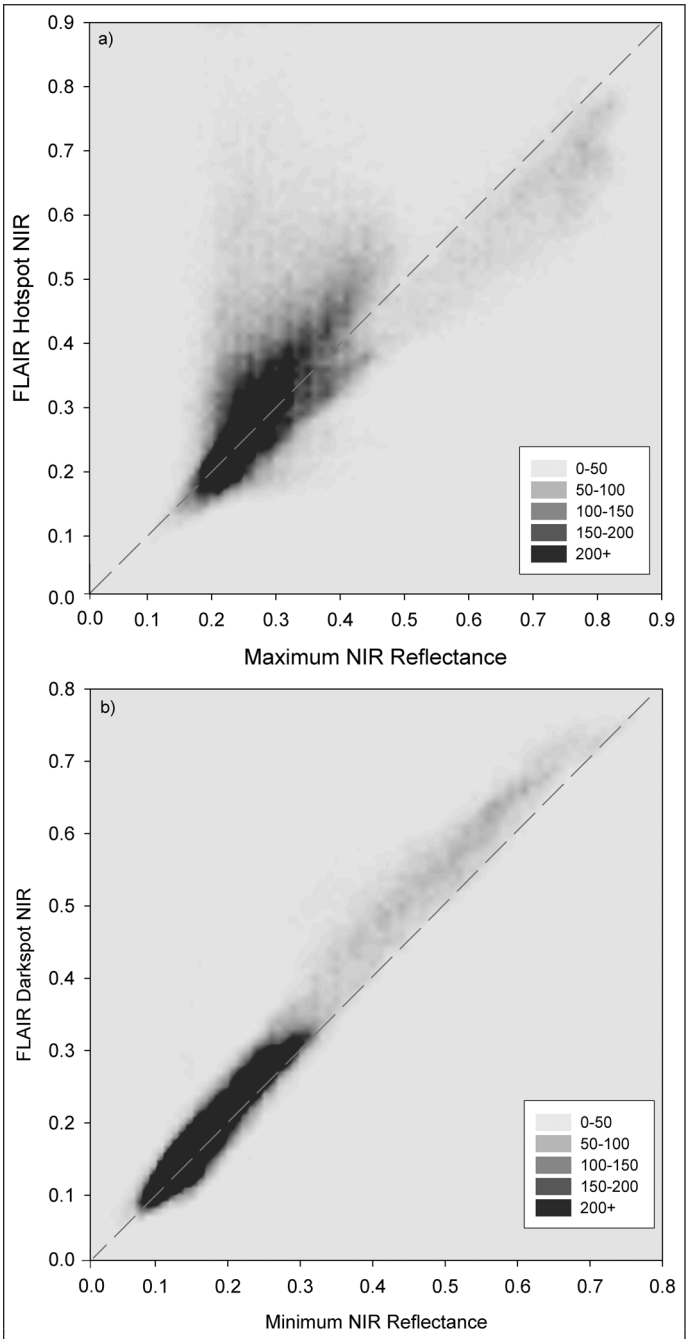

Figure 2. Effect of the FLAIR normalization at the (a) hot spot and (b) dark spot on the POLDER data. The FLAIR dark spot is found from view zenith angle less than 65°.

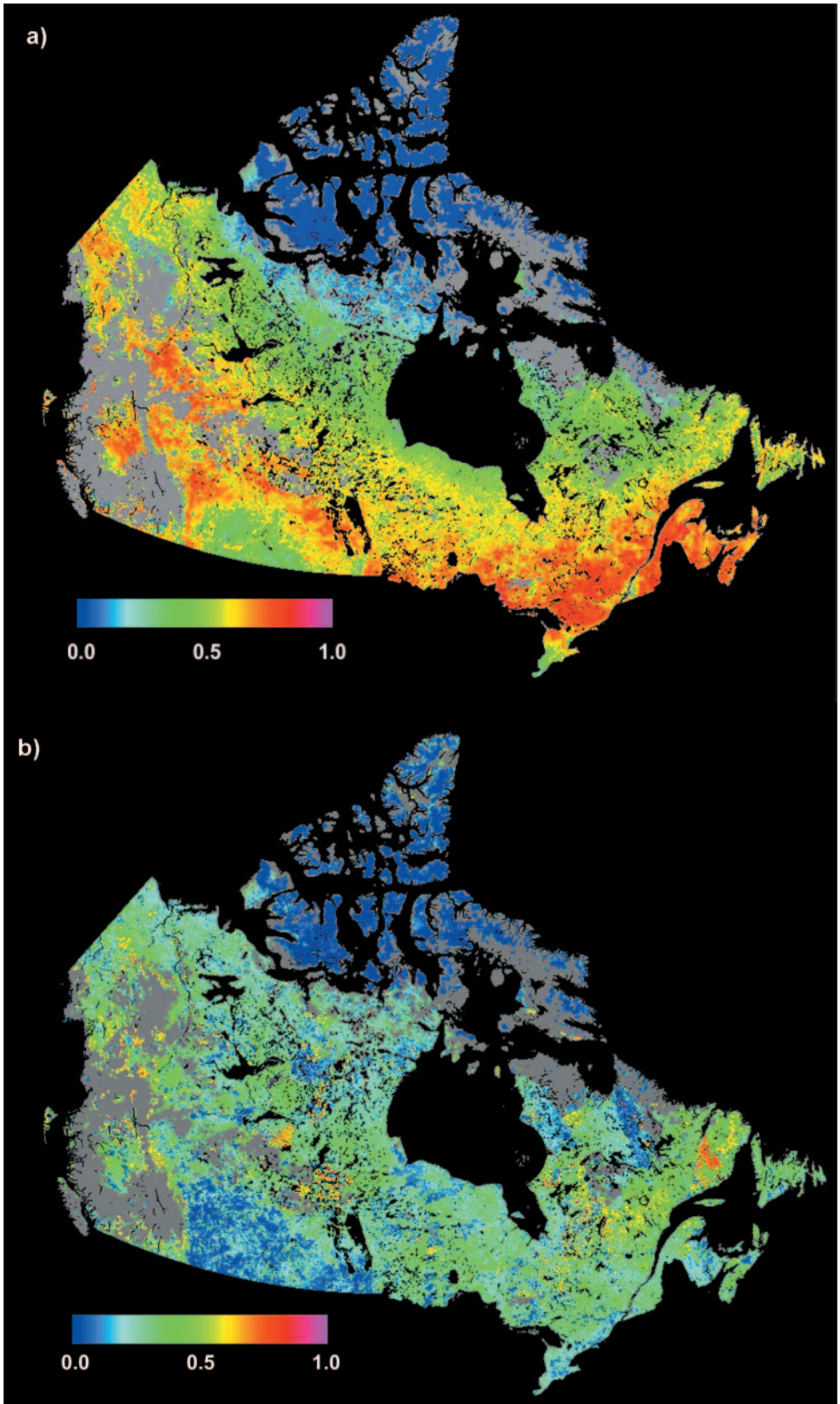

Figure 3. (a) FLAIR nadir normalized NDVI, where negative NDVI values from ice surfaces have been set to zero. (b) NDHD from FLAIR extracted hot spot and dark spot. POLDER data, 15–30 June 1997. The grey areas are pixels without data.

zenith angles were in the vicinity of the hot spot. Some values may have been either decreased or increased when a hot spot value was found because the POLDER data were from SZA greater or smaller than 35°. **Figure 2b** has the dark spot normalization effect. The dark spot normalization has less effect than the hot spot normalization because the reflectance does not vary much in the forward-scattering angular space for a given surface. Nadir normalization was also performed for both red and NIR bands, but these results are not shown because they are similar to the dark spot normalization shown in **Figure 2b**. Both nadir and dark spot reflectances are less affected by the normalization effects than the hot spot reflectances.

Remote sensing information content

Information in coarse-resolution remote sensing data is represented by the spectral, spatial, and temporal components. The dimensionality of spectral components is often reduced through band combinations, i.e., reflectance index. **Figure 3a** shows one of the most frequently used vegetation indices, the NDVI, based on the NIR and red bands of the POLDER data normalized at nadir and SZA of 35° by FLAIR. The largest NDVI values are found in very dense vegetated areas, mainly where broadleaf species are found. To visualize the directional information and to remove some of the effects of the different optical properties of the foliage and background, the NDHD index is calculated for the hot spot and dark spot reflectances extracted with FLAIR. Other angular indices have been used previously (see **Table 2**), but they are all mathematical transformations of each other. **Figure 3b** shows the resulting NDHD map. The prairies and far north generally have the lowest NDHD values, indicating very isotropic surfaces, and the forested areas have NDHD values close to 0.5. Overall, the NDHD values for broadleaf species are not that different from those for coniferous species. The NDVI map has smoother variations than the NDHD map. This behaviour can be explained in part by the extrapolation of the hot spot for pixels where the acquisition geometry did not get close to the hot spot, or it could be due to changes in the vegetation over the 2 weeks of measurements for the northern areas, as the vegetation vigour is still changing rapidly in those areas because the growing season starts later than it does in southern Canada. Moreover, the central Canada growing season started late in 1997, with leaf emergence around mid-May near Ottawa (Leblanc and Chen, 2001).

Figure 4 shows that the FLAIR-normalized nadir NDVI is not related to the FLAIR-normalized NDHD from the NIR band. This indicates that the information contents of these two indices are different. By using FLAIR to normalize and extrapolate the POLDER data to hot spot, dark spot, and nadir reflectances, smooth variations of the reflectance were generally found, indicating that FLAIR is good at assimilating data and reproducing physically valid reflectance. Moreover, FLAIR fits to the POLDER data also gave parameters such as LAI and clumping index directly. The retrieved values didn't seem to be consistent over Canada's landmass, however, and thus were not investigated in more detail in this study.

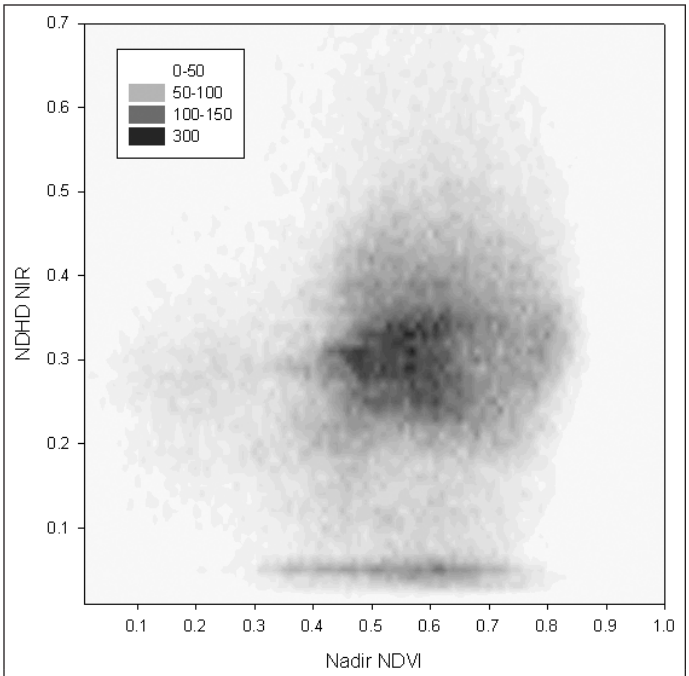

Figure 4. Relationship between the NDVI and the angular index NDHD based on the non-ice POLDER data over Canada (**Figures 3a** and **3b**) from 15–30 June 1997.

Simulation results

In this study, it is supposed that a large set of Five-Scale simulations can help in assessing the relationship between clumping index and angular properties of directional reflectance. The set of simulated parameters is large (see **Table 1**), but not continuous, and covers much more than the typical Canadian vegetation characteristics. Additional simulations were performed for low vegetation such as grassland and agriculture, which are included in the broadleaf results. Although Five-Scale was not designed for nonforested area, grass-like simulations can be obtained by using large numbers of small stems. Simulations with 500 000 – 1 000 000 stems per hectare and 0.01–2.00 m high with radius of 0.01–0.12 m were performed for LAI from 0.10 to 3.00. The simulation sets were run over many months and are combined to show the relationship between the clumping index and directional measurements. **Figures 5a** and **5b** show the relationship between clumping index and the hot spot and dark spot, respectively. Both red and NIR bands (based on **Table 1** input optical parameters) are shown. The analysis of simulated data did not provide evidence that the clumping index is directly related to the hot spot. However, there is some evidence that relationships between clumping index and dark spot exist because clumped canopies, i.e., dense tree crowns, branches, shoots, etc., cast dark shadows and decrease the dark spot reflectance. Two relationships can be seen in **Figure 5b**: one for the red band and one for the NIR band. Because of natural

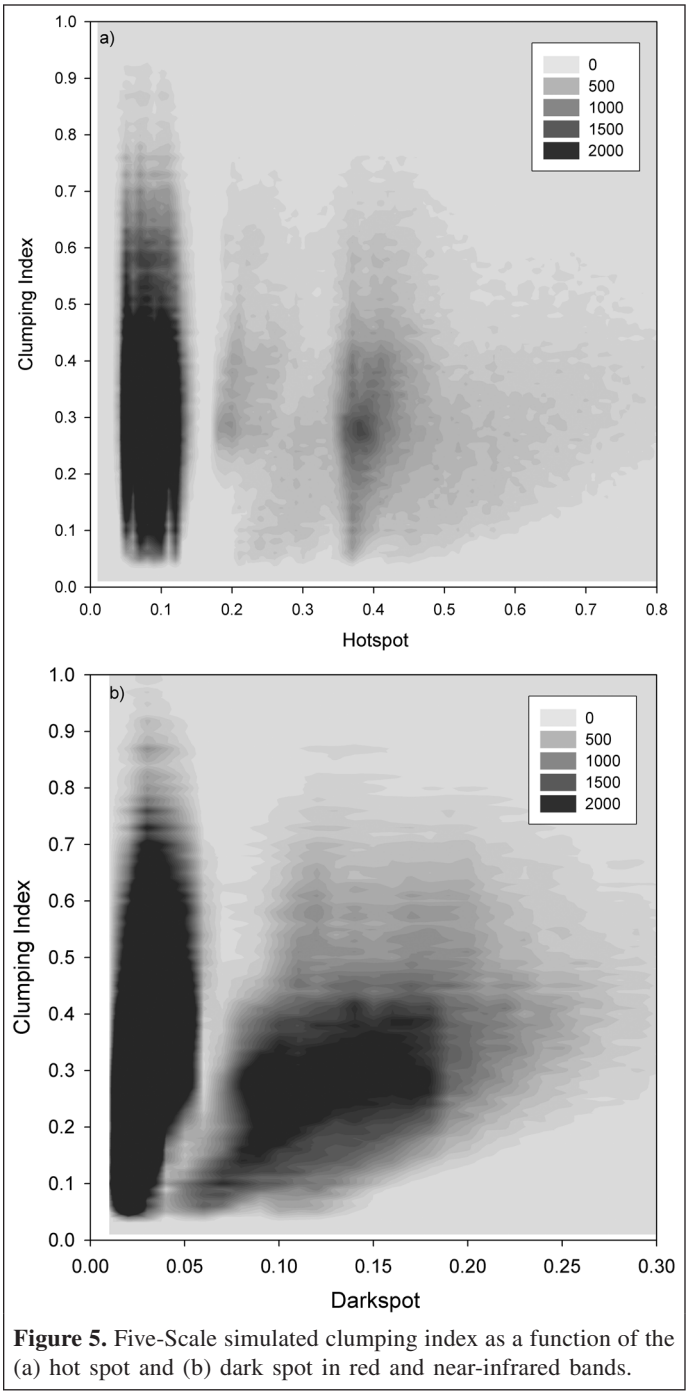

Figure 5. Five-Scale simulated clumping index as a function of the (a) hot spot and (b) dark spot in red and near-infrared bands.

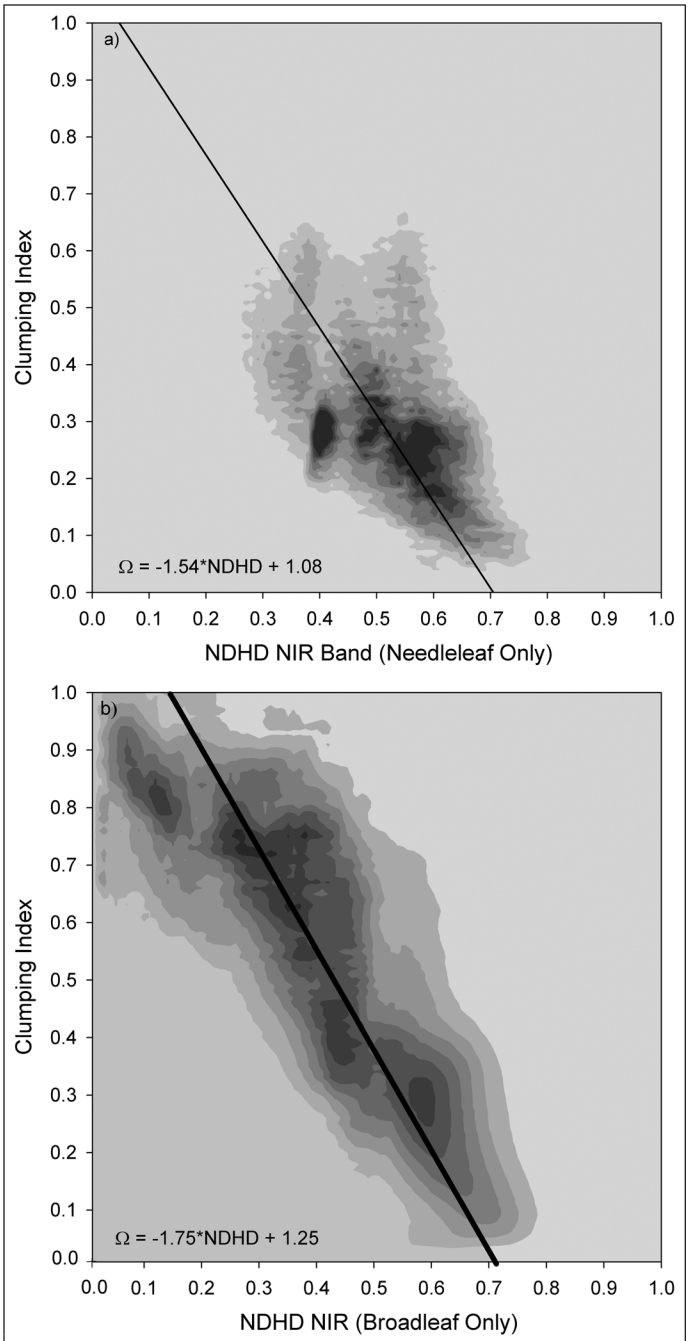

Figure 6. Five-Scale simulated relationships between near-infrared NDHD and the total foliage clumping index (Ω) for (a) needleleaf forests and (b) broadleaf forests and grassland.

variations in foliage optical properties, however, it seems more appropriate to use a normalized index such as NDHD. The clumping index information seems to be in the dark spot reflectance, whereas the hot spot can be seen as the normalizing factor when used in the NDHD.

Figures 6a and **6b** show the relationship between NDHD and the clumping index for coniferous and deciduous species, respectively. For clumping index values for low-density coniferous species, all simulations converge to a clear relationship, but at high clumping index values, for canopies with a more random foliage distribution, the relationship is not as clear. The relationship could have been improved by using more γ_E values. Only one case of needle clumping with $\gamma_E = 1.4$ was used in the simulation sets to save computational time, forcing the clumping index values to be lower than 0.7 (**Figure 6b**). The large scatter in **Figures 6a** and **6b** is due in large part to the large set of input parameters used for the simulations. The combinations of input that give very low foliage density in the crowns (<0.001 m^3/m^2), large vertical overlap crowns (>400%), and low canopy closure (<10%) were rejected. A robust

Table 3. Five-Scale NDHD clumping index fit values A and B ($\Omega = A \times \mathrm{NDHD} + B$).

Class	A	B
Conifer	–1.54	1.1
Broadleaf	–1.75	1.3

regression (Fernandes and Leblanc, 2005) is used to find a relationship between the NDHD and the clumping index. In this kind of regression, the median of the slopes and y-intercept are used instead of the mean values that are generally found in least-square regressions. This allows the regression line to be less influenced by outliers compared to a classical linear regression. Relationships for broadleaf and needleleaf species are found. The intercept and slope of the two linear relations are listed in **Table 3**. The following equation is used to apply these relationships to the POLDER data:

$$\Omega(35°) = [XA_C + (1-X)A_B]\mathrm{NDHD}(35°) + [XB_C + (1-X)B_B] \quad (4)$$

where X is the percentage of the pixel covered with needleleaf species; the constants A and B (**Table 3**) are found with the Five-Scale simulations; and the subscripts B and C denote broadleaf and coniferous, respectively.

Clumping index map

The POLDER dataset used in this study has large coverage gaps over Canada (25%), due most probably to cloud cover in June 1997. Thus to obtain a complete map of Canada, these pixels are filled with averaged NDHD values from the most frequently occurring cover type based on 40 spectral classes that were used to create the 12-class SPOT VEGETATION land cover map. Moreover, areas where the hot spot is farther than 10° from the closest measurements are discarded because of the uncertainties in extrapolating the hot spot; these are also replaced by the mean NDHD for the corresponding spectral classes. We used the spectral classes instead of the land cover type to have a more regional distribution of the clumping index. **Figure 7** shows the resulting clumping index map based on Equation (4) applied to the FLAIR-normalized POLDER NDHD. Northern, grass, and agricultural areas have a clumping index near unity. At the scale of the POLDER data, it is a very difficult, if not impossible, task to validate such a product. Contrary to near-nadir (or normalized to nadir) remote sensing, there is no sensor available at the moment at a resolution that

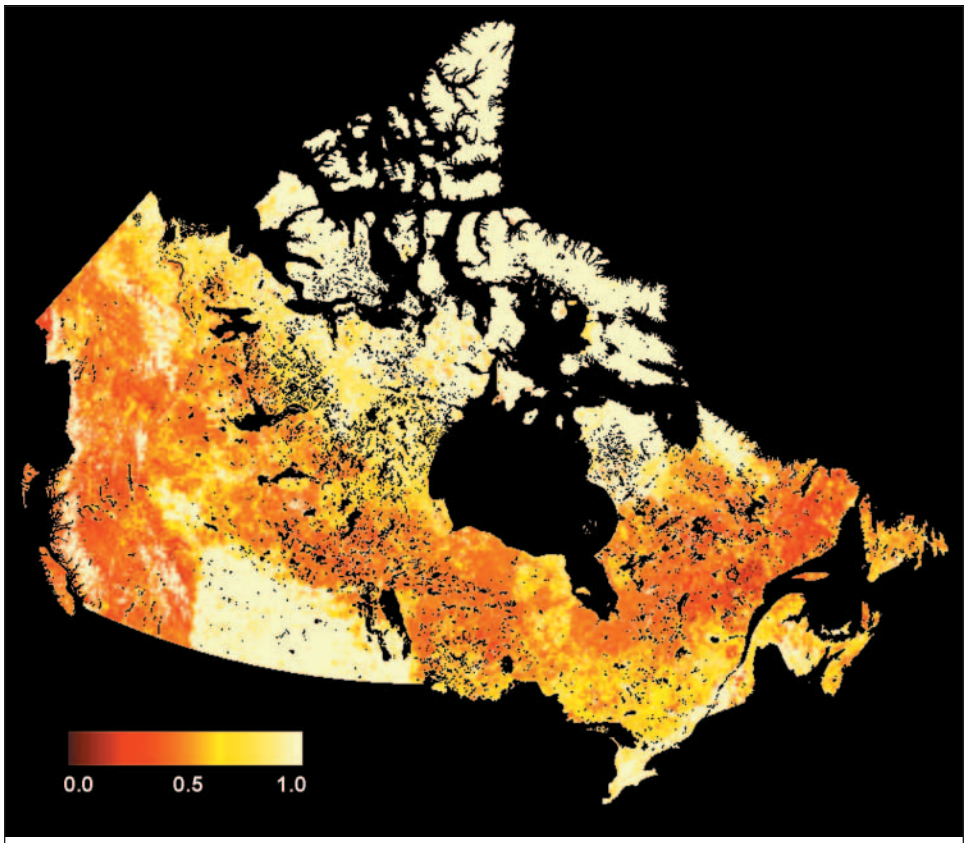

Figure 7. Clumping index map based on the NDHD POLDER based data from **Figure 3b** and a SPOT VEGETATION based land cover map. Only the pixels where the reflectance was measured within less than 10° from the hot spot were kept from **Figure 3b**; the remaining land pixels were filled with mean values from the associated cover type based on the land cover map. Values greater than unity were assigned a clumping index of one.

could be used as an intermediate scale. Sensors such as CHRIS on the PROBA platform, with a pixel resolution of the order of a plot (25–50 m), have multiangular view capabilities, but the angular sampling is not adequate for characterization of the hot spot for a given area because it has only five viewing angles (Barnsley et al., 2000). Airborne POLDER data were compared with field measurements in Lacaze et al. (2002), but with only five data points. The most clumped area is found in eastern Canada, on the north shore of the St. Lawrence River in the province of Quebec and in Labrador. **Figure 8** shows the statistical distribution of the retrieved clumping index values for pixels with vegetated cover types and with reflectance acquired within 10° of the hot spot. Clumping index values vary from near-random for broadleaf species (**Figure 8a**), with 86% of the values from 0.60 to 1.00, to more clumped for mixed broadleaf–needleleaf species (**Figure 8b**), with 85% of the values from 0.50 to 1.00, and to very clumped for needleleaf species, with 85% of the values from 0.35 to 0.60 (see **Figure 8c**). This is in agreement with measured clumping index values in boreal forests, as some black spruce stands have been shown to have a clumping index as low as 0.30, whereas deciduous species generally have values of between 0.70 and 0.90 (see **Table 4**). The averaged clumping index based on pixels with a reflectance acquired within 10° of the hot spot is not changed much if only pixels with a hot spot within 5° are used; all cover types are affected by at most a 1% relative change, except for the closed deciduous and mixed forests, which are increased by 3.6% and 2.0%, respectively. Although uncertainties from both the data and simulations affect the resulting clumping index values, the retrieved values are within the physically possible range. The retrieved dark spot should have a high accuracy, estimated at about 2% error based on **Figure 2**, and the hot spot may be estimated at around 5%. This implies that the retrieved NDHD has error at about 14% for the pixels with reflectance closer than 10°. The error for the relationship between clumping index and NDHD is more difficult to assess because we used a very large set of input variables. Previous Five-Scale simulation sets have shown better relationships between the clumping index and NDHD (Chen et al., 2003), since the input data were specific to a given species. We chose a larger set here to have less biased relationships, but at the cost of having less precise maps. Moreover, the relationships are dependent on the percentage of conifer in the pixels, adding another level of uncertainty to the final clumping index values. There is a difference of less than 15% between the factors found for the deciduous and coniferous relationships (**Table 3**). If we combined this with the error for the data, we get about 30% error for the retrieved clumping index. Ecological models have used a fixed clumping index value of 0.5 for coniferous forests (Liu et al., 1999), and this value has a root mean square difference of only 0.11 (22%) with the clumping index retrieved for pixels with 75% needleleaf, less than the estimated error of 30%.

Conclusions

Through canopy radiative transfer simulations and POLDER data analysis, it has been demonstrated that the angular remote sensing signal, in the form of the angular index NDHD, contains information that is complimentary to that of traditional

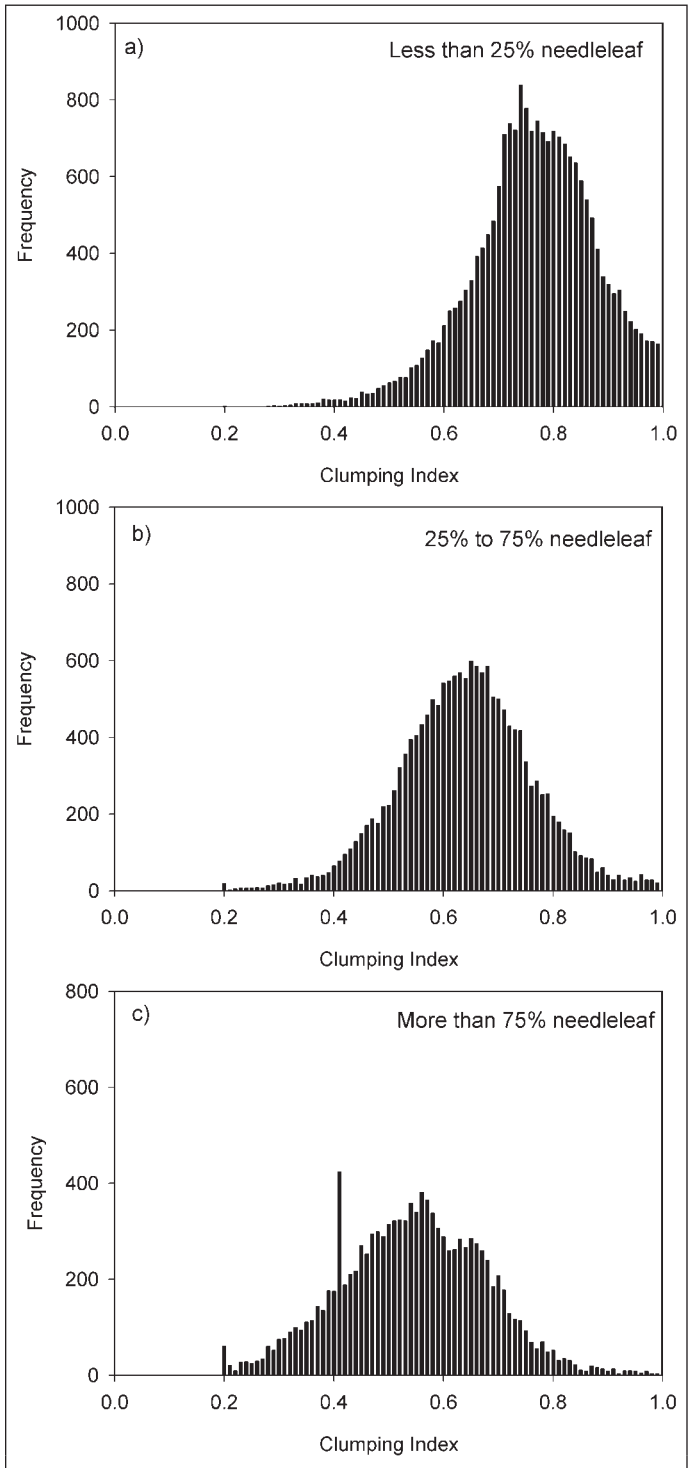

Figure 8. Clumping index histograms for different percentages of needleleaf species in the 7 km by 7 km pixels: (a) less than 25%, (b) between 25% and 75%, and (c) more than 75%.

Table 4. Mean retrieved clumping index and field measurement range of clumping index for each vegetated cover type.

Most frequently occurring cover type in 7 km × 7 km	Mean clumping index from POLDER	In situ clumping index	References for in situ clumping index
Closed evergreen forest	0.56	0.30–0.70	Chen et al., 1997; Leblanc et al., 2005
Closed deciduous forest	0.72	0.65–0.95	Chen et al., 1997; Leblanc and Chen, 2001
Closed mixed evergreen–deciduous forest	0.66	0.60–0.80	Unpublished data from sites in Chen et al., 2002
Open evergreen forest	0.61	0.25–0.80	Chen et al., 1997; Leblanc et al., 2005
Open mixed evergreen–deciduous forest	0.80	0.60–0.75	Unpublished data from sites in Chen et al., 2002
Herbaceous vegetation	0.88	0.70–0.95	Unpublished data from sites in Chen et al., 2002
Wetland	0.76	—	
Annual graminoid	0.91	0.70–0.95	Unpublished data from sites in Chen et al., 2002
Sparse vegetation	0.67	—	

Note: The classes are based on the most frequently occurring cover types based on SPOT VEGETATION classification (Cihlar et al., 2002).

vegetation indices such as the NDVI. Based on the simulated NDHD – clumping index relationships for different cover types, directional reflectance data were used to map the foliage clumping index over Canada. Although the map shown here has a low resolution with about 30% error, it gives a clumping index spatial distribution and can be used in carbon modelling to estimate the spatial distribution within cover types (Chen et al., 2003), which is an improvement over using fixed clumping index values for given cover types (Liu et al., 1999; 2002). An approach similar to that presented here is also being used to map the clumping index at the global scale (Chen et al., 2005), in which other considerations specific to global mapping are introduced.

Acknowledgements

The authors would like to thank Richard Fernandes and Robert Fraser who reviewed the manuscript before submission, the two anonymous reviewers for their constructive comments, and Josef Cihlar for supporting multiangular reflectance and foliage structure retrieval research over the years.

References

Asner, G P. 2000. Contribution of multi-view angle remote sensing to land-surface and biogeochemical research. *Remote Sensing Reviews*, Vol. 18, pp. 137–165.

Barnsley, M.J., Lewis, P., O'Dwyer, S., Disney, M.I., Hobson, P., Cutter, M., and Lobb, D. 2000. On the potential of CHRIS/PROBA for estimating vegetation canopy properties from space. *Remote Sensing Reviews*, Vol. 19, pp. 171–189.

Bicheron, P., and Leroy, M. 1999. A method of biophysical parameter retrieval at global scale by inversion of a vegetation reflectance model. *Remote Sensing of Environment*, Vol. 67, pp. 251–266.

Chen, J.M., and Cihlar, J. 1995. Plant canopy gap-size analysis theory for improving optical measurements of leaf area index. *Applied Optics*, Vol. 34, pp. 6211–6222.

Chen, J.M., and Cihlar, J. 1996. Retrieving leaf area index of boreal conifer forests using Landsat TM images. *Remote Sensing of Environment*, Vol. 55, No. 2, pp. 153–162.

Chen, J.M., and Leblanc, S.G. 1997. A four-scale bidirectional reflectance model based on canopy architecture. *IEEE Transactions on Geoscience and Remote Sensing*, Vol. 35, pp. 1316–1337.

Chen, J.M., and Leblanc, S.G. 2001. Multiple-scattering scheme useful for geometric optical modelling. *IEEE Transactions on Geoscience and Remote Sensing*, Vol. 39, pp. 1061–1071.

Chen, J.M., Rich, P.M., Gower, T.S., Norman, J.M., and Plummer, S. 1997. Leaf area index of boreal forests: theory, techniques and measurements. *Journal of Geophysical Research*, Vol. 102, pp. 29 429 – 29 444.

Chen, J.M., Lacaze, R., Leblanc, S.G., Roujean, J.-L., and Liu, J. 1999a. POLDER BRDF and photosynthesis: an angular signature useful for ecological applications. In *Proceedings of the 2nd International Workshop on Multiangular Measurements and Models*, 15–17 September 1999, Ispra, Italy. Abstract. JRC, Ispra, Italy. p. 98.

Chen, J.M., Liu, J., Cihlar, J., and Goulden, M.L. 1999b. Daily canopy photosynthesis model through temporal and spatial scaling for remote sensing applications. *Ecological Modelling*, Vol. 124, pp. 99–119.

Chen, J.M., Pavlic, G., Brown, L., Cihlar, J., Leblanc, S.G., White, H.P., Hall, R.J., Peddle, D., King, D.J., Trofymow, J.A., Swift, E., Van der Sanden, J., and Pellikka, P. 2002. Derivation and validation of Canada-wide coarse-resolution leaf area index maps using high resolution satellite imagery and ground measurements. *Remote Sensing of Environment*, Vol. 80, pp. 165–184.

Chen, J.M., Liu, J., Leblanc, S.G., Lacaze, R., and Roujean, J.-L. 2003. A demonstration of the utility of multi-angle remote sensing for estimating carbon absorption by vegetation. *Remote Sensing of Environment*, Vol. 84, pp. 516–525.

Chen, J.M., Menges, C.H., and Leblanc, S.G. 2005. Global mapping of the foliage clumping index using multi-angular satellite data. *Remote Sensing of Environment*, Vol. 97, No. 4, pp. 447–457.

Cihlar, J., Beaubien, J., and Latifovic, R. 2002. *Land cover of Canada 1998*. Special Publication, NBIOME Project. Canada Centre for Remote Sensing, Ottawa, Ont.

Dawson, T.P., Curran, P.J., and Plummer, S.E. 1998. LIBERTY — modelling the effects of leaf biochemistry on reflectance spectra. *Remote Sensing of Environment*, Vol. 65, pp 50–60.

Deschamps, P.Y., Bréon, F.M., Leroy, M., Podaire, A., Bricaud, A., Buriez, J.C., and Sèze, G. 1994. The POLDER mission: instrument characteristics and scientific objectives. *IEEE Transactions on Geoscience and Remote Sensing*, Vol. 32, pp. 598–615.

Du Pury, D.G.G., and Farquhar, G.D. 1997. Simple scaling of photosynthesis from leaves to canopies without the errors of big-leaf models. *Plant, Cell and Environment*, Vol. 20, pp. 537–557.

Fernandes, R., and Leblanc, S.G. 2005. Parametric (modified least squares) and non-parametric (Theil–Sen) linear regressions for predicting biophysical parameters in the presence of measurement errors. *Remote Sensing of Environment*, Vol. 95, pp. 303–316.

Fernandes, R., Butson, C., Leblanc, S., and Latifovic, R. 2003. Landsat-5 TM and Landsat-7 ETM+ based accuracy assessment of leaf area index products for Canada derived from SPOT-4 VEGETATION data. *Canadian Journal of Remote Sensing*, Vol. 29, No. 2, pp. 241–258.

Fougnie, B., Hagolle, O., and Cabot, F. 2001. In-flight measurement and correction of non-linearity of the POLDER-1's sensitivity. In *Proceedings of the 8th Symposium of the International Society for Photogrammetry and Remote Sensing*, 8–12 January 2001, Aussois, France. Centre National d'Études Spatiales (CNES), Toulouse, France. pp. 211–219.

Knyazikhin, Y., Martonchik, J.V., Diner, D.J., Myneni, D.J., Verstraete, M.M., Pinty, B., and Godron, N. 1998. Estimation of vegetation canopy leaf area index and fraction of absorbed photosynthetically active radiation from atmosphere-corrected MISR data. *Journal of Geophysical Research*, Vol. 103, pp. 32 239 – 32 256.

Kucharik, C.J., Norman, J.M., Murdock, L.M., and Gower, S.T. 1997. Characterizing canopy nonrandomness with a multiband vegetation imager (MVI). *Journal of Geophysical Research*, Vol. 102, pp. 29 455 – 29 473.

Lacaze, R. 1999. *Restitution des paramètres des surfaces continentales utiles à l'étude du climat à partir des observations multiangulaires de la télédétection optique*. Ph.D. thesis, Université Toulouse III (Paul Sabatier), Toulouse, France. 236 pp.

Lacaze, R., Chen, J.M., Roujean, J.-L., and Leblanc, S.G. 2002. Retrieval of vegetation clumping index using hot spot signatures measured by POLDER instrument. *Remote Sensing of Environment*, Vol. 79, pp. 84–95

Lang, A.R.G., and Xiang, Y. 1986. Estimation of leaf area index from transmission of direct sunlight in discontinuous canopies. *Agricultural and Forest Meteorology*, Vol. 35, pp. 229–243.

Leblanc, S.G. 2002. Correction to the plant canopy gap size analysis theory used by the tracing radiation and architecture of canopies (TRAC) instrument. *Applied Optics*, Vol. 31, pp. 7667–7670.

Leblanc, S.G., and Chen, J.M. 2000. A Windows graphic interface (GUI) for the Five-Scale model for fast BRDF simulations. *Remote Sensing Reviews*, Vol. 19, pp. 293–305.

Leblanc, S.G., and Chen, J.M. 2001. A practical scheme for correcting multiple scattering effects on optical LAI measurements. *Agricultural and Forest Meteorology*, Vol. 110, pp. 125–139.

Leblanc, S.G., Bicheron, P., Chen, J.M., Leroy, M., and Cihlar, J. 1999. Investigation of directional reflectance in boreal forests using an improved 4-scale model and airborne POLDER data. *IEEE Transactions on Geoscience and Remote Sensing*, Vol. 37, No. 3, pp. 1396–1414.

Leblanc, S.G., Chen, J.M., White, H.P., Cihlar, J., Lacaze, R., Roujean, J.-L., and Latifovic, R. 2001. Mapping vegetation clumping index from directional satellite measurements. In *Proceedings of the 8th Symposium of the International Society for Photogrammetry and Remote Sensing*, 8–12 January 2001, Aussois, France. Centre National d'Études Spatiales (CNES), Toulouse, France. pp. 450–459.

Leblanc, S.G., Chen, J.M., White, H.P., Latifovic, R., Fernandes, R., Roujean, J.-L., and Lacaze, R. 2002. Mapping leaf area index heterogeneity over Canada using directional reflectance and anisotropy models. In *IGARSS 2002, Proceedings of the IEEE International Geoscience and Remote Sensing Symposium*, 24–28 June 2002, Toronto, Ont. CD-ROM. IEEE, Piscataway, N.J.

Leblanc, S.G., Chen, J.M., Fernandes, R., Deering, D.W., and Conley, A. 2005. Methodology comparison for canopy structure parameters extraction from digital hemispherical photography in boreal forests. *Agricultural and Forest Meteorology*, Vol. 129, pp. 187–207.

Leroy, M., Deuze, J.L., Bréon, F.M., Hautecoeur, O., Herman, M., Buriez, J.C., Tanre, D., Bouffies, S., Chazette, P., and Roujean, J.L. 1997. Retrieval of atmospheric properties and surface bidirectional reflectances over the land from POLDER. *Journal of Geophysical Research*, Vol. 102, pp. 17 023 – 17 037.

Liu, J., Chen, J.M., Cihlar, J., and Park, W.M. 1997. A process-based boreal ecosystem productivity simulator using remote sensing inputs. *Remote Sensing of Environment*, Vol. 62, pp. 158–175.

Liu, J., Chen, J.M., Cihlar, J., and Chen, W. 1999. Net primary productivity distribution in the BOREAS study region from a process model driven by satellite and surface data. *Journal of Geophysical Research*, Vol. 104, No. D22, pp. 27 735 – 27 754.

Liu, J., Chen, J.M., Cihlar, J., and Chen, W. 2002. Remote sensing based estimation of net primary productivity over Canadian landmass. *Global Ecology and Biogeography*, Vol. 11, pp.115–129.

Myneni, R.B., Nemani, R.R., and Running, E.W. 1997. Algorithm for the estimation of global land cover, LAI and FPAR based on radiative transfer models. *IEEE Transactions on Geoscience and Remote Sensing*, Vol. 35, pp. 1380–1393.

Nilson, T. 1971. A theoretical analysis of the frequency of gaps in plant stands. *Agricultural Meteorology*, Vol. 8, pp. 25–38.

Nolin, A.W., Fetterer, F.M., and Scambos, T.A. 2002. Surface roughness characterizations of sea ice and ice sheets: case studies with MISR data. *IEEE Transactions on Geoscience and Remote Sensing*, Vol. 40, pp. 1605–1615.

Norman, J.M. 1993. Scaling processed between leaf and canopy levels. In *Scaling physiological processes: leaf to globe*. Edited by J.R. Ehleringer and C.B. Field. Academic Press, San Diego, Calif. pp. 41–76.

Pavlic, G., Fernandes, R., Chen, W., Fraser, R., and Leblanc, S.G. 2002. Canada wide geo-spatial datasets in support of environmental monitoring and modelling. In *Proceedings of ISPRS Technical Commission IV Symposium, Joint International Symposium on Geospatial Theory, Processing and Applications*, 9–12 July 2002, Ottawa, Ont. CD-ROM. ISRSE Office of the Secretariat, Tucson, Ariz.

Pinty, B., Widlowski, J.-L., Godron, N., Verstraete, M.M., and Diner, D.J. 2001. Uniqueness of multiangular measurements — Part 1: an indicator of subpixel surface heterogeneity from MISR. *IEEE Transactions on Geoscience and Remote Sensing*, Vol. 40, pp. 1559–1573.

Press, W., Teukolsky, S., Vetterling, W., and Flannery, B. 1994. *Numerical recipes in C*. Cambridge University Press, Cambridge, UK. 994 pp.

Privette, J.L., Myneni, R.B., Knyazikhin, Y., Mukufute, M., Roberts, G., Tian Y., Wang, Y., and Leblanc, S.G. 2002. Early spatial and temporal validation of MODIS LAI product in Africa. *Remote Sensing of Environment*, Vol. 83, pp. 232–243.

Roujean, J.L., and Lacaze, R., 2002. A global mapping of vegetation parameters from POLDER multi-angular measurements for surface–atmosphere interaction studies: a pragmatic approach and its validation. *Journal of Geophysical Research*, Vol. 107, No. D12, pp. 1029–1042.

Sandmeier, St., Muller, Ch., Hosgood, B., and Andreoli, G. 1998. Physical mechanisms in hyperspectral BRDF data of grass and watercress. *Remote Sensing of Environment*, Vol. 66, pp. 222–233.

Walter, J.-M.N., Fournier, R.A., Soudani, K., and Meyer, E. 2003. Integrating clumping effects in forest canopy structure: an assessment through hemispherical photographs. *Canadian Journal of Remote Sensing*, Vol. 29, No. 3, pp. 388–410.

Wang, Y.-P., and Leuning, R. 1998. A two-leaf model for canopy conductance, photosynthesis and partitioning of available energy: I. Model description and comparison with a multi-layered model. *Agricultural and Forest Meteorology*, Vol. 91, pp. 89–111.

White, H.P., Leblanc, S.G., Chen, J.M., Lacaze, R., and Roujean, J.-L. 2001a. Mapping biophysical parameters with modeled and inverted functions from directional satellite measurements. In *Proceedings of the 23rd Canadian Symposium on Remote Sensing*, 21–24 August 2001, Québec City, Que. Canadian Aeronautics and Space Institute (CASI), Ottawa, Ont. pp. 407–414.

White, H.P., Miller, J.R., and Chen, J.M. 2001b. Four-Scale linear model for anisotropic reflectance (FLAIR) for plant canopies — Part I: Model description and partial validation. *IEEE Transactions on Geoscience and Remote Sensing*, Vol. 39, pp. 1072–1083.

White, H.P., Miller, J.R., and Chen, J.M. 2002. Four-Scale linear model for anisotropic reflectance (FLAIR) for plant canopies — Part II: Validation and inversion with CASI, POLDER, and PARABOLA data at BOREAS. *IEEE Transactions on Geoscience and Remote Sensing*, Vol. 40, pp. 1038–1046.

Widlowski, J.-L., Pinty, B., Godron, N., Verstraete, M.M., and Davis, B. 2001. Characterization of surface heterogeneity detected at the MIRS/TERRA subpixel scale. *Geophysical Research Letters*, Vol. 28, pp. 4639–4642.

Can. J. Remote Sensing, Vol. 31, No. 5, pp. 377–390, 2005

Spatiotemporal variations in land surface albedo across Canada from MODIS observations

Andrew Davidson and Shusen Wang

Abstract. A detailed knowledge of spatiotemporal variations in surface albedo is crucial if surface–atmosphere energy exchanges are to be accurately represented in climate models. Satellite observations can provide this information. This study uses moderate resolution imaging spectroradiometer (MODIS) data to investigate how summer and winter albedos, and the intra-annual variation in albedo, vary across the Canadian landscape. We show that (*i*) albedos generally decrease as one moves from grassland to broadleaved forest to needleleaved and mixed forest; (*ii*) the effects of snow on albedo vary among cover types; (*iii*) the largest intra-annual albedo variations occur over grasslands, cropland, and tundra; (*iv*) significant differences in albedo occur not only among broadleaved forest, needleleaf forest, grassland, and tundra, but also among their various canopy types (e.g., open versus closed canopies); and (*v*) land cover types sharing similar albedos in winter do not necessarily share similar albedos in summer. These trends are caused by differences in canopy structure and are supported to varying degrees by other in situ and remote sensing studies. These results suggest that the use of overly general land cover classes (e.g., needleleaved forest, grassland, tundra) in climate models will ignore important local-scale spatial variations in surface albedo.

Résumé. Une connaissance approfondie des variations spatio-temporelles de l'albédo de surface est essentielle si les échanges d'énergie surface-atmosphère doivent être représentés de façon précise dans les modèles climatiques. Les observations satellitaires peuvent fournir cette information. Cette étude utilise les données MODIS (« moderate resolution imaging spectroradiometer ») pour étudier comment l'albédo d'été et d'hiver ainsi que la variation interannuelle de l'albédo varient à travers le paysage canadien. Nous montrons (*i*) que l'albédo diminue généralement lorsque l'on passe de la prairie à la forêt de feuillus puis à la forêt conifèrienne et mixte, (*ii*) que les effets de la neige sur l'albédo varient selon les types de couvert, (*iii*) que les plus grandes variations interannuelles de l'albédo sont observées au-dessus des prairies, des terres en culture et de la toundra, (*iv*) que des différences significatives de l'albédo sont observées non seulement entre la forêt de feuillus, la forêt de conifères, la prairie et la toundra, mais également en fonction du type de couvert (i.e., couvert ouvert vs fermé), et (*v*) que les types de couvert partageant des valeurs similaires d'albédo durant l'hiver ne partagent pas nécessairement les mêmes valeurs d'albédo durant l'été. Ces tendances sont causées par des différences dans la structure du couvert et sont corroborées à divers degrés par d'autres études in situ ou de télédétection. Ces résultats suggèrent que l'utilisation de classes de couvert trop générales (i.e., forêt conifèrienne, prairie, toundra) dans les modèles climatiques ne permet pas de tenir compte des variations spatiales importantes de l'albédo de surface à l'échelle locale.
[Traduit par la Rédaction]

Introduction

Land surface albedo, the fraction of incident (shortwave) solar radiation reflected in all directions by the land surface, is one of the most important parameters influencing the earth's climate (Pinty and Verstraete, 1992). Surface albedo is important because it controls the amount of radiation absorbed by the ground and hence determines the amount of energy available for heating the lower atmosphere, evaporating water, and driving the ecosystem processes that regulate greenhouse gas exchange (Rowe, 1991; Wang et al., 2002). Changes in surface albedo, which can result from various natural or anthropogenic phenomena, can significantly alter these ground–atmosphere interactions. For example, simulation studies suggest that higher surface albedos resulting from deforestation can lead to negative radiation forcing (Hansen et al., 1998) and reductions in precipitation and evapotranspiration (Xue and Shukla, 1993; Hahmann and Dickinson, 1997). A detailed knowledge of spatiotemporal changes in albedo is crucial if the global radiation balance and its influence on climate are to be adequately understood (Henderson-Sellers and Wilson, 1983; Lucht et al., 2000b).

The central role that surface albedo plays in the physical climate system makes it a key component of general circulation models (GCMs). The accurate parameterization of albedo in GCMs is crucial because its mis-specification usually generates large errors in modelled radiation balances (Betts and Ball, 1997). Unfortunately, however, surface albedo remains one of

Received 15 March 2005. Accepted 24 June 2005.

A. Davidson.[1] Noetix Research Inc., 265 Carling Avenue, Suite 403, Ottawa, ON K2S 2E1, Canada.

S. Wang. Environmental Monitoring Section, Applications Division, Canada Centre for Remote Sensing, 588 Booth Street, Ottawa, ON K1A 0Y7, Canada.

[1]Corresponding author. Present address: Canada and Environmental Monitoring Section, Applications Division, Canada Centre for Remote Sensing, 588 Booth Street, Ottawa, ON K1A 0Y7, Canada (e-mail: Andrew.Davidson@CCRS.NRCan.gc.ca

the largest radiative uncertainties associated with modelling attempts (Liang, 2002). GCMs generally represent albedo in one of two ways. The first (and more traditional) approach is to represent albedo as a prescribed surface, where in situ observations are used to estimate the "typical" albedos of classes in a global land cover map (Li and Garand, 1994; Jin et al., 2003a). This approach is limited by its reliance on point-based field measurements, which are rarely dense enough to accurately characterize the grid- and subgrid-scale spatiotemporal variations in albedo that are required by models (Gu and Smith, 1997; Gu et al., 1997; Song, 1999; Liang, 2002; Davidson and Wang, 2004). The second approach is to represent albedo as a set of processes within the model itself (Jin et al., 2003a; Zhou et al., 2003). This approach is limited because surface albedo calculations within the model still require an accurate parameterization of the soil and vegetation system, and these have limited availability (Jin et al., 2003a). Clearly, more reliable methods are needed to estimate surface albedo over large areas (Song and Gao, 1999).

Data from earth observation satellites can be used to improve the representation of surface albedo in models. The remote sensing approach is appealing for two main reasons. First, it is the only practical way to repeatedly map global land surface albedo at a spatial resolution adequate for climate modelling (Lucht et al., 2000b). Second, it can provide albedo datasets that are free of many of the uncertainties traditionally associated with prescribed and simulated data. The remote sensing approach has the potential to provide detailed information on how landscape albedo varies through space and time. This information can then be used to either improve the accuracy of prescribed albedo surfaces and albedo parameterizations in models or validate model-generated albedo values. To date, a number of satellite-borne sensors have been used to create fine-resolution (<20 km) albedo maps of the earth's surface. These include, but are not limited to the following: advanced very high resolution radiometer (AVHRR), Landsat-7 enhanced thematic mapper plus (ETM+), geostationary operational environmental satellite (GOES), multiangle imaging spectroradiometer (MISR), moderate resolution imaging spectroradiometer (MODIS), polarization and directionality of the earth's reflectances (POLDER), and Systeme pour l'observation de la terre – Vegetation (SPOT-VGT) (Liang, 2002). The publicly available MODIS albedo product (Schaaf et al., 2002) is particularly promising for use in climate models because it is the first to provide repeated coverage of the entire globe at a spatial resolution of 1 km (Jin et al., 2003b).

In this study, we use MODIS albedo data to describe and analyze the surface albedo characteristics of the dominant Canadian land cover types, and then use these results to identify the cover types whose albedos are most similar and those whose albedos are most different. More specifically, we ask the following questions: (1) How do summer and winter surface albedos, and the intra-annual variation in surface albedo, vary across the Canadian landscape? (2) How closely do these results compare with the findings of other studies? (3) Do land cover classes that share similar albedos in summer also share similar albedos in winter, and is this the same for classes whose albedos are significantly different? The information gained from answering these questions will provide a further understanding of how the surface albedo of Canada's landmass varies through space and time. This information is useful for a number of reasons. First, it may be used to identify the conditions (e.g., time of year, land cover type) under which GCM albedo model subcomponents need to be improved. Second, it may be used to identify where models can simplify or aggregate their land cover schemes without losing important information on the spatiotemporal characteristics of albedo. The aggregation of classes with similar albedo characteristics eliminates the need to explicitly parameterize the albedo of each land cover class, and the nonaggregation of classes with different albedo characteristics allows important interclass differences in surface albedos to be recognized.

Methods

Data sources

MODIS 16-day albedo data (MOD43B3)

The MODIS albedo product is generated from empirical and semiempirical models (Wanner et al., 1997; Schaaf et al., 2002). Every 16 days, multitemporal, atmospherically corrected, cloud-free data and a semiempirical kernel-driven bidirectional reflectance model are used to compute a global set of parameters describing the bidirectional reflectance distribution function (BRDF) of the land surface (Anonymous, 2003). These parameters are provided as a set of coefficients that describe the BRDF of each 1-km pixel in MODIS bands 1–7 (product MOD43B1). The MODIS albedo product (product MOD43B3) is generated by integrating the BRDF parameters over all viewing angles at local solar noon to produce black-sky (direct radiation) and white-sky (diffuse radiation) albedo datasets for each of these seven bands and for the visible, near-infrared, and total shortwave broadbands (0.3–0.7, 0.7–5.0, and 0.3–5.0 μm, respectively) (Schaaf et al., 2002). Broadband albedos are calculated using spectral-to-broadband conversion algorithms (Liang, 2000; 2002). The MODIS albedos represent the best quality data possible for each 16-day period (Zhou et al., 2003). Actual (blue-sky) albedos can be calculated from a linear combination of black- and white-sky albedos, depending on the fraction of diffuse sunlight (Anonymous, 2003). A detailed description of the MODIS albedo product, its creation, and validation is provided by Wanner et al. (1997), Lucht et al. (2000a), Schaaf et al. (2002), Jin et al. (2003a; 2003b), Zhou et al. (2003), and the *MODIS BRDF/albedo product (MOD43B3) user's guide* (Anonymous, 2003). MODIS albedo data can be freely downloaded from the US Geological Survey Land Processes Distributed Active Archive Center (LP-DAAC; available from http://edcimswww.cr.usgs.gov/pub/imswelcome/).

We acquired MODIS local noon black-sky albedo data (MOD43B3, validated version V004) for 2003 in the visible (α_{VIS}), near-infrared (α_{NIR}), and total shortwave (α_{TSW})

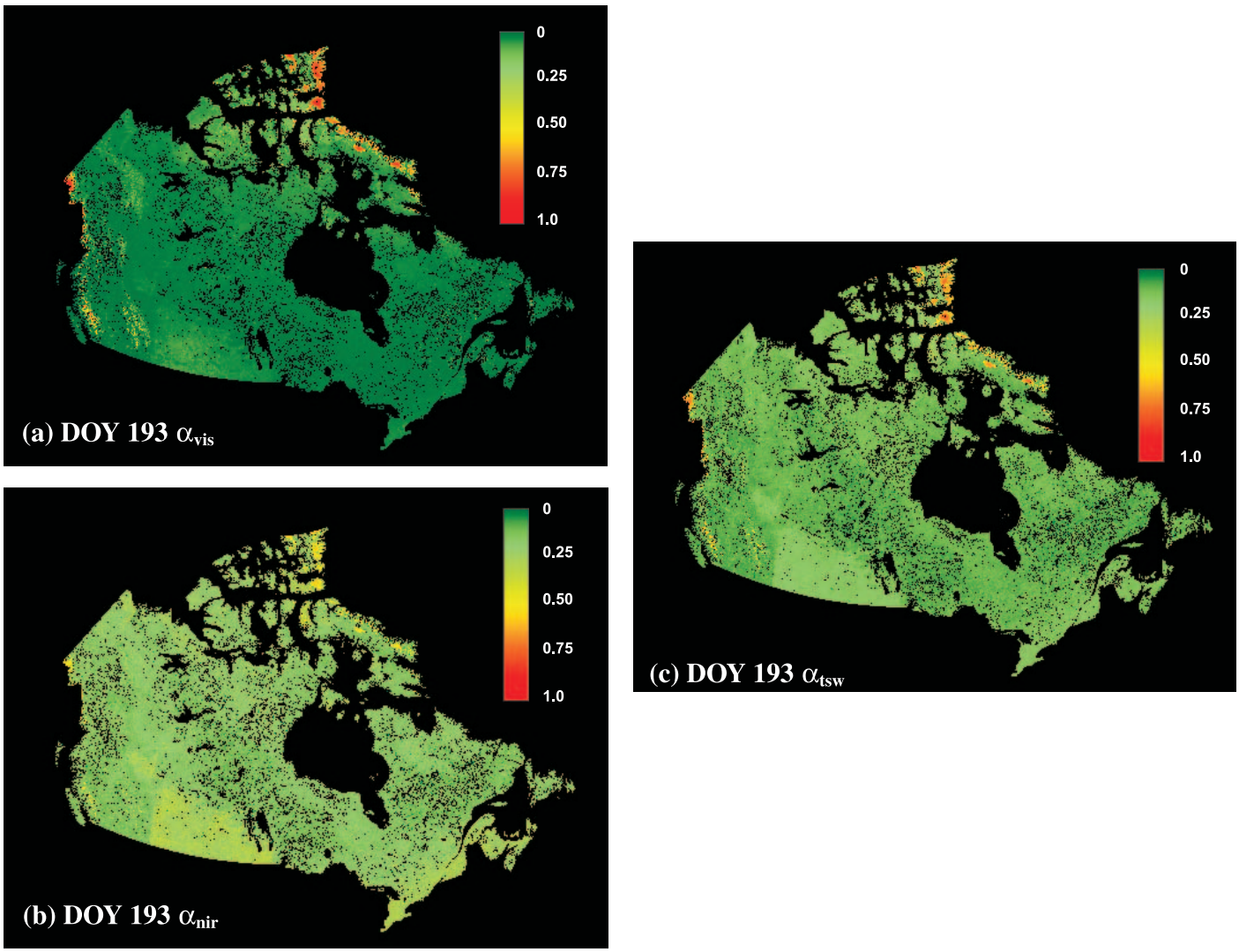

Figure 1. Visible (α_{vis}) and near-infrared (α_{nir}) black-sky albedos typical of summer 2003 (DOY 193).

wavelengths. Twenty-four tiles, each measuring approximately 1200 km × 1200 km, were mosaicked to create α_{VIS}, α_{NIR}, and α_{TSW} albedo composites of the entire Canadian landmass for each 16-day period using the MODIS reprojection tool (version 3.1, US Geological Survey, 2003). This tool was then used to project these composites to the Lambert conformal conic (LCC) projection, maintaining a spatial resolution of 1 km (see **Figure 1**). This approach provided 21 black-sky 16-day albedo composites for 2003 (days-of-year (DOY) 1, 17, 33, …, 353; data for DOY 321 and 337 were unavailable). We restrict our study to the analysis of black-sky albedo because noon-time albedo is dominated by the direct radiation component under clear sky conditions (see Wang et al., 2002). We also restrict our study to the analysis of the α_{VIS}, α_{NIR}, and α_{TSW} broadbands because they are most commonly used in climate models.

MODIS 8-day snow cover data (MOD10A2)

We used MODIS 8-day maximum snow extent data to identify periods of minimum and maximum snow cover during 2003. This dataset uses daily snow cover maps (product MOD10A1) to map maximum snow extent for 8-day periods (product MOD10A2). Pixels in these 8-day composites are classified as "snow covered" if they contained snow on 1 or more days during the 8-day period. A detailed description of the MODIS snow products, their creation, and their validation is provided by Hall et al. (1998; 2002a; 2002b) and Riggs et al. (2003). MODIS snow extent data can also be freely downloaded from the US Geological Survey LP-DAAC (see previous section).

We acquired MODIS 8-day maximum snow extent data for 2003 (MOD10A2, validated version V003). Data were mosaicked to create snow extent composites of the entire Canadian landmass for each 8-day period using the MODIS reprojection tool. This tool was then used to project the composites to the LCC projection, maintaining a spatial resolution of 500 m. We then combined consecutive composites to create snow extent maps for each of the 16-day MODIS albedo collection periods described previously.

Table 1. The land cover classes used in this study and their areal coverage (as a percentage of total Canadian landmass) as calculated separately for all pixels belonging to each class and for all water-free pixels (water fraction = 0) belonging to each class.

Land cover class	Land cover type	All pixels		Water-free pixels	
		No. of pixels	% of Canadian landmass	No. of pixels	% of Canadian landmass
1	Broadleaved deciduous forest (closed canopy)	229 694	2.9	146 520	1.9
2	Needleleaved evergreen forest (closed canopy)	1 031 226	13.2	576 803	7.4
3	Needleleaved evergreen forest (open canopy)	938 678	12.0	644 280	8.2
4	Needleleaved mixed forest (closed canopy)	274 136	3.5	175 464	2.2
5	Mixed broadleaved or needleleaved forest (closed canopy)	355 195	4.5	250 792	3.2
6	Needleleaved evergreen forest, lichen understory (open canopy)	427 572	5.5	250 620	3.2
7	Needleleaved evergreen shrubland (open canopy)	874 203	11.2	531 029	6.8
8	Temperate or subpolar grassland with sparse tree layer	462 030	5.9	236 211	3.0
9	Polar grassland with a sparse shrub layer	1 717 553	21.9	897 874	11.5
10	Polar grassland with a dwarf-sparse shrub layer	395 531	5.1	244 859	3.1
11	Temperate grassland	396 345	5.1	154 480	2.0
12	Cropland	211 413	2.7	158 799	2.0
13	Consolidated rock sparse vegetation	425 201	5.4	377 301	4.8
14	Snow and ice	101 144	1.3	57 499	0.8

Land cover data

We used the digital land cover map of North America 2000 (Latifovic et al., 2004) to map the spatial distribution of land cover types across the Canadian landmass. We used GEOMATICA software version 9.0 (PCI Geomatics Enterprises Inc., 2003) to project this dataset to the LCC projection, maintaining a spatial resolution of 1 km. We split the *temperate and subpolar grassland* cover type into separate *temperate grassland* and *subpolar grassland* classes. We then identified the land cover classes that covered >1% of the Canadian landmass. Fourteen cover types were identified (**Table 1**), the most dominant of which were (*i*) *polar grassland with a dwarf-sparse shrub layer*, (*ii*) *needleleaved evergreen forest (closed canopy)*, (*iii*) *needleleaved evergreen forest (open canopy)*, and (*iv*) *polar grassland with a sparse shrub layer*. We only consider these 14 land cover classes in this study.

Canada-wide water fraction data

We used the Canada-wide water fraction map (Fernandes et al., 2001) to identify the albedo observations that were collected from water-free pixels (see next section). This map was provided in the LCC map projection and at a spatial resolution of 1 km. Water fraction represents the fraction of area within each 1-km grid cell over Canada's land mass covered by water bodies, as mapped within the National Topographic Database (NTDB) version 3.1. This map can be downloaded directly from the Natural Resources Canada spatial data archive (GEOGRATIS; available from http://geogratis.cgdi.gc.ca/download/WaterFraction/).

Data analysis

We imported the albedo, snow extent, land cover, and water fraction datasets into a geographical information system (GIS) database (Geographical Resources Analysis Support System (GRASS), version 5.0, 2003). The albedo, land cover, and water fraction datasets were at a spatial resolution of 1 km. The snow extent maps were at a spatial resolution of 500 m. The use of a common map projection (LCC) allowed us to analyze spatiotemporal patterns in surface albedo using simple GIS overlay procedures.

First, we identified 16-day albedo composites that could be used to represent the "typical" spatial distribution of α_{VIS}, α_{NIR}, and α_{TSW} in summer and winter. We chose the time of year when snow extent was at a minimum to characterize summer albedos and the time of year when snow extent was at a maximum to characterize winter albedos. We identified the 16-day period starting 12 July 2003 (DOY 193) as the period when snow cover was at a minimum, and the 16-day period starting 18 February 2003 (DOY 49) as the period when snow cover was at a maximum. The α_{VIS} and α_{NIR} values from the DOY 193 composite were similar to those of other summer composites (e.g., 28 July (DOY 209) and 13 August (DOY 225)). The α_{VIS}, α_{NIR}, and α_{TSW} values from the DOY 49 composite were similar to those of other winter composites (e.g., 6 March 2003 (DOY 65)). To create as comprehensive a winter dataset as possible, we replaced missing albedo values in the DOY 49 albedo composite with values from the DOY 65 composite.

Second, we assessed how summer and winter surface albedos, and the intra-annual variation in surface albedo, varied across the Canadian landscape. We achieved this by writing and implementing various algorithms within the GIS. The output of these algorithms was (*i*) the mean summer and winter α_{VIS}, α_{NIR}, and α_{TSW} (and their associated standard deviations) for each of the 14 land cover types used in this study; and (*ii*) maps showing the intra-annual variability in α_{VIS}, α_{NIR}, and α_{TSW}. These maps were created by calculating the standard deviations in broadband albedos on a per-pixel basis using the 21 available α_{VIS}, α_{NIR}, and α_{TSW} composites for 2003. To eliminate the

potentially confounding effects of water on cover–albedo relationships, our analysis was limited to albedo observations from pixels that were completely water-free (i.e., where water fraction = 0%).

Third, we identified the land cover classes whose albedos were statistically similar and those whose albedos were significantly different. We tested the effects of land cover class on surface albedo using single-factor analysis of variance (ANOVA). Land cover class was treated as a fixed factor. We conducted six ANOVAs in total. These corresponded to the effects of land cover on (*i*) summer α_{VIS}, (*ii*) summer α_{NIR}, (*iii*) summer α_{TSW}, (*iv*) winter α_{VIS}, (*v*) winter α_{NIR}, and (*vi*) winter α_{TSW}. Each ANOVA was calculated using a total of 7.7 million albedo observations (55 000 randomly selected water-free observations from each of the 14 cover classes used in the study). We did not transform our data prior to ANOVA because the *F* statistic is robust to violations of the assumptions of normality and homogeneous variance as long as sample sizes are equal and sufficiently large (Srivastava, 1959; Glass et al., 1972). Where a significant effect of land cover class was detected, Tukey's pairwise comparisons were used to contrast mean values for significant differences. All ANOVAs and pairwise comparisons were conducted using the Origin statistical package, version 7.5 (OriginLab Incorporated, Northampton, Mass.), and $p < 0.05$ was used to determine significance in all tests.

Results

Spatial variations in summer and winter albedos

The spatial variations in summer α_{VIS}, α_{NIR}, and α_{TSW} are shown in **Figure 1**. The means and standard deviations of these broadbands for each land cover class are illustrated in **Figure 2** and **Table 2**. **Figures 1a** and **2a** and **Table 2** show that the summer α_{VIS} across Canada is generally low ($\alpha_{VIS} < 0.06$). Although low α_{VIS} values are typical of most cover types, they mostly correspond to the forested vegetation classes ($\alpha_{VIS} < 0.03$) (**Figure 2a**). Higher α_{VIS} values are restricted to temperate grassland (mean $\alpha_{VIS} = 0.062$), polar grassland with a dwarf-shrub layer (mean $\alpha_{VIS} = 0.072$), rock and sparse vegetation (mean $\alpha_{VIS} = 0.075$), and areas containing snow and ice (mean $\alpha_{VIS} = 0.350$). High α_{VIS} values caused by snow and ice cover are particularly evident in the Canadian High Arctic and in the Rocky and Coast mountains of British Columbia. **Figures 1b** and **2b** show that summer α_{NIR} values are higher than α_{VIS} for vegetated regions. The highest summer α_{NIR} values occur in parts of the Canadian far north ($\alpha_{NIR} > 0.50$), the croplands and grasslands of the prairie provinces, and the croplands of southern Ontario, Quebec, New Brunswick, Prince Edward Island, and Nova Scotia ($\alpha_{NIR} > 0.20$). The summer α_{NIR} values of croplands (mean $\alpha_{NIR} = 0.275$) and grasslands (mean $\alpha_{NIR} = 0.263$) are very similar (**Figure 2b**). **Figures 1c** and **2c** show that summer α_{TSW} falls somewhere between the α_{VIS} and α_{NIR} values. The highest summer α_{TSW} values occur in grassland (mean $\alpha_{TSW} = 0.165$), cropland (mean $\alpha_{TSW} = 0.161$), and regions of snow and ice (mean $\alpha_{TSW} = 0.319$).

The spatial variations in winter α_{VIS}, α_{NIR}, and α_{TSW} are shown in **Figure 3**. The means and standard deviations of these broadbands for each land cover class are illustrated in **Figure 4** and **Table 2**. **Figures 3a**, **4a**, and **Table 2** show that the lowest winter α_{VIS} mostly corresponds to the forested vegetation classes ($\alpha_{VIS} < 0.40$), and particularly the forests along the coast of the British Columbia mainland, Vancouver Island, and the Queen Charlotte Islands. In comparison, the winter visible albedos of cropland (mean $\alpha_{VIS} = 0.778$), grassland (mean $\alpha_{VIS} = 0.829$), and northern cover types (mean $\alpha_{VIS} > 0.750$) are higher. Indeed, the ranges in α_{VIS} for cropland, temperate and polar grassland, and snow and ice overlap considerably (**Figure 4a**). **Figures 3b** and **4b** show that winter α_{NIR} values are generally lower than α_{VIS}. The lowest winter α_{NIR} values occur for closed-canopy needleleaved evergreen forest and closed-canopy needleleaved mixed forest (mean $\alpha_{NIR} \approx 0.25$). The highest winter α_{NIR} values occur over subpolar and polar grasslands, temperate grassland, croplands, and snow and ice (mean $\alpha_{NIR} > 0.50$). **Figures 3c** and **4c** show that winter α_{TSW} falls somewhere between α_{VIS} and α_{NIR} albedo values. The highest winter α_{TSW} values occur for the grassland cover types (mean $\alpha_{TSW} > 0.670$), cropland (mean $\alpha_{TSW} = 0.662$), and snow and ice (mean $\alpha_{TSW} = 0.648$). The lowest winter α_{TSW} is found over closed-canopy needleleaved evergreen forest and closed-canopy needleleaved mixed forest (mean $\alpha_{TSW} < 0.250$).

Table 3 illustrates the effects of land cover type on summer and winter surface albedos. Empty white cells show where significant differences in summer albedo exist between pairs of land cover types. Empty grey cells show where significant differences in winter albedo exist between pairs of land cover types. Non-empty cells indicate where nonsignificant differences in mean α_{VIS} (V), α_{NIR} (N), and α_{TSW} (T) occur.

Table 3 shows that the summer α_{VIS} of *broadleaved deciduous forest (closed canopy)*; *needleleaved evergreen forest (open canopy)*; *mixed broadleaved or needleleaved forest (closed canopy)*; and *needleleaved evergreen forest, lichen understory (open canopy)*; and between *needleleaved evergreen forest (closed canopy)* and *needleleaved mixed forest (closed canopy)* are statistically similar. Similarities in summer α_{VIS} also occur between *needleleaved evergreen forest, lichen understory (open canopy)* and *needleleaved evergreen shrubland (open canopy)*, between *polar grassland with a sparse shrub layer* and *cropland*, and between *polar grassland with a dwarf-sparse shrub layer* and consolidated rock sparse vegetation. Fewer similarities occur among the summer α_{NIR} and α_{TSW} values of cover types. Nonsignificant differences in α_{NIR} only occur among *needleleaved evergreen shrubland (open canopy)*, *temperate or subpolar grassland with sparse tree layer*, and *polar grasslandwith a dwarf-sparse shrub layer.* Nonsignificant differences in α_{TSW} occur only between *broadleaved deciduous forest (closed canopy)* and *needleleaved evergreen forest (open canopy)*, and between *polar grassland with a sparse shrub layer* and *cropland.*

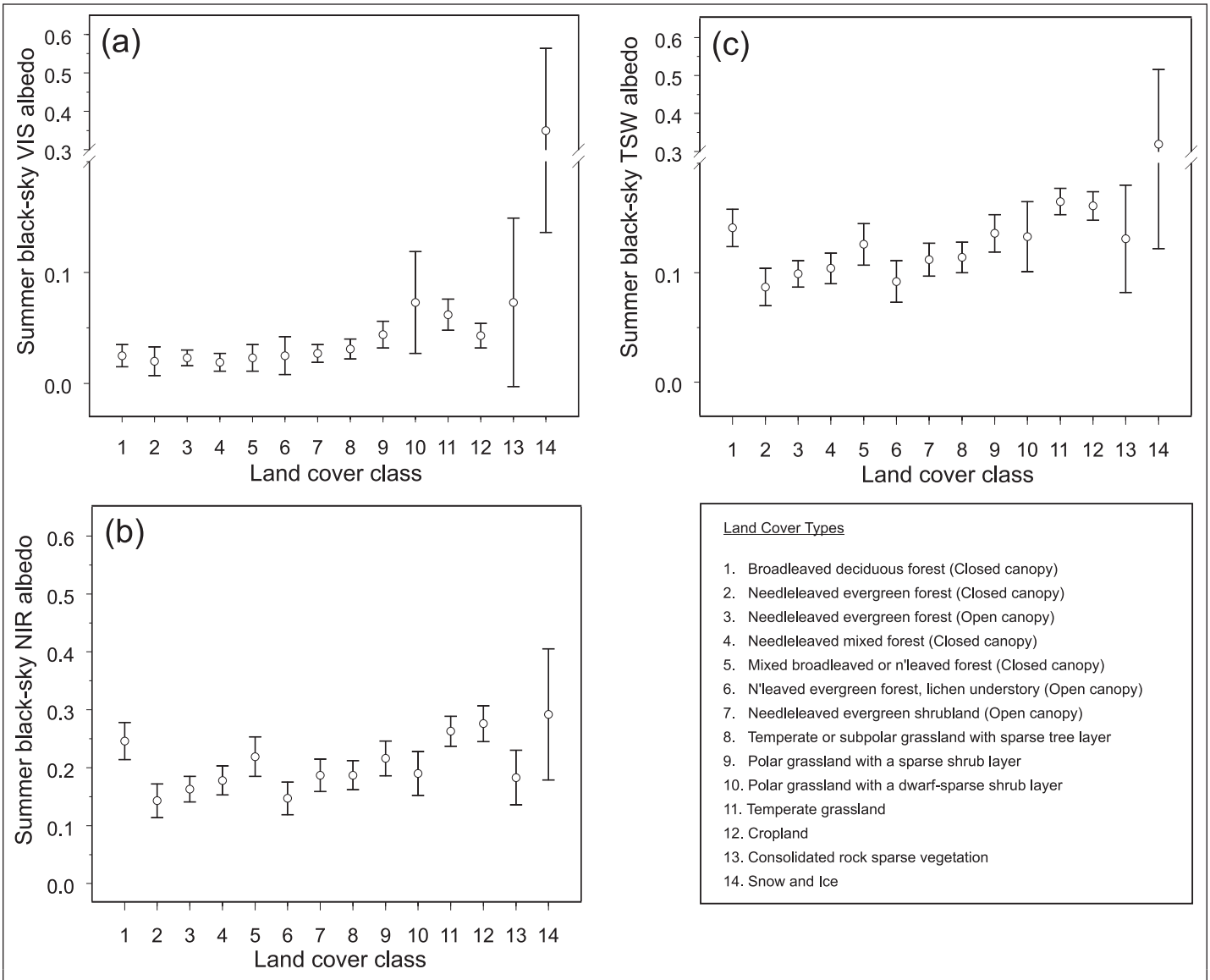

Figure 2. Means and standard deviations of MODIS-derived visible (a), NIR (b), and TSW (c) albedos for each of the most dominant Canadian land cover classes (derived from the Canada Land Cover Map 2000) for DOY 193 (2003) (Latifovic et al., 2004). The means and standard deviations associated with these plots are presented in **Table 2**.

Table 3 also shows that the winter α_{VIS}, α_{NIR}, and α_{TSW} values of land cover types are more spectrally separable compared with the summer values. In winter, nonsignificant differences in α_{VIS} occur between *broadleaved deciduous forest (closed canopy)* and *needleleaved evergreen forest, lichen understory (open-canopy)*; between *temperate or subpolar grasslandwith sparse tree layer* and *sparse vegetation*; and between *polar grasslandwith a sparse shrub layer* and *snow and ice*. Nonsignificant differences in α_{NIR} occur between *broadleaved deciduous forest (closed canopy)* and *needleleaved evergreen forest (open canopy)*, between *needleleaved evergreen forest (closed canopy)* and *needleleaved mixed forest (closed canopy)*, and between *polar grasslandwith a sparse shrub layer* and *cropland*. Nonsignificant differences in α_{TSW} occur between *temperate or subpolar grasslandwith sparse tree layer* and *consolidated rock sparse vegetation* and between *broadleaved deciduous forest (closed canopy)* and *needleleaved evergreen forest, lichen understory (open canopy)*.

Intra-annual variations in albedo

We used the 21 available MODIS composites to map the per-pixel intra-annual standard deviation in visible (σ_{VIS}), near-infrared (σ_{NIR}), and total shortwave (σ_{TSW}) surface albedos. In locations where pixel albedos were unavailable, such as parts of the Canadian north in January and February, standard deviations were calculated using fewer observations (**Figure 5a**). The σ_{VIS}, σ_{NIR}, and σ_{TSW} values are shown in **Figures 5b**, **5c**, and **5d**, respectively. **Figure 5b** shows that σ_{VIS} is lowest over forested cover types ($\sigma_{VIS} < 0.1$) and highest in the subarctic and arctic grasslands of Nunavut and the Northwest Territories ($\sigma_{VIS} > 0.4$). The σ_{VIS} of prairie grassland

Table 2. The effects of land cover type on summer and winter surface albedos in the visible (VIS), near-infrared (NIR), and total shortwave (TSW) wavelengths.

Land cover class	Summer						Winter					
	VIS		NIR		TSW		VIS		NIR		TSW	
	Mean	SD	Mean	SD	Mean	SD	Mean	SD	Mean	SD	Mean	SD
1	0.025	0.010	0.246	0.032	0.1416	0.017	0.388	0.171	0.327	0.096	0.359	0.130
2	0.020	0.013	0.143	0.029	0.0880	0.018	0.234	0.165	0.241	0.096	0.241	0.125
3	0.023	0.007	0.163	0.022	0.0991	0.013	0.379	0.188	0.323	0.112	0.352	0.145
4	0.019	0.008	0.178	0.025	0.1050	0.014	0.214	0.123	0.237	0.072	0.229	0.093
5	0.023	0.012	0.219	0.034	0.1269	0.019	0.276	0.134	0.274	0.076	0.278	0.101
6	0.025	0.017	0.147	0.028	0.0928	0.019	0.384	0.200	0.302	0.125	0.345	0.158
7	0.027	0.008	0.187	0.028	0.1126	0.016	0.470	0.191	0.373	0.116	0.421	0.147
8	0.031	0.009	0.187	0.025	0.1150	0.015	0.581	0.167	0.430	0.110	0.503	0.133
9	0.044	0.012	0.216	0.030	0.1368	0.017	0.807	0.143	0.549	0.118	0.672	0.125
10	0.073	0.046	0.190	0.038	0.1339	0.033	0.840	0.127	0.544	0.119	0.682	0.118
11	0.062	0.014	0.263	0.026	0.1652	0.012	0.829	0.144	0.582	0.084	0.706	0.119
12	0.043	0.011	0.276	0.031	0.1612	0.014	0.778	0.164	0.549	0.107	0.662	0.135
13	0.073	0.076	0.183	0.047	0.1316	0.050	0.584	0.233	0.418	0.164	0.494	0.191
14	0.350	0.288	0.292	0.113	0.3198	0.197	0.812	0.127	0.514	0.139	0.649	0.123

Note: Albedos are presented as their seasonal means and the standard deviations (SD) associated with observations used to calculate these means. These means and standard deviations correspond to those displayed graphically in **Figures 2** and **4**. The numbering of land cover classes in the tables follows that given in **Figures 2** and **4**.

and the forest–tundra transition zone lies between these two extremes ($0.3 < \sigma_{VIS} < 0.4$). The forest–tundra transition zone, identified as a thin yellow band stretching in a northwesterly direction from James Bay (**Figure 5b**), is a highly fragmented mosaic of subpolar grassland, shrubland, needleleaved forest, and burned land. This patchwork of cover types gives rise to a region whose σ_{VIS} is greater than that of boreal forest but less than that of subarctic grassland. **Figures 5c** and **5d** show that the α_{NIR} and σ_{TSW} values of forested vegetation types are similar to those described earlier for the visible broadband. These similarities do not extend to the other cover types, such as prairie or northern cover types, however, whose σ_{NIR} and σ_{TSW} values are less than their corresponding σ_{VIS} values.

Discussion

Variations in summer and winter surface albedo

Patterns of albedo among cover types

Figures 2 and **4** and **Table 2** highlight three important trends: (*i*) the mean albedos of cropland and grassland are higher than those of broadleaved forest that, in turn, are generally higher than those of needleleaved and mixed forests; (*ii*) the trend noted in (*i*) occurs during both summer and winter; and (*iii*) the effects of snow on surface albedo differ considerably among cover types. Although these trends are generally consistent with other in situ and remote sensing measurements (e.g., Betts and Ball, 1997; Sharrat, 1998; Baldocchi et al., 2000; Strugnell et al., 2001; Davidson and Wang, 2004), differences in spatial resolution (e.g., in situ (<100 m) versus remote sensing (≥1 km)), spectral resolution (e.g., MODIS α_{TSW} (wavelength $\lambda = 0.3–5.0\,\mu m$) versus GOES α_{TSW} ($\lambda = 0.3–3.0\,\mu m$)), and "sky type" (e.g., black-sky albedo versus blue-sky albedo) mean that the results of these studies are not strictly comparable. Independent observations are invaluable, however, because they provide information on the dynamics of land surface albedo from a variety of perspectives. Hence, with the aforementioned limitations in mind, here we compare the patterns of albedo among cover types (this section) and the actual albedo values of each cover type (next section) with the albedos reported in other studies.

The previously described patterns of α_{VIS} and α_{TSW} among grassland, broadleaved forest, and needleleaved forest (**Figures 2a**, **2c**, **4a**, **4c**; **Table 2**) are generally supported by the results of other studies. GOES-8 α_{VIS} ($\lambda = 0.4–0.7\,\mu m$) and α_{TSW} ($\lambda = 0.3–3.0\,\mu m$) observations collected over the Canadian boreal region (blue-sky albedo, 4-km spatial resolution; see Gu and Smith, 1997; Gu et al., 1999) follow trends similar to those described previously for both summer and winter (Davidson and Wang, 2004; unpublished data). The observed mean α_{TSW} values of grassland, broadleaved forest, and needleleaved forest are further supported by the in situ studies of Sellers et al. (1995), Betts and Ball (1997), and Davidson and Wang (2004), who used tower-based observations (blue-sky albedos; ~100 m spatial resolution) to describe the α_{TSW} characteristics of cover types over snow-free and snow-covered surfaces. We are unable to evaluate the observed trends in mean summer and winter α_{NIR} values because we were unable to locate independent albedo observations in this wavelength.

The differences in the summer and winter albedos of grassland, broadleaved forest, and needleleaved forest canopies are caused by differences in horizontal heterogeneity, leaf orientation, clumping of needles and leaves, and total biomass. As a result, the albedos of grassland are considerably higher than those of forest canopies, and the albedos of broadleaved forest are considerably higher than those of needleleaved forest. The effects of canopy structure on surface albedo are

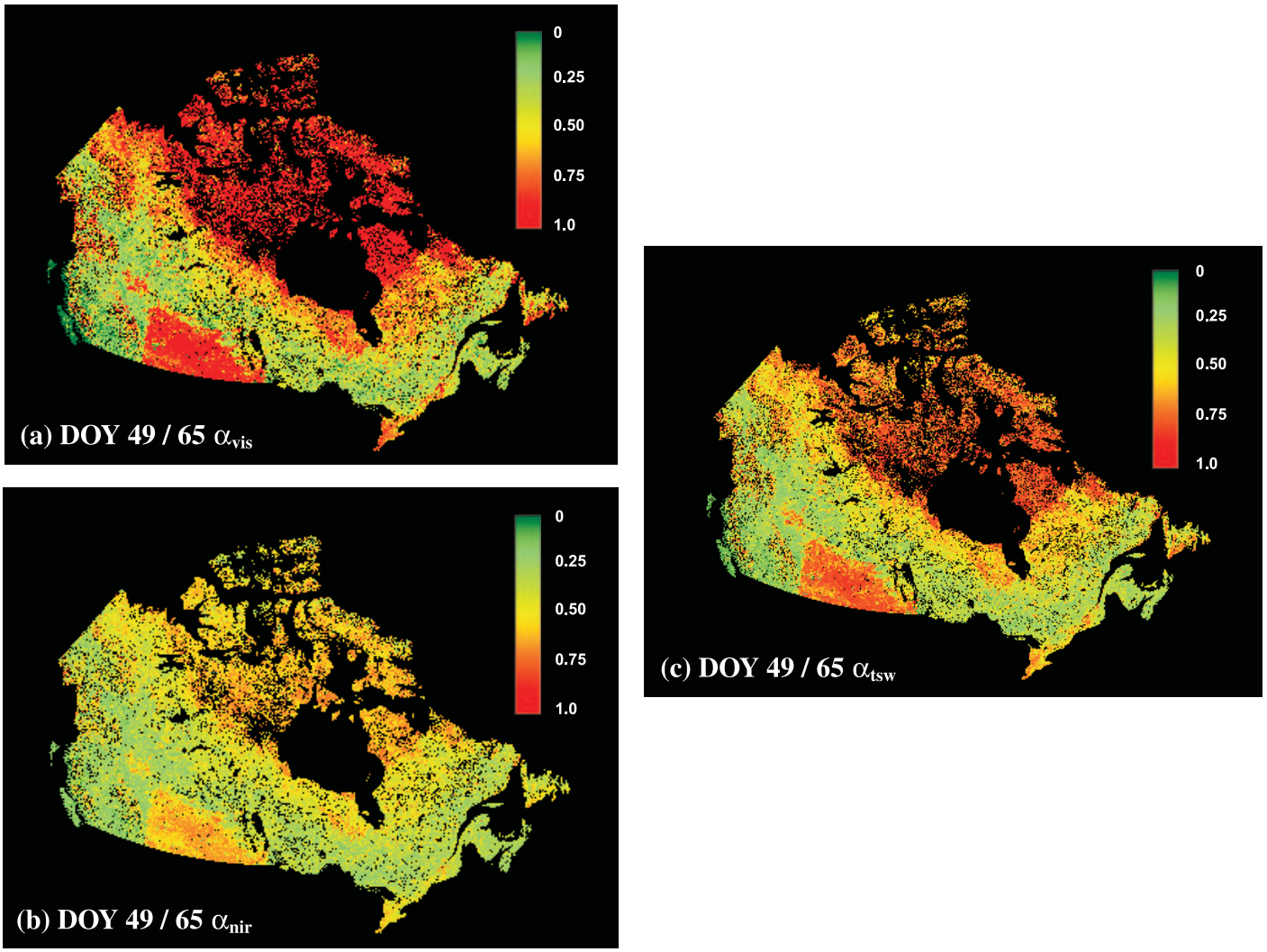

Figure 3. Visible (α_{vis}) and near-infrared (α_{nir}) black-sky albedos typical of winter 2003 (DOYs 49 and 65).

described in detail elsewhere (e.g., Dickinson, 1983) and are not discussed further here.

The variable effects of snow on the surface albedos of cover types are also supported by the results of other studies. Betts and Ball (1997), Sharrat (1998), Baldocchi et al. (2000), and Davidson and Wang (2004) all showed that snow-related increases in albedo are largest over grassland canopies and least over dense (closed-canopy) needleleaved and mixed forest canopies. These studies agree to a much lesser degree on the magnitudes of these increases (see next section), however. The varying effects of snow on surface albedo illustrate the large impact that canopy shading has on winter albedo values (Betts and Ball, 1997). The relatively short plant forms found in croplands and grasslands mean that even small snowfalls can produce highly reflective surfaces. In comparison, tree canopies protrude through snow cover, and cast shadow on it, thereby reducing the overall effects of snow presence on albedo (Baldocchi et al., 2000; Eugster et al., 2000). Canopy shadowing is the dominant mechanism controlling the influence of snow cover on surface albedo in the boreal ecozone because the snow that is intercepted by the forest canopy is quickly removed by wind (Pomeroy et al., 1998; Gamon et al., 2004).

Albedo values of cover types

The mean MODIS summer α_{VIS} values of broadleaved forest, needleleaved forest, and grassland (**Figures 1a**, **2a**; **Table 2**) are all lower than values obtained over the Canadian boreal region from the GOES-8 satellite (4 km spatial resolution; λ = 0.4–0.7 µm; Davidson and Wang, 2004; unpublished data). This disparity is largest for broadleaved and needleleaved forests, whose mean α_{VIS} is approximately one half of those calculated using GOES-8 data (GOES α_{VIS} = 0.052 ± 0.008 and α_{VIS} =0.040 ± 0.006, respectively), and least for grassland, whose mean α_{VIS} is approximately 80% of those calculated using GOES-8 data (GOES α_{VIS} =0.076 ± 0.006). In comparison, there is generally a closer agreement between the mean winter α_{VIS} values of forest canopies (**Figures 3a**, **4a**; **Table 2**) and those obtained from GOES-8 observations. Indeed, the mean winter α_{VIS} values of broadleaved forest and closed-canopy needleleaved forest are relatively consistent with GOES-derived mean α_{VIS} values (broadleaved forest

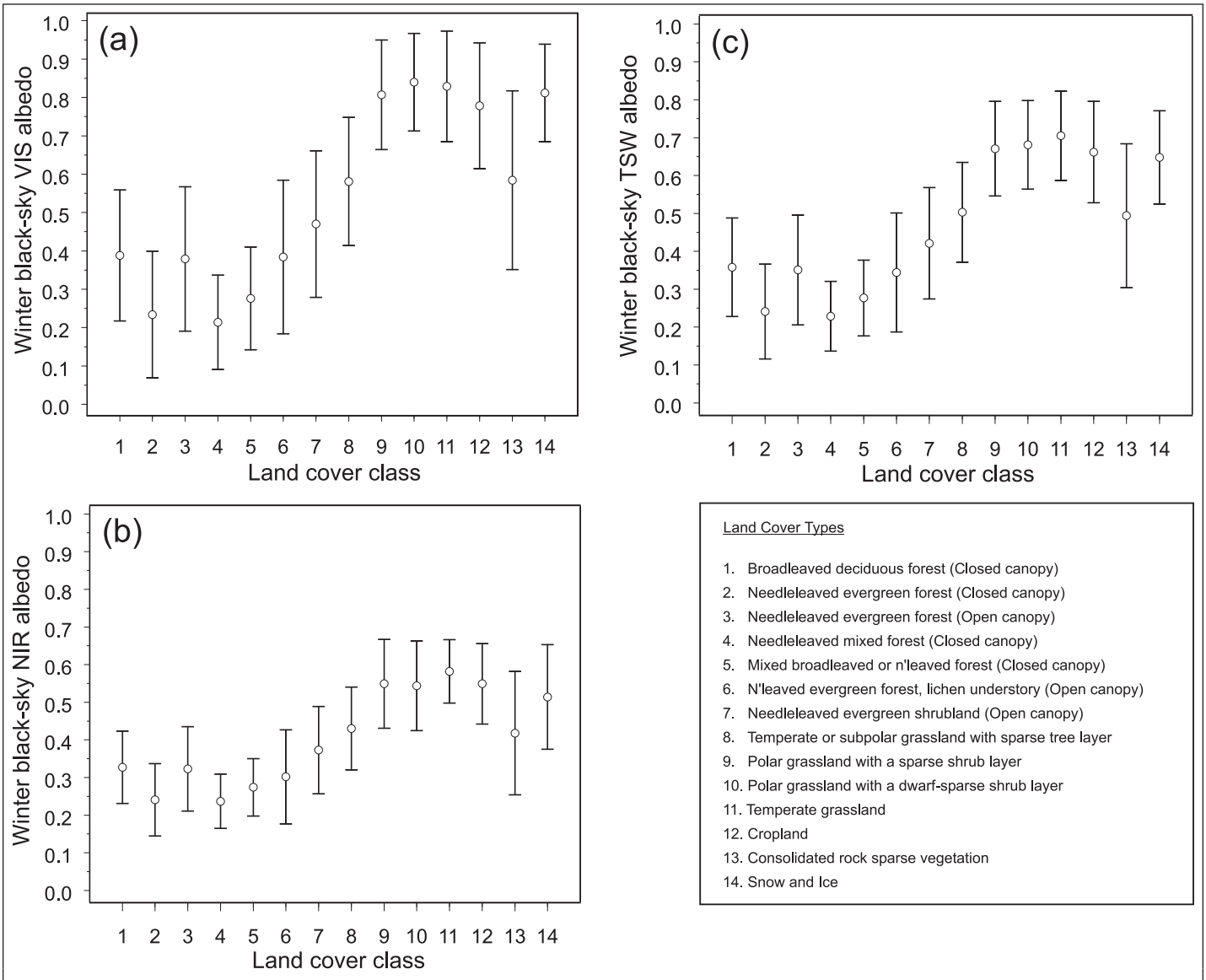

Figure 4. Means and standard deviations of MODIS-derived visible (a), NIR (b), and TSW (c) albedos for each of the most dominant Canadian land cover classes (derived from the Canada Land Cover Map 2000) for DOY 49 (and 65) (2003). The means and standard deviations associated with these plots are presented in **Table 2**.

(snow): $\alpha_{VIS} = 0.34 \pm 0.08$; high-density needleleaved forest (snow): $\alpha_{VIS} = 0.20 \pm 0.05$). It should be noted, however, that the standard deviations associated with the GOES-8 α_{VIS} observations are approximately half those associated with the MODIS-derived α_{VIS} observations. The mean α_{VIS} of grassland (and its associated standard deviation) in winter is approximately double that of the GOES-8 observations ($\alpha_{VIS} = 0.44 \pm 0.04$). Similar results were obtained when the previous comparisons were repeated using all pixels in the analysis (i.e., water fraction was not considered).

The mean MODIS summer α_{TSW} of broadleaved forest and its standard deviation are consistent with the in situ observations reported by Betts and Ball (1997) (aspen (in leaf, no snow): $\alpha_{TSW} = 0.156 \pm 0.013$) and Davidson and Wang (2004) (aspen (no snow): $\alpha_{TSW} = 0.140 \pm 0.010$). The mean summer α_{TSW} of needleleaved forest and its standard deviation are consistent with the in situ observations reported by Betts and Ball (Jack pine (no snow): $\alpha_{TSW} = 0.086 \pm 0.015$), Sharrat (1998) (spruce (summer): $\alpha_{TSW} = 0.080$), Baldocchi et al. (2000) (needleleaved forest (summer): $\alpha_{TSW} = 0.083$), and Davidson and Wang (Jack pine (no snow): $\alpha_{TSW} \approx 0.090 \pm 0.014$). The mean summer α_{TSW} of temperate grassland and its standard deviation are consistent with the in situ observations reported by Betts and Ball (grassland (no snow): $\alpha_{TSW} = 0.197$), Sharrat (grassland (summer): $\alpha_{TSW} \approx 0.200$), and Davidson and Wang (grassland (no snow): $\alpha_{TSW} \approx 0.210 \pm 0.018$). A close correspondence was also found between mean MODIS summer α_{TSW} values and the mean GOES-derived summer α_{TSW} values reported by Davidson and Wang (broadleaved forest (no snow): $\alpha_{TSW} = 0.130 \pm 0.030$; high- and medium-density needleleaved forest (no snow): $\alpha_{TSW} = 0.080 \pm 0.020$; grassland (no snow): $\alpha_{TSW} = 0.160 \pm 0.050$).

Table 3. Similarities and differences in albedos among land cover classes.

LAND COVER CLASS	1	2	3	4	5	6	7	8	9	10	11	12	13	14
1			N			V								
2				N										
3	V,T													
4		V												
5	V		V											
6	V		V		V									
7						V								
8							N						V,T	
9												N		V
10							N	N						
11														
12									V,T					
13										V				
14														

Forested types | Shrubland | Grassland types | Cropland | Non-vegetated

Note: Empty white cells show where *significant* differences exist between land cover types for summer VIS, NIR, and TSW albedos. Empty grey cells show where *significant* differences exist between land cover types for winter VIS, NIR, and TSW albedos. V, N, and T indicate where *nonsignificant* differences between classes were found for VIS, NIR, and TSW albedos, respectively. $P < 0.05$ was used to determine significance in all tests.

The standard deviations associated with the mean MODIS albedos were 50% (broadleaved forest) to 75% (grassland) smaller, however, than those associated with the GOES observations.

In comparison, the mean MODIS winter α_{TSW} values of forest canopies (**Figures 3c**, **4c**) are generally inconsistent with those reported by the aforementioned in situ studies but consistent with those reported by the aforementioned remote sensing studies. The mean MODIS winter α_{TSW} values of broadleaved and needleleaved forest types are considerably higher than the in situ observations reported by Betts and Ball (1997) (aspen (leafless, snow): $\alpha_{TSW} = 0.214 \pm 0.067$; Jack pine (snow): $\alpha_{TSW} = 0.150 \pm 0.035$), Baldocchi et al. (2000) (needleleaved (winter): $\alpha_{TSW} = 0.130$; Jack pine (winter): $0.120 \leq \alpha_{TSW} \leq 0.150$; spruce (winter): $\alpha_{TSW} = 0.110$), and Davidson and Wang (2004) (aspen (snow): $\alpha_{TSW} = 0.220 \pm 0.080$; Jack pine (snow): $\alpha_{TSW} \approx 0.180 \pm 0.130$). The standard deviations associated with the MODIS-derived means were generally higher than those derived from the in situ observations. There is a closer correspondence, however, between the mean winter α_{TSW} of forested cover types and the values of GOES-derived winter blue-sky α_{TSW} reported by Davidson and Wang. The mean MODIS winter α_{TSW} of broadleaved forest closely matches the GOES-8 α_{TSW} of broadleaved forest ($\alpha_{TSW} = 0.320 \pm 0.060$), and the mean winter α_{TSW} of closed-canopy needleleaved forest closely matches the mean GOES-8 α_{TSW} of medium- and high-density needleleaved forest ($\alpha_{TSW} = 0.250 \pm 0.060$ and 0.270 ± 0.070, respectively). It should be noted that in these cases, however, the standard deviations associated with the MODIS-derived albedo means are approximately double those associated with the mean GOES-8 albedo observations. The aforementioned trend is reversed for grasslands. Over grassland canopies, mean MODIS winter α_{TSW} is relatively similar to the in situ α_{TSW} reported by Davidson and Wang and Baldocchi et al. for snow-covered grassland (mean $\alpha_{TSW} \approx 0.750$), but approximately twice that calculated by Davidson and Wang from GOES-8 data ($\alpha_{TSW} = 0.440 \pm 0.040$). The standard deviation associated with the mean MODIS winter α_{TSW} is also almost four times higher than that calculated by Davidson and Wang. Similar results were obtained when the previous comparisons were repeated using all pixels in the analysis.

Unfortunately, a lack of available independent observations means that we are unable to assess the values of mean MODIS summer and winter α_{NIR} (**Figures 1b**, **2b**, **3b**, **4b**). To date, in situ and remotely sensed albedo studies have focused on the collection of albedo information in the visible and (or) total shortwave wavelengths (see earlier in the paper). Thus, we do not evaluate the relationships between cover type and α_{NIR} further here.

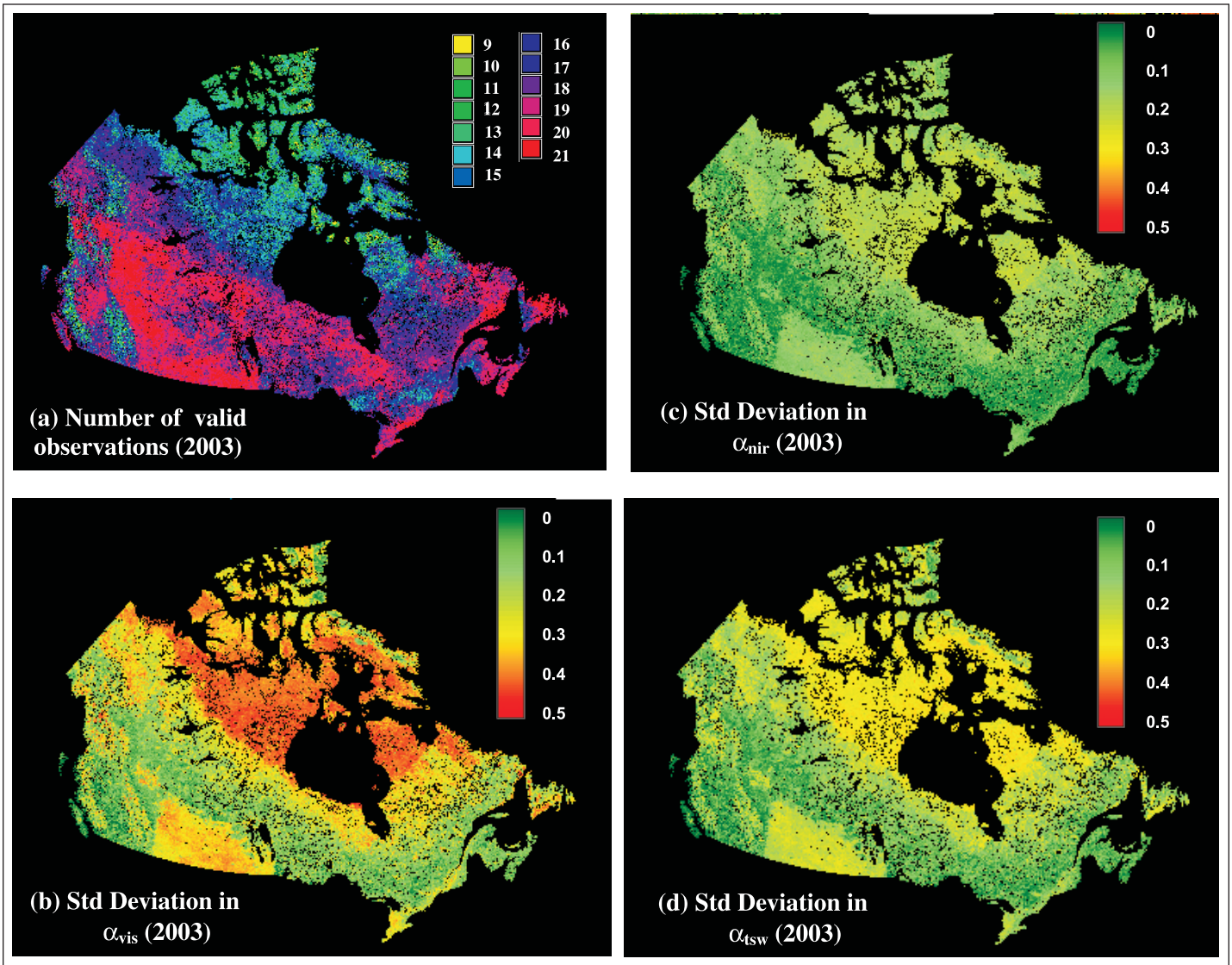

Figure 5. Standard deviation in annual albedos calculated from MODIS data.

Inconsistencies in the results given previously prompt us to further consider why the degree of correspondence between mean MODIS- and GOES-derived albedos appears to be independent of wavelength, land cover, and season. For example, MODIS-derived α_{VIS} observations correspond reasonably well to the GOES-8 α_{VIS} of forest canopies in winter, but not the GOES-8 α_{VIS} of grasslands in winter or the GOES-8 α_{VIS} of all cover types in summer. Furthermore, MODIS-derived α_{TSW} observations correspond reasonably well to the in situ and GOES-8 α_{TSW} of all cover types in summer and the in situ α_{TSW} of grassland and the GOES-8 α_{TSW} of forest in winter, but not the in situ α_{TSW} of forest or GOES-8 α_{TSW} of grassland in winter. We explain the observed consistencies and inconsistencies in our results as follows.

The close correspondence between MODIS and GOES-8 albedo observations over forest canopies in summer (for α_{TSW}) and winter (for α_{VIS} and α_{TSW}) is not surprising, since both albedo datasets were collected at relatively similar spatial and spectral resolutions, at similar times during the growing season, at the same time during the day and over large tracts of forest. As a result, these albedo observations not only were influenced by the same scale-dependent canopy-related properties, but also were able to capture the wide range in albedo values associated with needleleaved and broadleaved forest types.

The differences between MODIS and GOES-8 albedo observations over grassland canopies in summer (for α_{VIS}) and winter (for α_{VIS} and α_{TSW}) likely result from two main factors: (*i*) limitations in the GOES-8 albedo dataset used by Davidson and Wang (2004), and (*ii*) differences in grassland canopy conditions between the two datasets. The GOES-8 albedo dataset used by Davidson and Wang comprises albedo data collected over a portion of the Canadian boreal forest ecosystem during 1996. Less than 5% of this study area was covered by grassland, and much of this was interspersed with cropland. As a result, it is unlikely that sufficient GOES-8 observations were collected to reflect the actual ranges in albedo across the Canadian grassland ecosystem for either summer or winter. This actual range was more likely captured

by the prairie-wide observations of MODIS in 2003. Furthermore, grassland albedo has been shown to change more rapidly and more visibly with rainfall events than that of forested landscapes (Wang et al., 2004). As a result, natural interyear variations in factors controlling canopy development (e.g., rainfall and temperature) may cause the MODIS and GOES-8 summer α_{VIS} observations considered here to correspond to considerably different grassland canopy conditions. The differences in MODIS and GOES-8 winter α_{VIS} and α_{TSW} values are likely caused by natural interyear variations in snow cover.

The disparity between MODIS and GOES-8 α_{VIS} observations in summer is more difficult to explain. Our particular concern is the retrieval by MODIS of extremely low α_{VIS} values ($\alpha_{VIS} < 0.02$) from needleleaved and broadleaved forest landscapes across Canada. We have, however, discounted the possibility that low α_{VIS} values were caused by the effects of water bodies, which could lower the α_{VIS} of forest-dominated pixels, since the albedo–cover relationships presented here were calculated using pixels where water fractions equalled zero.

The general agreement between MODIS α_{TSW} observations and in situ measurements in summer, and the disparity between MODIS α_{TSW} observations and in situ measurements in winter, is consistent with the results of other studies. In a previous study (Davidson and Wang, 2004), we showed that weekly averaged in situ observations (100 m resolution) collected over grassland, broadleaved forest, mixed forest, and needleleaved forest corresponded closely to GOES-8 α_{TSW} observations over snow-free surfaces, but not over snow-covered surfaces. These differences were attributed to the scale-dependent influence of snow cover on shortwave albedo observations.

Intra-annual variations in albedo

Figure 5 shows that (*i*) the largest intra-annual variations in α_{VIS}, α_{NIR}, and α_{TSW} occur in the grasslands and croplands of the prairie provinces, the croplands of southwestern Ontario, and the subpolar and polar grasslands of the Canadian north; and (*ii*) these variations are greater for α_{VIS} than for α_{NIR} and α_{TSW}. These trends are generally consistent with the results of other studies.

Betts and Ball (1997), Sharrat (1998), Baldocchi et al. (2000), Chapin et al. (2000), Eugster et al. (2000), and Davidson and Wang (2004) all showed that the α_{TSW} of grassland and tundra is more variable than that of boreal forest. These results are caused by the differential effects that snow cover has on the winter albedos of these ecosystems and seasonal differences in canopy conditions. As mentioned previously, winter snow cover has a considerable influence on the albedos of grassland, tundra, and cropland because it masks the underlying vegetated surface, producing highly reflective surfaces even after smaller snowfalls. These high winter albedos and lower summer albedos give rise to the large intra-annual variability in albedo in these ecosystems. In comparison, snow cover has a smaller influence on the albedo of forested landscapes. This is because tree canopies protrude through snow cover, masking the surface and thereby reducing the overall effects of snow presence on albedo (Baldocchi et al., 2000; Eugster et al., 2000).

Grasslands, croplands, and tundra show large intra-annual variations in α_{VIS} because these canopies produce high α_{VIS} values in winter, but low α_{VIS} values in summer. In winter, snow cover dominates the ground surface, producing high α_{VIS} values ($\alpha_{VIS} > 0.80$) over these canopies. In summer, when canopies are in full leaf, most of the incident radiation in the visible part of the solar spectrum is absorbed by leaf chlorophyll, leading to low α_{VIS} values ($\alpha_{VIS} < 0.25$). In comparison, canopy α_{NIR} values are typically less than those of α_{VIS} in winter and higher than those of α_{VIS} in summer. This is because snow-covered surfaces typically reflect half as much near-infrared radiation as visible radiation (Dickinson, 1983) and because green vegetation reflects highly in the near-infrared part of the solar spectrum ($\alpha_{NIR} < 0.25$). This produces a smaller intra-annual variation in α_{NIR} compared with that in α_{VIS}. Intra-annual variations in α_{TSW} roughly correspond to the mean of α_{VIS} and α_{NIR} values for each vegetation type. This is because approximately half of incident solar energy is in the visible part of the solar spectrum, and the other half is in the near-infrared part of the solar spectrum.

Similarities and differences in albedos among land cover classes

Table 3 shows that (*i*) significant differences in mean albedo occur among most of the cover types considered in this study, (*ii*) land cover types sharing similar albedo characteristics in summer do not necessarily share similar albedo characteristics in winter, and (*iii*) these similarities generally occur between cover types that are dominated by similar plant forms (e.g., needleleaved and broadleaved forest; cropland and grassland).

These trends are relatively consistent with the results of our previous studies. A further analysis of the GOES-8 albedo data used by Davidson and Wang (2004) shows that the α_{TSW} values of broadleaved forest, needleleaved forest, and mixed forest are significantly different over snow-free and snow-covered surfaces, as are the α_{TSW} values of low-, medium-, and high-density needleleaved forest. These findings are consistent with **Table 3**, which shows that significant differences in α_{TSW} occur in winter and summer among broadleaved forest, needleleaved forest, and mixed forest and between closed- and open-canopy needleleaved forests. The discovery that the α_{TSW} of low-density needleleaved forest is significantly higher than those of medium- and high-density forest is important because this forest type covers a considerable portion of the Canadian boreal region. As a result, the failure of climate modellers to separately parameterize this cover type with a higher albedo than that typically used for needleleaved forest could lead to large errors in modelled energy balance across the boreal region.

It is important to note, however, that our results are spatial scale dependent. Chapin et al. (2000) used the results of several arctic studies to show that the summer α_{TSW} values of boreal forest and tundra were not statistically separable. Their study

was based on the assumption that the various cover types found within boreal forest (e.g., broadleaved forest, mixed forest, and needleleaved forest of varying densities) and tundra (e.g., grassland, grassland with sparse shrub layer, grassland with sparse tree layer) can be aggregated into two broad cover types whose α_{TSW} values are represented by a single value. Chapin et al. used their results to argue that the separate parameterization of boreal forest and tundra in climate models was unnecessary. Although we admit that the broad definition of forest, grassland, and tundra cover types would undoubtedly simplify the parameterization of surface albedo in climate models, and that cover type aggregation may not significantly affect modelled energy balances at a regional scale, we caution that it could lead to serious errors in modelled radiation balances across local scales. Future studies should assess the effects of land cover aggregations on the modelled radiation balance of the Canadian landmass.

Conclusions

The work presented here uses MODIS albedo data to investigate how summer and winter albedos, and the intra-annual variation in albedo, vary across the Canadian landscape. We have shown that (*i*) summer and winter albedos generally decrease as one moves from grassland to broadleaved forest to needleleaved and mixed forest; (*ii*) the effects of snow cover on albedo vary among land cover types; (*iii*) the largest intra-annual albedo variations occur over grasslands, cropland, and tundra; (*iv*) significant differences in albedo occur not only among broadleaved forest, needleleaf forest, grassland, and tundra, but also among their various canopy types (e.g., open versus closed canopies); and (*v*) land cover types sharing similar albedos in winter do not necessarily share similar albedos in summer. These trends are caused by the various canopy properties that influence within-canopy shadowing and are supported to varying degrees by other in situ and remote sensing studies. The differences in albedo among land cover types suggest that the use of overly general land cover classes in climate models will ignore important local-scale spatial variations in surface albedo, which could potentially lead to large errors in modelled energy balance across the Canadian landmass. From a modelling perspective, the value of the results presented here is threefold. First, they may be used to identify the conditions (e.g., time of year, land cover type) under which albedo model subcomponents need to be improved. Second, they may be used to identify where models can simplify or aggregate their land cover schemes without losing important information on the spatiotemporal characteristics of albedo. The aggregation of classes with similar albedo characteristics eliminates the need to explicitly parameterize the albedo of each land cover class, while the nonaggregation of classes with different albedo characteristics allows important interclass differences in surface albedos to be recognized. Third, they suggest that although the knowledge of land cover type is necessary to model land surface albedo in summer, it is less important in winter, where the effects of snow are dominant. The analysis herein is based on the broadband albedo of visible, near-infrared, and total shortwave wavelengths, whose spectral differentiation is common in current land surface schemes of climate models. Spectral albedo is sensitive to wavelength, especially in the near infrared. Along with the development of multiband land surface schemes in climate and ecosystem models, future studies should explicitly assess the albedo characteristics at different wavelengths.

Acknowledgements

We gratefully thank Feng Gao and Crystal Schaaf for their advice on data, its processing and interpretation. We also thank the insightful and detailed comments from the two anonymous reviewers. This work was funded by the Canadian Climate Change Action Fund (CCAF S02-13-07).

References

Anonymous. 2003. *MODIS BRDF/albedo product (MOD43B) user's guide*. Available from http://geography.bu.edu/brdf/userguide/intro.html.

Baldocchi, D., Kelliher, F.M., Black, T.A., and Jarvis, P. 2000. Climate and vegetation controls on boreal zone energy exchange. *Global Change Biology*, Vol. 6, No. S1, pp. 69–83.

Betts, A.K., and Ball, J.H. 1997. Albedo over the boreal forest. *Journal of Geophysical Research*, Vol. 102, No. D24, pp. 28 901 – 28 909.

Chapin, F.S.I., McGuire, A.D., Randerson, J., Pielke, R.A., Baldocchi, D., Hobbie, S.E., Roulet, N., Eugster, W., Kasischke, E., Rastetter, E.B., Zimov, S.A., and Running, S.W. 2000. Arctic and boreal ecosystems of western North America as components of the climate system. *Global Change Biology*, Vol. 6, No. S1, pp. 211–223.

Davidson, A., and Wang, S. 2004. Using in situ observations to characterize regional-scale patterns of surface albedo across the North American boreal region. *Eos Transactions*, Vol. 85, No. 17(Suppl.), Abstract.

Dickinson, R.E. 1983. Land surface processes and climate-surface albedos and energy balance. *Advances in Geophysics*, Vol. 25, pp. 305–353.

Eugster, W., Rouse, W.R., Pielke, R.A., McFadden, J.P., Baldocchi, D., Kittel, T.G.F., Chapin, F.S.I., Liston, G.E., Vidale, P.L., Vaganov, E., and Chambers, S. 2000. Land–atmosphere energy exchange in arctic tundra and boreal forest: available data and feedbacks to climate. *Global Change Biology*, Vol. 6, No. S1, pp. 84–115.

Fernandes, R.A., Pavlic, G., Chen, W., and Fraser, R. 2001. *Canada-wide 1-km water fraction derived from national topographic data base maps*. Canada Centre for Remote Sensing, Natural Resources Canada, Ottawa, Ont.

Gamon, J.A., Huemmrich, K.F., Peddle, D.R., Chen, J., Fuentes, D., Hall, F.G., Kimball, J.S., Goetz, S., Gu, J., and McDonald, K.C. 2004. Remote sensing in BOREAS: lessons learned. *Remote Sensing of Environment*, Vol. 89, pp. 139–162.

Glass, G.V., Peckham, P.D., and Sanders, J.R. 1972. Consequences of failure to meet assumptions underlying the fixed effects analysis of variance and covariance. *Review of Educational Research*, Vol. 42, pp. 239–288.

Gu, J., and Smith, E.A. 1997. High-resolution estimates of total solar and par surface fluxes over large-scale BOREAS study area from GOES

measurements. *Journal of Geophysical Research*, Vol. 102, No. D24, pp. 29 685 – 29 705.

Gu, J., Smith, E.A., Hodges, G., and Cooper, H.J. 1997. Retrieval of daytime surface net longwave flux over BOREAS from GOES estimates of surface solar flux and surface temperature. *Canadian Journal of Remote Sensing*, Vol. 23, No. 2, pp. 176–187.

Gu, J., Smith, E.A., and Merritt, J.D. 1999. Testing energy balance closure with GOES-retrieved net radiation and in situ measured eddy correlation fluxes. *Journal of Geophysical Research*, Vol. 104, No. D22, pp. 27 881 – 27 893.

Hahmann, A.N., and Dickinson, R.E. 1997. Ccm2-bats model over tropical South America: application to tropical deforestation. *Journal of Climate*, Vol. 10, pp. 1944–1964.

Hall, D.K., Tait, A.B., Riggs, G.A., Salomonson, V.V., Chien, J.Y.L., and Klein, A.G. 1998. *Algorithm theoretical basis document (ATBD) for the MODIS snow-, lake ice- and sea ice-mapping algorithms.* Version 4.0. Goddard Space Flight Center, Greenbelt, Md. 50 pp.

Hall, D.K., Riggs, G.A., Salomonson, V.V., DiGirolamo, N.E., and Bayr, K.J. 2002a. MODIS snow-cover products. *Remote Sensing of Environment*, Vol. 83, No. 1–2, pp. 181–194.

Hall, D.K., Kelly, R.E.J., Riggs, G.A., Chang, A.T.C., and Foster, J.L. 2002b. Assessment of the relative accuracy of hemispheric-scale snow-cover maps. *Annals of Glaciology*, Vol. 34, pp. 24–30.

Hansen, J., Sato, M., Lacis, A., Ruedy, R., Tegen, I., and Matthews, E. 1998. Climate forcings in the industrial era. *Proceedings of the National Academy of Sciences*, Vol. 95, pp. 12 753 – 12 758.

Henderson-Sellers, A., and Wilson, M.F. 1983. Surface albedo data for climatic modeling. *Reviews of Geophysics*, Vol. 21, pp. 1743–1778.

Jin, Y., Schaaf, C.B., Gao, F., Li, X., Strahler, A.H., Lucht, W., and Liang, S. 2003a. Consistency of MODIS surface bidirectional reflectance distribution function and albedo retrievals: 1. Algorithm performance. *Journal of Geophysical Research*, Vol. 108, No. D5, p. 4158.

Jin, Y., Schaaf, C.B., Woodcock, C.E., Gao, F., Li, X., Strahler, A.H., Lucht, W., and Liang, S. 2003b. Consistency of MODIS surface bidirectional reflectance distribution function and albedo retrievals: 2. Validation. *Journal of Geophysical Research*, Vol. 108, No. D5, p. 4159.

Latifovic, R., Zhu, Z.-L., Cihlar, J., and Olthof, I. 2004. Land cover mapping of North America — global land cover 2000. *Remote Sensing of Environment*, Vol. 89, No. 1, pp. 116–127.

Li, Z., and Garand, L. 1994. Estimation of surface albedo from space: a parameterization for global application. *Journal of Geophysical Research*, Vol. 99, No. D4, pp. 8335–8350.

Liang, S. 2000. Narrowband to broadband conversions of land surface albedo I. Algorithms. *Remote Sensing of Environment*, Vol. 76, pp. 213–238.

Liang, S. 2002. Narrowband to broadband conversions of land surface albedo II. Validation. *Remote Sensing of Environment*, Vol. 84, pp. 25–41.

Lucht, W., Schaaf, C.B., and Strahler, A.H. 2000a. An algorithm for the retrieval of albedo from space using semiempirical BRDF models. *IEEE Transactions on Geoscience and Remote Sensing*, Vol. 38, No. 2, pp. 977–998.

Lucht, W., Hyman, A.H., Strahler, A.H., Barnsley, M.J., Hobson, P., and Muller, J.-P. 2000b. A comparison of satellite-derived spectral albedos to ground-based broadband albedo measurements modeled to satellite spatial scale for a semidesert landscape. *Remote Sensing of Environment*, Vol. 74, pp. 85–98.

PCI Geomatics Enterprises Inc. 2003. *GEOMATICA software version 9.0*. PCI Geomatics Enterprises Inc., Richmond, B.C.

Pinty, B., and Verstraete, M. 1992. On the design and validation of surface bidirectional reflectance and albedo model. *Remote Sensing of Environment*, Vol. 41, pp. 155–167.

Pomeroy, J.W., Parviainien, J., Hedstrom, N., and Gray, D.M. 1998. Coupled modeling of forest snow interception and sublimation. *Hydrological Processes*, Vol. 12, pp. 2317–2337.

Riggs, G.A., Hall, D.K., and Salomonson, V.V. 2003. *MODIS snow products user guide for collection 4 data products*. Available from http://modis-snow-ice.gsfc.nasa.gov/sug_main.html.

Rowe, C.M. 1991. Modeling land-surface albedos from vegetation canopy architecture. *Physical Geography*, Vol. 12, No. 2, pp. 93–114.

Schaaf, C.B., Gao, F., Strahler, A.H., Lucht, W., Li, X., Tsang, T., Strugnell, N.C., Zhang, X., Jin, Y., Muller, J.-P., Lewis, P., Barnsley, M., Hobson, P., Disney, M., Roberts, G., Dunderdale, M., Doll, C., d'Entremont, R., Hu, B., Liang, S., and Privette, J.L. 2002. First operational BRDF, albedo nadir reflectance products from MODIS. *Remote Sensing of Environment*, Vol. 83, No. 1–2, pp. 135–148.

Sellers, P.J., Hall, F.G., Margolis, H., Kelly, B., Baldocchi, D., den Hartog, G., Cihlar, J., Ryan, M.G., Goodison, B., Crill, P., Ranson, K.J., Lettenmaier, D., and Wickland, E. 1995. The boreal ecosystem–atmosphere study (BOREAS): an overview and early results from the 1994 field year. *Bulletin of the American Meteorological Society*, Vol. 76, No. 9, pp. 1549–1577.

Sharrat, B.S. 1998. Radiative exchange, near-surface temperature and soil water of forest and cropland in interior Alaska. *Agricultural and Forest Meteorology*, Vol. 89, pp. 269–280.

Song, J. 1999. Phenological differences on the albedo of prairie grassland and crop fields. *International Journal of Biometeorology*, Vol. 42, pp. 153–157.

Song, J., and Gao, W. 1999. An improved method to derive surface albedo from narrowband AVHRR satellite data: Narrowband to broadband conversion. *Journal of Applied Meteorology*, Vol. 38, pp. 239–249.

Srivastava, A.B.L. 1959. Effects of non-normality on the power of the analysis of variance test. *Biometrika*, Vol. 45, pp. 421–429.

Strugnell, N.C., Lucht, W., and Schaaf, C.B. 2001. A global albedo data set derived from AVHRR data for use in climate simulations. *Geophysical Research Letters*, Vol. 28, pp. 191–148.

Wang, S., Chen, W., and Cihlar, J. 2002. New calculation methods of diurnal distributions of solar radiation and its interception by canopy over complex terrain. *Ecological Modelling*, Vol. 155, pp. 191–204.

Wang, S., Davidson, A., and Latifovic, R. 2004. The impact of drought on land surface albedo. *Eos Transactions*, Vol. 85, No. 17(Suppl.), Abstract.

Wanner, W., Strahler, A.H., Hu, B., Lewis, P., Muller, J.-P., Li, X., Schaaf, C.L.B., and Barnsley, M.J. 1997. Global retrieval of bidirectional reflectance and albedo over land from EOS MODIS and MISR data: theory and algorithm. *Journal of Geophysical Research*, Vol. 102, No. D14, pp. 17 143 – 17 162.

Xue, Y., and Shukla, J. 1993. The influence of land surface properties on sahel climate. Part I: desertification. *Journal of Climate*, Vol. 6, pp. 2232–2245.

Zhou, L., Dickinson, R.E., Tian, Y., Zeng, X., Dai, Y., Yang, Z.-L., Schaaf, C.B., Gao, F., Jin, Y., Strahler, A., Myeni, R.B., Yu, H., Wu, W., and Shaikh, M. 2003. Comparison of seasonal and spatial variations of albedos from moderate-resolution imaging spectroradiometer (MODIS) and common land model. *Journal of Geophysical Research*, Vol. 108, No. D15, pp. 4488–4688.

Can. J. Remote Sensing, Vol. 31, No. 5, pp. 391–399, 2005

A general two-stream algorithm for retrieving spectral surface albedo

Zhanqing Li, Howard W. Barker, and Louis Moreau

Abstract. Spectral surface albedo (SSA) has numerous applications in climate and environmental studies. Given that ground-based observations of SSA are very limited, space-borne remote sensing has been the primary means of acquiring SSA on large or global scales. To date, many satellite sensors measure reflectances in different spectral regions from which values of SSA are inferred. The inversion algorithms range from simple linear relationships to complex, full-fledged radiative transfer models. Often, algorithms were designed for application to a particular sensor or spectral band. In this study, we propose a more versatile parameterized algorithm that can be used for estimating SSA from satellite-measured spectral albedos at the top of the atmosphere (TOA). The algorithm was developed based on a three-layer atmospheric model. Monochromatic and band transmittances due to various absorbing species are parameterized. The reflectance and transmittance for direct and diffuse radiation in the second layer are determined by the generalized two-stream solutions. Except for the parameterization coefficients that vary with the bandpass and spectral response function of the satellite sensor, the framework of the inversion model is applicable to any sensor or spectral region. The model is tested by applying it to the results of detailed radiative transfer simulations for a wide range of conditions for various satellite sensors and spectral bands. The complexity and accuracy of the proposed model are intermediate relative to those of models currently in use.

Résumé. L'albédo spectral de surface (SSA) a plusieurs applications dans les études climatiques ou environnementales. Étant donné que les observations de SSA au sol sont très limitées, la télédétection satellitaire constitue le moyen privilégié d'acquisition de SSA à grande échelle ou à l'échelle du globe. Aujourd'hui, plusieurs capteurs satellitaires mesurent les réflectances dans différentes bandes spectrales à partir desquelles la valeur de SSA est déduite. Les algorithmes d'inversion varient des simples relations linéaires aux modèles plus complexes de transfert radiatif. Souvent, les algorithmes ont été développés pour application à un capteur particulier ou une bande spectrale spécifique. Dans cette étude, nous proposons un algorithme de paramétrage plus versatile qui peut être utilisé pour l'estimation de SSA à partir de mesures d'albédo spectral acquises par satellite au sommet de l'atmosphère (TOA). L'algorithme a été développé à partir d'un modèle atmosphérique à trois couches. Les transmittances monochromatiques et intégrées sur la bande dues aux différentes composantes absorbantes de l'atmosphère sont paramétrées. La réflectance et la transmittance du rayonnement direct et diffus dans la seconde couche sont déterminées au moyen de solutions généralisées à deux flux. À l'exception des coefficients de paramétrisation qui varient en fonction de la largeur de la bande et de la fonction de réponse spectrale du capteur satellitaire, le cadre du modèle d'inversion est applicable à n'importe quel capteur ou région spectrale. Le modèle est testé en l'appliquant aux résultats de simulations détaillées de transfert radiatif pour une grande variété de conditions et pour divers capteurs satellitaires et diverses bandes spectrales. La complexité et la précision du modèle sont intermédiaires par rapport à ce que l'on utilise à l'heure actuelle.
[Traduit par la Rédaction]

Introduction

The needs for spectral surface albedo (SSA) are multifold. First, the spectral variation of surface albedo is a unique signature of the target. Such a signature has been widely used in a variety of remote sensing applications. A chief example is the use of vegetation indices (VIs), which are often derived from measurements in two spectral bands, namely the visible (VIS) and near infrared (NIR) (Huete et al., 2002). The utilities of VIs in remote sensing are numerous, ranging from the retrieval of bio-geo-physical parameters (e.g., photosynthetically active radiation or PAR) (Li et al., 1997a) to the classification of land cover types (Cihlar et al., 1997a; 1997b). SSA is a fundamental input variable for inferring atmospheric parameters (cloud, aerosol, water vapour, etc.) from multispectral space-borne observations (Kaufman et al., 2002; King et al., 2003; Remer et al., 2005). It is because of inadequate knowledge of SSA that some remote sensing applications, such as aerosol optical thickness, have been limited to relatively uniform ocean surfaces (Nakajima and Higurashi, 1998; Mishchenko et al., 2003; Jeong and Li, 2005). Closure tests of radiative transfer calculations cannot be achieved unless SSA is known, especially under cloudy conditions due to multiple internal

Received 31 January 2005. Accepted 2 August 2005.

Z. Li.[1] Department of Atmospheric and Oceanic Science, University of Maryland, College Park, MD 20742, USA.

H.W. Barker. Meteorological Service of Canada, Downsview, ON, M3H 5T4, Canada.

L. Moreau. Intermap Information Corporation, Nepean, ON K2E 1A2, Canada.

[1]Corresponding author (e-mail: zli@atmos.umd.edu).

reflections between surface and atmosphere (Barker and Davies, 1989; Li et al., 2002).

As general circulation models (GCMs) advance, there is an increasing demand for high-resolution SSA data from satellites (Dickerson et al., 1990). Not long ago, two-band GCMs were typical, but now GCMs with four or more bands are more popular (Barker et al., 2003). Modelling Earth's climate and understanding the feedbacks between climate and land surface require a good knowledge of SSA on the global scale (Dickerson, 1983). A substantial amount of discrepancy in the simulation of Earth's energy budget originates from large differences in surface albedo datasets used by various GCMs (Li et al., 1997b). It is highly desirable to derive an accurate, global, spectral, and broadband albedo climatology to facilitate climate change studies (Sellers, 1985).

Satellite remote sensing remains a primary tool to meet the aforementioned requirements. Note that there are several steps to convert satellite-measured radiances to surface albedos, although an alternative approach was proposed recently to circumvent the steps by directly linking planetary reflectance with surface albedo following a hybrid modelling and statistical method (Liang, 2003). They include corrections of the spectral response function of the sensor (Trishchenko et al., 2002), the atmospheric effects (Vermote et al., 1997), conversion of reflectance as measured from a particular direction to an albedo defined over the entire hemisphere, or the commonly known bidirectional reflectance distribution function (Luo et al., 2005). If a broadband albedo is derived from narrow-band measurements, spectral conversion is required (Li and Trishchenko, 1999; Liang et al., 2005). Uncertainties are incurred in any of these steps. This study deals with one of the steps, namely, converting a planetary albedo into a surface albedo following atmospheric correction, assuming that the angular correction has been applied to convert the satellite-measured reflectance to a planetary albedo. Although most BRDF models are for broadband radiances, a limited number of BRDF models have also been proposed (e.g., Chang et al. (2000) for the visible region and Ciren and Li (2001) for the ultraviolet region).

At present, there exist some global broadband surface albedo datasets derived from various satellite sensors and systems such the Earth Radiation Budget Experiment (ERBE) (Li and Garand, 1994), the International Satellite Cloud Climatology Project (ISCCP) (Pinker and Laszlo, 1992), and the moderate-resolution imaging spectroradiometer (MODIS) (Schaaf et al., 2002), in addition to many regional albedo estimates (e.g., Barker and Davies, 1989). Most notable is MODIS, which has 36 channels, 23 of which are located at solar wavelengths up to 4.0 μm. SSA is one of the MODIS products following atmospheric correction (Vermote et al., 1997) and bidirectional correction (Lucht et al., 2000; Li et al., 2001).

The purpose of this study is to propose a satellite-based algorithm for retrieving SSA. The algorithm is intended for general application, instead of being tailored for a particular sensor. For a given satellite radiometer, the spectral filter function is required to derive specific coefficients in the parameterization schemes proposed in the paper. In terms of complexity, the proposed model is intermediate between the simple highly parameterized models (Chen and Ohring, 1984; Li and Garand, 1994) and more complicated radiative transfer models (Vermote et al., 1997), or a feed-forward neural network (Liang et al., 1999). The model developed here is more versatile and accurate relative to the simple parameterized models and at the same time involves less computation and fewer input parameters relative to the complicated models. Given that the parameters characterizing the state of the atmosphere contain many uncertainties, even in the era of Earth-observing systems (EOS), the model presented is of certain special utility.

Model

This model is based on a three-layer atmosphere–surface system as depicted in **Figure 1**. The top layer consists of ozone molecules that attenuate solar radiation due to absorption at some specific wavelengths. The radiative properties of this layer can thus be characterized by transmittance functions T_1 and T_1^* for direct and diffuse solar irradiance, respectively. For monochromatic radiation, transmittance due to ozone absorption is determined by Beer's law. The middle layer contains radiatively active constituents including air molecules, water vapour, CO_2 and other gases, and aerosols. These agents have strong interactions via scattering and absorption. The bulk radiative properties of this layer include reflectance and transmittance for direct (R_2 and T_2) and diffuse (R_2^* and T_2^*) sunlight. The third layer is the surface whose albedo (R_s) is to be derived.

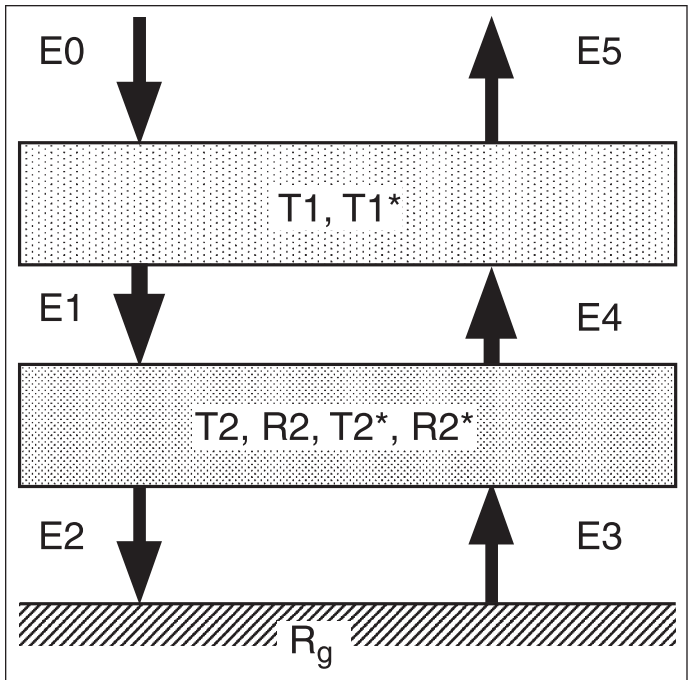

Figure 1. Schematic diagram of the radiative transfer in a three-layer atmosphere–surface system.

For such a system, the following six equations govern the transfer of fluxes between three levels:

$$\left.\begin{aligned} E_0 &= 1 \\ E_1 &= T_1 E_0 \\ E_2 &= T_2 E_1 + R_2^* E_3 \\ E_3 &= R_s E_2 \\ E_4 &= T_2^* E_3 + R_2 E_1 \\ E_5 &= T_1^* E_4 \end{aligned}\right\} \tag{1}$$

from which surface albedo is solved as an analytic function of the planetary albedo ($R_p = E_5$) and other atmospheric radiative quantities:

$$R_p = T_1 T_1^* \left(R_2 + \frac{R_s T_2 T_2^*}{1 - R_s R_2^*} \right) \tag{2}$$

$$R_s = \frac{R_p - R_2 T_1 T_1^*}{R_2^* (R_p - R_2 T_1 T_1^*) + T_2 T_2^* T_1 T_1^*} \tag{3}$$

Reflectance and transmittance of the middle layer can be solved by a generalized two-stream approximation for any set of single-scattering properties, namely optical thickness, single-scattering albedo, and asymmetry factor (Meador and Weaver, 1980). Since the layer contains several atmospheric species, its total optical thickness (τ) is the sum of individual thicknesses:

$$\tau = \tau_a + \tau_R + \tau_{H_2O} + \tau_{CO_2} + \tau_{abs} \tag{4}$$

where the variables on the right-hand side represent optical thicknesses of aerosols (τ_a), atmospheric molecules (Rayleigh scattering) (τ_R), water vapour (τ_{H_2O}), carbon dioxide (τ_{CO_2}), and other absorbing materials (τ_{abs}). Their values are discussed in the following section. Effective values for single-scattering albedo (ω) and asymmetry factor (g) for the layer are given by the following (Leighton, 1980):

$$\omega = \frac{\omega_a \tau_a + \tau_R}{\tau} \tag{5}$$

$$g = \frac{g_a \omega_a \tau_a}{\omega \tau} \tag{6}$$

where ω_a and g_a are single-scattering albedo and asymmetry factors, respectively, for aerosols. With these single-scattering quantities, the generalized two-stream solutions for the second layer are as follows:

$$R_2(\mu_0) = \frac{\omega}{a} \frac{r_+ \exp(k\tau) - r_- \exp(-k\tau) - r_0 \exp(-\tau/\mu_0)}{\exp(k\tau) - \beta \exp(-k\tau)}, \tag{7}$$

$$T_2(\mu_0) = \exp(-\tau/\mu_0) \times \left[1 - \frac{\omega}{a} \frac{t_+ \exp(k\tau) - t_- \exp(-k\tau) - t_0 \exp(-\tau/\mu_0)}{\exp(k\tau) - \beta \exp(-k\tau)} \right], \tag{8}$$

$$R_2^* = \frac{\gamma_2}{k + \gamma_1} \frac{1 - \exp(-2k\tau)}{1 - \beta \exp(-2k\tau)}, \tag{9}$$

$$T_2^* = \frac{2k}{k + \gamma_1} \frac{\exp(-k\tau)}{1 - \beta \exp(-2k\tau)}, \tag{10}$$

where $r_\pm = (1 \mp k\mu_0)(\gamma_1\gamma_3 - \gamma_2\gamma_4 \pm k\gamma_3)$, $r_0 = 2k[\gamma_3 - (\gamma_1\gamma_3 - \gamma_2\gamma_4)\mu_0]$, $t_\pm = (1 \pm k\mu_0)(\gamma_1\gamma_4 - \gamma_2\gamma_3 \pm k\gamma_4)$, $t_0 = 2k[\gamma_4 - (\gamma_1\gamma_4 - \gamma_2\gamma_3)\mu_0]$, $a = [1 - (k\mu_0)^2](k + \gamma_1)T$, $k = (\gamma_1^2 - \gamma_2^2)^{0.5}$, $\beta = -(k - \gamma_1)/(k + \gamma_1)$, $\gamma_1, \ldots, \gamma_4$ depend on the choice of a two-stream method; and μ_0 is the cosine of the solar zenith angle. For the delta-Eddington approximation (Joseph et al., 1976),

$$\left.\begin{aligned} k &= \frac{1}{2}\sqrt{3(1 - \omega')(1 - \omega' g')} \\ \gamma_1 &= \frac{7 - \omega'(4 + 3g')}{4} \\ \gamma_2 &= \frac{1 - \omega'(4 - 3g')}{4} \\ \gamma_3 &= \frac{2 - 3\mu_0 g'}{4} \\ \gamma_4 &= 1 - \gamma_3 \end{aligned}\right\}, \tag{11}$$

in which

$$\left.\begin{aligned} \tau' &= (1 - \omega g^2)\tau \\ \omega' &= \frac{\omega(1 - g^2)}{1 - \omega g^2} \\ g' &= \frac{g}{1 + g} \end{aligned}\right\}, \tag{12}$$

The values of transmittance due to absorption are available from precalculated look-up tables using such standard codes as LOWTRAN7 or MODTRAN4. In this study, we used LOWTRAN7 because it has been implemented in our double-adding code, which is used for validation tests under a wide range of conditions. The spectral interval is 25 cm^{-1} for LOWTRAN7. The tables span from 2000 cm^{-1} (5 μm) to 50 000 cm^{-1} (0.2 μm). The look-up tables were generated for varying amounts of gases embedded in the standard atmosphere. Transmittance for any amount of an absorbing gas is determined by a spline interpolation method.

Since transmittance over narrow spectral intervals as used in LOWTRAN7 can be approximated by Beer's law, the optical

thickness for absorbing species can be easily obtained. For example, the optical thickness for ozone is

$$\tau_{o_3} = -\mu_0 \ln[T(O_3/\mu_0)] \tag{13}$$

where T denotes the mean ozone transmittance from look-up tables, and O_3 is the vertical depth of the ozone. Likewise, we can obtain the optical thickness for other gases such as water vapour and CO_2. The aerosol optical properties are treated as input variables and have been retrieved with a reasonable accuracy over some relatively dark surfaces (e.g., Remer et al., 2005).

Having spectral values of the optical properties for all the components, one can solve for surface albedo averaged over the bandpass of a sensor by spectrally integrating Equation (2) with a weighting factor of the product of the incoming solar irradiance $S(\lambda)$ and sensor filter function $f(\lambda)$. This is achieved by solving

$$\frac{\sum_{j=1}^{J} S(\lambda_j) f(\lambda_j) \mathrm{T}_1(\lambda_j) \mathrm{T}_1^* \{\mathrm{R}_2(\lambda_j) + [\mathrm{T}_2(\lambda_j) \mathrm{T}_2^* R_s]/[1 - \mathrm{R}_2^* R_s]\}}{\sum_{j=1}^{J} S(\lambda_j) f(\lambda_j)} - R_p = 0 \tag{14}$$

where λ is the wavelength. This equation can be solved numerically rather quickly by Newton's method. Using planetary albedo as an initial guess for surface albedo, it takes typically only two iterations of computation for R_s to converge to an accuracy of 10^{-5}.

Note that the same approach may not be applied to Equation (3) to compute surface albedo directly due to the strong spectral dependence of planetary albedo, especially at shorter wavelengths because of Rayleigh scattering and scattering by fine aerosol particles. An unphysical value (i.e., larger than unity) would be obtained for a band containing strong absorption lines. Over a narrow band without strong absorption, the two approaches end up with similar results. If weighted spectral integration is conducted for each individual term in Equation (3), however, the resulting surface albedo is very close to that from Equation (14) for any band.

For the narrow bandwidths of many remote sensing instruments, spectrally integrated effective radiative values may be used. They are obtained by averaging over the sensor band (λ_1, λ_2) weighted by $S(\lambda)$ and $f(\lambda)$:

$$\varphi = \frac{\int_{\lambda_1}^{\lambda_2} S(\lambda) f(\lambda) \tilde{\varphi}(\lambda) \mathrm{d}\lambda}{\int_{\lambda_1}^{\lambda_2} S(\lambda) f(\lambda) \mathrm{d}\lambda}, \tag{15}$$

where $\tilde{\varphi}(\lambda)$ is the spectral-dependent radiative variable under study.

Determination of band-mean reflectance and transmittance

Effective optical properties for direct solar radiation

Gases absorption

The effective direct transmittance due to ozone absorption over a sensor's bandpass is approximated by

$$\mathrm{T}_1 = \frac{\int_{\lambda_2}^{\lambda_1} S(\lambda) f(\lambda) \exp(-\tau_{\lambda_{O_3}} r_{O_3}/\mu_0) \mathrm{d}\lambda}{\int_{\lambda_2}^{\lambda_1} S(\lambda) f(\lambda) \mathrm{d}\lambda} \tag{16}$$

The direct effective monochromatic optical thickness is then derived from T_1 as

$$\tau_{O_3} = -\frac{1}{\mu_0} \ln \mathrm{T}_1 \tag{17}$$

Likewise, we can obtain the effective transmittance and optical thickness for water vapour, CO_2, and other absorbing gases, as well as aerosols. Since the spectral function of the direct solar energy transmitting into the second layer is modified by the overlaying ozone, the weighting function in the spectral integration of the monochromatic transmittance includes the transmittance of the ozone layer, in addition to the top of the atmosphere (TOA) incoming solar spectrum. The direct transmittance due to water vapour absorption, for example, is given by

$$T_{H_2O} = \frac{\int_{\lambda_2}^{\lambda_1} S(\lambda) f(\lambda) \exp(-\tau_{\lambda_{O_3}} r_{O_3}/\mu_0) \exp(-\tau_{\lambda_{H_2O}} r_{H_2O}/\mu_0) \mathrm{d}\lambda}{\int_{\lambda_2}^{\lambda_1} S(\lambda) f(\lambda) \exp(-\tau_{\lambda_{O_3}} r_{O_3}/\mu_0) \mathrm{d}\lambda} \tag{18}$$

where $\tau_{\lambda_{H_2O}}$ is the monochromatic optical thickness of water vapour absorption read from the look-up table; and r_{H_2O} is the specified amount of water vapour divided by the reference amount of water vapour, which was set at 2.34 g·cm^{-2} in this investigation.

Rayleigh optical depth

Spectral Rayleigh optical depths for the standard atmosphere are approximated as (Hansen et al., 1983)

$$\tau_{R,o}(\lambda) = 0.008569\lambda^{-4}(1 + 0.0113\lambda^{-2} + 0.00013\lambda^{-4}) \tag{19}$$

Values of τ_R for any atmosphere are equal to $(P/P_0)\tau_{R,0}$, where P is the actual surface air pressure, and P_0 = 1013.25 mbar (1 bar = 100 kPa). The corresponding monochromatic reflectance for a direct beam is given by

$$R_R[\mu_0, \tau_R(\lambda)] = \frac{3\tau_R(\lambda) + (2 - 3\mu_0)\{1 - \exp[-\tau_R(\lambda)/\mu_0]\}}{4 + 3\tau_R(\lambda)} \quad (20)$$

The effective reflectance over the sensor bandpass is determined by

$$R_R[\mu_0] = \frac{\int_{\lambda_1}^{\lambda_2} S(\lambda) f(\lambda) R[\mu_0, \tau_R(\lambda)] d\lambda}{\int_{\lambda_1}^{\lambda_2} S(\lambda) f(\lambda) d\lambda}. \quad (21)$$

Effective optical thickness for diffuse solar radiation

The diffuse flux incident into the middle level is the flux reflected by the surface. The flux incoming on the surface is the sum of the direct flux transmitted through the middle layer and the flux diffused downward by aerosol particles and atmospheric molecules. The direct spectral transmittance is

$$T_{\lambda_2} = \exp\left(-\frac{\tau_{\lambda_2}}{\mu_0}\right) \quad (22)$$

where τ_{λ_2} is the sum of the monochromatic optical thickness of the components in the lower layer (aerosol, water vapour, CO_2, and air molecules). The fraction of the flux diffused downward is approximated by a single scattering process:

$$F_{\lambda_2} = 0.5[1 - \exp(-\tau_{\lambda_R}/\mu_0)] + [1 - \beta(\lambda, \mu_0)] \times \omega_\lambda[1 - \exp(-\tau_{\lambda_a}/\mu_0)] \quad (23)$$

where τ_{λ_R} is the monochromatic optical thickness of the Rayleigh scatterers, ω_λ is the single scattering albedo of the aerosol at the wavelength λ, τ_{λ_a} is the monochromatic optical thickness of the aerosol, and β is the fraction of radiation backscattered by the aerosol. Assuming the Henyey–Greenstein phase function, β is obtained by integrating the function over the upper hemispheric domain:

$$\beta(\lambda, \mu) = \frac{(1 - g_\lambda^2)}{4g_\lambda(g_\lambda^2 + 2g_\lambda + 1)^{0.5}} - \frac{1}{2} + (g_\lambda^2 + 2g_\lambda \sin\theta_0 + 1)^{-0.5} + (g_\lambda^2 - 2g_\lambda \sin\theta_0 + 1)^{-0.5} \quad (24)$$

where g_λ is the asymmetry factor of the aerosol at the wavelength λ, and θ_0 is the solar zenith angle.

Over a narrow spectral interval, it is assumed that the surface does not alter the spectral dependence of the upwelling flux. As such, the weighting factors used to determine the diffuse effective transmittance and optical thickness of the radiative constituents in the middle layer should include the sum of T_{λ_2} and F_{λ_2}, in addition to the transmittance due to ozone absorption.

Diffuse equivalent optical thickness for ozone

The upwelling diffuse irradiance onto the ozone layer has two origins, namely backscatter by the aerosol and the Rayleigh scatterers and reflection from the surface. Both of these affect the spectral distribution of the diffuse radiation incoming in the ozone layer.

For the diffuse flux passing through the middle layer, the transmittance $T_{\lambda_2}^*$ is

$$T_{\lambda_2}^* = \exp(-D\tau_{\lambda_2}) \quad (25)$$

where D = 1.66 is the diffusivity factor. The backscattered fraction of the downward radiation incoming in the middle layer is

$$B_{\lambda_2} = 0.5[1 - \exp(-\tau_{\lambda_R}/\mu_0)] + \beta(\lambda, \mu_0)\omega_\lambda[1 - \exp(-\tau_{\lambda_a}/\mu_0)] \quad (26)$$

so the total weighting factor to be used in Equation (12) is

$$\exp(-\tau_{\lambda_{O_3}} r_{O_3}/\mu_0)[(T_{\lambda_2} + F_{\lambda_2})T_{\lambda_2}^* + B_{\lambda_2}] \quad (27)$$

For upwelling radiation reflected by the surface, the effective τ in Equations (4)–(6) is approximated by

$$\tau_{H_2O}^{\uparrow} \equiv -\frac{1}{D}\log\left[\frac{T(w_{H_2O}/\mu_0 + Dw_{H_2O})}{T(w_{H_2O}/\mu_0)}\right]. \quad (28)$$

Assuming Lambertian surface reflectance, D varies between 1.50 (thick limit) and 2.00 (thin limit); D = 1.66 is used in practice.

Evaluation

The analytic model described herein is evaluated by applying it to TOA reflectances computed by an adding–doubling radiative transfer model (Li and Garand, 1994). To this end, we conducted a large number of simulations with different atmospheric and surface conditions. The latter is specified by the spectral functions of surface albedo for some typical land cover types such as green vegetation, barren land, desert, and snow (Li et al., 2002). These types are considered as input to the radiative transfer model from which the TOA albedos were computed. The computed albedos were then substituted into the parameterized model to estimate surface albedos.

Figure 2 shows the relationship between TOA and surface albedo. The model was run for 292 different combinations of

solar zenith angles ranging from 0° to 70°, surface albedos from 0.05 to 0.98, aerosol optical thicknesses from 0.00 to 0.68, and ozone amount from 0.16 to 0.50 cm. The two variables are shown to have an approximately linear relationship. A great deal of variation in the TOA albedo cannot be explained by the changes in surface albedo, however. Therefore, use of a simple linear regression may result in a large uncertainty in the estimates of surface albedo from TOA albedo, or vice versa. The values of the regression coefficient R^2, mean bias, and random errors are 0.953, 0.021, and 0.111, respectively, should one apply a simple linear regression to estimate the surface albedos.

Figure 3 shows the surface albedos calculated by the model presented here compared with the true surface albedos used in the radiative transfer model simulations. The improvement over **Figure 2** is significant. The model is able to take into account most of the atmospheric and solar zenith angle effects. Some discrepancies remain (mainly for large solar zenith angles and aerosol loadings), but overall the performance is sound. The values of R^2, bias, and random errors are 0.997, 0.026, and 0.021, respectively, which are improvements over those from the simple linear regression model.

To test the performance of the model in different spectral regions, we applied it to the ultraviolet (UV, 320–400 nm), visible (400–700 nm), and near infrared (NIR, 700–1100 nm) spectral bands and the entire solar spectrum (0 – 26 000 nm). A comparison of the input and estimated spectral albedos is presented in **Figure 4**. Overall, the performance is good. The best and worst performance correspond to no or weak absorption bands (UV and visible) and strong absorption bands (NIR). This is because the parameterizations suffer from some deficiencies due to the strong spectral variation of atmospheric transmittances over fairly wide bands. Fortunately, the majority of sensors used at present have much narrower bandwidths, so in practice estimation errors are expected to be less than those shown here. This is confirmed in **Figure 5**, which shows similar comparisons but for narrower spectral regions, including the advanced very high resolution radiometer (AVHRR) visible channel and 0.7–0.8, 0.8–0.9, and 0.9–1.1 μm. Other simulations (not shown) indicate that the performance of the model depends on water vapour amount and aerosol loading.

Conclusions

Knowledge of surface spectral albedo (SSA) is required for a variety of climatic, ecological, and environmental studies. To obtain SSA from satellite observations requires an inversion algorithm to account for the effects of the intervening atmosphere. The majority of inversion algorithms were designed for particular sensors or spectral regions using either highly simplified models or detailed complex models. A generalized model of intermediate complexity has been lacking. This paper presents a general inversion model for retrieving SSAs in any spectral region.

From a three-layer atmosphere–surface system, an analytical relationship can be established between albedos at the top and bottom of the atmosphere. Solving the relationship requires determination of reflectance and transmittance in each layer. Major absorption and scattering processes are parameterized such as absorption due to water vapour and ozone and Rayleigh

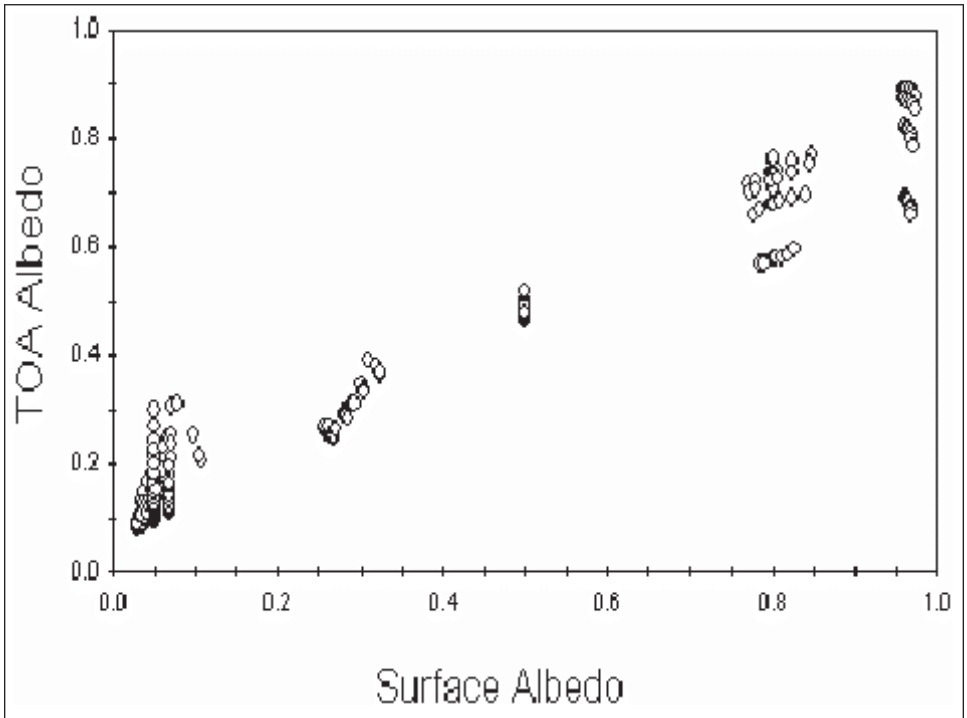

Figure 2. Model-simulated relationship between surface albedo and TOA albedo under a wide range of atmospheric and surface conditions as described in the text.

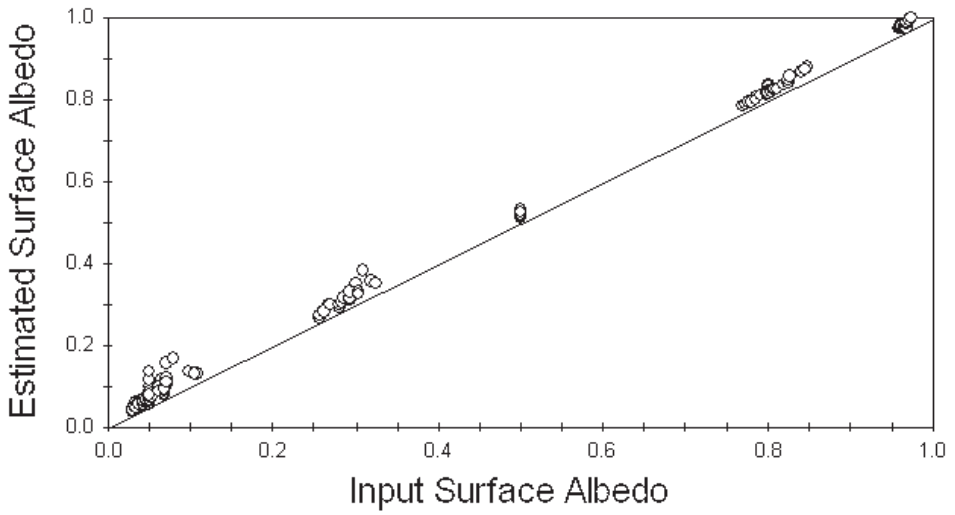

Figure 3. Comparison of surface albedo as input to the full radiative transfer model with that estimated from TOA albedo using the parameterized inversion algorithm for the same conditions as in **Figure 2**.

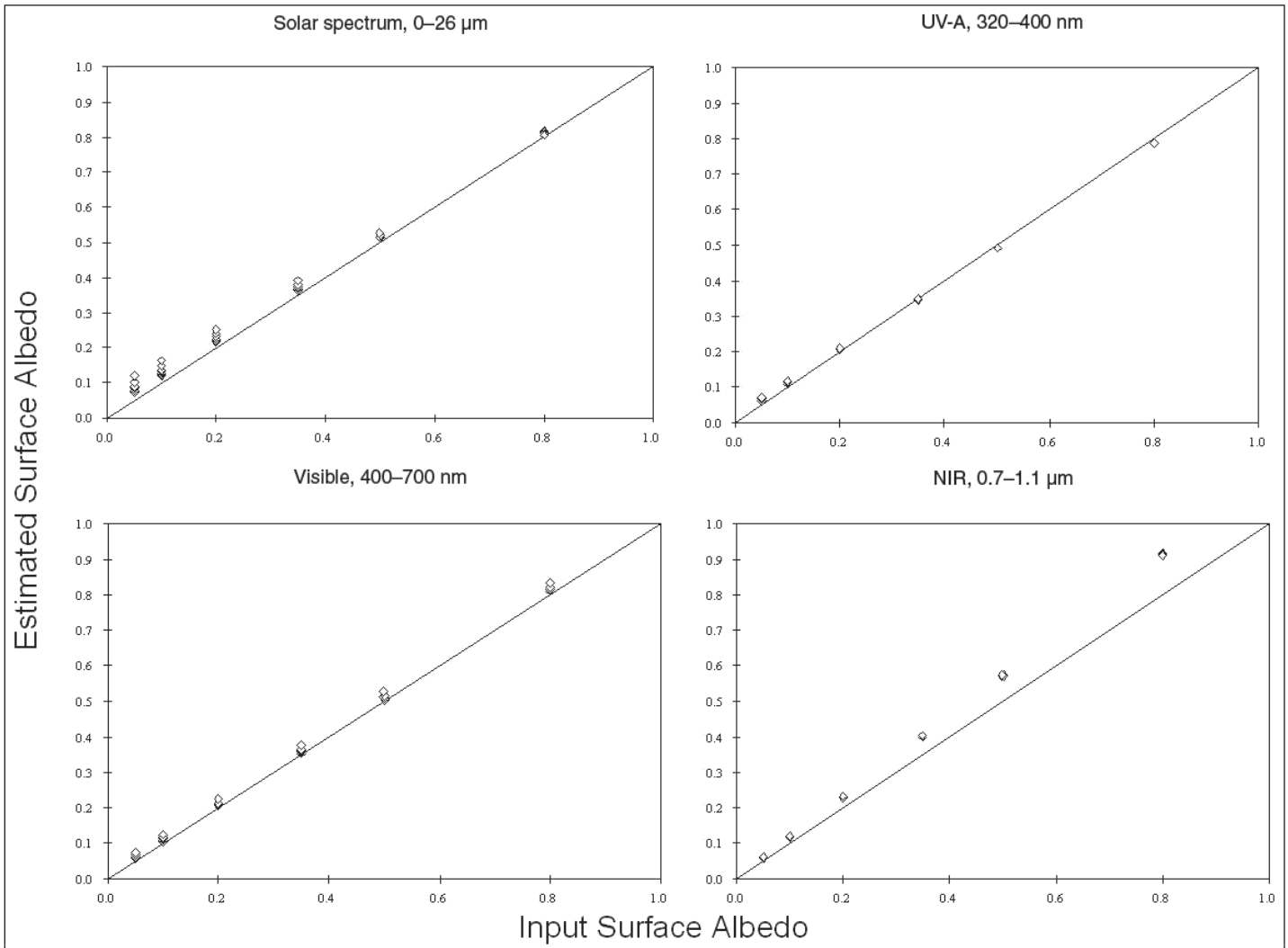

Figure 4. Similar to **Figure 3** but for different spectral regions and fewer conditions.

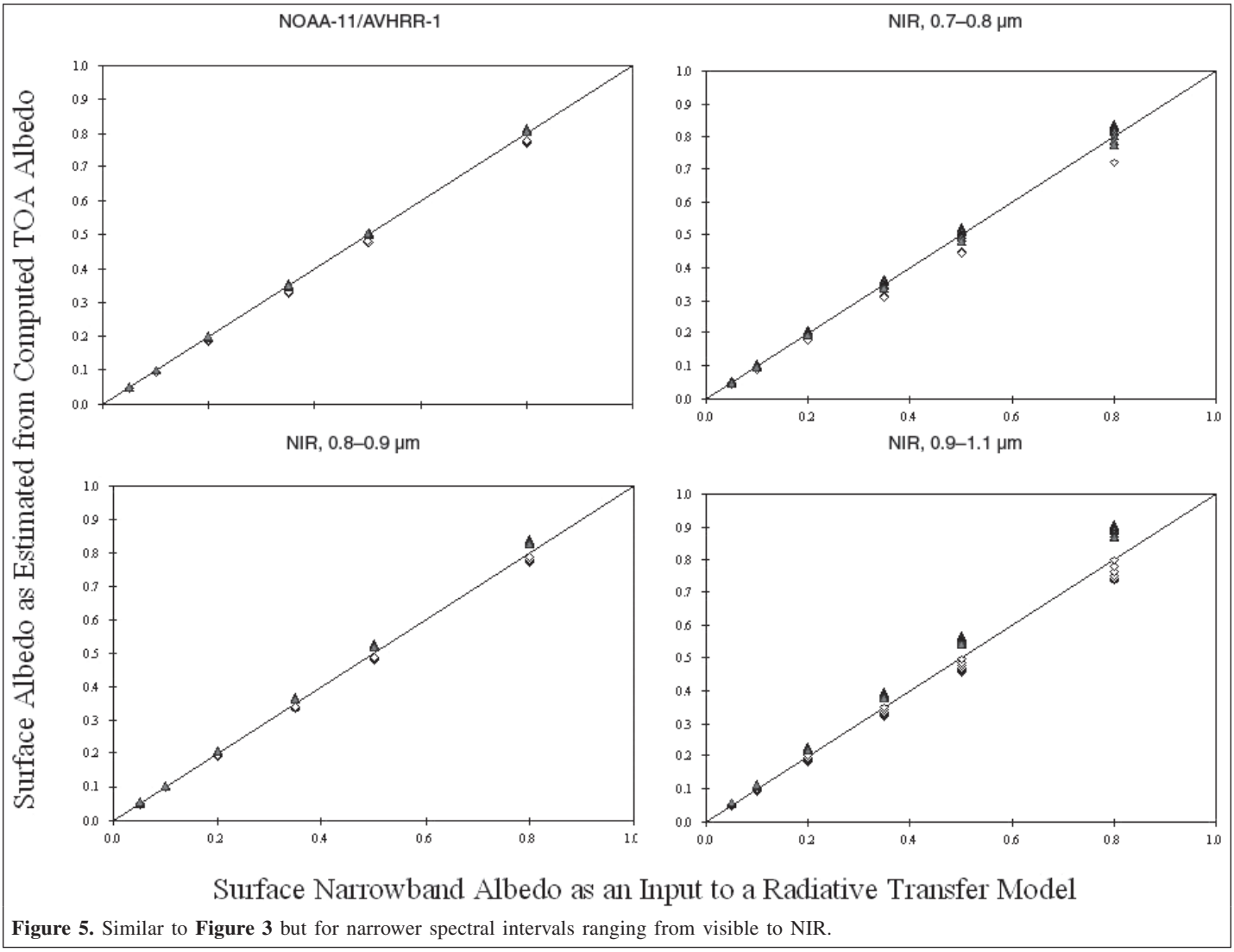

Figure 5. Similar to **Figure 3** but for narrower spectral intervals ranging from visible to NIR.

scattering. Complications arise in determining band-mean transmittance, which was dealt with by separating downward and upward direct and diffuse fluxes in each layer. The parameterized model was evaluated against a detailed radiative transfer model by comparing SSAs as input for the radiative transfer model with those estimated by the approximate inversion algorithm, which used TOA albedo simulated by the detailed model. The inversion model proved to be generally valid over a wide range of spectral intervals from UV to the total solar spectrum, with relatively large errors occurring only for wide bands that contain highly variable absorption.

Acknowledgements

The study was supported by the US Department of Energy Atmospheric Radiation Program with grants DEFG0201ER63166 and DEFG0202ER63351 and National Aeronautics and Space Administration (NASA) grant NNG04GE79G.

References

Barker, H.W., and Davies, J.A. 1989. Surface albedo estimates from Nimbus-7 ERB data and a two-stream approximation of the radiative transfer equation. *Journal of Climate*, Vol. 2, pp. 409–418.

Barker, H.W., Stephens, G.L., Partain, P.T., Bergman, J.W., Bonnel, B., Campana, K., Clothiaux, E.E., Clough, S., Cusack, S., Delamere, J., Edwards, J., Evans, K.F., Fouquart, Y., Freidenreich, S., Galin, V., Hou, Y., Kato, S., Li, J., Mlawer, E., Morcrette, J.-J., O'Hirok, W., Räisänen, P., Ramaswamy, V., Ritter, B., Rozanov, E., Schlesinger, M., Shibata, K., Sporyshev, P., Sun, Z., Wendisch, M., Wood, N., and Yang, F. 2003. Assessing 1D atmospheric solar radiative transfer models: interpretation and handling of unresolved clouds. *Journal of Climate*, Vol. 16, pp. 2676–2699.

Chang, F.-L., Li, Z., and Trishchenko, A. 2000. The dependence of TOA anisotropic reflection on cloud properties inferred from ScaRaB satellite data. *Journal of Applied Meteorology*, Vol. 39, pp. 2480–2493.

Chen, T.S., and Ohring, G. 1984. On the relationship between clear sky planetary and surface albedos. *Journal of Atmospheric Sciences*, Vol. 41, pp. 156–158.

Cihlar, J., Chen, J., Li, Z., Huang, F., and Pokrant, H. 1997a. Can interannual land surface signal be discerned in composite AVHRR data? *Journal of Geophysical Research*, Vol. 103, pp. 23 163 – 23 172.

Cihlar, J., Beaubien, J., Xiao, Q., Chen, J., and Li, Z. 1997b. Land cover of the BOREAS region from AVHRR and LANDSAT data. *Canadian Journal of Remote Sensing*, Vol. 23, pp. 163–175.

Ciren, P., and Li, Z. 2001. The TOA anisotropic reflection of UV radiation, characteristics and models obtained from Meteor-3/TOMS. *Journal of Geophysical Research*, Vol. 106, pp. 4741–4755.

Dickerson, R.E. 1983. Land surface processes and climate-surface albedos and energy balance. *Advances in Geophysics*, Vol. 25, pp. 305–353.

Dickerson, R.E., Pinty, B., and Verstraete, M.M. 1990. Relating surface albedos in GCMs to remotely sensed data. *Agricultural and Forest Meteorology*, Vol. 52, pp. 109–131.

Hansen, J.E., Russell, D., Rind, D., Stone, P., Lacis, A., Travis, L., Lebedeff, S., and Ruedy, R. 1983. Efficient three-dimensional global models for climate studies: models I and II. *Monthly Weather Review*, Vol. 111, pp. 609–662.

Huete, A., Didan, K., Miura, T., Rodrigue, E.P., Gao, X., and Ferreira, L.G. 2002. Overview of the radiometric and biophysical performance of the MODIS vegetation indices. *Remote Sensing of Environment*, Vol. 83, pp. 195–213.

Jeong, M.-J., and Li, Z. 2005. Quality, compatibility and synergy analyses of global aerosal products derived from the advanced very high resolution radiometers and total ozone mapping spectrometers. *Journal of Geophysical Research*, Vol. 110, No. D10S08, doi:10.1029/2004JD00464.

Joseph, J.H., Wiscombe, W.J., and Weinman, J.A. 1976. The delta-Eddington approximation for radiative transfer. *Journal of the Atmospheric Sciences*, Vol. 33, pp. 2452–2459.

Kaufman, Y.J., Tanré, D., and Boucher, O. 2002. A satellite view of aerosols in the climate system. *Nature (London)*, Vol. 419, pp. 215–223.

King, M.D., Menzel, W.P., Kaufman, Y.J., Tanré, D., Gao, B.C., Platnick, S., Ackerman, S.A., Remer, L.A., Pincus, R., and Hubanks, P.A. 2003. Cloud and aerosol properties, precipitable water, and profiles of temperature and humidity from MODIS. *IEEE Transactions on Geoscience and Remote Sensing*, Vol. 41, pp. 442–458.

Leighton, H.G. 1980. Application of the delta-Eddington method to the absorption of solar radiation in the atmosphere. *Atmosphere–Ocean*, Vol. 18, pp. 43–52.

Li, Z., and Garand, L. 1994. Estimation of surface albedo from space: a parameterization for global application. *Journal of Geophysical Research*, Vol. 99, pp. 8335–8350.

Li, Z., and Trishchenko, A. 1999. A study towards an improved understanding of the relationship between visible and SW albedo measurements. *Journal of Atmospheric and Oceanic Technology*, Vol. 16, pp. 347–360.

Li, Z., Moreau, L., Cihlar, J. 1997a. Estimation of the photosynthetically active radiation absorbed at the surface over the BOREAS region. *Journal of Geophysical Research*, Vol. 102, pp. 29 717 – 29 727.

Li, Z., Moreau, L., and Arking, A. 1997b. On solar energy disposition, a perspective from observation and modeling. *Bulletin of the American Meteorological Society*, Vol. 78, pp. 53–70.

Li, X., Gao, F., Wang, J., and Strahler, A.H. 2001. A priori knowledge accumulation and its application to linear BRDF model inversions. *Journal of Geophysical Research*, Vol. D106, pp. 11 925 – 11 935.

Li, Z., Cribb, M., and Trishchenko, A. 2002. Impact of surface inhomogeneity on solar radiative transfer under overcast conditions. *Journal of Geophysical Research*, Vol. 107, No. D16, doi:10.1029/2001JD000976.

Liang, S. 2003. A direct algorithm for estimating land surface broadband albedos from MODIS imagery. *IEEE Transactions on Geoscience and Remote Sensing*, Vol. 41, pp. 136–145.

Liang, S., Strahler, A., and Walthall, C. 1999. Retrieval of land surface albedo from satellite observations: a simulation study. *Journal of Applied Meteorology*, Vol. 38, pp. 712–725.

Liang, S., Yu, Y., and Defelice, T.P. 2005. VIIRS narrowband to broadband land surface albedo conversion: formula and validation. *International Journal of Remote Sensing*, Vol. 26, No. 5, pp. 1019–1025.

Lucht, W., Schaaf, C.B., and Strahler, A.H. 2000. An algorithm for the retrieval of albedo from space using semiempirical BRDF models. *IEEE Transactions on Geoscience and Remote Sensing*, Vol. 38, pp. 977–998.

Luo, Y., Trishchenko, A.P., Latifovic, R., and Li, Z. 2005. Surface bidirectional reflectance and albedo properties derived using a land cover-based approach with moderate resolution imaging spectroradiometer observations. *Journal of Geophysical Research*, Vol. 110, No. D01106, doi:10.1029/2004JD004741.

Meador, M.E., and Weaver, W.R. 1980. Two-stream approximations to radiative transfer in planetary atmospheres: a unified description of existing methods and a new improvement. *Journal of the Atmospheric Sciences*, Vol. 37, pp. 630–643.

Mishchenko, M.I., Geogdzhayev, I.V., Liu, L., Ogren, J.A., Lacis, A.A., Rossow, W.B., Hovenier, J.W., Volten, H., and Munoz, O. 2003. Aerosol retrievals from AVHRR radiances: effects of particle nonsphericity and absorption and an updated long-term global climatology of aerosol properties. *Journal of Quantitative Spectroscopy and Radiative Transfer*, Vol. 79–80, pp. 953–972.

Nakajima, T., and Higurashi, A. 1998. A use of two-channel radiances for an aerosol characterization from space. *Geophysical Research Letters*, Vol. 25, No. 20, pp. 3815–3818.

Pinker, R., and Laszlo, I. 1992. Modeling surface solar irradiance for satellite applications on a global scale. *Journal of Applied Meteorology*, Vol. 31, pp. 194–211.

Remer, L.A., Kaufman, Y.J., Tanré, D., Mattoo, S., Chu, D.A., Martins, J.V., Li, R.-R., Ichoku, C., Levy, R.C., Kleidman, R.G., Eck, R.F., Vermote, E., and Holben, B.N. 2005. The MODIS aerosol algorithm, products and validation. *Journal of the Atmospheric Sciences*, Vol. 62, pp. 947–973.

Schaaf, C.B., Gao, F., Strahler, A.H., Lucht, W., Li, X., Tsang, T., Strugnell, N.C., Zhang, X., Jin, Y., Muller, J.-P., Lewis, P., Barnsley, M., Hobson, P., Disney, M., Roberts, G., Dunderdale, M., Doll, C., d'Entremont, R., Hu, B., Liang, S., and Privette, J.L. 2002. First operational BRDF, albedo and nadir reflectance products from MODIS. *Remote Sensing of Environment*, Vol. 83, pp. 135–148.

Sellers, P.J. 1985. Canopy reflectance, photosynthesis and transpiration. *International Journal of Remote Sensing*, Vol. 6, pp. 1335–1372.

Trishchenko, A.P., Cihlar, J., and Li, Z. 2002. Effects of spectral response function on surface reflectance and NDVI measured with moderate resolution satellite sensors. *Remote Sensing of Environment*, Vol. 81, pp. 1–18.

Vermote, E.F., El Saleous, N.Z., Justice, C.O., Kaufman, Y.J., Privette, J., Remer, L., Roger, J.C., and Tanré, D. 1997. Atmospheric correction of visible to middle infrared EOS-MODIS data over land surface, background, operational algorithm and validation. *Journal of Geophysical Research*, Vol. 102, pp. 17 131 – 17 141.

Can. J. Remote Sensing, Vol. 31, No. 5, pp. 400–411, 2005

Variability of seasonal CASI image data products and potential application for management zone delineation for precision agriculture

Jiangui Liu, John R. Miller, Driss Haboudane, Elizabeth Pattey, and Michel C. Nolin

Abstract. The delineation of management zones is an important step to implementing site-specific crop management practices. Remote sensing is a cost-effective way to acquire information needed for delineating management zones, since it has been successfully used for mapping soil properties and monitoring crop growth conditions. Remotely sensed hyperspectral data are particularly effective in deriving crop biophysical parameters in agricultural fields; therefore, the potential of hyperspectral data to contribute to management zone delineation needs to be assessed. In this study, the spatial variability of soil and crops in two agricultural fields was studied using seasonal compact airborne spectrographic imager (CASI) hyperspectral images. Different spectral features including soil brightness and colouration indices, principal components of soil reflectance data, and crop descriptors (leaf area index (LAI) and leaf chlorophyll content) were derived from CASI data and used to partition the fields into homogeneous zones using the fuzzy *k* means unsupervised classification method. The reduction of variances of soil electrical conductivity, LAI, leaf chlorophyll content, and yield was inspected to determine the appropriate number of zones for each field. The zones obtained were interpreted according to the soil survey map and field practices. Analysis of variance (ANOVA) was conducted to examine the effectiveness of the delineation. The study shows that the spatial patterns of the resulting soil zones faithfully represent the soil classes described by the soil survey maps, and the spatial patterns of the resulting crop classes discriminated the different crop growth conditions well. These results show that hyperspectral data provide important information on field variability for management zone delineation in precision agriculture.

Résumé. La délimitation des zones de gestion homogènes est une étape importante dans la mise en place des procédures de gestion localisée des ressources agricoles. La télédétection peut s'avérer éonomiquement viable pour l'acquisition des données requises à la délimitation de ces zones. En effet, elle a déjà permis de cartographier des propriétés de sols et de suivre la croissance des cultures. Les données hyperspectrales sont très utiles pour dériver des descripteurs biophysiques des champs en cultures; il faut donc évaluer le potentiel de la télédétection hyperspectrale à définir adéquatement la délimitation des zones de gestion homogènes. À l'aide d'une série temporelle d'mages hyperspectrales du capteur aéroporté CASI (« compact airborne spectrographic imager »), la variabilité spatiale des propriétés du sol et des cultures dans deux champs agricoles ont été étudiés. Divers indicateurs spectraux, dont les indices de brillance et de coloration du sol, des composantes principales de réflectance du sol et des descripteurs du couvert végétal agricole (l'indice de surface foliaire (LAI) et la teneur en chlorophylle) ont été extraits des données CASI et utilisés pour segmenter les champs en zones homogènes à l'aide d'une classification non dirigée utilisant la méthode de groupement flou à *k* moyens. L'observation de la réduction de la variance de la conductivité électrique du sol, du LAI, de la teneur en chlorophylle des feuilles, et du rendement agricole a permis de déterminer le nombre approprié de zones homogènes dans chaque champ. Les résultats ainsi obtenus ont été évalués et interprétès grâce à l'utilisation de la carte pédologique et des informations sur les pratiques agricoles. Une analyse de variance (ANOVA) a été réalisée pour évaluer la précision de la segmentation retenue. Les vérifications ont confirmé que les zones homogènes déterminées à partir des propriétés spectrales du sol représentaient bien les classes décrites sur la carte pédologique, et que les zones homogènes établies à partir des descripteurs biophysiques du couvert agricole décrivaient bien les diverses conditions de croissance des cultures étudiées. Cela montre bien que la télédétection hyperspectrale est une source d'information importante pour la détection de la variabilité spatiale des champs agricoles ainsi que pour la délimitation des zones de gestion homogènes en agriculture de précision.

Received 15 December 2004. Accepted 10 June 2005.

J. Liu[1] and E. Pattey. Agriculture and Agri-Food Canada, 960 Carling Avenue, Ottawa, ON K1A 0C6, Canada.

J.R. Miller. Department of Physics and Astronomy, York University, Toronto, ON M3J 1P3, Canada.

D. Haboudane. Département des Sciences Humaines, UQAC, Chicoutimi, QC G7H 2B1, Canada.

M.C. Nolin. Agriculture and Agri-Food Canada, Québec, QC G1W 2L4, Canada.

[1]Corresponding author (e-mail: liuj@agr.gc.ca).

Introduction

One of the important inputs to site-specific management practices in agriculture is the delineation of management zones. A management zone is defined as a portion of a field that expresses a homogeneous combination of yield-limiting factors for which a single rate of a specific crop input is appropriate (Doerge, 1998). The delineation of management zones relies on the exploitation of spatial variability of the agriculture field. Zhang et al. (2002) classified the variability into six groups: yield variability, field variability, soil variability, crop variability, variability in anomalous factors, and management variability. Information on the variability can be ascribed as follows: (*i*) seasonally stable conditions, such as yield-based or soil-based management units, which need to be determined only once every season; and (*ii*) seasonally variable conditions, such as soil moisture, weeds, and crop disease, which need to be monitored continuously during the season (Moran et al., 1997).

Remote sensing offers a quick and cost-effective way to obtain information on the variability of agricultural fields, such as soil properties, crop vigour, crop stress, and relative crop yield (Moran et al., 1997). Remotely sensed hyperspectral data have been successfully used in crop studies for estimation of biophysical descriptors (Haboudane et al., 2002; 2004; Thenkabail et al., 2000), prediction of crop vigour and yield (Tomer et al., 1995; Shibayama and Akiyama, 1991), and monitoring of environmental impact (Strachan et al., 2002; Pattey et al., 2001; Leone and Escadafal, 2001; Lelong et al., 1998). These studies demonstrated that hyperspectral remote sensing provides a powerful tool for precision agriculture applications.

The objective of this study was to explore the potential and ability of hyperspectral remote sensing data for management zone delineation in precision agriculture. Crop fields were delineated into homogeneous zones using soil and crop properties extracted from multitemporal compact airborne spectrographic imager (CASI) hyperspectral data, and the acquired zones were interpreted according to the soil survey maps and the treatments applied in the fields.

Study site and hyperspectral data

The study site is located in the former greenbelt farm of Agriculture and Agri-Food Canada, Ottawa, Ontario, Canada (45°18′N, 75°45′W). The two neighbouring fields investigated in the present study are referred to as fields 25 and 23. Field 25 is primarily composed of two soil associations (D3, Brandon series; M3–NG2, Montain, Allendale, and North Gower series) that share similar drainage conditions (poorly drained) and taxonomic classification (orthic humic gleysol). They are differentiated by the subsurface texture, which is finer in D3 (silty clay loam to clay loam) than in M3–NG2 (sandy clay loam to fine sandy loam). Field 23 is composed of seven soil landscape units with variable drainage classes, profile textures, and genetic evolution (Perron et al., 2002). **Figure 1** shows the detailed soil survey map of the two fields, and **Table 1** gives the soil classification legend.

A survey was made in the two fields in November 2002 (Perron et al., 2003) to obtain soil electrical conductivity at two depths, namely 0–30 cm (EC30) and 0–100 cm (EC100). In the year 2001, uniform nitrogen (N) was applied in field 23, and a specific N application pattern was imposed on field 25 (see **Figure 5d** later in the paper).Yield data were acquired during

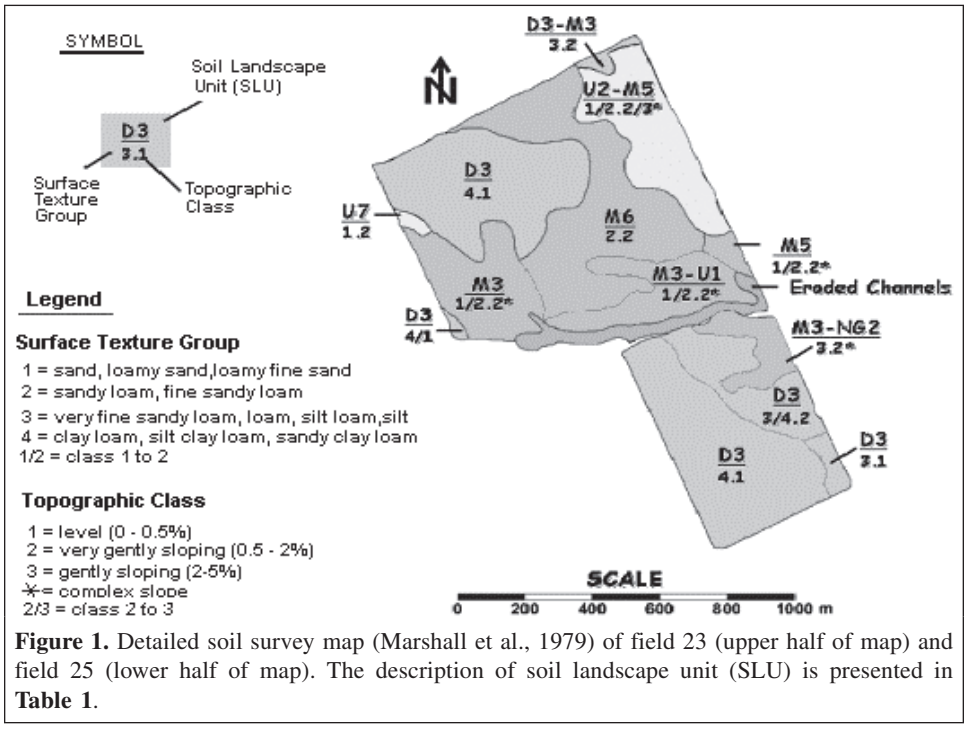

Figure 1. Detailed soil survey map (Marshall et al., 1979) of field 23 (upper half of map) and field 25 (lower half of map). The description of soil landscape unit (SLU) is presented in **Table 1**.

Table 1. Soil classification legend for the two studied fields (see **Figure 1**).

Parent material	SLU[a]	Slope (%)	Soil series	Soil taxonomy	Drainage
Fine-textured marine material (40%–60% clay)	D3	2–5	Brandon	Orthic humic gleysol	Poorly drained
Strongly acid, sandy veneer (25–100 cm) over clayey material	M3	1–3	Mountain	Gleyed sombric brunisol	Imperfectly drained
			Allendale	Orthic humic gleysol	Poorly drained
	M5	0.5–2.0	Allendale	Orthic humic gleysol	Poorly drained
			Montain	Gleyed sombric brunisol	Imperfectly drained
	M6	0–2	Allendale	Orthic humic gleysol	Poorly drained
Moderately fine textured marine material (25%–40% clay)	NG2	0–2	North Gower	Orthic humic gleysol	Poorly drained
Medium- to fine-grained deep sandy material (>100 cm)	U1	2–7	Carlsbad	Orthic sombric brunisol	Well drained
	U2	2–5	Carlsbad	Orthic sombric brunisol	Well drained
			Ramsayville	Gleyed sombric brunisol	Imperfectly drained
	U7	1–2	Ramsayville	Gleyed sombric brunisol	Imperfectly drained
			St. Samuel	Orthic humic gleysol	Poorly drained

[a]Soil landscape unit.

harvest using a combine equipped with a yield monitor for both fields. CASI hyperspectral data were collected four times in 2000 and three times in 2001, spanning crop growing conditions, by intensive field campaigns (IFCs). CASI was operated in the hyperspectral mode with 2 m spatial resolution and 7.5 nm bandwidth. The 72 spectral channels acquired by the sensor covered the visible and near-infrared portions of the solar spectrum, ranging from 408 to 947 nm. The data acquired on 20 June 2000 were chosen for soil partitioning, as the two fields were almost bare of vegetation at that time. In 2001, corn and spring wheat were planted in fields 23 and 25, respectively. Acquisition dates in 2001 were planned to coincide with different phenological development stages, providing image data covering the early, active growth and reproductive crop growth stages. The data from the three IFCs in 2001, acquired on 14 June (IFC1), 26 June (IFC2), and 19 July (IFC3), were used for crop field partitioning to study the spatial and temporal variability of the two crop fields. CASI data were processed to absolute ground reflectance by an operational processing procedure, which includes radiance calibration, atmospheric correction using the CAM5S model, and flat field correction, as described by Haboudane et al. (2004).

Methods

Feature extraction

Feature extraction and selection is a necessary step in hyperspectral data processing due to the large number of spectral channels available. Effective methods for feature extraction are objective oriented. This can be demonstrated by recently developed vegetation indices. The modified triangular vegetation index (MTVI2) is presented as an excellent estimator of leaf area index (LAI) that minimizes leaf chlorophyll content variation (Haboudane et al., 2004), whereas the combined use of the transformed chlorophyll absorption in reflectance index (TCARI) and the optimized soil-adjusted vegetation index (OSAVI) provides a good estimation of leaf chlorophyll content while minimizing LAI variation (Haboudane et al., 2002). Nevertheless, feature selection and extraction inevitably results in information loss; therefore, special care should be taken when implementing any procedure of feature extraction.

Soil reflectance has direct relationships with soil optical properties (colour and brightness) and other soil properties such as texture, soil moisture, and organic matter content (Mattikalli, 1997). Soil brightness and colour are important in differentiating between soil types (Leone and Escadafal, 2001). They are believed to be determined by the amount and state of iron and the content of soil organic matter, carbonate, moisture, etc. Indeed, Huete and Escadafal (1991) concluded that reflectance intensity (or brightness) represents the dominant or principal source of spectral variance among soils, whereas the difference of spectral curve shape (chromatic) is secondary. A common practice to obtain brightness and chromatic information is to convert from a red, green, and blue (RGB) colour composite constructed with multispectral bands to a hue, saturation, and intensity (HSI) colour representation system. In the HSI system, the intensity (I) component represents brightness information, and the hue (H) and saturation (S) components represent chromatic information. In this study, the I and S components are extracted from CASI soil reflectance data of 2000 and are referred to as brightness index (BI) and colouration index (CI). The formulae, presented by Liu and Moore (1990) and modified by Escadafal et al. (1994), are as follows:

$$\mathrm{BI} = (R_{800} + R_{670} + R_{550})/\sqrt{3} \quad (1)$$

$$\mathrm{CI} = (R_{800} - R_{550})/R_{800} \quad (2)$$

where R is the reflectance of the channel, with the central wavelength (in nm) indicated by the subscript. BI is equivalent to the average reflectance of the three channels and is a measure of the brightness of the soil. CI is equivalent to a measure of the

slope of the soil spectrum and therefore soil colour (Escadafal et al., 1994). Thus, BI and CI calculated using these two formulae are the first features to be used for soil-based partitioning.

Principal component (PC) analysis is an effective way of feature extraction. It compresses information into a few components and is a powerful tool for feature reduction in hyperspectral data processing. Principal component transformation based on the covariance matrix of soil reflectance data of 2000 was applied to images of fields 23 and 25. The first three components (PC1, PC2, PC3) made up 99.5% of the spectral information in field 23 (82.5%, 16.2%, and 0.9% for the first, second, and third principal components, respectively) and 99.7% in field 25 (91.7%, 7.8%, and 0.2% for the first, second, and third principal components, respectively). They accounted for almost the total variability of soil reflectance data, and thus they were used as another feature set for soil-based partitioning for comparison with the soil BI and CI measures.

LAI and leaf chlorophyll content are two important crop descriptors. They are critical to understanding biophysical processes and for predicting growth and productivity (Tucker et al., 1980; Moran et al., 1997). Therefore, CASI multitemporal products of LAI and leaf chlorophyll content were used for crop-based partitioning. The formulae for LAI estimation are as follows (Haboudane et al., 2004):

$$\mathrm{MTVI2} = \frac{1.5[1.2(R_{800} - R_{550}) - 2.5(R_{670} - R_{550})]}{\sqrt{(2R_{800} + 1)^2 - (6R_{800} - 5\sqrt{R_{670}}) - 0.5}} \quad (3)$$

$$\mathrm{LAI} = 0.2227 \exp(3.6566 \times \mathrm{MTVI2}) \quad (4)$$

The formulae for leaf chlorophyll content estimation are as follows (Haboudane et al., 2002):

$$\mathrm{OSAVI} = 1.16(R_{800} - R_{670})/(R_{800} + R_{670} + 0.16) \quad (5)$$

$$\mathrm{TCARI} = 3[R_{700} - R_{670} - 0.2(R_{700} - R_{550})R_{700}/R_{670}] \quad (6)$$

$$\mathrm{Chl} = -33.3 \ln(\mathrm{TCARI/OSAVI}) - 19.7 \quad (7)$$

where Chl represents leaf chlorophyll content ($\mu g \cdot cm^{-2}$). The data from the three IFCs were clustered in an attempt to reveal the crop spatial patterns and their temporal variation.

Overall, five sets of features were derived from CASI reflectance data and used for field partitioning: soil features BI and CI, soil features PCs (PC1, PC2, and PC3) from soil reflectance data of 2000, and crop features LAI and leaf chlorophyll content derived from CASI crop reflectance data for the three IFCs in 2001. The soil features represent the relatively stable properties of the field, whereas crop features of the three IFCs reveal the seasonally variable conditions in the fields.

Feature preprocessing

More than one feature is used in this study for field partitioning to integrate different aspects of information. Although all the features were extracted from the same source of data, their typical dynamic ranges are quite different. The values of the features within the range relative to 1%–99% of the cumulative histogram were scaled to [0, 1] through a linear stretch. One of the reasons for this processing is that the relative importance of the features to the delineation is unknown, and therefore they were given the same weight via data stretching. This processing also eliminates the outliers from the typical distribution range.

Clustering method

Because the number of management zones and their spatial distribution are unknown, unsupervised methods were used to cluster the field into homogeneous regions by dividing the feature space. The features from the sites are then extracted and related to the measured variables at the same sites to define the class map of the variable of interest. Since the proposition by Bezdek (1981), fuzzy *k* means has become one of the most widely used unsupervised classification methods. It is the most accurate among the unsupervised methods to reproduce the ground data in a complex landscape (Duda and Canty, 2002) and has been used by many researchers to classify remotely sensed image data. The FUZCLUS module provided in the PCI software (PCI Geomatics Enterprises Inc. 2001) was used in our study to partition the selected features.

Determination of the number of zones

The number of management zones is determined by the size of the field, the natural variability within the field, and certain management factors (Zhang et al., 2002). The choice of an appropriate number of classes is a prerequisite before performing unsupervised classification. We determine the optimum number of zones using the method used by Fridgen et al. (2000), which is based on the inspection of the relative total within-class variance (RTWCV) reduction of selected field variables:

$$\mathrm{RTWCV} = \sum_{i=1}^{C} \sum_{j \in \mathrm{class}C} [x_{ij} - \mu_i]^2 / \sum_{j \in \mathrm{field}} [x_j - \mu]^2 \quad (8)$$

where C is the number of zones, x_{ij} is an observation of the variable from zone i, x_j is an observation of the variable in the whole field, μ_i is the average of the variable in zone i, and μ is the average in the whole field. As the number of zones increases, RTWCV will decrease and then level off. The value at which RTWCV levels off, or stops decreasing significantly, is a reasonable estimate of the number of zones that can be used to partition the field.

In this study, to determine the appropriate number of zones, fields 25 and 23 were partitioned into 2–7 zones using the derived soil and crop feature sets. For each of the partitioned

results, RTWCV was calculated for the selected variables. The selected variables included (*i*) yield, which is often considered as the ultimate dependent variable; (*ii*) LAI and leaf chlorophyll content, which are the most important crop descriptors; and (*iii*) soil electrical conductivity. Electrical conductivity was measured at depths of 0–0.3 and 0–1.0 m (Perron et al., 2003). The RTWCV values of these selected variables are plotted against the number of zones, and the appropriate number of zones was determined from the plots.

Another factor that should be taken into consideration is the spatial distribution of the samples in a given zone. Pixel-based image classification usually divides the feature space. Thus, pixels in a zone are continuous in feature space but are not necessarily so in the spatial domain. From the point of view of the agricultural producer, management zones should encompass significant areas with continuous spatial distribution. Postclassification spatial filtering improves the delineation by removing the isolated small clusters. In this study, the isolated clusters with fewer than the given number of pixels (i.e., 16 in this study) were detected and marked. For each pixel in the marked clusters, its class attribute was determined by inspecting its neighbour pixels: it was assigned to the class that appeared most in this neighbourhood.

Analysis of variance

Analysis of variance (ANOVA) was conducted to test the difference among the delineated zones for the selected soil and crop properties. The technique is a single-factor ANOVA, with the zone identification as the independent variable and the field descriptors, such as yield, electrical conductivity, LAI, and leaf chlorophyll content, as dependent variables. Rafter et al. (2002) concluded that Tukey's test is the most useful for all pairwise comparisons, and the actual family-wise error rate (FWER) exactly equals the specified value. Therefore, Tukey's multiple comparison method (MCM) was applied to test the difference between the means for the dependent variables in the delineated zones.

Results and discussion

Determination of appropriate number of zones

Figures 2 and **3** show the variance reduction of the selected variables in fields 25 and 23, respectively. Results from five delineations are given: two soil delineations using BI, CI, and principal components (PCs) and three crop delineations using LAI and leaf chlorophyll content at IFC1, IFC2, and IFC3. Variance reduction of all the variables is given for the soil

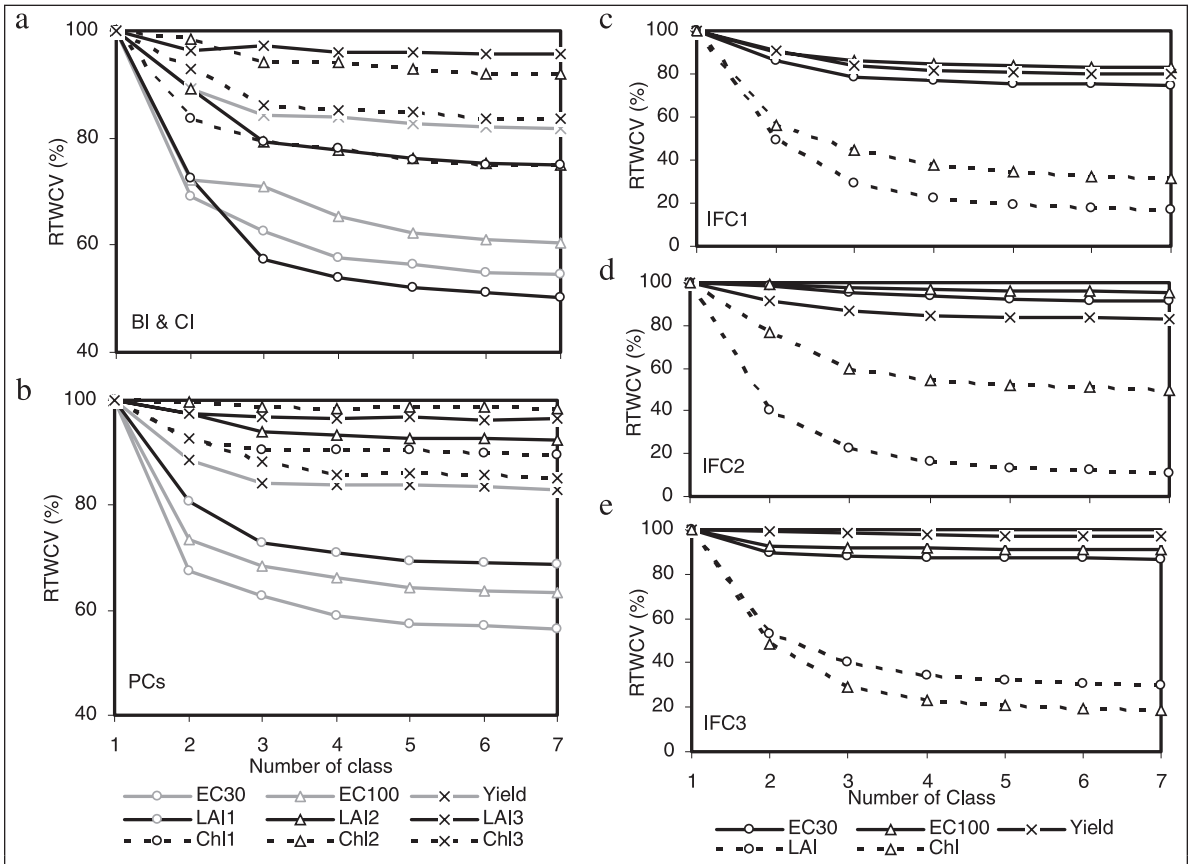

Figure 2. Variance reduction by partitioning field 25 into 2–7 classes using (a) soil brightness and colouration indices (BI and CI, respectively), (b) the first three principal components (PCs) of soil reflectance, and (c–e) leaf area index (LAI) and chlorophyll (Chl) content from IFC1, IFC2, and IFC3, respectively. RTWCV, relative total within-class variance.

delineations, and variance reduction of yield, electrical conductivity, and LAI and leaf chlorophyll content at the specific IFC is given for the crop delineations. In **Figures 2** and **3**, EC30 and EC100 refer to electrical conductivity between 0 and 0.3 m and 0 and 1.0 m depth; LAI1, LAI2, and LAI3 and Chl1, Chl2, and Chl3 represent LAI and leaf chlorophyll content at IFC1, IFC2, and IFC3, respectively.

Three to four zones were recommended for field 25 from an inspection of **Figure 2**. Based on BI and CI, classification of field 25 into four soil zones reduces the variances of EC30, EC100, LAI1, LAI2, and Chl1 to 58%, 65%, 54%, 78%, and 78%, respectively. The results using principal components were almost the same for the first three descriptors, with the variances of the variables specified previously reduced to 59%, 66%, and 71%, and with a limited reduced variance of LAI2 and Chl1 to 93% and 91%, respectively. The soil features as identified by hyperspectral reflectance seem to appropriately reveal the soil properties, as indicated by variance reduction of soil electrical conductivity. Inherent soil fertility indicators like soil texture components (sand, silt, and clay content) and exchangeable cations (Ca and Mg) are closely related to soil electrical conductivity (Nolin et al., 2002; Perron et al., 2002). Soil properties highly influenced by soil fertility management like soil pH and soil tests (available P and K), however, are less closely related to soil electrical conductivity (Perron et al., 2002; 2003). BI–CI and principal components classifications significantly reduced the variances of yield and Chl3 to about 85%, which tends to indicate that the detected soil properties had a restricted impact on growth conditions toward the end of the growing season in this field. In this field, soil properties seemed to explain mainly the variability related to the emergence of the spring wheat. With the progression of the growing season, soil properties captured by soil features did not significantly impact the variability of LAI and leaf chlorophyll content, indicating that there was no detection of N limitation.

Based on LAI and leaf chlorophyll content, classification of field 25 into four crop zones reduces the variances of LAI to about 23%, 16%, and 34% and those of leaf chlorophyll content to 37%, 54%, and 24% at IFC1, IFC2, and IFC3 stages, respectively. The crop zones delineated at IFC1 reduced the variances of EC30 and EC100 to 77% and 82%, respectively. This also indicates that the crop growth condition revealed by LAI and leaf chlorophyll content at IFC1 stage is more affected by the soil properties than those at IFC2 and IFC3. Another observation is that the crop zones delineated at IFC1 and IFC2 reduced the variance of yield to about 82% and 85%, respectively. Thus crop descriptors LAI and leaf chlorophyll content at the earlier development stages have more impact on wheat yield in field 25 than later on.

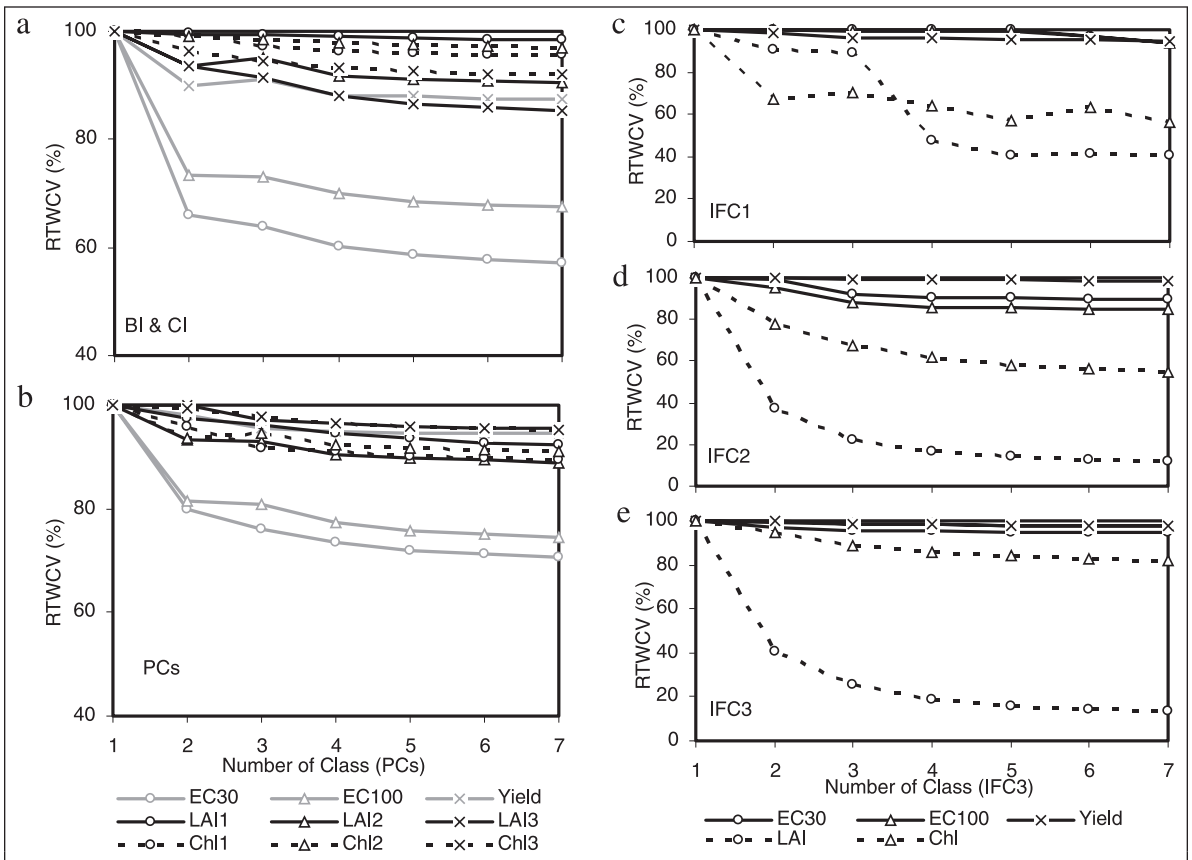

Figure 3. Variance reduction by partitioning field 23 into 2–7 classes using (a) soil brightness and colouration indices (BI and CI, respectively), (b) the first three principal components (PCs) of soil reflectance, and (c–e) LAI and chlorophyll.

Figure 3 suggests that two to three zones are recommended for field 23. When the field was partitioned into three soil zones, the variances of EC30 and EC100 were reduced to about 64% and 73% when BI and CI were used and to about 76% and 81% when PCs were used. Again, the soil features extracted from hyperspectral data seemed to capture the variability of some soil properties in the field. The variances of LAI and leaf chlorophyll content had a limited reduction, however, and the variance of yield was only reduced to 91%. When the field was partitioned using LAI and leaf chlorophyll content, the variances of LAI and leaf chlorophyll at a specific IFC had significant reductions, whereas the variances of yield and electrical conductivity had very limited reductions. The variance reduction of LAI and leaf chlorophyll is not very stable at IFC1. This is because the fraction of crop cover (corn) was very low at that time and therefore the estimated LAI has a very small dynamic range and the estimated leaf chlorophyll content is somewhat uncertain (Haboudane et al., 2002; 2004). For the crop-based delineation, the variances of LAI and leaf chlorophyll content were reduced to about 22% and 67% at IFC2 and 26% and 89% at IFC3, respectively. Compared with field 25, the variance of corn yield in field 23 is less accounted for by soil features and crop descriptors.

Spatial patterns in field 25

Figure 4 shows the results of soil zone delineations in field 25 using the two soil feature sets, e.g., BI and CI and PCs. The results of crop zone delineation using LAI and leaf chlorophyll content for IFC1, IFC2, and IFC3 are given in **Figure 5**. For convenience, the partitioned zones from the two soil feature sets are referred to as soil-based zones, and those from LAI and leaf chlorophyll content as crop-based zones. Soil-based zones and crop-based zones are indicated by the subscripts s and v, which refer to soil and vegetation, respectively.

The soil zones delineated from BI and CI and PCs show some similarities. The spatial patterns of the soil-based zones generally match the soil type distribution as revealed by the soil survey map (**Figure 1**). $C1_s$ and $C2_s$ mostly represent D3 soil series, and $C4_s$ mostly represents M3–NG2 soil series. $C3_s$ distributed in between these two regions may be the transition

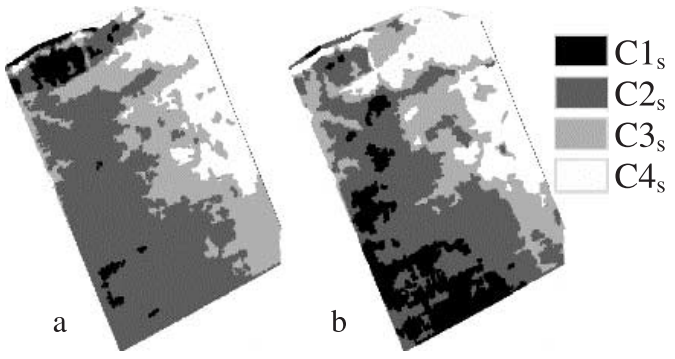

Figure 4. Soil delineation of field 25 into four classes using (a) soil brightness and colouration indices, and (b) principal components. $C1_s$–$C4_s$, soil-based zones 1–4, respectively.

of these two soil associations. The patterns of $C1_s$ and $C2_s$ delineated using BI and CI are not consistent with the delineation using soil PCs. The soil properties may not be very different between these two delineated zones. $C1_s$ delineated using BI and CI at the upper boundary of the field represents the slope area with low organic matter, low sand content, and high clay content, which indicates soil erosion due to the slope heading toward the creek flowing between the wheat (field 25) and corn (field 23) fields. This pattern is also well defined in the crop zones at IFC1 and IFC2 stages and is typical of low LAI and yield. Soil leveling and stabilization might be required in this area.

Different levels of N were applied with a specific pattern in the wheat field (**Figure 5d**). The applied N was 0, 41, or 68 kg N ha^{-1} (referred to as 0N, 41N, and 68N, respectively). The crop-based zones derived from the partitioning of LAI and leaf chlorophyll content show the combined effects of soil properties and N application. The 0N application area at the southwestern corner is clearly delineated as $C1_v$ throughout the season. Statistics show that this region has lower final yield, lower LAI, and lower leaf chlorophyll content at all the three IFCs compared with the other zones. N deficiency is the major critical concern. Although recommended amounts of nitrogen (68N) were applied to the slope area, LAI in this region was significantly lower at IFC1 and IFC2 stages. This region, being clearly delineated as $C1_v$ at IFC1 and IFC2 stages, is not favourable for crop growth and led to a lower yield, which was presumably caused by the lack of organic matter as a result of soil erosion toward the creek. Class $C4_v$ defined in IFC1 (upper right corner) overlaps with regions of the M3–NG2 soil series. In this zone, LAI and leaf chlorophyll content of the first two IFCs and final yield have higher values, indicating that the soil type in this area is favourable for crop growth. The crop developed faster in this area than in the other areas, which makes wheat reaching its senescence stage earlier. The decrease of leaf chlorophyll content and green LAI in this region accounted for it being classified as $C1_v$ and $C2_v$ at the IFC3 stage.

Spatial patterns in field 23

Figure 6 shows the results of soil-based zone delineation in field 23 using the two soil feature sets. Results of crop-based zone delineations for IFC1, IFC2, and IFC3 are given in **Figure 7**.

The similarity is weaker between the soil-based zones resulting from BI and CI and PCs in field 23. $C1_s$ mostly represents the poorly drained, fine-textured Brandon series (D3), $C2_s$ is mostly associated with poorly drained and imperfectly drained soils of Allendale and Montain series associations (M6 and M3), and $C3_s$ represents a well-drained to imperfectly drained sandy soil association (U2–M5) regrouping deep (>100 cm) sandy soils (Carlsbad and Ramsayville series) and shallow (25–100 cm) sandy soils over clay material (Allendale and Montain series).

Corn planted in field 23 received a uniform recommended N application. The spatial patterns of the crop classes are therefore mostly caused by the interaction between soil and weather conditions. Crop-based delineation is difficult at IFC1 because corn was at the early emergence stage in the field. Differentiation of $C1_v$, $C2_v$, and $C3_v$ at the IFC1 stage is mainly due to the amount of vegetation cover and the soil properties. At IFC1, LAI in $C3_v$ generally ranges from 0.3 to 0.6, whereas in $C1_v$ and $C2_v$ it is less than 0.3. $C3_v$ delineated at the IFC1 stage also has higher LAI values at IFC2 (from 2.5 to 4.0) and IFC3 (>4.0) than the other delineated zones. The crop-based zones are best delineated at the IFC2 stage, in that the variances of both LAI and leaf chlorophyll content are significantly reduced (**Figure 3**).

Statistical analysis

Relationship between the two soil feature sets

Soil brightness dominates the spectral variance among soils. The first principal component of soil data accounts for the

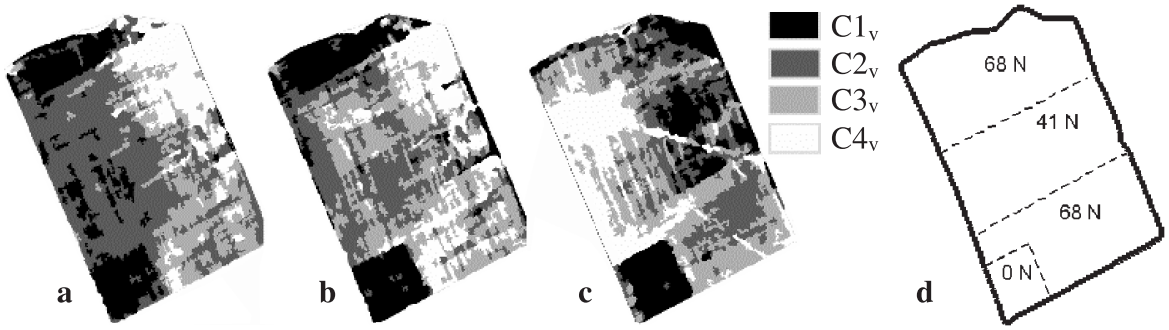

Figure 5. (a–c) Crop delineation of field 25 into four classes using LAI and leaf chlorophyll content at IFC1, IFC2, and IFC3, respectively. $C1_v$–$C4_v$, vegetation (crop) based zones 1–4, respectively. (d) Nitrogen application pattern (0N, 41N, and 68N denote applications of 0, 41, and 68 kg N ha^{-1}, respectively).

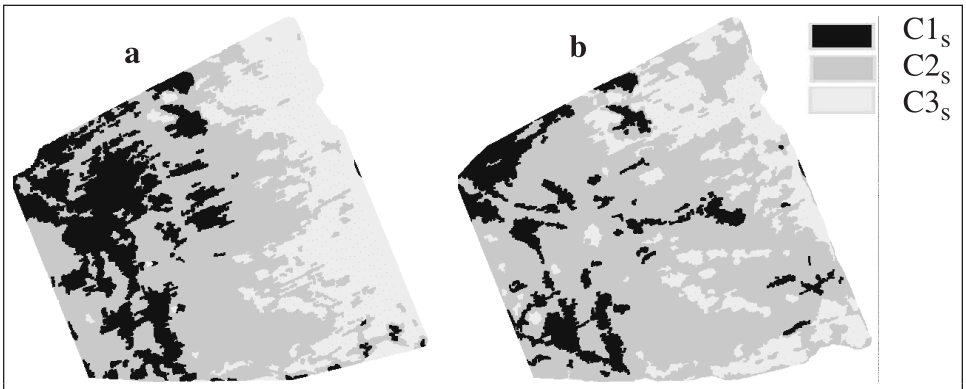

Figure 6. Soil delineation of field 23 into three classes using (a) soil brightness and colouration indices and (b) principal components.

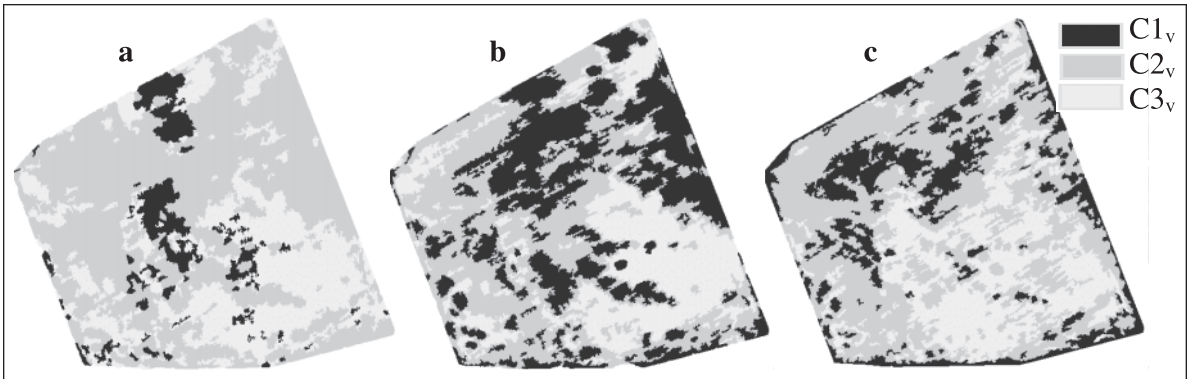

Figure 7. Crop delineation of field 23 into three classes using LAI and leaf chlorophyll content at (a) IFC1, (b) IFC2, and (c) IFC3.

majority of the variability and represents approximately the average value of the spectrum, and therefore it is a measure of soil brightness. The first principal component and soil brightness calculated using Equation (1) are highly linearly correlated, with determination coefficients (R^2) of 0.998 and 0.970 in fields 25 and 23, respectively. This explains the similar results of delineations using PCs and BI and CI (**Figures 2**, **3**, **4**, and **6**). The different information content between the higher order principal components (the second and third) and the chromatic component CI mainly accounts for the difference of the delineations.

Correlation between crop descriptors and yield

The correlation between crop descriptors and yield was analyzed, and the results are given in **Table 2**. In field 25, the correlations between LAI and wheat yield and between leaf chlorophyll content and wheat yield are significant at IFC1 and IFC2 but not significant at IFC3. In field 23, yield is not significantly correlated with LAI or leaf chlorophyll content. This is consistent with the results shown in **Figures 2** and **3**: the variance of yield in field 25 was reduced to 82% and 85% for the crop-based delineation at IFC1 and IFC2, respectively, but there was no significant reduction for the crop-based delineation at IFC3, and there was very limited variance reduction of corn yield in field 23 for the crop-based delineation at any of the three IFCs. The possible reason for the poor correlation in field 23 is that LAI and leaf chlorophyll content did not capture a high productivity spatial feature across the field, which decreased the overall correlation. If this high productivity feature is masked out, then a significant correlation is observed between corn yield and leaf chlorophyll content at IFC2 and IFC3 (**Table 2**, field 23A). The highest correlations were obtained with leaf chlorophyll content.

Zone means and analysis of variance

Figures 8 and **9** show the zone means and standard deviations of the variables in the delineated zones of fields 25 and 23, respectively. For variables EC30, EC100, and yield, the figures show zone means and deviations of the five delineations: crop-based delineations at the three IFCs, and soil-based delineations using BI and CI and PCs. For LAI and leaf chlorophyll content, zone means and deviations of crop delineations at the three IFCs were illustrated. Tukey's test was applied to test the difference of zone means of the variables to evaluate the uniqueness of the delineated zones. The results are also shown in **Figures 8** and **9**. Zones in which the mean values do not differ significantly at the 95% confidence interval are marked with a box above the data bars. For instance, in field 25, the means of soil zones C1 and C2 delineated by BI and CI do not differ significantly at the 95% confidence interval. In this case, a box is shown above the data bar spanning C1 and C2 (see **Figure 8a**).

Table 2. Correlation coefficients between yield and crop descriptors in the two fields.

Field	LAI1	LAI2	LAI3	Chl1	Chl2	Chl3
25	0.57**	0.51**	0.23	0.54**	0.43*	0.15
23	–0.09	–0.10	–0.08	–0.19	–0.13	0.22
23A	0.04	0.15	0.22	–0.13	0.54**	0.68**

Note: The suffixes 1–3 to LAI and Chl represent IFC1–IFC3, respectively. *, significant at $p < 0.01$; **, significant at $p < 0.001$. For field 23A, the high productivity feature was masked out.

In field 25, EC30, EC100, and yield differ significantly between soil-based zones except between C1 and C2. This means that soil features extracted from hyperspectral data revealed some of the soil properties, and the detected soil properties had an important impact on the final yield. It can be observed that yield in this field is negatively related to electrical conductivity. Yield is highest in the soil-based zone C4 and lowest in zones C1 and C2, and EC30 and EC100 are lowest in zone C4 and highest in zones C1 and C2. The high electrical conductivity corresponds to heavier soil texture, and these soils tend to stay saturated for longer periods of time, which is negative for yield. For the crop-based zones, LAI and leaf chlorophyll content differ significantly among the zones, whereas EC30 and EC100 do not differ significantly between some of the crop-based zone pairs. The crop-based zones at IFC3 do not effectively differentiate wheat yield, whereas they are indicative of yield at IFC1 and IFC2. This means that the effective time for delineation of the wheat crop should be earlier than that at IFC3.

In field 23, soil electrical conductivity differs significantly between all pairs of soil-based zones, whereas there is no significant difference in electrical conductivity between the crop-based zones (**Figure 9**). Yield does not differ significantly among the soil-based zones as well as it does among the crop-based zones in this field. Except for LAI at IFC1 and leaf chlorophyll content at IFC3, crop descriptors differ significantly between all pairs of crop-based zones. Zone C1 delineated at IFC1 has a high yield compared with that in the other zones because it is completely within a high-production region in the field. From IFC1 to IFC3, LAI in field 23 increased steadily. For corn in field 23, the effective time for delineation of crop-based zones should be later than that for IFC1.

Conclusions

In this study, multitemporal CASI hyperspectral data were used for zone delineation of two agricultural fields. Different features extracted from hyperspectral data related well to some of the field variables and revealed the variability of seasonally stable and variable information useful for management zone delineation for precision agriculture.

The variability in soil electrical conductivity can be accounted for to a significant extent by the features extracted from hyperspectral soil reflectance data. Several inherent soil fertility indicators like soil texture components (sand, silt, and clay content) and exchangeable cations (Ca and Mg) and soil drainage and related soil moisture conditions could be related to soil electrical conductivity. This is rarely the case, however, for the organic matter content of the surface layer, which is

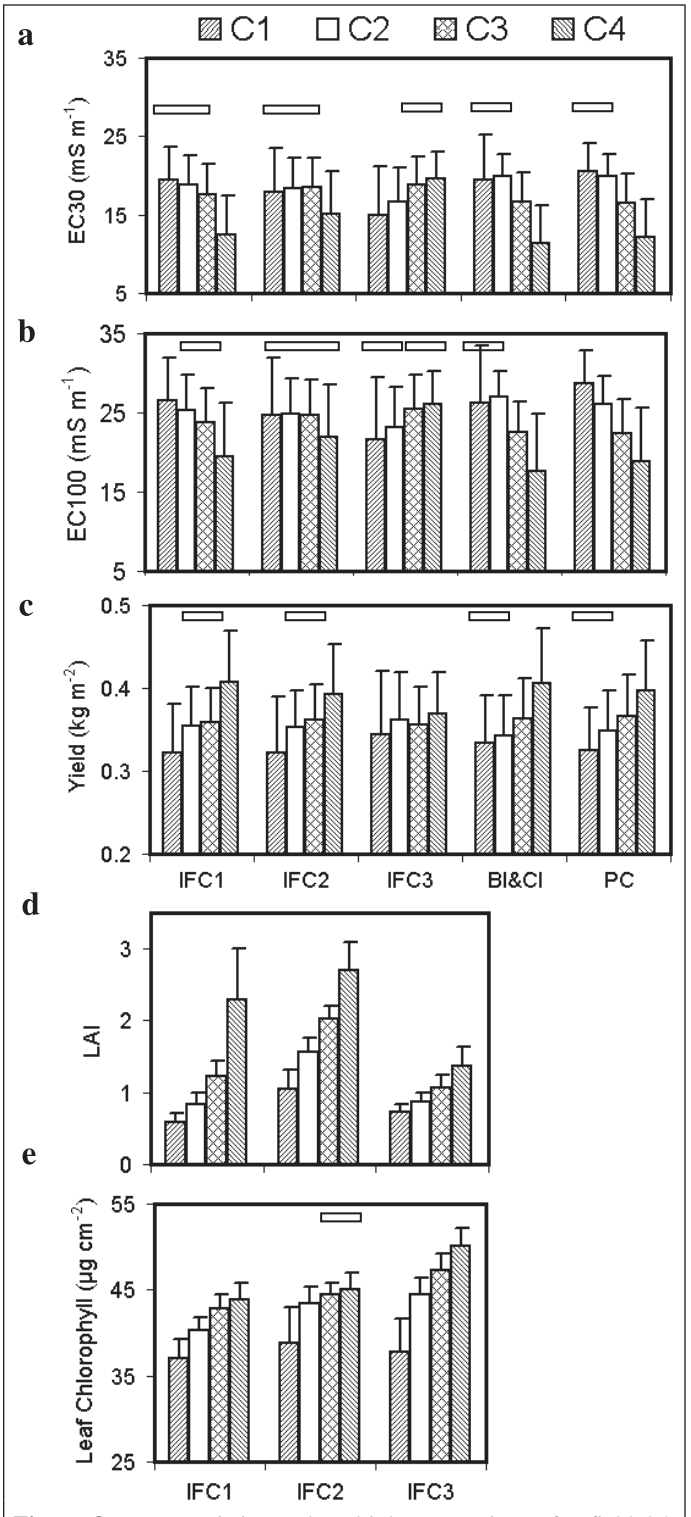

Figure 8. Zone statistics and multiple comparisons for field 25. Variables include electrical conductivity at 0–30 cm (EC30) and 0–100 cm (EC100), yield, LAI, and leaf chlorophyll content; delineations include crop-based delineation at IFC1, IFC2, and IFC3 and soil-based delineations using BI and CI and PCs. The boxes above the data bars indicate the classes that do not differ significantly at the 95% confidence interval. The vertical bars denote standard deviation.

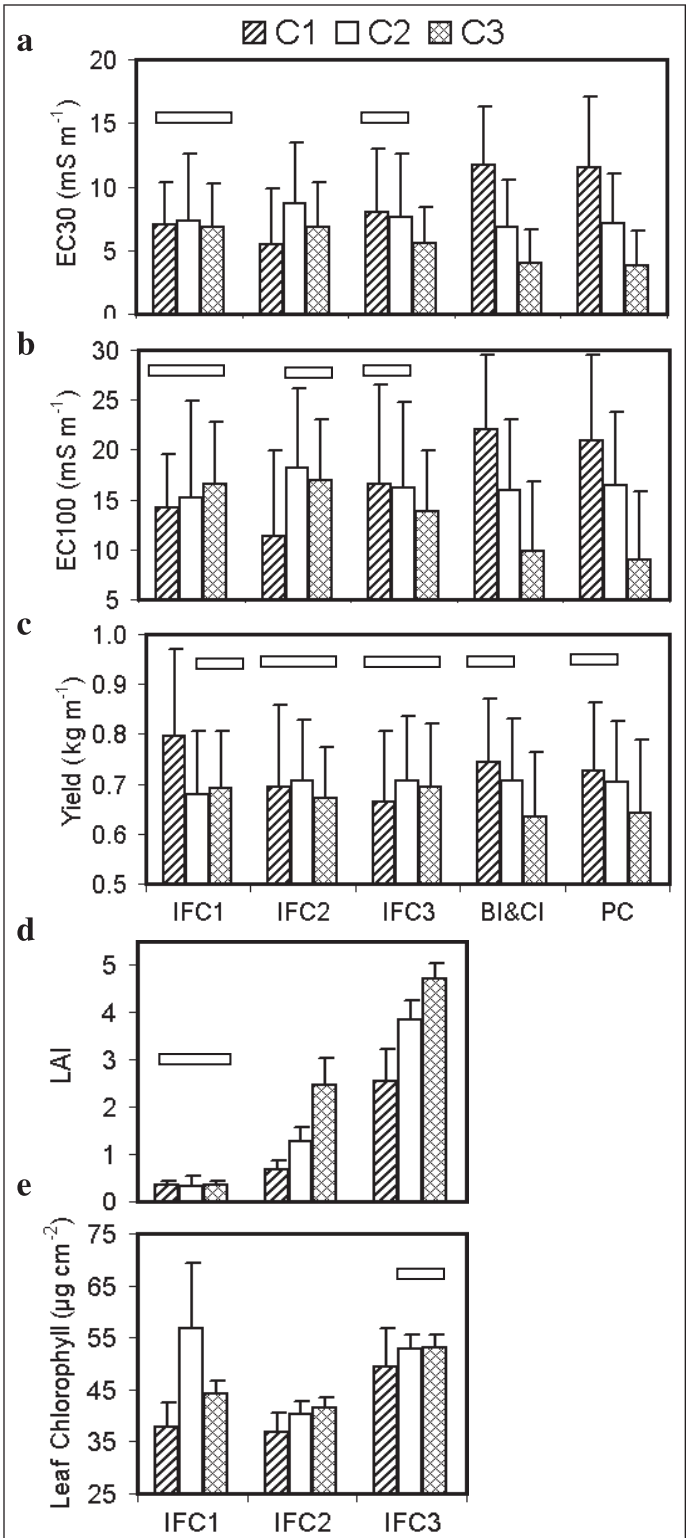

Figure 9. Zone statistics and multiple comparisons for field 23. Variables include electrical conductivity at 0–30 cm (EC30) and 0–100 cm (EC100), yield, LAI, and chlorophyll content; delineations include crop-based delineation at IFC1, IFC2, and IFC3 and soil-based delineations using BI and CI and PCs. The boxes above the data bars indicate the classes that do not differ significantly at the 95% confidence interval. The vertical bars denote standard deviation.

most directly associated with soil reflectance. Therefore, remote sensing data have been shown to play a strong role in soil delineation and could be viewed, under given conditions, as an efficient alternative to soil conductivity mapping for defining within-field homogeneous management zones.

The crop descriptors derived from hyperspectral data are very useful for monitoring crop growth conditions. They revealed the effects of soil properties under natural growth conditions and the effects of special nitrogen application under controlled conditions. The appropriate time to delineate wheat in field 25 was at IFC1 and IFC2 (prior to senescence), and the appropriate time to delineate corn in field 23 was after IFC1 (after complete emergence). Crops can be monitored frequently using LAI and leaf chlorophyll content to monitor seasonally variable information to guide the real-time field practices.

Zone delineation was evaluated by the variance reduction of yield. From this perspective, field 25 is better delineated because the variance of yield was reduced significantly for soil and crop delineations. The soil properties in this field have an important impact on final yield, and crop descriptors LAI and leaf chlorophyll content at the earlier stages (IFC1 and IFC2) are indicative of final yield. Field 23 is not well delineated in terms of variance reduction of yield.

In this study, delineation of management zones of the fields is based solely on the classification of the features extracted from hyperspectral data. Soils and crops were delineated independently using multitemporal hyperspectral data. The combination of soil features and crop descriptors before delineation, or the combination of the delineated results, could give better results for delineation of management zones. The integration of other sources of information, such as soil properties, environmental conditions, and field management factors, may also greatly improve the quality and usefulness (i.e., interpretability) of management zone delineation. In addition to the acquisition of the information on field variability, a more complete understanding of the causes of crop production variability is of great importance, since it will improve the efficiency of the information integration for management zone delineation and its usefulness for development of management strategy. This can be achieved by performing field delineation over several growing seasons to capture the effects of several weather pattern incidences on crop growth.

Acknowledgements

This study was funded by the Government Related Initiatives Program (GRIP) project between the Canadian Space Agency and Agriculture and Agri-Food Canada and a GEOIDE (Canadian Networked Centre of Excellence in geomatics) project for CASI acquisition in 2000.

References

Bezdek, J. (Editor). 1981. *Pattern recognition with fuzzy objective function algorithm*. Plenum Press, New York.

Doerge, T. 1998. Defining management zones for precision farming. *Crop Insights*, Vol. 8, No. 21. Pioneer Hi-Bred International, Inc., Johnston, Iowa.

Duda, T., and Canty, M. 2002. Unsupervised classification of satellite imagery: choosing a good algorithm. *International Journal of Remote Sensing,* Vol. 23, No. 11, pp. 2193–2212.

Escadafal, R., Belghith, A., and Ben Moussa, H. 1994. Indices spectraux pour la télédétection de la dégradation des milieux naturels en Tunisie aride. In *Proceedings of the 6th International Symposium on Physical Measurements and Signatures in Remote Sensing*, 17–21 January 1994, Val d'Isère, France. CNES. pp. 253–259.

Fridgen, J.J., Kitchen, N.R., and Sudduth, K.A. 2000. Variability of soil and landscape attributes within sub-field management zones. In *Proceedings of the 5th International Conference on Precision Agriculture*, 16–19 July 2000, Bloomington, Minn. CD-ROM. Edited by P.C. Robert, R.H. Rust, and W.E. Larson. ASA–CSSA–SSSA, Madison, Wis.

Haboudane, D., Miller, J.R., Tremblay, N., Zarco-Tejada, P.J., and Dextraze, L. 2002. Integrated narrow-band vegetation indices for a prediction of crop chlorophyll content for application to precision agriculture. *Remote Sensing of Environment*, Vol. 81, pp. 416–426.

Haboudane, D., Miller, J.R., Pattey, E., Zarco-Tejada, P.J., and Strachan, I. 2004. Hyperspectral vegetation indices and novel algorithms for predicting green LAI of crop canopies: modeling and validation in the context of precision agriculture. *Remote Sensing of Environment*, Vol. 90, pp. 337–352.

Huete, A.R., and Escadafal, R. 1991. Assessment of biophysical soil properties through spectral decomposition techniques. *Remote Sensing of Environment*, Vol. 35, pp. 149–159.

Lelong, C.C.D., Pinet, P.C., and Poilve, H. 1998. Hyperspectral imaging and stress mapping in agriculture: a case study on wheat in Beauce (France). *Remote Sensing of Environment*, Vol. 66, pp. 179–191.

Leone, A.P., and Escadafal, R. 2001. Statistical analysis of soil colour and spectroradiometer data for hyperspectral remote sensing of soil properties (example in a southern Italy Mediterranean ecosystem). *International Journal of Remote Sensing*, Vol. 22, No. 12, pp. 2311–2328.

Liu, J.G., and Moore, J.Mcm. 1990. Hue image RGB colour composition: a simple technique to suppress shadow and enhance spectral signature. *International Journal of Remote Sensing*, Vol. 11, No. 8, pp. 1521–1530.

Marshall, I.B., Dumanski, J., Huffman, E.C., and Lajoie, P. 1979. *Soils capability and land use in the Ottawa urban fringe*. Land Resource Research Institute, Agriculture Canada, Ottawa, Ont. 59 pp.

Mattikalli, N.M. 1997. Soil colour modelling for the visible and near infrared bands of Landsat sensors using laboratory spectral measurements. *Remote Sensing of Environment*, Vol. 59, pp. 14–28.

Moran, M.S., Inoue, Y., and Barnes, E.M. 1997. Opportunities and limitations for image-based remote sensing in precision crop management. *Remote Sensing of Environment*, Vol. 61, pp. 319–346.

Nolin, M.C., Gagnon, B., Leclerc, M.-L., Cambouris, A.N., Belanger, G., and Simard, R.R. 2002. Influence of pedodiversity and land uses on the within-field spatial variability of selected soil and forage quality indicators. In *Proceedings of the 6th International Conference on Precision Agriculture*, 14–17 July 2002, Minneapolis, Minn. CD-ROM. Edited by P.C. Robert et al. ASA–CSSA–SSSA, Madison, Wis.

Pattey, E., Strachan, I.B., Boisvert, J.B., Desjardins, R.L., and McLaughlin, N.B. 2001. Detecting effects of nitrogen rate and weather on corn growth

using micrometeorological and hyperspectral reflectance measurements. *Agriculture and Forest Meteorology*, Vol. 108, pp. 85–99.

PCI Geomatics Enterprises Inc. 2001. *EASI/PACE software, version 8.2.3*. PCI Geomatics Enterprises Inc., Richmond Hill, Ont.

Perron, I., Cluis, D.A., Nolin, M.C., and Leclerc, M.-L. 2002. Influence of microtopography and soil electrical conductivity on soil quality and crop yields. In *Proceedings of the 6th International Conference on Precision Agriculture*, 14–17 July 2002, Minneapolis, Minn. CD-ROM. Edited by P.C. Robert et al. ASA–CSSA–SSSA, Madison, Wis.

Perron, I., Nolin, M.C., Pattey, E., Bugden, J.L., and Smith, A. 2003. Comparaison de l'utilisation de la conductivite électrique apparente (CEa) des sols et des donnees polarimetriques RSO pour delimeter des unites d'amenagement agricole. In *25th Canadian Symposium on Remote Sensing – 11^{e} Congrès de l'Association québécoise de télédétection*, 14–16 October 2003, Montréal, Que. CD-ROM.

Rafter, J.A., Abell, M.L., and Braselton, J.P. 2002. Multiple comparison methods for means. *SIAM Review*, Vol. 44, No. 2, pp. 259–278.

Shibayama, M., and Akiyama, T. 1991. Estimating grain yield of maturing rice canopies using high spectral resolution reflectance measurements. *Remote Sensing of Environment*, Vol. 36, pp. 45–53.

Strachan, I.B., Pattey, E., and Boisvert, J.B. 2002. Impact of nitrogen and environmental conditions on corn as detected by hyperspectral reflectance. *Remote Sensing of Environment*, Vol. 80, pp. 213–224.

Thenkabail, P.S., Smith, R.B., and De Pauw, E. 2000. Hyperspectral vegetation indices and their relationships with agricultural crop characteristics. *Remote Sensing of Environment*, Vol. 71, pp. 158–182.

Tomer, M.D., Anderson, J.L., and Lamb, J.A. 1995. Landscape analysis of soil and crop data using regression. In *Proceedings of Site-specific Management for Agriculture Systems*, 27–30 March 1994, Minneapolis, Minn. Edited by P.C. Robert, R.H. Rust, and W.E. Larson. ASA–CSSA–SSSA, Madison, Wis. pp. 273–284.

Tucker, C.J., Holben, B.N., Elgin, J.H., Jr., and McMurtrey, J.E. 1980. Relationship of spectral data to grain yield variations. *Photogrammetric Engineering and Remote Sensing*, Vol. 46, pp. 657–666.

Zhang, N., Wang, M., and Wang, N. 2002. Precision agriculture — a worldwide overview. *Computers and Electronics in Agriculture*, Vol. 36, pp. 113–132.

Can. J. Remote Sensing, Vol. 31, No. 5, pp. 412–419, 2005

Research Note / Note de recherche

Landsat ETM+ mosaic of northern Canada

Ian Olthof, Chris Butson, Richard Fernandes, Robert Fraser, Rasim Latifovic, and Jonathan Orazietti

Abstract. Mapping northern Canada with medium spatial resolution (30 m) Landsat data is important to complement national multiagency activities in forested and agricultural regions, and thus to achieve full Canadian coverage. Northern mapping presents unique challenges due to limited availability of field data for calibration or class labeling. Additional problems are caused by variability between individual Landsat scenes acquired under different atmospheric conditions and at different times. Therefore, the generation of radiometrically consistent coverage is highly desirable to reduce the amount of reference data required for land cover mapping and to increase mapping efficiency and consistency by stabilizing spectra of land cover classes among hundreds of Landsat scenes. The production chain and dataset of a normalized, 90 m resolution Landsat enhanced thematic mapper plus (ETM+) mosaic of northern Canada is presented in this research note. A robust regression technique called Thiel–Sen (TS) is used to normalize Landsat scenes to consistent coarse-resolution VEGETATION (VGT) imagery. The derived dataset is available for any interested user and can be employed in applications aimed at studying processes in the Canadian Arctic regions above the tree line.

Résumé. La cartographie du nord canadien à l'aide des données Landsat à résolution moyenne (30 m) est importante à titre de complément pour plusieurs agences nationales ayant des activités dans les régions forestières et agricoles et ainsi, pour assurer une couverture canadienne complète. La cartographie en région nordique présente des défis uniques dû à la disponibilité réduite de données de terrain pour l'étalonnage ou l'étiquetage des classes. La variabilité entre les scènes individuelles Landsat acquises sous différentes conditions atmosphériques et à différentes époques pose également des problèmes. Ainsi, la génération d'une couverture radiométriquement cohérente est hautement souhaitable afin de réduire la quantité de données de référence requises pour la cartographie du couvert et pour accroître l'efficacité et la cohérence de la cartographie en stabilisant les spectres des classes de couvert parmi des centaines de scènes Landsat. On présente, dans cette note de recherche, la chaîne de production et l'ensemble de données d'une mosaïque Landsat ETM+ normalisée, à une résolution de 90 m, du nord canadien. Une technique robuste de régression, la technique Thiel–Sen (TS), est utilisée pour normaliser les scènes Landsat par rapport à des images VGT à résolution grossière qui sont plus homogènes. L'ensemble de données ainsi dérivé est disponible à tout utilisateur intéressé et peut être utilisé dans des applications visant l'étude des divers processus dans les régions de l'Arctique canadien au-dessus de la limite forestière.
[Traduit par la Rédaction]

Introduction

Northern environments are expected to undergo unprecedented change in the coming century due to northern development and climate change. These changes are predicted to manifest themselves in vegetation and land cover distributions. The need to establish a baseline of land cover and land use has been recognized for carbon accounting, global modeling, and quantifying the regional to national impacts of vegetation and land cover change. This baseline should be comprehensive for national-level reporting and for modeling and mapping subtle, large-scale changes that may not be detected using intensive, plot-based analysis. Subtle changes that have been predicted to occur as a result of climate change and northern warming have already been observed, including permafrost melting, increased plant growth, migration of the tree line, and changes to water bodies (Serreze et al., 2000; Stow et al., 2004).

Satellite remote sensing offers the only effective means to obtain a national coverage of Canada's northern environments. To date, such coverage has been provided using coarse-resolution (1 km) instruments. The advanced very high resolution radiometer (AVHRR) onboard the National Oceanic and Atmospheric Administration (NOAA) series of satellites served as a primary data source for the Circumpolar Arctic Vegetation Map (CAVM) (Gould et al., 2002). The Systeme pour l'Observation de la Terre (SPOT) VEGETATION (VGT) sensor was used in the multiagency Global Land Cover (GLC) 2000 initiative to produce 1 km gridded land cover, which included a small number of northern classes (Latifovic et al., 2004). Coarse-resolution data are attractive for northern

Received 17 January 2005. Accepted 9 September 2005.

I. Olthof,[1] C. Butson,[2] R. Fernandes, R. Fraser, R. Latifovic, and J. Orazietti.[3] Environmental Monitoring Section, Applications Division, Canada Centre for Remote Sensing, Natural Resources Canada, 588 Booth Street, Ottawa, ON K1A 0Y7, Canada.

[1]Corresponding author (e-mail: iolthof@ccrs.nrcan.gc.ca).
[2]Present address: Prologic Consulting, 75 Albert Street, Suite 206, Ottawa, ON K1P 5E7, Canada.
[3]Present address: Noetix Research Inc., 403-265 Carling Avenue, Ottawa, ON K1S 2E1, Canada.

mapping applications because problems such as frequent cloud cover and low and rapidly changing solar elevation angles (Hope et al., 1999) can be overcome to some extent by frequent repeat coverage and multitemporal compositing techniques (Walker et al., 2002).

Although 1 km data possess certain desirable characteristics for northern mapping, their coarse resolution prevents capturing many subtle or small-scale changes expected to occur in northern environments. For example, United Nations Framework Convention on Climate Change (UNFCCC) reporting requires a baseline of land use in 1990 and land use changes since, as these portray the influence of humans on the climate system (Veldkamp and Fresco, 1996). A large percentage of land use consists of roads, towns, and other features too small to detect with coarse-resolution data. The Canadian Forest Service (CFS) and the Canadian Space Agency have responded to the need for detailed land cover information by forming a joint project called Earth Observation for Sustainable Development of Forests (EOSD) aimed at producing a land cover map of forested areas of Canada from Landsat data (Wulder et al., 2003). Land cover is an important determinant of land use; it is therefore our intention to use northern land cover as a primary data input with integration of ancillary data to prepare a northern land use map (Cihlar and Jansen, 2001). Integration of the northern map and maps produced by other sectors may provide necessary detailed geospatial information Canada-wide.

Although there is a need for extensive and detailed land cover, there are no efficient methods to provide such information in a temporally and spatially consistent manner. Most national land cover mapping initiatives with Landsat have been relatively labour intensive, requiring separate classifications for each scene or group of scenes forming a regional tile within the national coverage database (Vogelmann et al., 2001; Wulder et al., 2003). Conventional radiometric normalization techniques, such as overlap regression using stable elements between scenes (Elvidge et al., 1995; Du et al., 2001), have been employed to match several scenes within regional tiles so that each may be classified and labeled as an entity, thereby reducing the labour required. However, normalization methods themselves can be time consuming or difficult to implement and often require a considerable amount of user input.

A new normalization technique was developed at the Canada Centre for Remote Sensing (CCRS) to facilitate detailed mapping with 30 m resolution composites consisting of a large number of Landsat scenes (Olthof et al., 2005). The technique was applied here to generate a Landsat product over Canada's northern region above the tree line. The technique uses coarse-resolution composite data from SPOT VGT as a reference for normalizing Landsat enhanced thematic mapper plus (ETM+) imagery, thereby exploiting and combining the best features of both data types: the high temporal coverage of coarse-resolution data with the detail present in medium-resolution data. A robust regression technique called Thiel–Sen (TS) (Kendall and Stuart, 1967), which was first presented to the remote sensing community in Fernandes and Leblanc (2005), is used to generate the normalization equation between Landsat and VGT imagery. The TS slope estimator corresponds to the median of the pairwise slopes of all data points separated by a minimum distance in x and y. The intercept is then determined by using the TS slope in a linear equation of the form $y = mx + b$ for each pairwise predictor and response (x, y) variable and determining the median offset (b) of the set. An evaluation of this normalization technique performed by Olthof et al. (2005) revealed that radiometric error propagation commonly found in mosaics normalized using overlap areas was avoided. Furthermore, because of the insensitivity of the TS regression to ~29% of outliers, it provides an unbiased prediction in the presence of measurement errors in x and y due to atmospheric effects or land cover change (**Figure 1**). Thus, the generation of normalization coefficients requires minimal user input and can be fully automated and applied to generate a national coverage with Landsat data.

This research note describes the application of the TS regression normalization method for the generation of a seamless mosaic covering northern Canada using Landsat-7 ETM+ data. Due to the prohibitively large size of the mosaic at full 30 m resolution, the coverage is currently available at 90 m spatial resolution obtained by resampling the 30 m ETM+ data. Radiometric consistency among all scenes in the northern database will allow generation of full-resolution mosaics consisting of any number of scenes and consistent land cover class labeling between scenes.

Source data

Landsat

Clear-sky Landsat-7 ETM+ level L1G orthoimagery was acquired from the Centre for Topographic Information (CTI) of Natural Resources Canada, the Yukon Government, the Canadian Forest Service, and the University of Maryland (UMd) Global Land Cover Facility (GLCF). These data consisted of top-of-atmosphere (TOA) ETM+ bands 3 (red: 0.63–0.69 μm), 4 (near infrared (NIR): 0.75–0.90 μm), and 5 (shortwave infrared (SWIR): 1.55–1.75 μm). Additional Landsat-5 TM data were downloaded from UMd. A total of 446 scenes were entered into the final mosaic, 437 of which were captured with Landsat-7 ETM+ from 14 July 1999 to 28 August 2002, 75% of which were acquired in the months of July and August at or near peak of the growing season. Landsat-5 scenes from 1989 and later were substituted where suitably clear Landsat-7 scenes were not available, mainly over the Rocky Mountains in the Yukon. Due to the relatively small area captured by each individual Landsat scene (approximately 185 km × 185 km), atmospheric conditions under clear skies are expected to be quite uniform, and therefore image normalization by means of linear transformation can be applied to relate Landsat TOA products to surface reflectance from VGT.

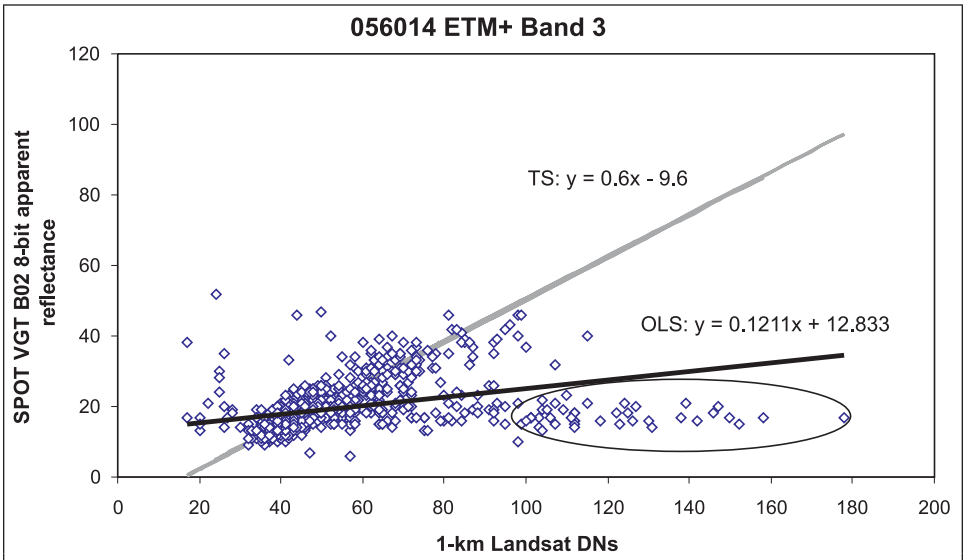

Figure 1. Ordinary least squares (OLS) and Thiel–Sen (TS) regressions showing the relative insensitivity of TS to haze and cloud outliers (circled) in the red band (ETM+ band 3) of scene 056014.

The CTI Landsat orthoimage dataset was created with the most accurate positional control data available at the time of creation (CTI, 2003). The imagery has been corrected with updated road network (URN) vector data, provincial vector data, accurate National Topographic Database (NTDB) data, federal aerotriangulation data, and other sources. The objective was to obtain an accuracy of 30 m or better in the south and 50 m or better in the north at a 90% confidence level. Other Landsat data were originally from the National Aeronautics and Space Administration (NASA) global orthorectified Landsat dataset, which has a geodetic root mean square accuracy of better than 50 m (Tucker et al., 2004).

One kilometre SPOT VGT

SPOT data consisted of a peak of growing season composite produced for the Global Land Cover 2000 project (GLC 2000) (Latifovic et al., 2004). Daily VGT-S01 data acquired between April and October 2000 consist of 1 km at-surface apparent reflectance bands in red (B02: 0.61–0.68 µm), NIR (B03: 0.78–0.89 µm), and SWIR (B04: 1.58–1.75 µm), which have wavelengths that are nearly identical to those of Landsat bands 3, 4, and 5, and six pseudobands specifying acquisition time and solar and view geometry (azimuth and zenith) for each pixel. Daily data were combined into 20 individual 10 day composites using a maximum normalized difference vegetation index (NDVI) criterion. The cloud elimination from composites using albedo and the NDVI trend (CECANT) algorithm (Cihlar, 1996; Cihlar et al., 1999) was used to cloud screen 10 day composites. Bidirectional distribution function (BRDF) normalization was performed to standardize 10 day composites to a common viewing geometry of 0° viewing angle and 45° solar zenith angle using the nonlinear temporal angular (NTAM) bidirectional reflectance model (Latifovic et al., 2003). Ten day composites were combined using a maximum NDVI criterion to produce the final peak of growing season composite, which was then scaled to eight bits for comparison to Landsat. Specific details on VGT data processing are presented by Latifovic et al. (2004).

Masks

The extent of the northern Landsat mosaic was approximately defined using a new 1 km resolution forest crown closure map of Canada (Leblanc et al., 2003) by selecting all terrestrial ecoregions (Ecological Stratification Working Group, 1996) with an average crown closure of less than 15%. Some ecoregions with closures larger than 15% were added to create a contiguous coverage. Imagery above 72.25° north latitude was also masked due to the northern limit of the VGT coverage. Perennial sea ice was removed by applying a mask generated from the 1 : 250 000 NTDB coastline vector coverage.

Compositing methods

Landsat scenes were resampled to 1 km resolution using the VGT point-spread function and then randomly sampled to generate approximately 1200 1-km Landsat pixels per scene with spatially coincident pixels from the VGT imagery. These data were used to generate Landsat scene-wise normalization functions using TS regression separately for red, NIR, and SWIR bands with the Landsat data as the regressor and VGT as the response variable. Once the set of normalization coefficients was finalized, scaling factors were applied to all normalization functions to minimize data compression or saturation of each band during normalization, as in Du et al. (2001). The scaled TS gain and offset coefficients were then

applied to the Landsat imagery on a per-scene and per-band basis. The few scenes that did not normalize well were identified with a visual quality check of the mosaic and adjusted by applying coefficients from an adjacent scene acquired during the same orbit, or by adjusting the offset slightly to minimize the appearance of seam lines.

Once the coefficients were finalized using the 1 km data, they were applied to the original Landsat images resampled to 90 m. Resampling was done by averaging 30 m pixels on a 3 pixel by 3 pixel basis, producing an effective spatial resolution of approximately 98 m in *x* and 94 m in *y* when the point-spread function of the ETM+ sensor is accounted for (NASA, 2005), and thus a minimum mapping unit of 0.92 ha. The normalized scenes were first mosaiced north to south along paths and east to west along rows. A second mosaic was generated by entering scenes in the opposite order, i.e., south to north along paths and west to east along rows. Each of these two mosaics represented one of two overlap areas between adjacent scenes. The best data in overlap regions from the two mosaics were selected using a maximum NDVI criterion to produce the final image data, as this criterion has been widely shown to preferentially select clear-sky pixels over haze or cloud for vegetated surfaces (Holben, 1986). Masks were applied to the final mosaic to remove unwanted data such as sea ice in the far north. (**Figure 2**).

Discussion

The database now consists of 446 georeferenced Landsat scenes containing bands 3, 4, and 5 and the normalization coefficients for each scene. A software tool has been developed so that any number of scenes within a range of specified paths and rows can be resampled to a desired resolution, normalized, and mosaiced. This tool will facilitate mapping regions of interest with more detail than what is currently provided in the 90 m northern database.

This data product demonstrates the application of the normalization technique developed in Olthof et al. (2005) to a large dataset for detailed national-level mapping. A thorough quantitative assessment of the product is beyond the scope of this research note, and readers are encouraged to refer to Olthof et al. for a comparative assessment of the methodology in relation to more conventional overlap normalization techniques. Although results based on a visual assessment of the product are encouraging, problems persist where within-scene variability exists due to phenology or atmospheric effects. Compositing techniques using multiple acquisitions of a given scene after TS normalization between acquisitions can be performed to produce clear-sky data or to infill scan line corrector-off data still being acquired by Landsat-7 (Orazietti et al., 2005).

An examination of individual spectral bands shows their relative sensitivity to variable atmospheric conditions. The NIR and SWIR bands normalized very well, as they appear to be seamless, whereas most residual inconsistencies visible in

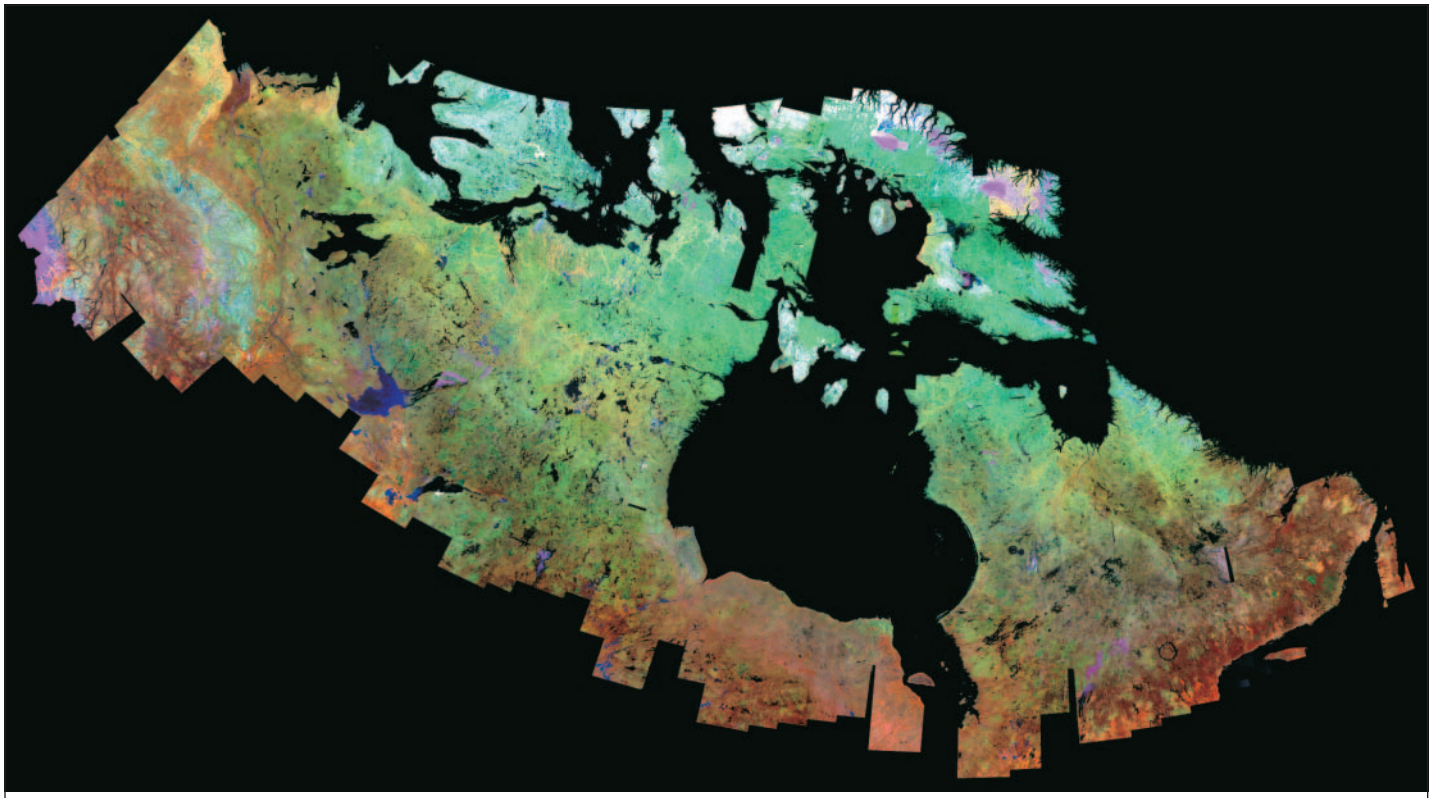

Figure 2. Normalized seamless 90 m ETM+ mosaic of northern Canada (446 scenes; ca. 2000).

Figure 2 remain due to aerosol, cloud–haze presence, and ozone variations in the red band. These effects may limit the ability to radiometrically normalize visible bands that are sensitive to such atmospheric effects (Kaufman et al., 1997). However, other band combinations from a number of medium-resolution sensors may be normalized provided that high-quality coarse-resolution composite data are available with spectral bands similar to those of the medium-resolution data. Several possible band combinations exist with medium-resolution sensors such as SPOT, advanced spaceborne thermal emission and reflection radiometer (ASTER), and imaging spectroradiometer (IRS) normalized to coarse-resolution data available from such sensors as the AVHRR, moderate-resolution imaging spectroradiometer (MODIS), and multiangle imaging spectroradiometer (MISR).

Residuals were examined at 1 km resolution on a mosaic consisting of a working set of 361 scenes for both the un-normalized and TS-normalized NIR band (**Figure 3**). The residual distributions show that the TS normalization reduced the bias in the residuals from 11.6 to 2.6 digital numbers (DN), and the standard deviations of the residuals indicate that the normalization decreased the radiometric variability relative to VGT surface reflectance. By reducing variability among scenes, the set of linear transformations applied to each scene should allow nationally consistent land cover mapping similar to that of the GLC 2000 project, which has been shown to be more accurate and spatially consistent in the north than other national 1 km land cover maps to which it was compared in Latifovic and Olthof (2004). Because the Landsat DNs were empirically calibrated to surface reflectance derived from SPOT VGT, the normalization technique also produces an atmospheric correction, and therefore data may also represent physical units of reflectance. When converted to units of VGT apparent reflectance, the 2.6 DN bias mentioned previously represents less than 0.7% reflectance. Given such a low bias between TS-normalized Landsat and VGT reflectance, generic

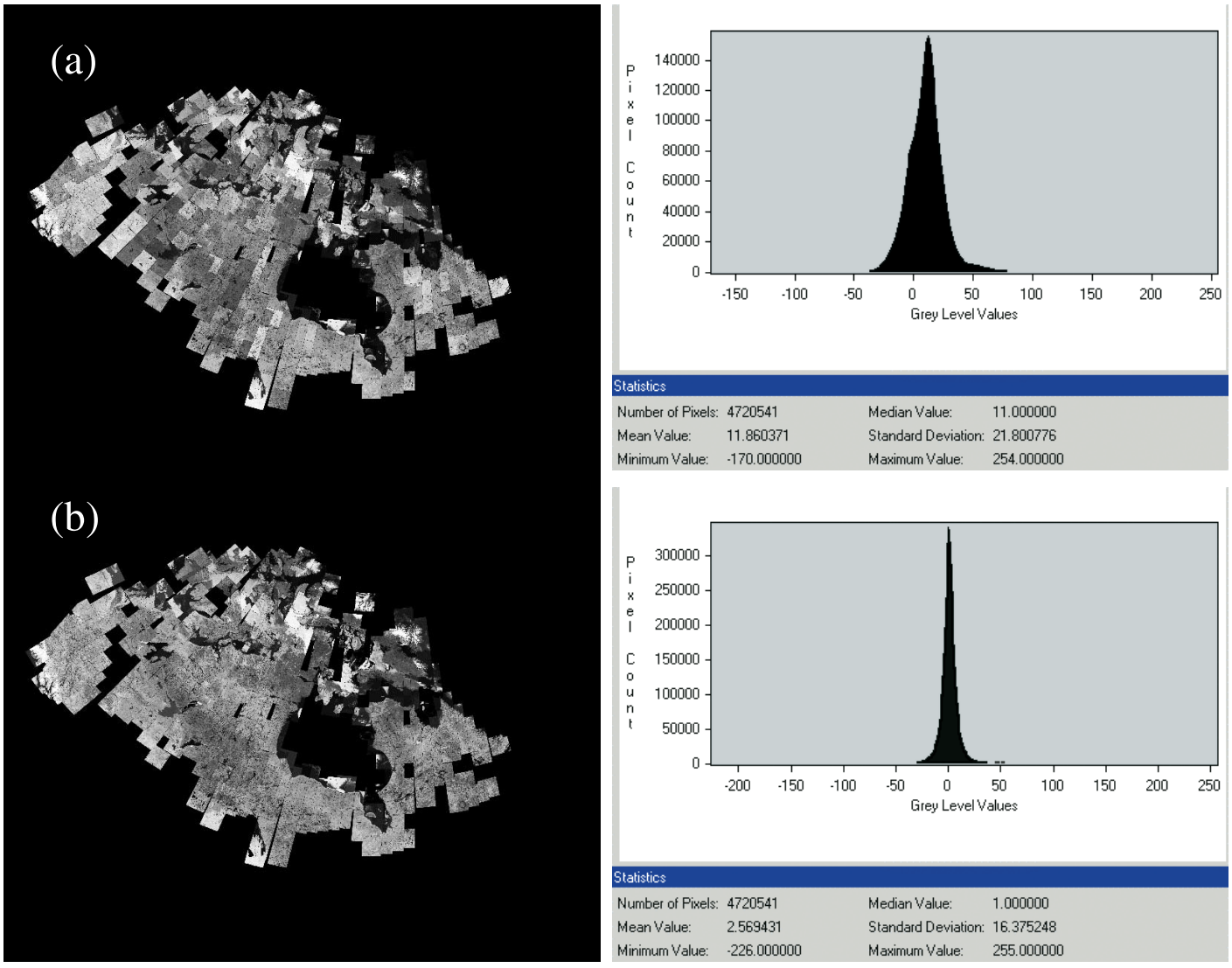

Figure 3. One kilometre un-normalized (a) and TS-normalized (b) NIR mosaics consisting of 361 scenes with corresponding residual distributions between 1 km Landsat and SPOT VGT.

algorithms developed to convert reflectance to biophysical units may be applied to these data to map biophysical parameters such as crown closure (Leblanc et al., 2005).

These data provide certain advantages over coarse-resolution imagery in the amount of detail they provide (**Figure 4**). Capturing this detail is essential to characterize land cover related to land use because many relevant cover types, such as roads and smaller developments, can only be detected at this scale. These data also have certain limitations, however. One of their primary limitations is that many of the 446 scenes were captured at a different time of year, representing a different stage of plant phenology within the growing season. Although every attempt was made to use scenes acquired during the peak of growing season (July–August), we were limited by the clear scenes that were available. Radiometric normalization can reduce the effects of phenology on data consistency but cannot remove them altogether due to the fact that different cover types exhibit different rates and timing of phenological development. Coarse-resolution imagery suffers from the same limitations, only to a lesser degree due to a shorter revisit time, thereby allowing selection of clear-sky data from a larger temporal sample. A medium-resolution data mosaic of this size must include data acquired at different times during the growing season and also spanning an approximate 5 year period to achieve an acceptable low level of atmospheric contamination. Updating of these data may be continuous as new data are acquired, but an entirely new picture of northern Canada cannot be expected for another 5 years. Thus, change detection using an update approach will include different time lags for different areas depending on data availability for a given location, whereas coarse-resolution data may be used to detect changes on an annual basis and generally as close to the peak of growing season as possible.

This dataset has numerous applications for those requiring detailed land cover and vegetation information over Canada's northern regions above the tree line and is currently available through the Geogratis portal at the GeoAccess Division of Natural Resources Canada.

Acknowledgements

The authors would like to acknowledge Joseph Cihlar, whose leadership and vision led to the development of much of the methodology presented in this paper. We gratefully

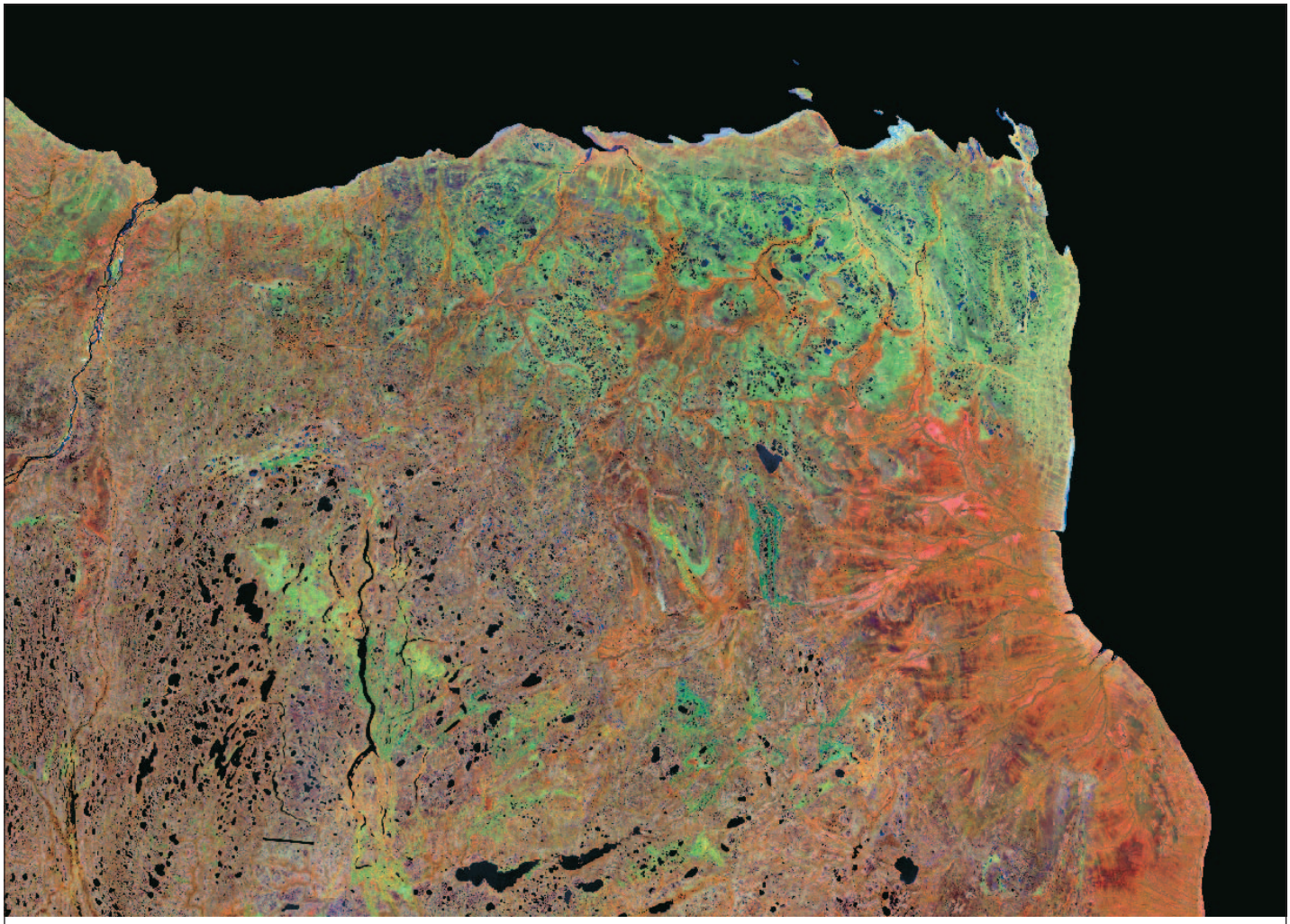

Figure 4. Blowup of 90 m data showing an area of the Hudson Bay Lowlands at the inlet of James Bay.

acknowledge Alexander Trichtchenko for constructive comments during preparation of this manuscript and Gunar Fedosejevs for internal review. This work was conducted as a joint collaboration between the Climate Change and Groundwater programs of the Earth Sciences Sector, Natural Resources Canada. Funding for this work was provided by the Canadian Space Agency through the Government Related Initiatives Program (GRIP) proposal EO-based view of our landmass in support of northern development. We also acknowledge Geomatics Yukon, Yukon Department of Infrastructure, for data.

References

Cihlar, J. 1996. Identification of contaminated pixels in AVHRR composite images for studies of land biosphere. *Remote Sensing of Environment*, Vol. 56, No. 3, pp. 149–163.

Cihlar, J., and Jansen, L.J.M. 2001. From land cover to land use: a methodology for efficient land use mapping over large areas. *Professional Geographer*, Vol. 53, No. 2, pp. 275–289.

Cihlar, J., Latifovic, R., Chen, J.M., and Li, Z. 1999. Testing near real-time detection of contaminated pixels in AVHRR composites. *Canadian Journal of Remote Sensing*, Vol. 25, No. 2, pp. 160–170.

CTI. 2003. *Landsat 7 orthorectified imagery over Canada, Level 1 product specifications, edition 1*. Centre for Topographic Information (CTI), Natural Resources Canada, Ottawa, Ont.

Du, Y., Cihlar, J., and Latifovic, R. 2001. Radiometric normalization, compositing, and quality control for satellite high resolution image mosaics over large areas. *IEEE Transactions on Geoscience and Remote Sensing*, Vol. 39, No. 3, pp. 623–634.

Ecological Stratification Working Group. 1996. *A national ecological framework for Canada*. Centre for Land and Biological Resources Research, Research Branch, Agriculture and Agri-Food Canada, and State of Environment Directorate, Environment Canada, Ottawa, Ont. Available from http://www.ec.gc.ca/soer-ree/English/Framework/framework.cfm.

Elvidge, C.D., Yuan, D., Weerackoon, R.D., and Lunetta, R.S. 1995. Relative radiometric normalization of Landsat Multi-spectral Scanner (MSS) data using an automatic scattergram-controlled regression. *Photogrammetric Engineering and Remote Sensing*, Vol. 61, No. 10, pp. 1255–1260.

Fernandes, R.A., and Leblanc, S.G. 2005. Parametric (modified least squares) and non-parametric (Theil–Sen) linear regressions for predicting biophysical parameters in the presence of measurement errors. *Remote Sensing of Environment*, Vol. 95, No. 3, pp. 303–316.

Gould, W.A., Edlund, S., Zoltai, S., Raynolds, M., Walker, D.A., and Maier, H. 2002. Canadian Arctic vegetation mapping. *International Journal of Remote Sensing*, Vol. 23, No. 21, pp. 4597–4609.

Holben, B. 1986. Characteristics of maximum-value composite images from temporal AVHRR data. *International Journal of Remote Sensing*, Vol. 7, No. 11, pp. 1417–1434.

Hope, A., Coulter, L., and Stow, D. 1999. Estimating lake area in an arctic landscape using linear mixture modelling with AVHRR data. *International Journal of Remote Sensing*, Vol. 20, No. 4, pp. 829–835.

Kaufman, Y.J., Wald, A.E., Remer, L.A., Gao, B., Li, R., and Flynn, L. 1997. The MODIS 2.1 µm channel — correlation with visible reflectance for use in remote sensing of aerosols. *IEEE Transactions on Geoscience and Remote Sensing*, Vol. 35, pp. 1286–1297.

Kendall, M.G., and Stuart, A.S. 1967. *Advanced theory of statistics. Vol. 2. Inference and relationship*. Charles Griffin and Company, London, UK.

Latifovic, R., and Olthof, I. 2004. Accuracy assessment using sub-pixel fractional error matrices of global land cover products derived from satellite data. *Remote Sensing of Environment*, Vol. 90, No. 2, pp. 153–165.

Latifovic, R., Cihlar, J., and Chen, J.M. 2003. A comparison of BRDF models for the normalization of satellite optical data to a standard sun–target–sensor geometry. *IEEE Transactions on Geoscience and Remote Sensing*, Vol. 41, No. 8, pp. 1889–1898.

Latifovic, R., Zhi-Liang, Z., Cihlar, J., Giri, C., and Olthof, I. 2004. Land cover mapping of North and Central America — Global Land Cover 2000. *Remote Sensing of Environment*, Vol. 89, No. 1, pp. 116–127.

Leblanc, S.G., Chen, W., and Fernandes, R.A. 2003. Forest cover indicator based on multi-scale remote sensing information. In *Proceeding of the 30th International Symposium on Remote Sensing of Environment*, 10–14 November 2003, Honolulu, Hawaii. CD-ROM. ISRSE Office of the Secretariat, Tucson, Ariz. 4 p.

Leblanc, S.G., Orazietti, J., Chen, W., Olthof, I., and Fernandes, R. 2005. Finding the tree-line: a quantitative derivation of forest cover estimates. In *Proceedings of the 31st International Symposium on Remote Sensing of Environment*, 20–24 June 2005, Saint Petersburg, Russian Federation. CD-ROM. ISRSE Office of the Secretariat, Tucson, Ariz. 3 p.

NASA. 2005. *Landsat-7 science data user's handbook*. National Aeronautics and Space Administration (NASA), Goddard Space Flight Center (GSFC), Greenbelt, Md. Available from http://ltpwww.gsfc.nasa.gov/IAS/handbook/handbook_toc.html.

Olthof, I., Pouliot, D., Fernandes, R., and Latifovic, R. 2005. Landsat ETM+ radiometric normalization comparison for northern mapping applications. *Remote Sensing of Environment*, Vol. 95, No. 3, pp. 388–398.

Orazietti, J., Olthof, I., and Fraser, R. 2005. Landsat 7 SLC-off gap-filling for interim data continuity in northern regions using a robust radiometric normalisation technique. In *Proceedings of the 26th Canadian Remote Sensing Symposium*, 14–16 June 2005, Wolfville, NS. Canadian Aeronautics and Space Institute, Ottawa, Ont. In press.

Serreze, M.C., Walsh, J.E., Chapin, F.S., III, Osterkamp, T., Dyurgerov, M., Romanovsky, V., Oechel, W.C., Morison, J., Zhang, T., and Barry, R.G. 2000. Observational evidence of recent change in the northern high-latitude environments. *Climatic Change*, Vol. 46, Nos. 1–2, pp. 159–207.

Stow, D.A., Hope, A., McGuire, D., Verbyla, D., Gamon, J., Huemmrich, F., Houston, S., Racine, C., Strum, M., Tape, K., Hinzman, L., Yoshikawa, K., Tweedie, C., Noyle, B., Silapswan, C., Douglas, D., Griffith, B., Jia, G., Epstein, H., Walker, D., Daeschner, S., Petersen, A., Zhou, L., and Myneni, R. 2004. Remote sensing of vegetation and land-cover change in Arctic Tundra Ecosystems. *Remote Sensing of Environment*, Vol. 89, No. 3, pp. 281–308.

Tucker, C.J., Grant, D.M., and Dykstra, J.D. 2004. NASA's global orthorectified Landsat data set. *Photogrammetric Engineering and Remote Sensing*, Vol. 70, No. 3, pp. 313–322.

Veldkamp, A., and Fresco, L.O. 1996. CLUE: a conceptual model to study the conversion of land use and its effects. *Ecological Modelling*, Vol. 85, pp. 253–270.

Vogelmann, J.E., Howard, S.H., Yang, L., Larson, C.R., Wylie, B.K., and Van Driel, N. 2001. Completion of the 1990s national land cover data set for the conterminous United States from Landsat Thematic Mapper data and

ancillary data sources. *Photogrammetric Engineering and Remote Sensing*, Vol. 67, No. 6, pp. 650–662.

Walker, D.A., Gould, W.A., Maier, H.A., and Raynolds, M.K. 2002. The Circumpolar Arctic Vegetation Map: AVHRR-derived base maps, environmental controls, and integrated mapping procedures. *International Journal of Remote Sensing*, Vol. 23, No. 21, pp. 4551–4570.

Wulder, M.A., Dechka, J.A., Gillis, M.A., Luther, J.E., Hall, R.J., Beaudoin, A., and Franklin, S.E. 2003. Operational mapping of the land cover of the forested area of Canada with Landsat data: EOSD land cover program. *Forestry Chronicle*, Vol. 79, pp. 1075–1083.

CASI Corporate Partners / IASC membres corporatifs

AeroVations Associates
39 Westpark Drive, Gloucester, ON K1B 3G6, Canada
Contact: Gerry Marsters
Tel: (613) 837-9326, Fax: (613) 837-9326
E-mail: marsters@celeris.ca
www.aerovations.com

COM DEV INTERNATIONAL
155 Sheldon Drive, Cambridge, ON N1R 7H6
Contact: Mr. Tony Stajcer
Vice President, Research and Development
Tel: (519) 633-2300, Ext. 2231, Fax: (519) 622-1691
E-mail: tony.stajcer@comdev.ca

BELL HELICOPTER TEXTRON
DIVISION OF TEXTRON CANADA LTD.
12 800 rue de l'Avenir Mirabel, QC J7J 1R4
Contact: Dennis Lacroix, Marketing Director, Canada
Tel: (450) 437-3400, Fax: (450) 437-2006
E-mail: dlacroix@bellhelicopter.textron.com

CONCORDIA UNIVERSITY
Concordia Institute for Aerospace Design and Innovation (CIADI)
1455 de Maisonneuve Blvd. W.
Montreal, QC H3G 1M8
Contact: Dr. Hany Moustapha
Director
Tel: (514) 848-7931
Fax: (514) 848-7890
E-mail: Hany.Moustapha@pwc.ca

BOMBARDIER AEROSPACE
P.O. Box 6087, Station Centre-Ville, Montréal, QC H3C 3G9
Contact: Mr. Pierre Beaudoin, President and COO
Tel: (514) 855-7900, Fax: (514) 855-7903

CRESTech
4850 Keele Street, Toronto, ON M3J 3K1
Contact: Mr. Richard Worsfold
Director, Business Development
Tel: (416) 665-3311, Fax: (416) 665-2032
E-mail: enquiries@crestech.ca

CANADIAN ARMED FORCES – AIR FORCE
National Defence Headquarters
MGen George R. Pearkes Building
101 Colonel By Drive, Ottawa, ON K1A 0K2
Contact: Col R.M. Williams, Director, Air Strategic Planning
Tel: (613) 995-9565, Fax: (613) 995-0063

DYNACON INC.
3565 Nashua Drive
Mississauga, ON L4V 1R1
Contact: Mr. Stephen J. Sorocky, CEO
Tel: (905) 672-8828, Fax: (905) 672-8829
E-mail: sjs@dynacon.ca

CANADIAN SPACE AGENCY
6767 route de l'Aéroport, Saint-Hubert, QC J3Y 8Y9
Contact: CSA Communications Directorate
Tel: (450) 926-4800, Fax: (450) 926-4352
www.space.gc.ca

EMS TECHNOLOGIES
21025 Trans Canada, Ste-Anne de Bellevue, QC H9X 3R2
Contact: Mr. J. Gareth Lewis
Vice President, Sales and Marketing
Tel: (514) 425-3077, Fax: (514) 425-3005

CARLETON UNIVERSITY
Mechanical and Aerospace Engineering
1125 Colonel By Drive, Ottawa, ON K1S 5B6
Contact: Professor Paul Straznicky
Tel: (613) 520-5684, Fax: (613) 520-5715
E-mail: pstrazni@mae.carleton.ca

GASTOPS LTD.
1011 Polytek Street, Ottawa, ON K1J 9J3
Contact: Mr. Dave Muir, V.P. Marketing and Sales
Tel: (613) 744-3530, Fax: (613) 744-8846

IMP GROUP INTERNATIONAL INC.
Aerospace Division, P.O. Box 970, Enfield, NS B2T 1L5
Contact: Mr. Carl F. Kumpic, VP International Marketing
Tel: (902) 873-2250, Fax: (902) 873-2290
E-mail: carl.kumpic@impaerospace.com
www.impgroup.com/impaero

MACDONALD DETTWILER AND ASSOCIATES LTD.
13800 Commerce Parkway, Richmond, BC V6V 2J3
Contact: Wendy Keyzer, Manager, Marketing Support Dept.
Tel: (604) 278-3411, Fax: (604) 278-2936
www.mda.ca

MANNARINO SYSTEMS & SOFTWARE INC.
10 345 Papineau, Suite 250, Montreal, QC H2B 2A3
Contact: John Mannarino
E-mail: info@mss.ca
Tel: (514) 381-1360 Ext. 31, Fax: (514) 381-7511

MARINVENT CORPORATION
50 Rabastaliere East, Suite 23
St-Bruno, QC J3V 2A5, Canada
Contact: John Maris
Tel: (450) 441-6464, Fax: (450) 441-2411
E-mail: info@marinvent.com

MESSIER-DOWTY INC.
574 Monarch Avenue, Ajax, ON L1S 2G8
Contact: Mr. Tim Whittier, Director
Marketing and Business Development
Tel: (905) 683-3100, Fax: (905) 686-2914

INSTITUTE FOR AEROSPACE RESEARCH
NATIONAL RESEARCH COUNCIL CANADA
Montreal Road, Ottawa, ON K1A 0R6
Contact: Mr. J. Mackwood, Marketing Manager
Tel: (613) 990-0765, Fax: (613) 952-7214
E-mail: jeff.mackwood@nrc-cnrc.gc.ca
www.nrcaerospace.com

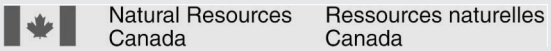

CANADA CENTRE FOR REMOTE SENSING
588 Booth Street, Ottawa, ON K1A 0Y7
Contact: Willy Bruce
Tel: (613) 996-2648, Fax: (613) 996-9843
E-mail: Willy.Bruce@NRCan.gc.ca
www.ccrs.nrcan.gc.ca

PRATT & WHITNEY CANADA
1000 Marie Victorin Blvd, Longueuil, QC J4G 1A1
Contact: Dr. Hany Moustapha, Manager
P&WC Technology Programs
Tel: (450) 647-7593, Fax: (450) 647-3336
E-mail: Hany.Moustapha@pwc.ca

QUEEN'S UNIVERSITY
99 University Avenue
Kingston, ON K7L 3N6, Canada
Contact: Mr. Thomas J. Harris
Dean, Faculty of Applied Science
Professor of Chemical Engineering
Tel: (613) 533-2000, Fax: (613) 533-6500
E-mail: harris@post.queensu.ca
www.queensu.ca

ROYAL MILITARY COLLEGE OF CANADA
P.O. Box 17000, Station Forces, Kingston, ON
K7K 7B4
Contact: LCdr Douglas Burrell, Ph.D.
Tel: (613) 541-6000 Ext. 6340
E-mail: Douglas.Burrell@rmc.ca

RYERSON UNIVERSITY
SCHOOL OF AEROSPACE ENGINEERING
Department of Mechanical, Aerospace and Industrial Engineering
350 Victoria St., Toronto, ON M5B 2K3, Canada
Contact: Kamran Behdinan, Ph.D., P.Eng.
Tel: (416) 979-5000 Ext. 6414
Fax: (416) 979-5265
E-mail: kbehdina@ryerson.ca

Telesat Canada
1601 Telesat Court, Gloucester, ON K1B 5P4
Contact: Roger Tinley, Vice-President
Space Systems
Tel: (613) 748-0123 Ext. 2339
Fax: (613) 748-8712
E-mail: info@telesat.ca

TRANSPORT CANADA
Safety and Security Group, 12th Tower C, Place de Ville
330 Sparks Street, Ottawa, ON K1A 0N8
Contact: Mr. William Elliott, Assistant Deputy Minister
Tel: (613) 990-3838, Fax: (613) 990-2947
E-mail: elliowj@tc.gc.ca

TRANSPORTATION SAFETY BOARD OF CANADA (TSB)
1901 Research Road, Bldg. U-100, NRC Uplands
Ottawa, ON K1A 1K8
Contact: Mr. Jim Foot, Acting Director, Engineering Branch
Tel: (613) 990-0913, Fax: (613) 998-5572

UNIVERSITY OF ALBERTA
FACULTY OF ENGINEERING
E6-050 Engineering Teaching and
Learning Complex
Edmonton, AB T6G 2V4
Contact: Dr. David Lynch
Tel: (780) 492-3596, Fax: (780) 492-0500
E-mail: david.lynch@ualberta.ca

UNIVERSITY OF CALGARY
DEPARTMENT OF GEOMATICS ENGINEERING
2500 University Dr. NW, Calgary, AB T2N 1N4
Contact: Marguerite Anderson
Tel: (403) 220-5834, Fax: (403) 284-1980
E-mail: geomatics@geomatics.ucalgary.ca
www.geomatics.ucalgary.ca

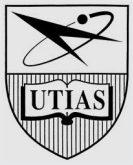

UNIVERSITY OF TORONTO
INSTITUTE FOR AEROSPACE STUDIES
4925 Dufferin Street, Toronto, ON M3H 5T6
Contact: Dr. Tony Haasz
Tel: (416) 667-7717, Fax: (416) 667-7743
E-mail: aahaasz@utias.utoronto.ca

Types of Contributions to the Canadian Journal of Remote Sensing

Research Article

A Research Article is the most common type of manuscript submitted to CJRS. Peer-reviewed research in remote sensing applications and methodology involves original contributions that apply the scientific method to new problems involving the acquisition, processing, validation, and interpretation of remotely sensed data and (or) its application within a geographic context. These contributions must be more than a collection of accepted or previously published facts: they must be the proof or rejection of a hypothesis; research risk must be involved.

In observational sciences such as remote sensing, the risk may be difficult to perceive since papers might test or compare known or previously published methods on new or old datasets, or might consider new sensors of fundamentally similar design. In these cases, the acid test for peer-reviewed approval is whether the authors: (*i*) apply appropriate, pertinent, and innovative testing/evaluation procedures or tools and (*ii*) provide methodological or applications insight that enhances understanding beyond a mere observational presentation of data.

Research Note

A Research Note is usually a shorter contribution than a Research Article. They are normally comprised of up to six double-spaced pages with up to four accompanying figures. This is original work that shows potential and innovation, but where it may be too early to perform a comprehensive validation. We strive for rapid publication of Research Notes, and we encourage the electronic submission of papers in this category, preferably via e-mail. All interactions with the author and reviewers are via e-mail.

Review Paper

A Review Paper is a review of an application or methodology that is normally made by a senior researcher who has the capacity to analyze the theoretical and experimental ramifications of previous research with a global perspective. This unique viewpoint should contribute to a clear understanding and synthesis of past work and provide innovative guidelines as to which directions future research should or will take. Typically it should delineate (or extrapolate to) an algorithm, methodology, or process that best synthesizes and generalizes previous work. This type of contribution is not intended to be a bibliographic summary or a tutorial. It is also not intended as a forum for reviewing remote sensing policy issues or for projecting organizational trends.

Technical Note

A Technical Note may include, for example, the technical specifications of hardware or software systems, critiques or corrections of past papers, book or thesis reviews, bibliographic summaries, market surveys, tutorials, and case studies.

A more detailed discussion on the types of papers in CJRS and guidelines for reviewers appear in the document General Guidelines for Associate Editors & Reviewers, which can be found on the CASI Web site at http://www.casi.ca/index.php?pg=cjrs.

Types de contribution au Journal canadien de télédétection

Article de recherche

L'article de recherche est le genre de document plus communément soumis pour publication dans le JCT. La recherche passée en revue par les pairs, pour les applications de la télédétection et de la méthodologie, implique les contributions originales qui appliquent la méthode scientifique à de nouveaux problèmes comportant la saisie, le traitement, la validation, et la traduction des données de la télédétection et/ou de son application dans un contexte géographique. Ces contributions doivent être plus qu'une collection de faits reçus ou précédemment édités: elles doivent être la preuve ou le rejet d'une hypothèse; le risque de recherches doit être impliqué.

En sciences d'observation telles que la télédétection, le risque peut être difficile à percevoir puisque les articles pourraient tester ou comparer des méthodes connues ou précédemment éditées sur de nouveaux ou vieux ensembles de données; ou encore, pourraient considérer de nouveaux capteurs de conception fondamentalement semblable. Dans ces cas, le critère d'approbation d'une revue par les pairs dépendrait des conditions suivantes: les auteurs auraient: (*i*) appliqué les procédures appropriées, convenables, et innovatrices ou les derniers outils de test/évaluation, et (*ii*) fournit un aperçu de méthodologie ou d'applications qui met en valeur la compréhension au delà d'une seule présentation d'observation des données.

Note de recherche

Une note de recherche est habituellement une contribution plus courte qu'un article de recherche. Cette note est ordinairement composée de jusqu'à six pages espacées doubles avec jusqu'à quatre figures d'accompagnement. C'est un travail initial qui montre le potentiel et une innovation, mais où il peut être trop tôt pour exécuter une validation complète. Nous essayons d'obtenir la publication rapide des notes de recherches, et nous encourageons la soumission électronique des papiers dans cette catégorie, de préférence par l'intermédiaire du courriel. Toutes les interactions avec l'auteur et les critiques sont par l'intermédiaire du courriel.

Article de revue

Un article de revue est l'examen d'une application ou d'une méthodologie qui est ordinairement faite par un chercheur aîné qui a la capacité d'analyser les ramifications théoriques et expérimentales de la recherche précédente avec une perspective globale. Ce seul point de vue devrait contribuer à une compréhension et à une synthèse claires de travail passé et fournir les directives innovatrices dirigeant les recherches futures. Typiquement, il devrait tracer (ou extrapoler) un algorithme, une méthodologie, ou un processus qui mieux synthétise et généralise les travaux précédents. Ce type de contribution n'est pas destiné pour être un sommaire bibliographique ou un cours d'instruction. On ne le destine également pas comme forum pour passer en revue les aspects politiques de télédétection ou pour projeter des tendances d'organisation.

Note technique

Une note technique peut inclure, par exemple, les caractéristiques techniques des systèmes de matériel ou logiciels, des critiques ou des corrections d'anciens papiers, des revues de livre ou de thèse, des sommaires bibliographiques, des études de marché, des cours d'instruction, et des études de cas.

Un texte plus détaillé sur les types de contribution au JCT et les directives aux lecteurs est présenté dans le document Directives générales pour les rédacteurs associés et les membres du comité de lecture sur la page Web au http://www.casi.ca/index.php?pg=cjrs.

Postage paid at Ottawa
Publications mail
Registration No. 40069141

Port payé à Ottawa
Poste-publication
Enregistrement n° 40069141

USPS periodical postage paid at Champlain, NY 12919

October 2005 octobre

Volume 31, No. 5

Canadian Journal of Remote Sensing / Journal canadien de télédétection
Contents / Table des matières

Special issue
Earth observation of Canada's landmass: results and future needs
A workshop in honour of Josef Cihlar on the occasion of his retirement
Ottawa, 30 September – 1 October 2004

Numéro spécial
L'observation satellitaire de la masse continentale canadienne : résultats et besoins futurs
Un atelier en l'honneur de Josef Cihlar à l'occasion de son départ à la retraite
Ottawa, 30 septembre – 1 octobre 2004